UNIVERSITY OF OKLAHOMA
GRADUATE COLLEGE

FREQUENCY-AGILE FILTERING ANTENNAS FOR S-BAND AND X-BAND APPLICATIONS

A THESIS
SUBMITTED TO THE GRADUATE FACULTY
in partial fulfillment of the requirements for the
Degree of
MASTER OF SCIENCE

By
ROSALIND AGASTI
Norman, Oklahoma
2023

FREQUENCY-AGILE FILTERING ANTENNAS FOR S-BAND AND X-BAND APPLICATIONS

A THESIS APPROVED FOR THE
SCHOOL OF ELECTRICAL AND COMPUTER ENGINEERING

BY THE COMMITTEE CONSISTING OF

Dr. Hjalti Sigmarsson, Co-Chair

Dr. Jessica Ruyle, Co-Chair

Dr. Kiersten C Kerby-Patel

Dr. Jay McDaniel

Acknowledgments

I want to express my deepest gratitude to my advisors, Dr. Jessica Ruyle and Dr. Hjalti Sigmarsson, for their continual support and guidance throughout the past two years. They have taught me to approach every research roadblock patiently and embrace each challenge with a curious and learning mindset. I am blessed to have had such great mentorship during the preliminary years of my research career.

I could not have undertaken this journey without the encouragement of my undergraduate advisor and committee member, Dr. KC Kerby-Patel. She has always guided me toward the right opportunities and projects while offering me advice at critical junctions of my career. Additionally, I would like to sincerely thank Dr. Jay McDaniel for agreeing to be a part of my thesis committee and taking the time to improve the quality of my thesis by providing constructive feedback.

I am thankful to my fellow research group member Adrian Bauer for helping me understand the world of filtennas through our long lab discussions. I would be remiss in not mentioning the immense help and training provided by Dr. Nawaf Almuqati in the fabrication processes of my designs. I appreciate the help provided by Dale Sexton to improve the quality of my design prototypes. My sincere thanks also go to Clayton Blosser for his assistance with the high-power measurements presented in this thesis.

It would have been impossible for me to complete my thesis work without the moral support and company of my friends at ARRC, including Adrian Bauer, Clayton Blosser, César Salazar, Jorge Alva, Gökhan Arıtürk, Mark Cash, Elizabeth Joyce, Nim Ccoillo

Ramos, Emily King, and many others. I would also like to thank my best friends from back home, Simran Kapoor and Saumya Sharma, for being there for me through challenging times. Finally, and most importantly, I want to express my deepest gratitude to my wonderful family–it wouldn't do justice to write out what I feel about them; words are not enough.

Table of Contents

List of Figures

List of Tables

Abstract

Multi-functional, highly flexible, and tightly integrated Radio-Frequency Front-Ends (RFFEs) are at the forefront of the current developments to improve the performance of next-generation wireless RF systems. In the past decade, filtering antennas, or filtennas, have emerged as a potential solution to minimize the Radio-frequency system's cost and complexity while maximizing performance in a highly integrated module. The RF co-design approach of combining the filtering and radiation functionalities into a single unit is beneficial for improving a system's Signal-to-Noise (SNR) performance while limiting interference in a congested frequency spectrum. Furthermore, frequency-agile filtennas can enhance an RF system's adaptation to changing radio environments.

The work presented in this thesis utilizes conventional bandpass filter synthesis techniques to enhance the performance of tunable filtennas for next-generation RFFEs. By using high-Q Evanescent-mode (EVA-mode) cavity resonators and highly efficient slot antennas, multiple filtenna designs are demonstrated. First, the building blocks of the filtennas are individually developed. A novel Evanescent-mode Cavity-Backed Slot Antenna (ECBSA) with contactless capacitive tuning is designed for radiation functionality. Long-range external linear actuators are deployed to tune the critical gap size of the cavity. Experimental results of the antenna demonstrate a high power-handling capacity and wide tuning from 1.7 GHz to 2.6 GHz (40%). The ECBSA is then integrated with a contactless-tuned EVA-mode resonator to form a 2nd-order tunable filtenna. The fabricated filtenna demonstrates frequency tuning from 2-2.6 GHz (26%), with a peak realized gain ranging from 2.7 dB to 5.2 dB.

The filtenna showed excellent tuning reliability due to the deployed closed-loop monitoring system and exhibits state-of-the-art performance in the class of tunable cavity-based filtennas.

The frequency scalability of the tunable filtenna is next investigated in the X-band (8-12 GHz) frequency regime. A new filtenna structure and tuning scheme is conceptualized by incorporating varactor diodes on a novel superstrate-loaded cavity-backed slot antenna. The performance trade-offs and loss analysis is completed by analyzing the resistive losses associated with tuning varactors. In addition, a new technique is proposed to estimate a varactor's quality factor for high-frequency applications. The proposed method does not require any calibration or de-embedding processes. The varactor-Q estimation technique can effectively estimate the bias and frequency-dependent varactor quality factor for any reconfigurable RF application.

Chapter 1

Introduction

1.1 Overview

With the rapid development of next-generation technologies like Software-defined Radio (SDR) and cognitive radio (CR), there is an ever-increasing demand for the next-generation Radio-Frequency Front-End (RFFE) systems to possess multi-functional capabilities [1]. These technologies are being developed as a solution to the issue of a crowded frequency spectrum by deploying a “sense, adapt, and learn” algorithm, where the surrounding radio environment can be evaluated, and the system can adapt to it accordingly. Such a radio-environment monitoring capability can potentially maximize spectral efficiency, connectivity, and security.

A major constituent of the CR and SDR technology is the RF Front-end, which is at the forefront of receiving and transmitting information to and from the module, as seen in Fig. 1.1. To sense the spectrum and alter the operational parameters of the system (like frequency, bandwidth, etc.), the RF front-end (RFFE) is required to accommodate some flexibility in its operational parameters over a wide frequency range.

In addition to these stringent requirements, the system must also meet the size, weight, and power (SWaP) requirements. In most RF systems, SWaP seems to be the key driving factor, providing difficult trade-offs over system performance enhancement and multi-functional

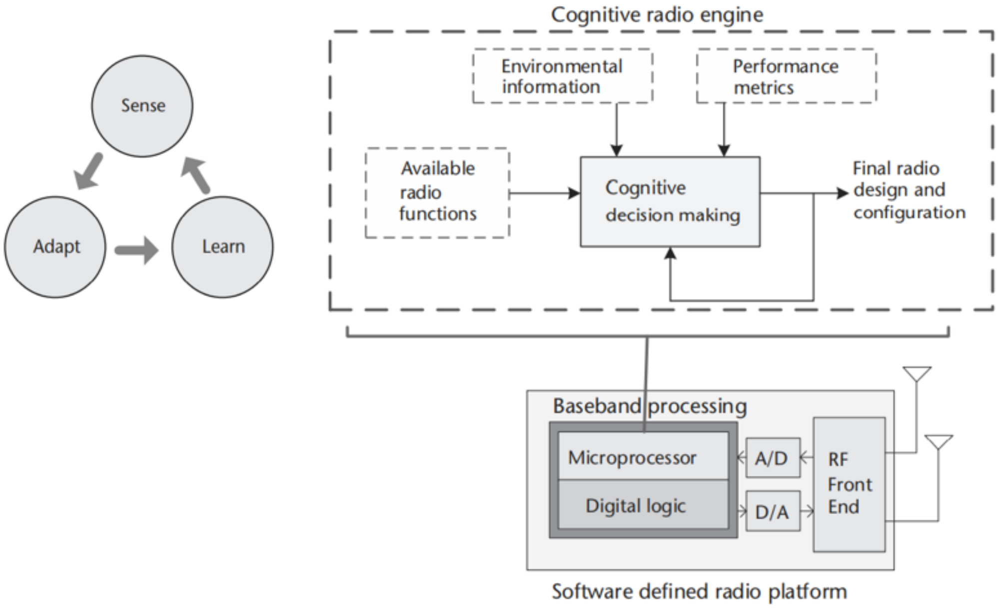

Figure 1.1: Concept diagram of a cognitive radio engine operating on a software-defined radio platform. As a result of CR's ability to sense, adapt, and learn about its surrounding radio environment, it requires the communication system it operates on to be highly versatile. [1]

architectures. For instance, Satellite Communication (SAT-COM) systems need to meet the ongoing demands for global coverage while also maximizing payload efficiency [2]. These space-borne systems need to feature greater onboard functionality without compromising the SWaP requirements of the system. Therefore, the RF communication system must be carefully designed to exhibit higher performance flexibility while maintaining a small footprint.

Based on the above discussion, the major demands on the next-generation Radio-Frequency Front-ends (RFFEs) can be broadly categorized as follows:

- Multi-functional systems with frequency agility
- Tightly integrated and miniaturized RF module
- Meet the system's SWaP requirements

1.2 Developments in RFFE Architectures

Traditionally, a high-performance RF front-end consists of a wideband antenna connected to a larger switchable filter bank through transmission line interfaces. The filters can switch across a wide frequency range and reject any unwanted interference signals from the frequency band of operation. The large bandwidth of the antenna facilitates a larger coverage of operational frequencies over which the signals can be transmitted or received. Despite such a system's large frequency band coverage, there are several drawbacks. Firstly, the filter bank and wideband antenna inevitably result in a bulky system and are not ideal for applications with strict SWaP requirements. Secondly, the broader bandwidth of the antenna results in passing a higher amount of noise signals, which results in low system performance in terms of the Signal-to-Noise Ratio (SNR).

As a solution to the issue of large switchable filter banks, reconfigurable filters have been extensively developed to replace the filter banks to maintain a small profile while also ensuring multi-functionality in the system [3]-[5]. A further improvement in this direction has been made by also incorporating frequency reconfigurability into the antennas [6]-[8]. A fixed wide-band antenna can degrade system performance by passing more interference signals spread out across a wide range of frequency bands. Instead, a single tunable narrowband antenna can provide greater frequency selectivity in a compact size while reducing co-site interference and jamming. Therefore, incorporating frequency agility into filters and antennas can significantly enhance the multi-functional capabilities of the RF front-ends.

In the past decade, a new class of integrated RF modules has been developed by combining the filtering and radiation functionalities into a single device. These integrated units, known as 'filtennas' or filtering antennas, can replace the cascading connection between a filter and an antenna to realize a tightly-integrated RF module. The filtenna offers several

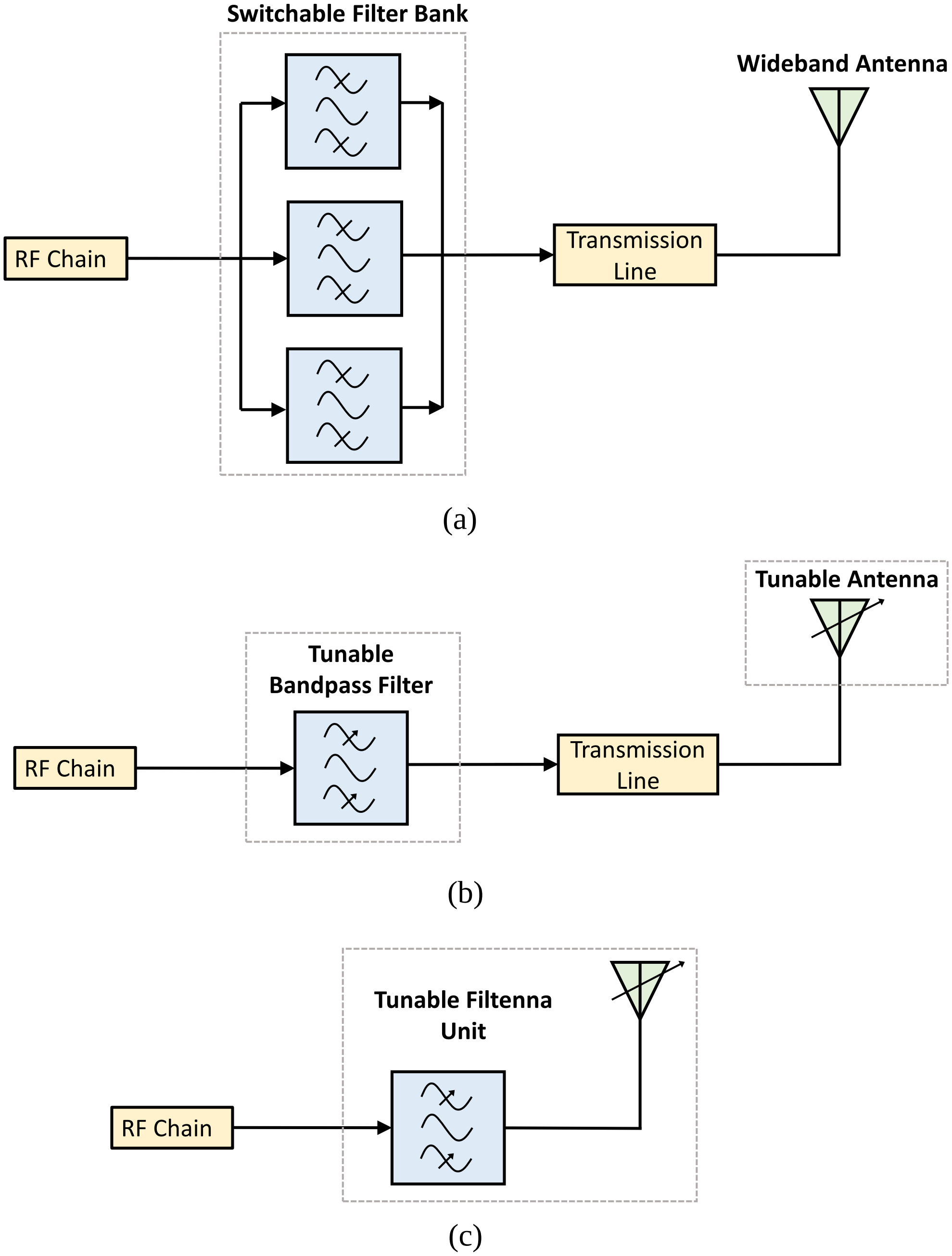

Figure 1.2: Developments in high-performance RF Front-end architectures (a) Traditional design with cascaded filter bank and wideband antenna (b) reconfigurable filter and reconfigurable antenna architectures (c) Tunable filtering antenna (filtenna) unit

advantages over the individual filter-antenna cascaded unit. The first obvious benefit is the overall improvement in the system's SWaP requirements due to a compact and miniaturized module. The second advantage is the removal of transmission line losses from the filter-antenna interface. Typically, the 50 Ω transmission line has a considerable electrical length to ensure minimum field coupling between the filter and antenna. This results in an increased footprint and significant losses that may cause higher system noise. Note that the antenna and filter are positioned at the very front of the RFFE chain. Therefore any losses in the first block of the architecture have the highest impact on the system's overall noise performance [9].

Compared to the antenna's in-band gain response, a typical filter response is flatter in the passband and sharper along the edges. When the antenna and filter are designed to have overlapping pass-bands, the response at the band edges can degrade and lead to unwanted signal distortions [10]. In a properly co-designed filtenna architecture, the antenna and filter are seamlessly integrated to eliminate any degradation in the filter response. Additionally, the filtenna has better out-of-band radiation suppression due to the incorporated filtering functionality than a conventional antenna. This makes the filtenna a good candidate for applications where interference due to cross-coupling between closely-spaced elements needs to be eliminated.

1.3 Filtenna Synthesis Techniques

Several methods have been presented in the current literature to design and implement a filtenna unit. Most of the proposed designs can be categorized into three broad categories - (i) the direct-integration or cascaded filter-antenna approach, (ii) the fusion method, and (iii) filtenna synthesis based on coupled-resonator theory using bandpass filter synthesis.

In the direct-integration approach of filtenna design, filtering circuits are directly cascaded into the antenna structure either through a matching network [11]-[13], or directly into the feed circuitry of the antenna [14]-[16]. The concept of directly-integrated filtenna is illustrated in Fig. 1.3(a). The main goal of this design methodology is to eliminate the use of lossy and complex transitional networks between the filter and antenna. However, this method still requires independent design and implementation of the filter and antenna section. The discontinuities between the two passive devices also lead to parasitic modes, affecting overall radiation performance. The imperfect connection between the filter-antenna interface due to bandwidth mismatches in the two devices may cause signal distortions at the band edges. The design and implementation of filtennas using the direct-integration approach does not lead to significant SWaP benefits or system performance improvements.

A recently popular filtenna design approach, more oriented towards the antenna's performance optimization, involves the elimination of any filtering circuits and is known as the fusion technique. The basic concept is to shape the gain response of the antenna to resemble that of a bandpass filter as seen in Fig. 1.3(b). Eliminating additional filtering circuits removes the effect of insertion loss on the overall system, thereby improving the noise performance. The gain response of the antenna is shaped by adding resonant structures in parallel with the antenna to realize radiation nulls across frequencies. These parasitic structures resonate outside the antenna's passband and typically do not affect the in-band radiation performance. One of the drawbacks of the fusion method is the design complexity involving the generation and placement of transmission zeroes in the gain response. There is limited control over the bandwidth of the in-band gain response, and the out-of-band rejection level is not as high as a typical filtering response.

A different method to design and implement filtennas is by applying the coupled-resonator theory commonly used for synthesizing bandpass filters. In a conventional bandpass filter, resonators form the building blocks, which are electromagnetically coupled with each other to attain a specific filtering performance. When applied to the design of filtennas, the antenna replaces the last resonator of the bandpass filter. As seen in Fig. 1.4, the resonator is represented by an equivalent LC tank circuit, and the antenna is modeled

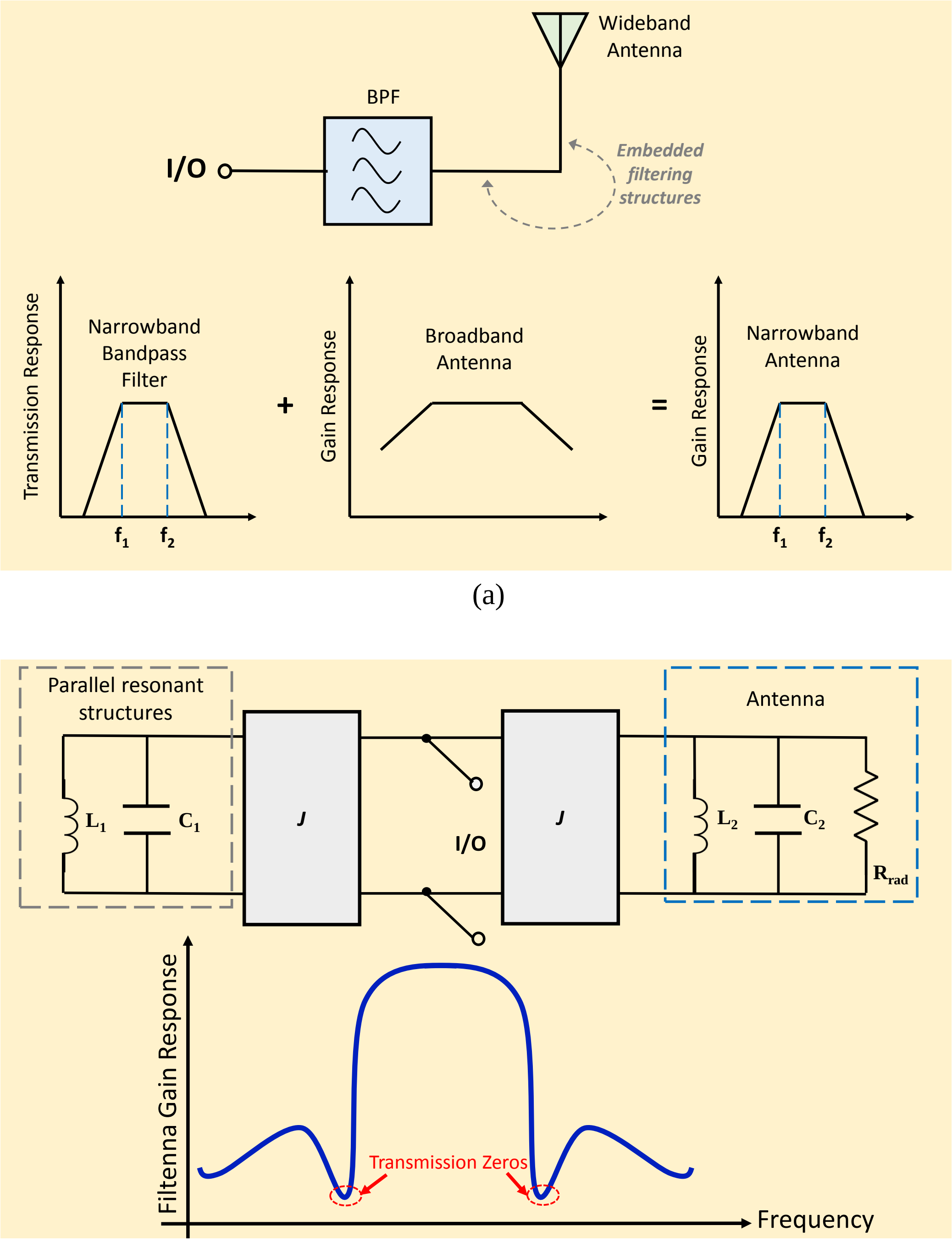

(a)

(b)

Figure 1.3: Filtenna Design Approaches (a) Tradition Cascaded design with a narrowband band-pass filter attached to the end of a broadband antenna (b) Fusion technique of filtenna synthesis without any additional filtering circuits. Adapted from [10].

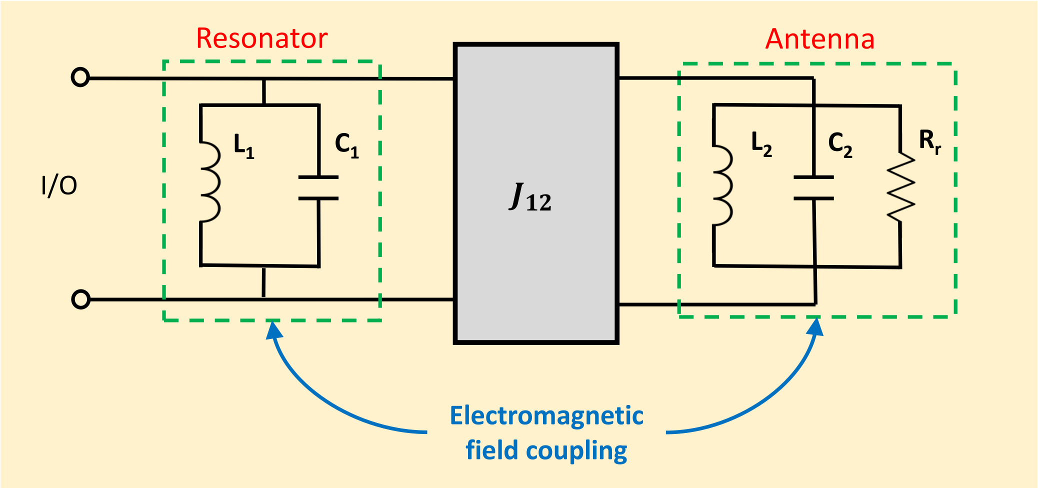

Figure 1.4: Coupled-resonator synthesis method representation for a second-order filtenna consisting of a resonator, represented by an LC tank circuit, and the antenna. The antenna is modeled as a shunt resistor–inductor–capacitor resonator, with R representing the radiation resistance. The J-inverter, J_{12}, represents the coupling between them.

as a lossy resonator with the resistance corresponding to the radiation losses. The antenna performs double duty by contributing an additional pole to the filtering response while also performing the radiation functionality in the same module. Due to the elimination of an additional resonator, there are immediate SWaP benefits for the overall system. Additionally, the coupled-resonator method of filter synthesis enables seamless integration of the filter and

Table 1.1: Summary of different filtenna synthesis techniques

Method	**Description**	**Advantage**	**Limitation**
Direct Integration	BPF cascaded into antenna feed directly, or through a matching network	Elimination of complex transitional interfaces	Signal distortions at band-edges, and large footprint
Fusion Technique	Parasitic resonant structures added to the antenna; create transmission zeros in gain response	No insertion loss from extra-filtering circuits	Low out-of-band radiation suppression and complex design
Coupled-Resonator Method	Antenna functions as the last resonator of a BPF and contributes to filtering response	Compact module due to lesser resonators and higher out-of-band rejection	Insertion loss of filter absorbed into antenna efficiency

antenna, with greater control over the filtering characteristics of the antenna, including the out-of-band rejection performance. The in-band performance of the antenna in the filtenna configuration is almost identical to that of the individual antenna structure. Given these advantages, the bandpass filter synthesis method of filtenna design has been applied in the design of filtennas throughout this work.

1.4 Reconfigurable Filtennas

Since a filtenna combines the functionalities of the two crucial passive devices constituting the RF front end– filters and antennas – it is an ideal candidate for applying the concept of frequency reconfigurability. The multi-functional capabilities of a frequency tunable filtenna can further reduce the requirement of implementing different units to achieve functional diversity, thereby attaining a more compact RF system with improved SWaP benefits.

Frequency reconfigurability is attained by incorporating a tuning element into the passive structure. In an ideal scenario, a tuning element should exhibit low loss, low dc power consumption, good linearity, high RF power handling, wide tuning range, high reliability and precision, low area usage, and is preferably continuously tunable with a high tuning speed. In practicality, no single tuning scheme can simultaneously satisfy all these requirements. An appropriate tuning element is chosen based on its feasibility of integration into the passive structure and the device's intended applications.

Several tuning methods have been investigated in designing and implementing frequency-agile filtenna designs. The most commonly used tuning scheme is electronic tuning through active switching elements like semiconductor varactor diodes and PIN diodes [18]-[29]. Semiconductor tuning elements are of particular interest due to their compact structure, high tuning speeds, and ease of availability. A PIN diode can be operated in two modes - the ”ON” state, which is forward-biased, and the ”OFF” state, which is unbiased. As a result,

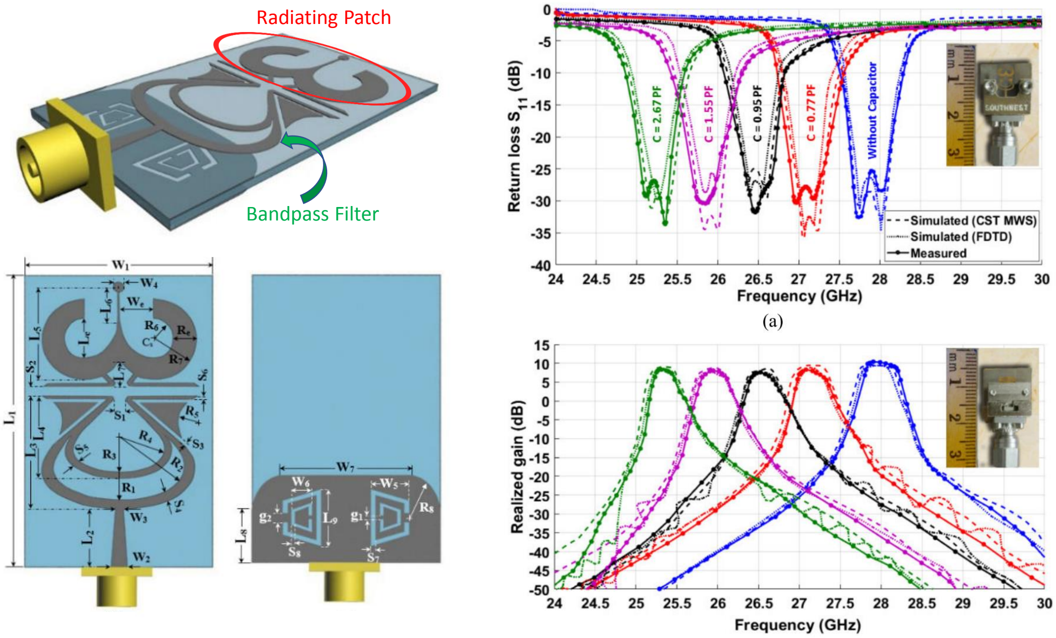

Figure 1.5: Filtenna using DGS Structures proposed in [17]. The tuning concept is demonstrated by using varying values of lumped capacitors. A direct-integration approach is used to combine the radiating and filtering sections.

discrete frequency tuning states can be achieved by incorporating PIN diodes into the filtenna structure [23]-[29]. In [29], a frequency-reconfigurable filtenna was designed by integrating two PIN diodes into the filtering section. The filtenna is synthesized using coupled-resonator theory and consists of an interdigital E-shaped resonator (IER), an interdigital coupler (IC), and a slot antenna. Measured results showed that the device could operate at 5.2/5.5 GHz with 1.21 dBi/2.32 dBi peak gains within the passband in the ON/OFF states, respectively.

For applications that require continuous frequency reconfiguration, semiconductor varactor diodes can be used in place of PIN diodes [18]-[30]. With varying bias voltages, the variable junction capacitance of the varactor can be used to tune the capacitive reactance in the passive structure. In [18], Tawk et al. presented a design in which a varactor-diode tuned bandpass filter is incorporated into the feed-line of a wide-band Vivaldi antenna. Tuning is achieved from 6.16-6.47 GHz, and the maximum antenna gain is 6.77 dB at the highest tuning frequency. Alternatively, in [20], a third-order planar filtenna was designed by applying filter synthesis techniques to couple a patch antenna with two hairpin resonators. Tuning varactor diodes were integrated into the filtering and radiating sections, and two frequency-agile filtennas were presented. The first design demonstrated an increasing bandwidth in the tuning range from 1.62-2.08 GHz, with the gain increasing from -7.3 to 3.6 dBi. The second filtenna exhibited a nearly static bandwidth across the tuning range from 1.65-1.9 GHz, with a gain variation from -6.1 dBi to 4.3 dBi.

Despite the popularity of PIN diodes and varactors in reconfigurable filtenna designs, they exhibit some serious limitations in terms of increased RF losses, complex bias circuitry, low-power handling as well as degraded linearity performance [31]-[33]. Alternatively, optical reconfiguration techniques can be used to prevent non-linear behavior due to intermodulation distortions and avoid RF losses due to DC biasing networks. An optically-tuned filtenna using photo-conductive switches is presented in [34], where a defected microstrip structure (DMS) is used as the bandpass filter and is integrated with a printed patch antenna. The photo-conductive switch operates from ”OFF” to ”ON” mode when the electrons move from the valence band to the conduction band. This is achieved by illuminating the switch with an appropriate light wavelength through a laser diode. A disadvantage of optical switches is their lossy behavior and complex activation mechanism needed for using laser diodes.

Generally, mechanical reconfiguration schemes using tuning elements like metal screws or movable posts demonstrate a higher performance in terms of low losses, good linearity, and a relatively high power-handling capacity. In [35], a millimeter-wave horn filtenna is presented with mechanical tuning screws to vary the center frequency from 17.4 GHz to 24 GHz. The filtenna is a metal-based implementation and is realized by combining dual-post resonators with a pyramidal horn antenna. Another mechanically tunable filtenna using tuning screws was presented in [36], where a coaxial cavity-based filter is formed within a standard rectangular waveguide. The open port of the waveguide is used as the

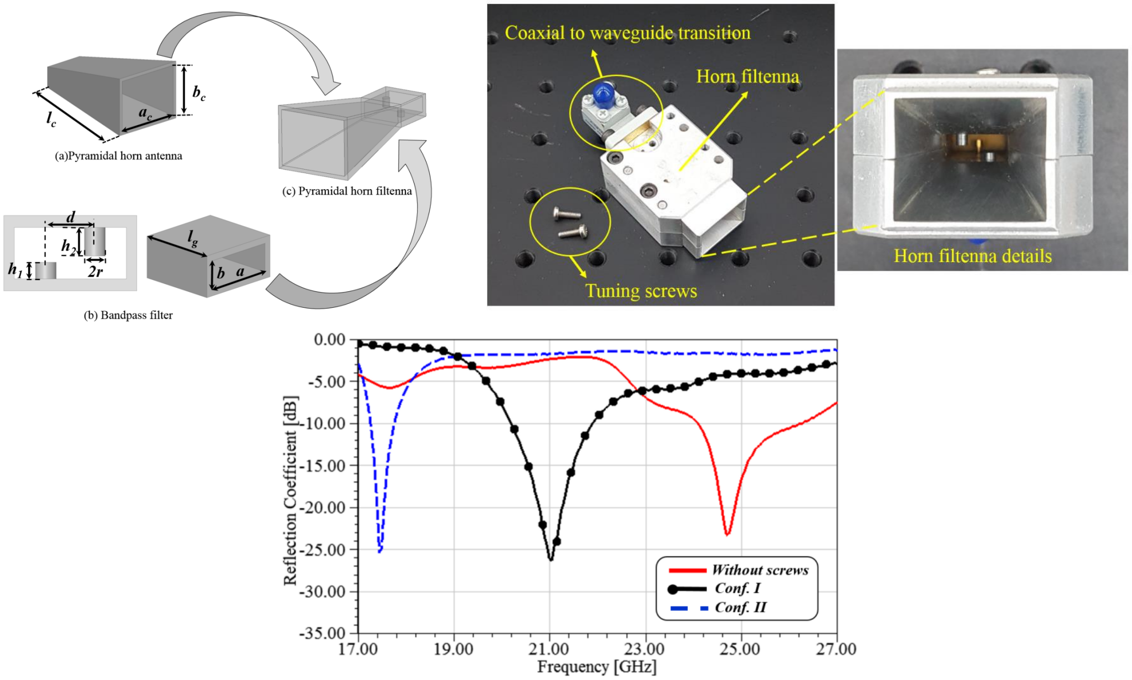

Figure 1.6: Mechanically-tuned mm-wave filtenna presented in [35]. Tuning screws are used to reconfigure the center frequency of the dual-post cavity resonators in the filtering section.

radiating port, and tuning screws are accommodated in the preceding resonators to change the frequency and bandwidth of the filtenna. The tunable range of center frequency is from 9.25 GHz to 10.75 GHz, while the fractional bandwidth is tuned from 2% to 8%.

The mechanically-tunable filtennas in [35] and [36] are expected to handle high powers and demonstrate a linear performance due to the metal-based passive structures. However, one of the drawbacks of such metal-based structures is that they are inevitably bulky and cannot be easily integrated with other planar Printed-circuit Boards (PCB) RF designs. The problem regarding the integrability of metal-based structures into other planar RF devices can be solved by transitioning to a Substrate-Integrated Waveguide (SIW) implementation. Mechanical reconfiguration in a SIW-based filtenna is presented in [37], where electronically-controlled piezoelectric disks and linear actuators tune the filtenna's center frequency across S-band from 2-4 GHz. The piezoelectric disks are controlled through external bias voltage to tune the resonator's frequency. At the same time, linear actuators are deployed to physically

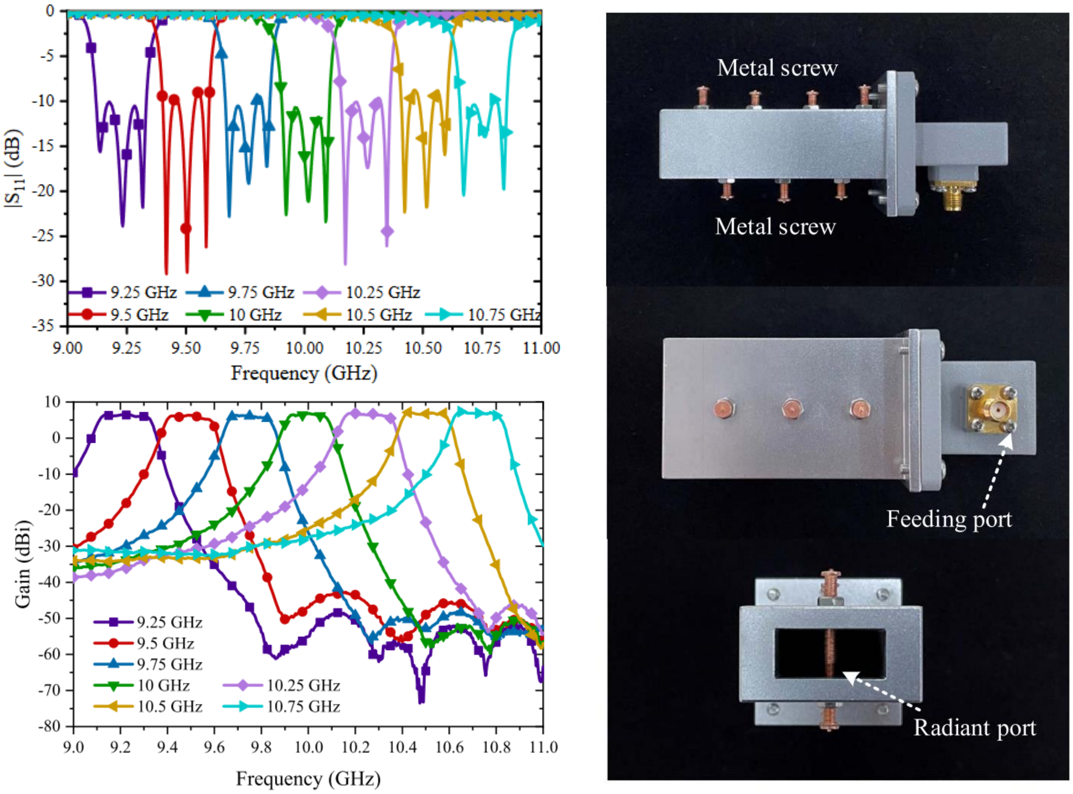

Figure 1.7: Mechanically-tuned multi-order filtenna using metal-based coaxial resonators topology presented in [36]

move a metal post that sits at the aperture of a slot antenna. The device was predicted to handle a power greater than 23 dBm across the entire tuning range and up to a maximum of 42 dBm at 4 GHz.

Despite the performance benefits of mechanical tuning, one of the drawbacks is that the achievable tuning speed is very low, especially when compared to semiconductor switches that exhibit tuning speeds in the range of microseconds. Additionally, there are potential problems with tuning reliability of mechanical actuation elements due to the necessary physical displacements, which result in repetitive stress, mechanical fatigue, or wear of one or more components over time.

A summary of the widely-used tuning schemes in current filtenna literature is given in Table 1.2. As a result of the different performance trade-offs in the present state-of-the-art

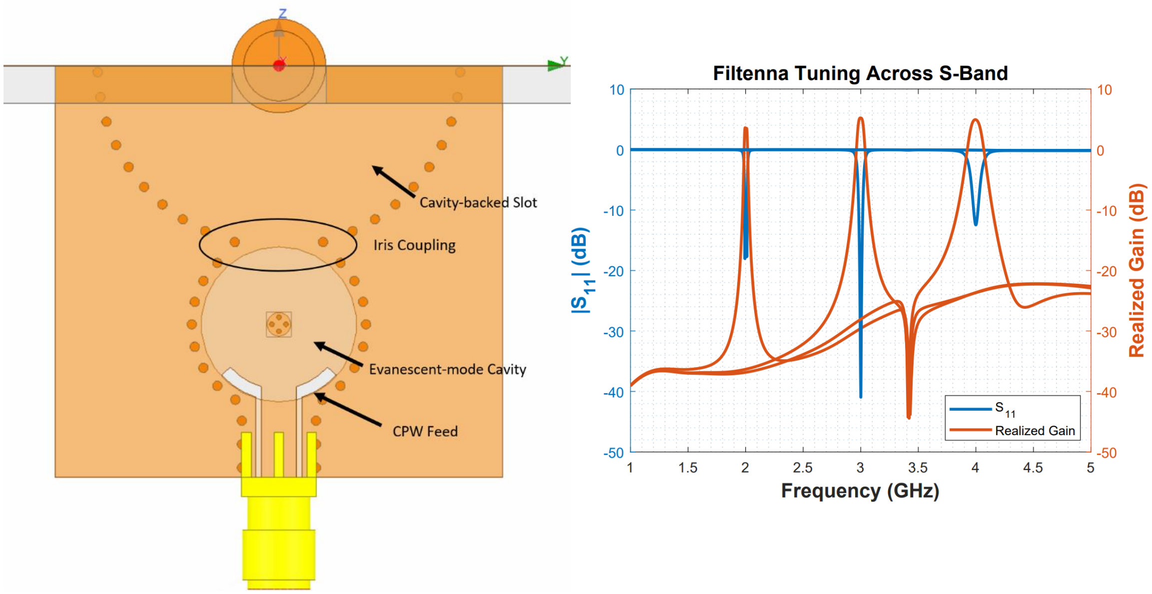

Figure 1.8: Octave-tunable filtenna presented in [37] for S-Band (2-4 GHz) applications.

Table 1.2: Performance comparison of popular tuning schemes used in tunable filtennas

Technique	Components	Attributes
Semiconductor diodes	- PIN diodes - Varactors	- Discrete tuning with PIN diode - Continuous tuning with varactor diode - Easy integration and high response time - Low to medium bias voltages - Low power handling and linearity - Low quality factor and higher losses
Optical	- Photoconductive switch	- No bias circuitry required - High linearity performance - Laser diode activation required - Switches may add losses
Mechanical	- Tuning screws, posts - Piezoelectric actuators - Motor Actuators	- Continuous tuning states - High power-handling and linearity - Low reliability and tuning speeds

tuning technologies, the current literature on tunable filtennas has not been extensively explored, especially for high-frequency applications above 6 GHz. Due to the space limitations at higher microwave frequencies, there are several challenges in accommodating a tuning mechanism into the passive RF module. Furthermore, the loss mechanisms at higher frequencies are more pronounced, and the chosen tuning scheme should not further add losses and degrade the overall system performance. Due to these difficulties, few tunable filtenna designs have been demonstrated at higher frequencies. Simple electrical-size scaling of the designed tunable filtenna from a lower to a higher frequency does not work, and a complete redesign of the filtenna structure and tuning scheme is necessary.

1.5 Thesis Outline

This thesis aims to investigate various performance trade-offs in state-of-the-art tuning technologies and, based on that knowledge, implement frequency-agile filtennas. Since the accommodation of tuning elements into the filtenna structure is particularly challenging for high-frequency applications, the frequency scalability of a tunable filtenna element is also investigated in this work. An essential aspect of the present work is ensuring the proposed designs' manufacturing feasibility while optimizing the filtenna's performance across the tuning range.

In Chapter 2, the fundamental theory behind the design of microwave filters using coupled-resonator theory is discussed. The conventional filter synthesis techniques are applied in filtenna design to integrate the radiating element into a bandpass filter seamlessly. Furthermore, the process of time-domain tuning, which is applied to quickly tune filtennas throughout this work, is briefly explained.

The design and implementation of the first building block of a filtenna, which is a tunable microwave resonator, is detailed in Chapter 3. The evanescent-mode cavity topology is used to realize the filtenna's first resonator. The resonator's theoretical modeling and SIW implementation with a contactless-capacitive tuning scheme are detailed. The resonators are designed, fabricated and tested for S-band and X-band applications.

Chapter 4 details the design of a second-order contactless-tuned filtenna for S-band applications. First, a tunable cavity-backed slot antenna, which functions as the last building block of the filtenna, is simulated and fabricated. The antenna is then seamlessly integrated into a tunable filtenna using filter synthesis techniques described in Chapter 2. As a proof-of-concept, the filtenna is fabricated, and experimental results indicate that the filtenna can operate across a frequency range of 2 GHz to 2.6 GHz.

In Chapter 5, the frequency scalability of the filtenna element for X-band (8-12 GHz) applications is investigated. Electronic reconfiguration with varactor diodes is applied in the design of a novel superstrate-loaded cavity-backed slot antenna. Two different prototypes of the antenna are presented to highlight the trade-offs between tuning and radiation performance. In the last section of the chapter, the varactor-tuned superstrate loaded slot antenna is integrated into a tunable filtenna structure for X-band applications.

Chapter 6 details the practical limitations of tuning varactors for applications at microwave frequencies. Given that varactor diodes are used to implement a frequency-agile antenna and filtenna for X-Band, the practical non-idealities of tuning varactors needed to be evaluated. Specifically, the effects of a varactor's quality factor on an antenna's radiation efficiency are addressed. Finally, a theoretical method of determining the quality factor of a varactor diode is presented and validated through simulations.

In Chapter 7, a summary of the thesis work is presented, and the scientific impact is highlighted. Additional future work is proposed to extend the performance scope of the proposed frequency-agile filtennas.

Chapter 2

Filtenna Design and Theory

In this chapter, the fundamental procedure of designing microwave filters is described and applied to design filtennas. The basic concept of filter theory using coupled resonators can be almost directly applied in filtenna design. However, since a filtenna incorporates a radiating element as the last resonator, the procedure for synthesizing the desired filtering response from a filtenna topology needs to be reconsidered. In order to efficiently and quickly tune filtennas, a method of tuning filters in the time domain is applied throughout this work. A basic summary of the time-domain tuning method, as applied in the design of filtennas, is outlined at the end of the chapter.

2.1 Coupled Resonator Filter Theory

The general design of a filter starts with a low-pass prototype ladder network which uses ideal capacitors and inductors as the building blocks [38]-[40]. The values of the elements are defined by a set of filter coefficients called g-coefficients that generate a certain filter type. For instance, the g-coefficients of an Nth-order Butterworth or maximally flat filter are

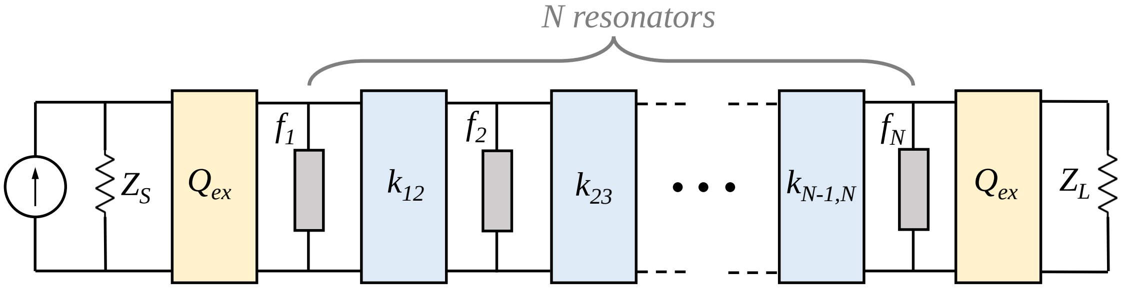

Figure 2.1: Circuit diagram of an Nth-order coupled-resonator filter (assuming only mainline coupling). The resonant frequency of each resonator (f_N) and the respective field coupling between the resonators as well as the external ports, are shown.

given by the closed-form expressions [39],

$$g_0 = g_{N+1} = 1 \tag{2.1a}$$

$$g_k = 2sin\left(\frac{(2k-1)\pi}{2N}\right) \text{ for k = 1,2,3, ...,N} \tag{2.1b}$$

where g_0 and g_{N+1} correspond to the normalized source and load resistances or conductances, and g_k represents the value of either a series inductor or a shunt capacitor.

The abstract low-pass prototype filter can be easily transformed to generate a high-pass, band-pass, or band-stop filter response at the desired frequency and terminal port impedances for the system. This method of filter design based on the transformation of low-pass ladder prototype networks is well-established and can be directly implemented for realizing lumped element and planar filters [38]-[40].

Another design approach that Dishal proposed in [41] is more useful for synthesizing direct-coupled resonator filters. The filter network is modeled by the different resonators and coupling elements, as shown by the circuit diagram in Fig. 2.1. Considering a mainline coupling topology and synchronous frequency tuning, the main parameters for filter synthesis are: the external quality factor at the input port into the first resonator Q_{ex1}, the external quality factor at the output port Q_{ex2}, the inter-resonator coupling coefficient $k_{i,i+1}$, and the synchronous resonant frequency of each resonator f_0. The values of the coupling coefficients and the input/output quality factors are related to the g-coefficients of the low-pass prototype and the fractional bandwidth, Δ, given as [39] [41],

$$Q_{ex1} = \frac{g_0 g_1}{\Delta}, \;\; Q_{ex2} = \frac{g_N g_{(N+1)}}{\Delta}, \;\; k_{i,i+1} = \frac{\Delta}{\sqrt{g_i g_{i+1}}} \text{ for i = 1 to } (N-1) \tag{2.2}$$

By mapping the coupling coefficients and external quality factors to the physical dimensions of the filter, the desired filtering response can be synthesized. The design curves relating the coupling value and the physical design dimensions of the filter are generally extracted using full-wave electromagnetic (EM) solvers.

2.1.1 Input External Coupling

The external quality factor, Q_{ex1}, at the input port of the first resonator, is generally extracted by simulating a singly-terminated resonator [42]. The phase response of the reflection function at the input port of the resonator can be used to determine Q_{ex1}. In order to isolate the effect of the port on the first resonator, the loading effects of the excitation port on the remaining resonators must be eliminated. Therefore, either all the other resonators are short-circuited, or a singly-loaded resonator is used to extract the design curve for the input external coupling, Q_{ex1}.

Based on the phase response of the reflection function S_{11}, as illustrated in Fig. 2.2, Q_{ex1} is calculated by determining the points about the center frequency, ω_0, where the phase response changes by $\pm 90^\circ$, given as

$$Q_{ex1} = \frac{\omega_0}{\Delta\omega_{\pm 90^\circ}} \tag{2.3}$$

where $\Delta\omega_{\pm 90^\circ}$ is the absolute bandwidth between the $\pm 90^\circ$ points, as depicted in Fig. 2.2.

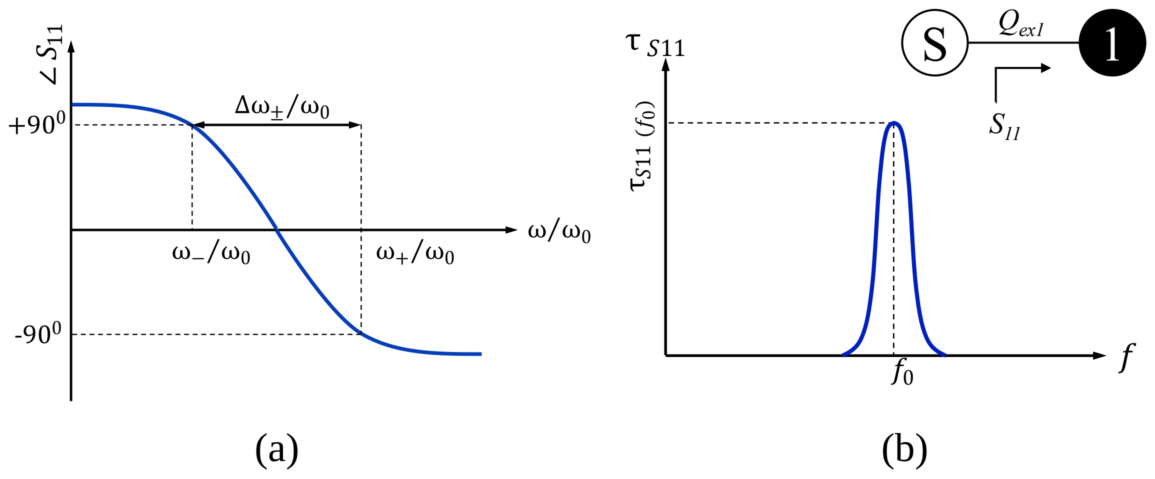

Figure 2.2: Method for extracting input external Q of a singly-terminated microwave resonator from (a) the phase response of reflection coefficient, and (b) the group-delay of the reflection response

Alternatively, the input external coupling can also be determined from the peak group delay of the reflection coefficient $\tau_{S_{11}}(f_0)$ given by the relation,

$$Q_{ex1} = \frac{2\pi f_0 \, \tau_{S_{11}}(f_0)}{4} \tag{2.4}$$

It should be noted that the reference plane of S_{11} in the EM simulation may include an extra phase shift such that the phase of S_{11} is not centered around zero at resonance. Corresponding to the phase shift, an extra group delay may be added, which can be accounted for by properly de-embedding the reference plane for S_{11} in the simulation.

The external quality factor at the input port, for both a conventional filter and a filtenna, typically corresponds to a 50-Ω feed line termination into the first resonator. Therefore, the technique of extracting the input external coupling from a singly-loaded resonator can be directly applied in the design of filtennas.

2.1.2 Inter-Resonator Coupling

Based on the general theory of electromagnetic coupling, the coupling coefficient k of coupled microwave resonators, irrespective of the specific physical structure, is defined on the basis of a ratio of coupled to stored energy given as [42],

$$k = \frac{\iiint \epsilon \underline{E}_1 \cdot \underline{E}_2 \, dv}{\sqrt{\iiint \epsilon |\underline{E}_1|^2 \, dv \times \iiint \epsilon |\underline{E}_2|^2 \, dv}} + \frac{\iiint \mu \underline{H}_1 \cdot \underline{H}_2 \, dv}{\sqrt{\iiint \mu |\underline{H}_1|^2 \, dv \times \iiint \mu |\underline{H}_2|^2 \, dv}} \tag{2.5}$$

where $\underline{E_1}$ and $\underline{E_2}$ represent the electric field vector of the first and the second resonator, respectively, and $\underline{H_1}$ and $\underline{H_2}$ represent the magnetic field vectors in the two resonators, as seen in the concept diagram Fig. 2.3. The volume integrals of the fields encompass entire affecting regions with permittivity of ϵ and permeability of μ. All the fields are determined at the resonant frequency of the two resonators. In Eq. (2.5), the first term represents the electric-field coupling between the two resonators, while the second term represents the magnetic coupling.

A direct evaluation of the coupling coefficient using Eq. (2.5) requires full knowledge of the field distributions and the space integrals, which are complicated to determine for a given physical structure. Instead, full-wave EM simulations are generally used to determine the coupling coefficient. A general method to extract the value of inter-resonator coupling is by using the *split-pole* technique [39][42]. In Fig. 2.4, the concept of splitting the resonant poles of two resonators is depicted. The two-coupled resonators, synchronously tuned at a frequency of f_0, are weakly coupled at the input and output ports to minimize the effects of reactive loading from the ports. With an increased overlap of fields between the coupled resonators, the magnitude response of the transmission coefficient shows a double peak response. Due to the interaction between the two resonators, the resonant modes degenerate, and the frequencies split into multiple modes.

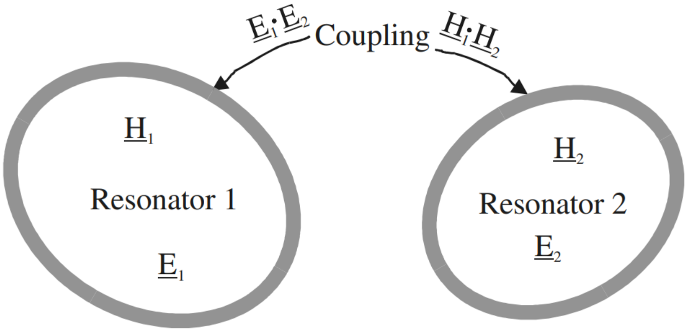

Figure 2.3: General concept of inter-resonator field coupling, as presented in [42].

The main effect of the coupling coefficient is on the bandwidth of the synthesized filter. An increase of field interaction between coupled resonators results in a larger separation between the split-peaks observed in Fig. 2.4, corresponding to a larger value of k. The mathematical expression for determining the coupling coefficient is related to the locations of the split peaks f_a and f_b given as [42],

$$k = \frac{f_b^2 - f_a^2}{f_b^2 + f_a^2} \tag{2.6}$$

A universal formulation for the coupling coefficient that can be applied for both synchronously and asynchronously tuned coupled resonators with electric, magnetic, or mixed-coupling mechanisms is given by the following equation [42],

$$k = \pm\frac{1}{2}\left(\frac{f_{02}}{f_{01}} + \frac{f_{02}}{f_{01}}\right)\sqrt{\left(\frac{f_b^2 - f_a^2}{f_b^2 + f_a^2}\right)^2 - \left(\frac{f_{02}^2 - f_{01}^2}{f_{02}^2 + f_{01}^2}\right)^2} \tag{2.7}$$

If the resonant frequencies of the first resonator f_{01} and the second resonator f_{02} are the same, then Eq. (2.7) reduces to Eq. (2.6). The sign of the coupling is dependent on the physical coupling structure, and the meaning of positive or negative coupling is rather relative. If a particular coupling is referred to as a positive coupling, then the coupling that

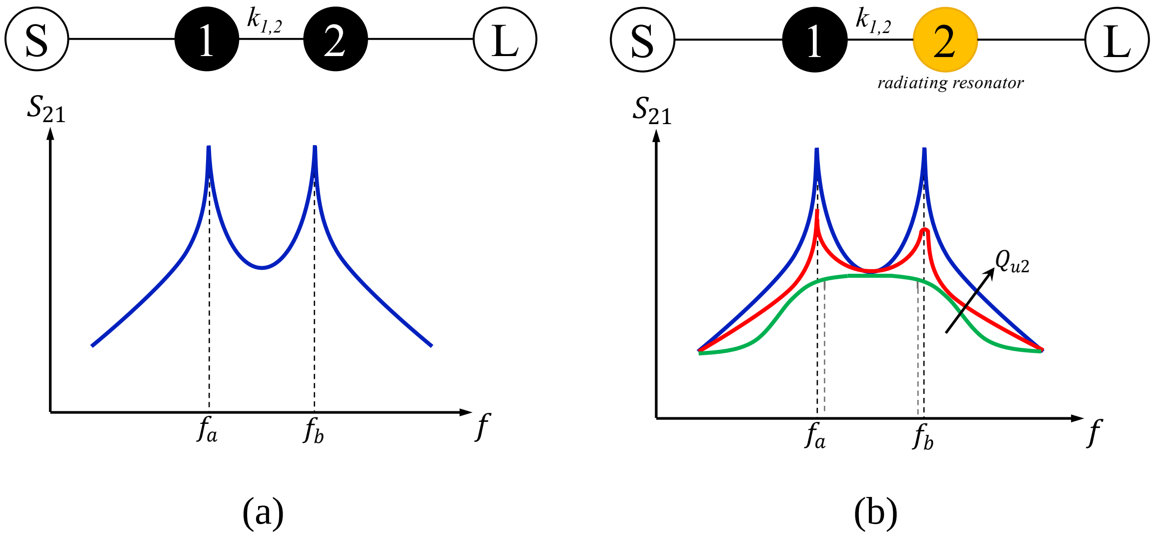

Figure 2.4: (a) Split-pole Technique for extracting the coupling coefficient between coupled resonators in a filter topology (b) Split-pole method applied to extract coupling coefficient between a filtenna and an antenna. Due to a very low unloaded quality factor of the radiating element, Q_{u2}, the peaks in the transmission response are washed down and difficult to distinguish.

has the opposite phase response is referred to as a negative coupling.

The traditional split-pole extraction method presents some challenges when applied in the design and synthesis of filtennas. Observing the natural frequencies of coupled resonators through steep peaks in the transmission coefficient only occurs when the resonators are lossless or when their unloaded Q factors are relatively high. However, in a filtering antenna, the last resonator is a radiating element, and therefore it functions as a lossy resonator with a very low unloaded quality factor due to radiation losses. The steep peaks observed under weak-external coupling will be severely degraded, resulting in one flat response, as illustrated in Fig. 2.4(b). This may result in a large error in k_{12} calculation, or sometimes, calculating it may not even be possible due to the disappearance of peaks.

In [43], a theoretical method is presented to accurately extract the coupling coefficient in filtennas by removing the parasitic effect of the antenna's radiation losses. The unique relationship between the ABCD matrices of lossy and lossless networks is leveraged to essentially remove the degradation of Q due to the lossy radiator. As a result, the two steep peaks observed in the transmission response can be re-extracted, and the split-pole technique can be directly applied to extract the design curve corresponding to the inter-stage coupling coefficient.

The equivalent circuit diagram of a filtenna, weakly coupled to the external ports, is depicted in Fig. 2.5. The antenna, when modeled near resonance, can be considered as an equivalent GLC resonator, where the conductance resulting from radiation losses is represented as G_2. The whole circuit network can be divided into three parts, corresponding to the LC tanks of the two resonators and the lossy part, G_2, represented by a single matrix. The overall circuit response of the filtenna with lossy radiation conductance can be represented by a cascaded ABCD matrix and is given by,

$$\begin{pmatrix} A_m & B_m \\ C_m & D_m \end{pmatrix} = \begin{pmatrix} A_1 & B_1 \\ C_1 & D_1 \end{pmatrix} \cdot \begin{pmatrix} 1 & 0 \\ G_2 & 1 \end{pmatrix} \cdot \begin{pmatrix} A_2 & B_2 \\ C_2 & D_2 \end{pmatrix} = \tag{2.8}$$

$$\begin{pmatrix} A_1A_2 + B_1C_2 + B_1A_2G_2 & A_1B_2 + B_1D_2 + B_1B_2G_2 \\ A_2C_1 + D_1C_2 + D_1A_2G_2 & C_1B_2 + D_1D_2 + D_1B_2G_2 \end{pmatrix} \tag{2.9}$$

Considering the lossless counterpart of the circuit in Fig. 2.5, with $G_2 = 0$ signifying no radiation losses, the resultant ABCD matrix cascade can be written as [43],

$$\begin{pmatrix} A'_m & B'_m \\ C'_m & D'_m \end{pmatrix} = \begin{pmatrix} A_1 & B_1 \\ C_1 & D_1 \end{pmatrix} \cdot \begin{pmatrix} A_2 & B_2 \\ C_2 & D_2 \end{pmatrix} = \begin{pmatrix} A_1A_2 + B_1C_2 & A_1B_2 + B_1D_2 \\ A_2C_1 + D_1C_2 & C_1B_2 + D_1D_2 \end{pmatrix} \tag{2.10}$$

Based on the intrinsic properties of ABCD matrices, A and D in the ABCD matrix only contain the real part, while B and C only contain the imaginary part. Therefore the

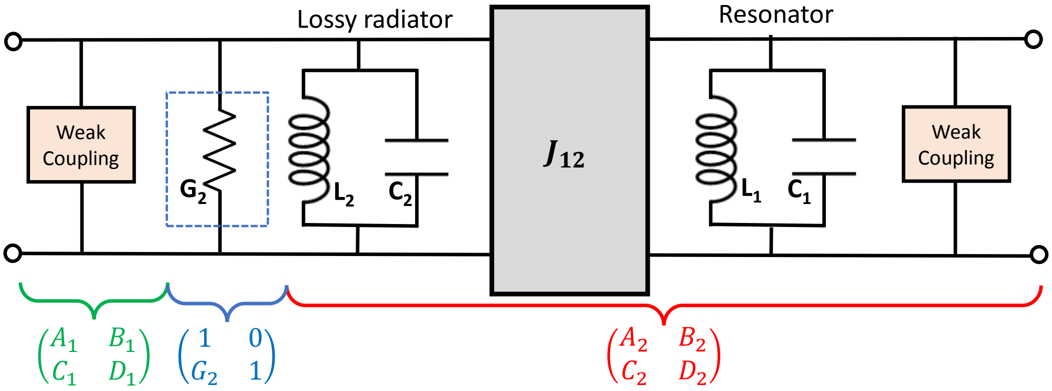

Figure 2.5: Circuit representation of weakly-coupled resonator-antenna topology for extracting the inter-resonator coupling coefficient. The lossy radiator is represented by an additional conductance G_2. The respective ABCD matrices for each section are labeled.

lossless ABCD parameters can be determined from the lossy counterpart using the following relations,

$$A'_m = Re(A_m) \tag{2.11a}$$

$$B'_m = jIm(B_m) \tag{2.11b}$$

$$c'_m = jIm(c_m) \tag{2.11c}$$

$$d'_m = Re(d_m) \tag{2.11d}$$

In Eq. (2.11), A_1, A_2, D_1 and D_2 are real, while B_1, B_2, C_1 and D_1 are equal. The transmission coefficient of the weakly-coupled resonators, excluding the radiation losses, can be re-extracted from the following equation,

$$S'_{21} = \frac{2}{A'_m + B'_m/Z_0 + C'_m Z_0 + D'_m} \tag{2.12}$$

This numerical extraction method for determining the coupling coefficient in filtennas relies on only one condition, which is to have weak coupling at the input and output ports. As noted in [43], the method can be successfully applied in most filtenna topologies.

2.1.3 Output External Coupling

In a typical filter topology, the input and output coupling structures correspond to 50-Ω feed lines that couple into the first and last resonator of the filter. Furthermore, most filter topologies are symmetric because the input/output (I/O) structures are identical. Therefore, a single design curve for the external quality factor, extracted using the procedure described in Section 2.1.1, is sufficient to determine the external coupling at both the input and output ports.

A distinction between the conventional filter structure and a filtenna topology is the existence of a radiating element at the output port of a filtenna. The antenna is the last resonator and is coupled with the free space. The filtenna is asymmetrically loaded with a 50-Ω feed-line at the input and a 377-Ω port resistance at the output, corresponding to the intrinsic impedance of free space. In order to meet a given set of filter specifications, the output external quality factor must be accurately matched with the theoretically derived values.

In most filtenna designs, the output external quality factor is adjusted by optimizing one or more physical dimensions of the radiating element. The reasoning applied is based on intuition, where it makes sense to adjust the free-space coupling by controlling the radiation properties through the antenna element. However, the theoretical foundations and extraction methods of a filtenna's second external coupling using the radiating element have been somewhat inconsistently discussed in filtenna literature.

The subject of filtenna's external quality factor was thoroughly investigated in [44], specifically by analyzing the field coupling between the antenna and free space. The study established that the output external quality factor of a filtenna, Q_{ex2}, is equal to the lossless radiation quality factor, Q_{rad}, of the antenna element. Therefore, the external quality factor of the radiating element is simply the quality factor from the power radiated by the antenna.

The theoretical basis for Q_{rad} is very well established in the field of antennas. However, applying the antenna's radiation quality factor in filtenna design was not well-communicated within the filtenna community before the research work presented in [44].

With the added knowledge of the output external quality factor of a filtenna, a design curve corresponding to Q_{ex2} can be extracted by determining Q_{rad} as a function of one or more physical parameters of the radiating element. It should be noted that there are several methods of extracting the lossless radiation quality factor of an antenna, which can be directly applied in filtenna synthesis. A rather straight-forward method to obtain Q_{rad} is from the lossless antenna's input impedance, as given by the equation [44],

$$Q_{rad}(\omega) = \frac{\omega}{2R_0(\omega)} \sqrt{[R_0'(\omega)]^2 + \left[X_0'(\omega) + \frac{|X_0|}{\omega}\right]^2} \tag{2.13}$$

, where $R_0(\omega)$ is the antenna's resistance, $R_0'(\omega)$ is the derivative of the antenna resistance with respect to frequency, and $X_0'(\omega)$ is the derivative of the reactance of the antenna with respect to the frequency.

The discussion of the external output coupling of the filtenna completes the basic overview of filtenna synthesis using traditional band-pass filter synthesis techniques. For a general second-order filtenna topology, three main design curves are required to synthesize a filtering response, corresponding to the input external quality factor Q_{ex1}, output external quality factor Q_{ex2}, and the coupling coefficient k.

2.2 Time Domain Tuning

The parametric extraction method described in Section 2.1 to synthesize coupled-resonator filters is a good initial step to achieve the desired filtering characteristics. However, separate simulations of individual resonators are needed to distinguish and extract the individual coupling mechanisms. When the final filter structure is simulated with the extract values of external and inter-resonator couplings, the filter response often needs further fine-tuning to precisely match a given set of specifications. However, directly tuning each resonator and coupling value from the filter's frequency domain response can be difficult and time-consuming. A more efficient method of tuning coupled-resonator filters with improved accuracy was presented by Joel Philip Dunsmore using the time-domain response of the filter [45]. The automated filter tuning method utilizes time-domain gating of the filter's reflection response to determine individual resonances and distinguish the different field interactions between the resonators and at the input and output ports.

As an example, consider a three-pole coupled-resonator filter designed for a 20 dB equi-ripple Chebyshev response seen in Fig. 2.6(a). By taking a windowed inverse Fourier transform of the reflection response, the time-domain (TD) response of the filter's S_{11} magnitude can be obtained as shown in Fig. 2.6(b). It is important to note that the center frequency of the frequency span over which the Inverse Discrete Fourier Transform (IDFT) is performed should be equal to the filter's center frequency. Each characteristic null in the TD plot corresponds to the individual resonances of the constituent resonators. The humps represent the electromagnetic field interactions between the resonators and the input/output ports. The first hump corresponds to the external coupling at the input port. The following humps are sequenced as per the respective inter-resonator coupling between each resonator. The last hump in the time-domain response is the external coupling at the output port. These individual field interactions cannot be accurately singled out in the frequency-domain response, Fig. 2.6(a). Therefore, introducing the automated time-domain tuning of filters facilitates a quicker and more efficient means of synthesizing coupled-resonator filters.

Another advantage of the time-domain tuning technique is that it relies on only a single filter port. Since the filtenna is a one-port device, the time-domain tuning can be easily applied to fine-tune all filtennas designed using coupled-resonator theory. The mathematical derivation and modeling of the time-domain tuning method are detailed in references [45]

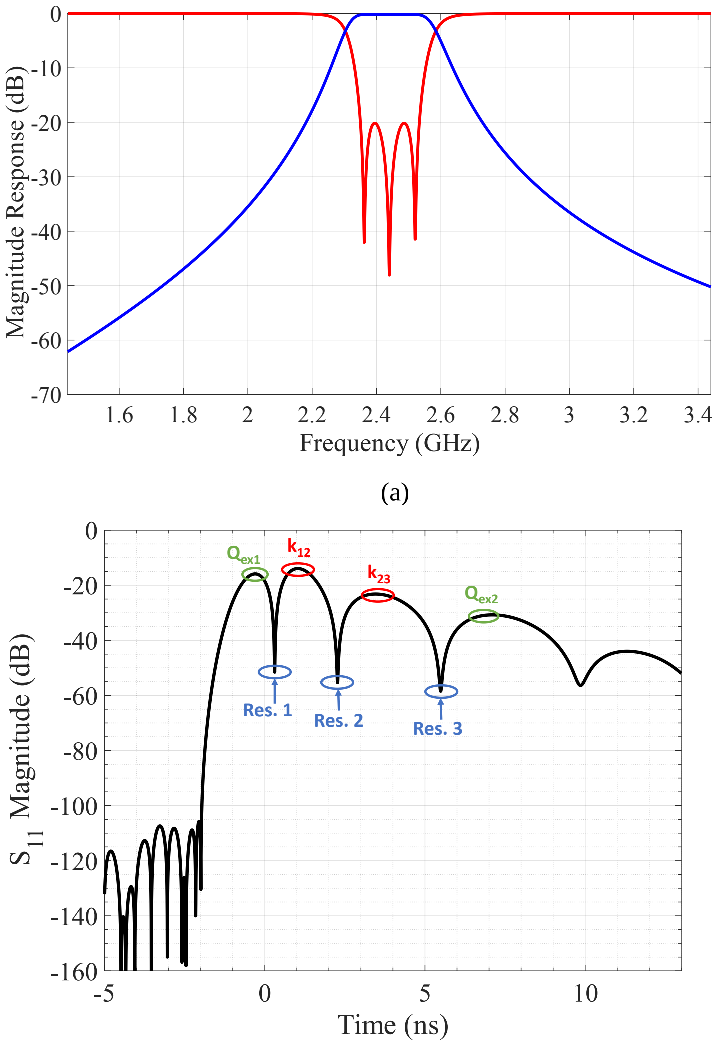

(a)

(b)

Figure 2.6: Example template of a three-pole Chebyshev band-pass filter response centered at 2.44 GHz with a 5% fractional bandwidth (a) Frequency-domain magnitude response of S_{21} and S_{11} and, (b) time-domain magnitude response of S_{11} with the distinct features labeled.

and [37]. A brief overview of the time-domain tuning procedure is provided in the following sections.

2.2.1 Tuning Resonators

The nulls in the S_{11} time domain response indicate how precisely the individual resonators are tuned to the center frequencies. A higher depth of the null corresponds to a precisely

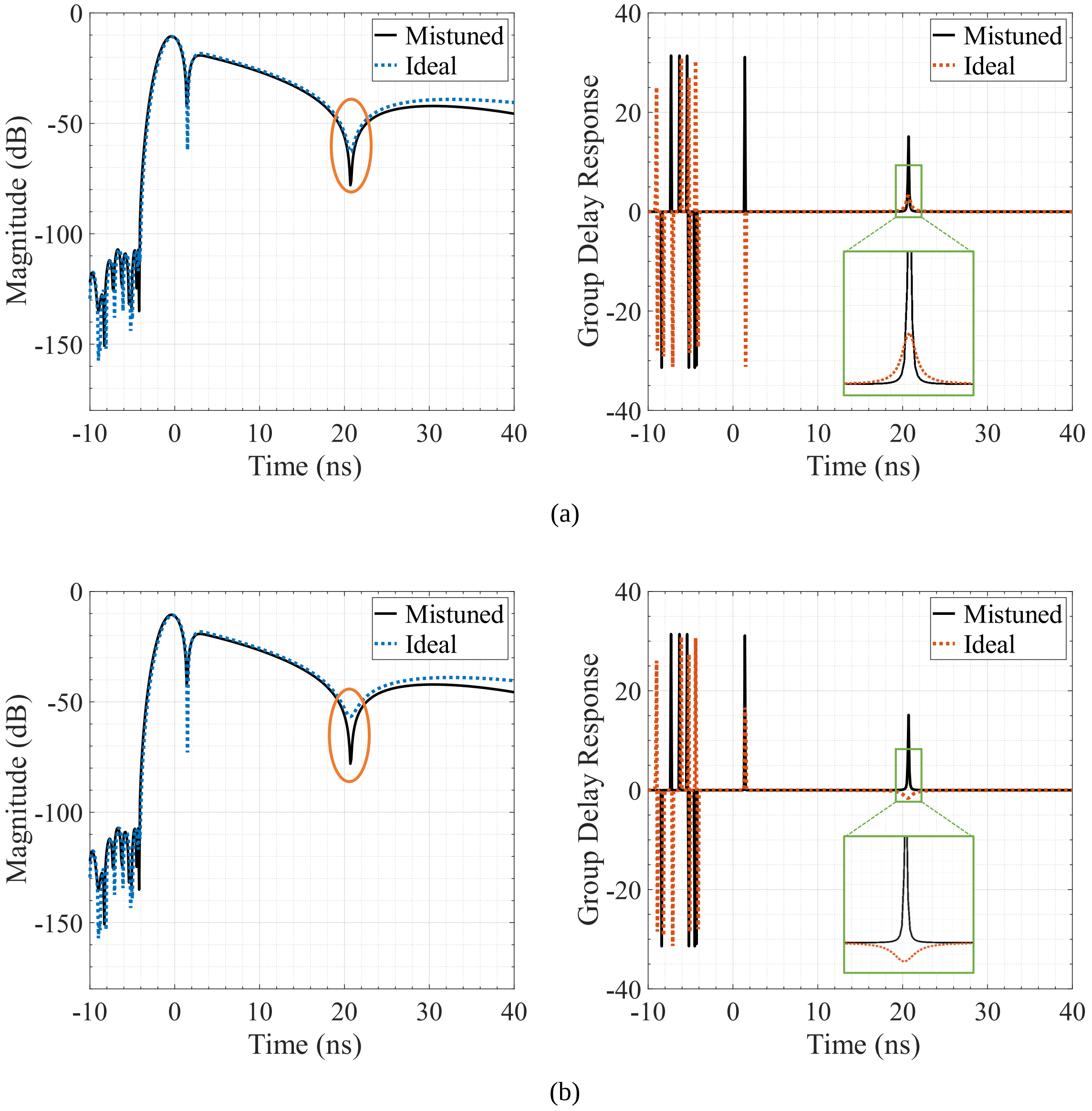

(a)

(b)

Figure 2.7: Effect of mistuned resonators on the time-domain reflection magnitude response, The first resonator is accurately tuned to the center frequency, whereas the second resonator is mistuned as seen by the rise of the null from its minimum peak value. The direction of frequency shift is evaluated from the group delay response (a) Over-tuned Resonator (b) Under-tuned resonator

tuned resonator. Further insight into the direction of error in the resonant frequency of each resonator is attained by looking at the group delay response as a function of time, as seen in Fig. 2.7. The sharp peaks of the ideal filter response in the positive vertical axes of the group-delay response correspond to well-tuned resonances. If the peak of the resonator being tuned is lower in magnitude than ideal and lies in the positive half of the group delay TD plot, then the resonator is tuned higher in frequency as seen in Fig. 2.7(a). The opposite effect is observed for a resonator tuned to a lower frequency than ideal, where the peak value is negative, and the magnitude is lower than ideal, Fig. 2.7(b). Note that the reflection time-domain response, Fig. 2.7(a), only shows the disappearance of the null irrespective of over-tuning or under-tuning and does not provide a clear indication of the direction in which the resonator's center frequency is shifted. Therefore, the TD group-delay response should be used in conjunction with the TD reflection response for tuning each resonator's center frequency accurately.

2.2.2 Tuning Field Couplings

Each hump seen in the time-domain S_{11} magnitude response is sequenced as per the electromagnetic field interactions in the coupled-resonator filter topology, as pointed out in the circuit diagram of Fig. 2.1. The first and the last humps correspond to the external coupling at the input and output ports, respectively. To accurately tune the external coupling, the direction of the null shift and the magnitude of the hump are used as references. If the first null is shifted forward in time and the hump overshoots that of the ideal response, as seen in Fig. 2.8(a), then the external coupling at the input feed is lower and needs to be increased. Conversely, if the external coupling at the feed is too strong, then the time-domain response shows the first null to be shifted backward in time, and the magnitude of the hump is lower than ideal.

The inter-resonator coupling between each resonator, corresponding to the consecutive humps after the external input coupling, follows a similar trend where an over-coupled resonator indicates a forward shift in time with a higher magnitude, and an under-coupled

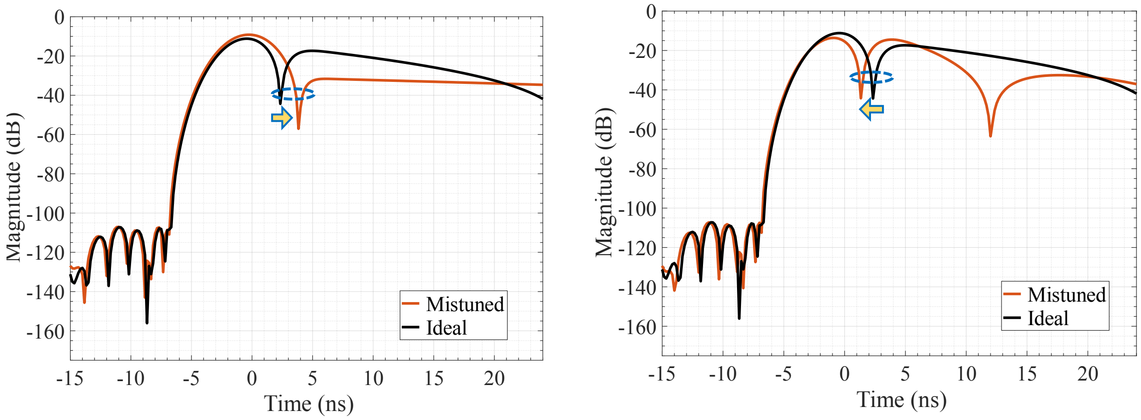

(a) (b)

Figure 2.8: Tuning of external input coupling using the time-domain reflection response (a) Lower than ideal Q_{ext1} (b) Higher than ideal Q_{ext2}.

resonator depicts a backward shift in time with a lower magnitude, as seen in Fig. 2.9(a) and (b) respectively.

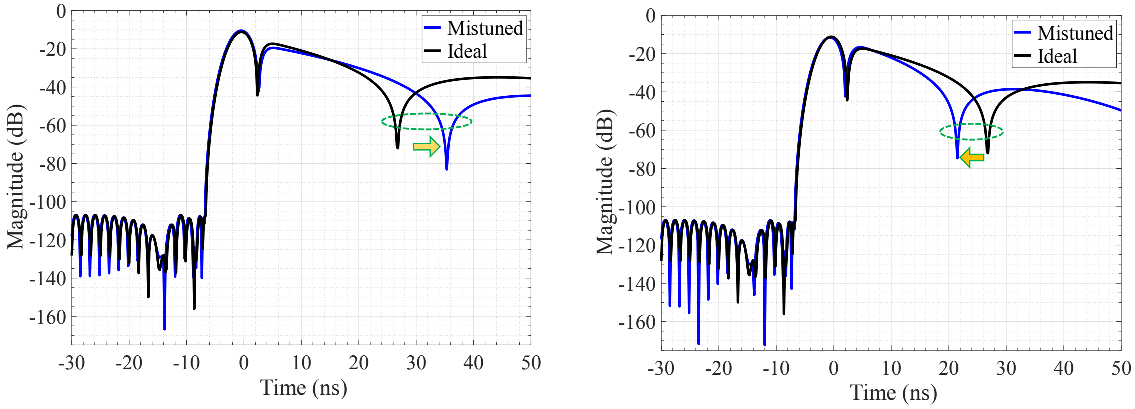

(a) (b)

Figure 2.9: Tuning of inter-resonator coupling in time-domain (a) Under-coupled resonators (b) Over-coupled resonators

An important aspect of the TD tuning method is to ensure that the filter is tuned in a sequence, starting from the first external coupling at the input and then moving through each field coupling until the output port. As illustrated in Fig. 2.8 and Fig. 2.9, if the first input external coupling is mistuned, all the secondary resonances and coupling factors start to disappear in the time domain response. However, the effect of mistuned couplings positioned later in time does not heavily impact the previous couplings. Some back and forth is required throughout the tuning process. The recommended first step is maximizing the depth of each null by tuning the individual resonators and then adjusting different coupling factors, starting at the input port.

Although the time-domain tuning method dramatically simplifies and automates the process of filter tuning, it can result in higher error accumulation through different iterations of tuning each resonance and the coupling factors. Specific rules of thumb can be followed to minimize these errors and ensure that the individual characteristic responses of the filter can be discerned in the TD response. First, it is essential to set the center frequency of the span under observation equal to the filter's center frequency, which it will eventually be tuned to. Second, the overall frequency span should be large enough to provide sufficient resolution to differentiate between each filter section. However, the span should not be too large, or the tuning sensitivity will be reduced due to a higher energy reflection. A good design rule is to set the total frequency span at approximately 2 to 5 times the filter's bandwidth (BW). Third, the start time can be set to $t = -(2/\pi BW)$, corresponding to the delay of approximately one resonator on the minus side. Finally, the stop time should be about 2 to 3 times the total filter delay, approximated at $t = (2N + 1)/(\pi BW)$, where N is the number of resonators. The tuning method should begin with increasing the depth of each null corresponding to the resonances in the filter, starting from the input port. Once each resonator is tuned to the center frequency, the coupling factors can be adjusted, starting from the input to the output port.

2.3 Conclusion

An overview of the fundamental filter design using coupled-resonator theory for band-pass filter synthesis was presented in this chapter. A filtenna, synthesized using coupled-resonator theory, consists of two main building blocks: a resonator and an antenna that acts as a resonator as well as a radiator. Due to the presence of the lossy radiator as the last resonator of the filtenna structure, there are significant differences in the filtenna design process as compared to the conventional filter synthesis method, which was addressed in detail. Finally, the basics of time-domain tuning for efficiently tuning filters and filtennas using just one port of the device. Based on the coupled resonator theory-based filtenna topology, the first building block of a tunable filtenna is a tunable resonator topology. The specific resonator technology, which is an evanescent-mode cavity, is discussed in detail in Chapter 3.

Chapter 3

Tunable Evanescent-mode Cavity Resonator

In a frequency-agile filtenna topology, the first critical building block is the selection of a tunable microwave resonator to achieve a specified filtering performance. Some of the major requirements for such a tunable resonator include wide tunability, a high unloaded quality factor to ensure low insertion loss, high power-handling capacity, and a small form factor. A promising resonator technology developed to meet most of these requirements is the evanescent-mode cavity resonator. Several high-performance miniaturized filters with wide tunability, high power-handling capacity, and low losses have been presented based on the evanescent-mode cavity topology[46]-[49]. This chapter details the theory and implementation of evanescent-mode cavity resonator technology to realize the frequency-agile filtenna's first resonator.

An evanescent-mode (EVA-mode) cavity resonator is realized by inserting a metal post at the center of a cavity, such that the post-top nearly touches the cavity ceiling. As seen in Fig. 3.1, heavily loading the cavity by placing the metal obstacle results in the formation of a highly sensitive capacitive region above the post due to the formation of an air gap between the post-top and cavity ceiling.

The main advantage of a post-loaded cavity is the miniaturization and reduction in the volume occupied by the resonator. As seen in Fig. 3.2, an EVA-mode cavity provides approximately 96% volume reduction, as compared to a regular circular cavity, while

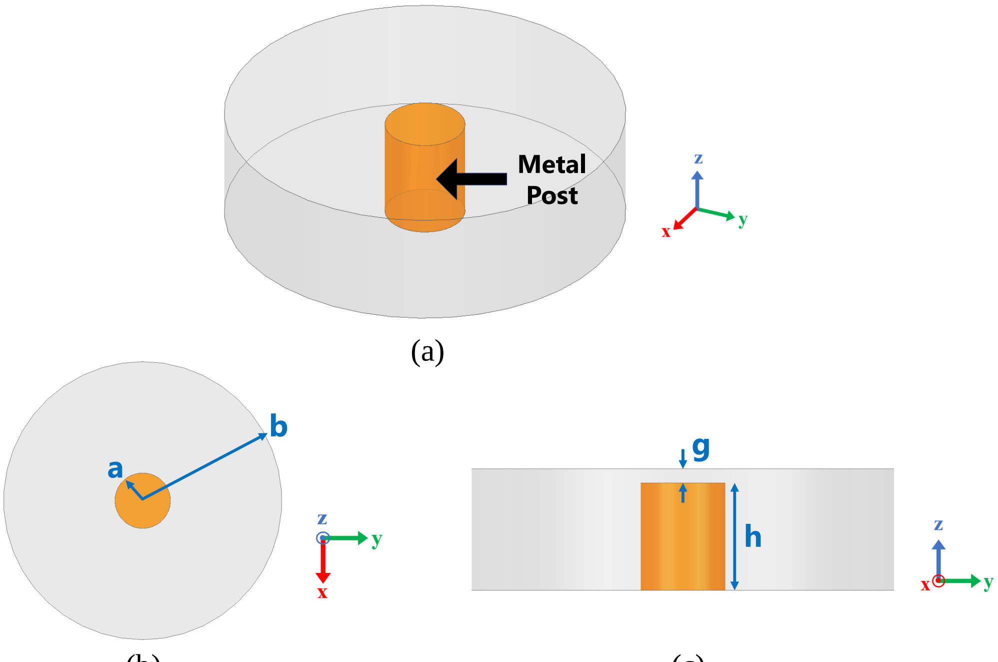

(a)

(b) (c)

Figure 3.1: Evanescent-mode cavity resonator model consisting of a centrally loaded metal post. (a) 3-D view (b) Top View (c) Side-view. The cavity radius a, post radius b, substrate height h, and gap size g are the primary variables for the resonator

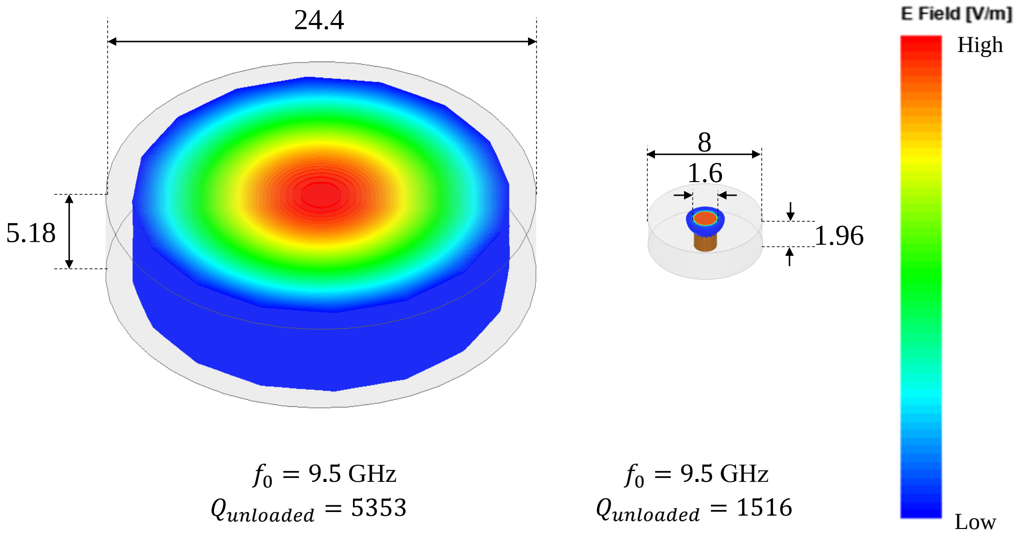

Figure 3.2: Comparison of the volume and field distributions in a regular circular cavity and an evanescent-mode cavity. Both cavities resonate at the same frequency of 9.5 GHz, but the EVA-mode cavity shows a 97% reduction in the total volume as compared to the circular resonator, with a forgiving 72% quality factor reduction from 5353 to 1516.

maintaining the same resonant frequency of 9.5 GHz. This miniaturization benefit comes at a graceful trade-off in the resonator's quality factor, which shows approximately 72% reduction from 5353 to 1516 compared to the unloaded cavity. Additionally, EVA-mode resonators provide a wide spurious free range, greater than 35:1, as compared to an unloaded cavity resonator which is less than 2:1 [46].

3.1 Piezoelectric Tuning Method

The presence of a metal post at the center of the cavity concentrates the electric field in a small region above the post, making it amenable to capacitive tuning. By tuning the gap between the post-cavity ceiling, the overall capacitive loading of the structure can be varied, thus tuning the resonator's center frequency. A popular technique to implement the capacitive tuning of EVA-mode cavities is by attaching electromechanical actuators like piezoelectric discs or RF-MEMS actuators on top of the flexible conductive cavity ceiling. A piezoelectric disc-tuned EVA-mode cavity schematic is shown in Fig. 3.3. An externally applied DC-bias voltage is used to actuate the flexible cavity ceiling mechanically. A thin copper foil is typically used to form the conductive membrane. The resulting deflection of the actuator changes the gap between the post-top and cavity ceiling on a μm scale, thereby tuning the cavity's resonant frequency.

Piezoelectric tuning technologies have been used to realize widely tunable and high-Q evanescent-mode cavities [47]-[39]. In [47], an octave tunable filter from 2.3 GHz to 4.6 GHz is reported using piezo-disk tuned EVA-mode technology, with an unloaded quality factor of 360 to 700. Substrate-integrated widely tunable EVA-mode cavity filters are presented in [48] and [49] with piezoelectric disks for tuning the cavity's critical gap size.

Despite the popularity of piezoelectric disks to tune EVA-mode resonators, the tuning technology has several challenges that limit its use for high-frequency applications above

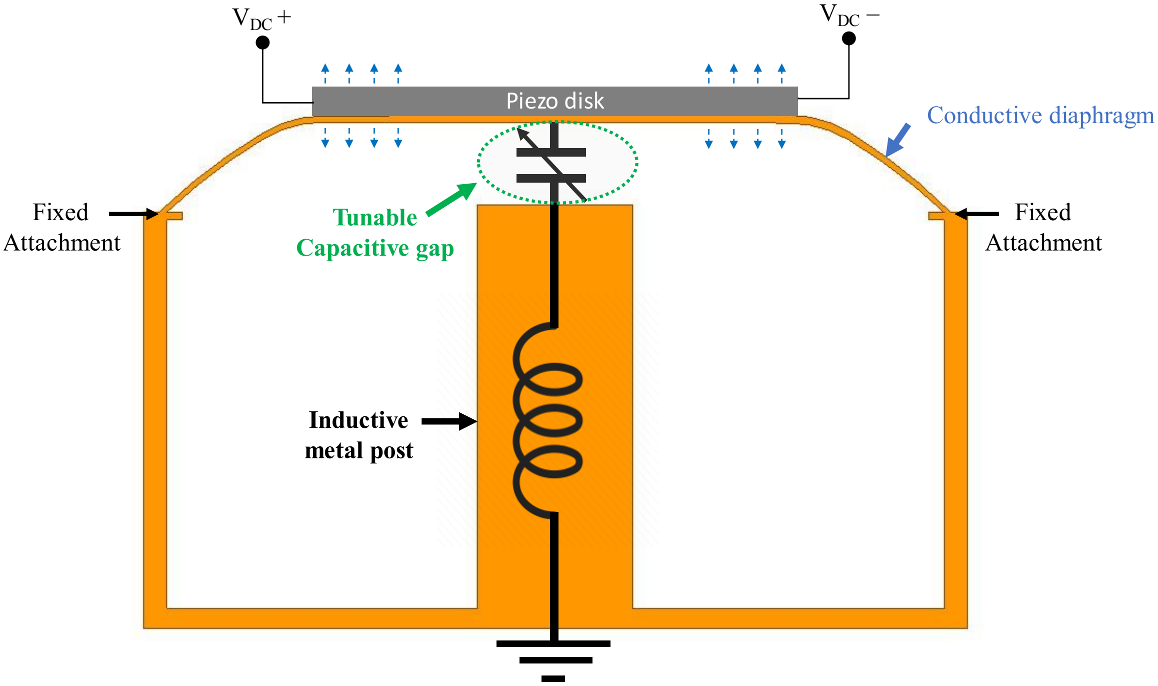

Figure 3.3: Piezoelectric tuning of EVA-mode cavity resonator. The piezo disk needs external bias voltage, typically in the range of ±180-200 V, to deflect the conductive diaphragm on a μm scale and change the tuning capacitance above the post.

10 GHz [46]. The main disadvantage is the piezoelectric disc's limited deflection range, which is typically between 15-50 μm. The piezo disk actuation range is even more constricted at higher frequencies due to the smaller sizes of the available piezo discs. As a result, the achievable frequency tuning range of the resonator is severely restricted.

In order to achieve wide tunability with piezoelectric disk tuners, the initial critical gap size between the post and cavity ceiling needs to be less than 5 μm, which complicates the assembly of the tuner into the passive structure. An additional detrimental effect of having a small starting gap is that it reduces the Power Handling Capability (PHC) of the resonator [39]-[52] As seen in Fig. 3.2, about 90% of the total electric field is confined in the small region between the post-top and the cavity ceiling. With large input powers, the electric field density increases until a gas breakdown of the air-dielectric occurs in the gap, and the resonator is shorted. The initial gap needs to be as large as possible to increase the power-handling capability.

An additional practical challenge encountered with the piezo-disk tuning scheme is the issue of mechanical reliability. The membrane performance is affected by mechanical creep and fatigue due to the repeated bending of the tuner across fixed attachment points. In addition, piezo hysteresis effects are observed as the actuation does not have a constant mode of bending when the applied bias voltage changes in ascending versus descending manner. To solve the mechanical reliability drawback, some closed-loop monitoring and control systems have been proposed in [53], [54], and [55], to externally observe the tuner displacement. Alternatively, piezoelectric actuation has been replaced with electrostatic actuation using micromechanical systems or RF-MEMS switches with silicon micro-machining implementations [56]. However, these systems do not alleviate the requirement for a small initial gap size and cause more manufacturing constraints or complexities due to the additional sensitive assembly of the monitoring devices within the cavity. To overcome the aforementioned drawbacks, a different tuning concept is needed to implement high-performance tunable EVA-mode resonators with simplified manufacturing and easier design scalability for higher-frequency applications.

3.2 Contactless Capacitive Tuning Concept

A novel tuning technique was presented in [57] where long-range external linear actuators were used to vertically displace a contactless conductive plate and tune evanescent-mode cavity resonators. By avoiding the bonding of the tuner to the cavity, the contactless tuning scheme showed substantial improvement in the PHC and mechanical reliability of the tuner. The contactless tuning scheme is compatible with any actuator that can provide sufficiently large vertical displacement. This tuning method has been applied to design high-power

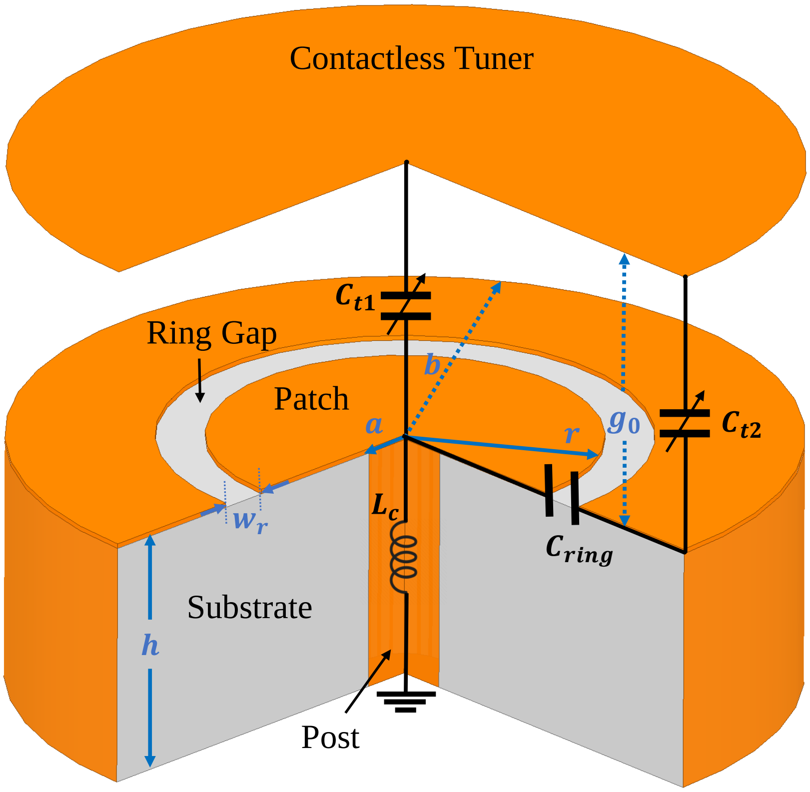

Figure 3.4: Concept of contactless tuning technique proposed in [57] for tuning EVA-mode cavity filters. The cavity's resonant frequency is tuned by increasing the gap size, g_0, through the vertical displacement of the tuner disc.

tunable filters up to Ka-Band [58] and in high-power impedance tuners [59].

A conceptual depiction of the contactless tuning scheme is shown in Fig. 3.4, where a ring-gap capacitance is formed by shorting the central metal post of an EVA-mode cavity resonator to the top metal wall. A floating tuner above the cavity forms capacitances with the isolated post patch and the cavity walls. The gap size, g_0, between the post-patch and the tuner disc directly affects the capacitive loading on the resonator. As g_0 increases, the overall capacitive loading on the cavity is reduced - increasing the resonant frequency. Therefore, the resonant frequency f_0 of the cavity can be tuned by vertically displacing the tuner.

3.2.1 Theoretical Model

The lumped element model of the tunable cavity resonator is shown in Fig. 3.4. Without the floating tuner disc, the cavity has a fundamental TEM resonant mode due to the shorted coaxial transmission line, which contributes an inductance L_c, and the annular gap capacitance C_{ring}. The cavity inductance, L_c, is given as [60],

$$L_c = \frac{60}{\omega\sqrt{\epsilon_r}} tan\left(\frac{\omega h\sqrt{\epsilon_r}}{c}\right) ln\left(\frac{b}{a}\right) \tag{3.1}$$

where b is the cavity radius, h is the cavity height, a is the post radius, c is the speed of light, and ϵ_r is the dielectric constant of the cavity substrate.

When neglecting the copper thickness, the annular capacitance C_{ring} is given as a function of the patch radius r, and ring-width w_r as [57],

$$C_{ring} = \frac{2\pi r\epsilon_0(1+\epsilon_r)}{ln\left(1+\frac{w_r}{r}\right)} \int_0^\infty [J_0(\zeta r) - J_0(\zeta(r+w_r))]\frac{J_1(\zeta r)}{\zeta}\, d\zeta \tag{3.2}$$

where J_n is the nth-order Bessel function of the first kind.

The added conductive tuner on top of the cavity introduces additional capacitances between the isolated center patch and the top wall. The floating tuner forms parallel capacitances between the center patch, C_{t1}, and the cavity top wall, C_{t2}, as seen in Fig. 3.4. An equivalent series capacitance, C_{t12}, is formed by the two capacitance C_{t1} and C_{t2} as

$$C_{t12} = \frac{C_{t1}C_{t2}}{C_{t1}+C_{t2}} = \frac{\epsilon_0\pi r^2}{g_0 b^2}\left(b^2 - (r+w_r)^2\right) \tag{3.3}$$

The equivalent capacitance network is a parallel combination of C_{ring} and C_{t12}, and is a function of the gap-size g_0 expressed as

$$C_{eq}(g_0) = C_{ring} + C_{t12}(g_0) \tag{3.4}$$

In the presence of the tuner disc, the resonant frequency of the cavity ω_0 is tuned by varying the gap g_0 through the vertical displacement of the tuner disc, as shown by the relation

$$\omega_0(g_0) = \frac{1}{\sqrt{C_{eq}(g_0)\, L_c}} \tag{3.5}$$

As shown in Eq. (3.4), the cavity consists of a fixed capacitance C_{ring} and a variable capacitance C_{t12} as a function of g_0. For a fixed value of the ring-gap w_r, the variation of C_{eq} is dominated by the value of r/b. In [57], the optimum value of the ring radius for maximum tuning was found as $r = 0.57b$. Therefore, the general guideline for maximizing the tuning range of the resonator is to adjust the ratio of r/b while maintaining constant f_0 or constant C_{eq} for the same value of the critical gap size. Alternatively, the initial gap size can be reduced to enable a larger tuning range.

3.2.2 Resonator Quality Factor

The total quality factor, Q_{tot}, of the contactless tuned EVA-mode resonator consists of more loss mechanisms than the traditional sealed EVA-mode resonator tuned with a piezo disk. In addition to the conduction and dielectric losses, the ring-loaded cavity resonator also consists of radiation losses due to the open ring circumference around the post-patch. The total Q factor consists of the individual quality factor for each loss mechanism: conduction loss Q_{cond}, dielectric loss Q_{die}, and radiation loss Q_{rad}, is given as [57],

$$Q_{tot} = \left(\frac{1}{Q_{cond}} + \frac{1}{Q_{die}} + \frac{1}{Q_{rad}}\right) \tag{3.6}$$

The finite conductivity of the cavity walls causes the conduction losses and lowers the conduction quality factor, Q_{cond}. The effect of the conduction loss mechanism is maximum for lower values of g_0 due to larger capacitive loading of the cavity. Increasing the cavity size will increase Q_{cond} as the inductance L_c increases and more energy is stored within the cavity. Furthermore, the optimum ratio between cavity and post radius for highest Q_{cond} is reported to be $b/a = 3.6$ [60].

The dielectric losses result from the finite loss-tangent, $tan\,\delta$, of the dielectric substrate inside the cavity, which has a dielectric constant ϵ_r. There exists a parasitic fringing capacitance, C_{sub}, emerging from the ring-gap and passing through the cavity substrate, as seen in Fig. 3.5. Ideally, all the fields should pass through the air dielectric between the tuner top and the cavity ceiling. However, for smaller values of ring radius r, the fringing fields C_{sub} can become quite significant, thereby reducing the value of Q_{die}. A larger value of the copper thickness will increase Q_{die} by reducing the parasitic capacitance C_{sub} as a larger fraction of the fields will pass through the air. Additionally, a larger ring radius will increase C_{eq} and therefore maximize Q_{die}. The losses due to the dielectric can also be minimized by

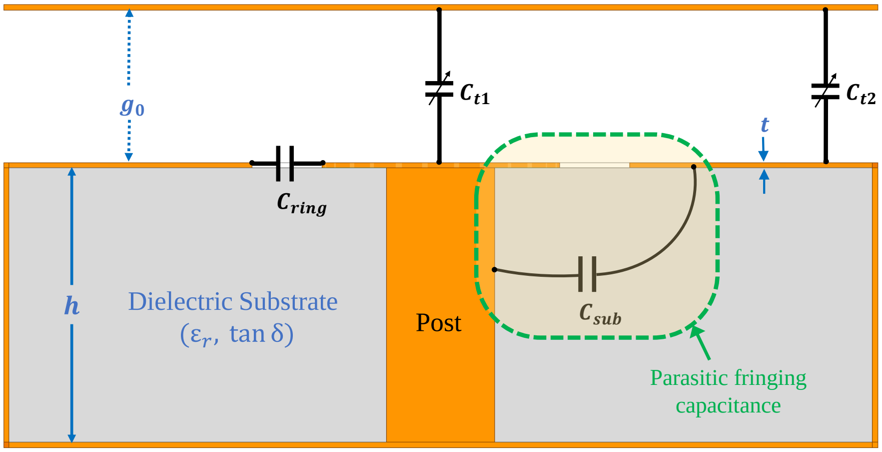

Figure 3.5: Parasitic capacitance, C_{sub} exists within dielectric between top wall and post. A large value of copper thickness t ensures minimal fringing fields within the dielectric.

choosing a substrate with a low value of the substrate loss tangent.

Lastly, the radiation losses which lower Q_{rad} occur from the open ring aperture around the post-patch. The value of Q_{rad} can be maximized by reducing the ring length ($2\pi r$) and the ring width w_r. The effect of Q_{rad} on the total Q of the cavity is negligible for smaller values of g_0 since the ring aperture is electrically smaller at a lower resonant frequency.

3.3 Realization of Contactless-tuned Resonators with SIW Technology

The most commonly used fabrication method for implementing EVA-mode cavity resonators and filters is through the substrate-integrated waveguide (SIW) technology. Using the SIW technology, almost any non-planar structure can be implemented in a planar form. This significantly simplifies the integration of RF passive devices with other PCB-based designs. For the EVA-mode cavity technology, the cavities loaded with central posts are realized by creating boundaries of plated vias. Several design guidelines for SIW technology exist to minimize performance degradation due to the replacement of solid metal walls with plated vias.

The practical implementation of the contactless-tuned EVA-mode cavity resonators using SIW technology is depicted in Fig. 3.6. The top conductive layer contains the ring-gap circumference and the post-patch. In the bottom cavity ground plane, a Grounded Co-planar Waveguide (GCPW) feed is implemented to couple RF energy into the cavity. Weak external coupling, which is used to extract the unloaded quality factor, Q_u, from the S_{21} measurements, is realized by increasing the distance between the short-circuited end of the GCPW slots and the cavity center. The substrate in between comprises the plated vias, which form the cavity walls, feed lines, and the central post.

The iterative design procedure in [57] can be used to optimize the cavity's dimensions and achieve certain specifications for the frequency tuning range, power handling, and

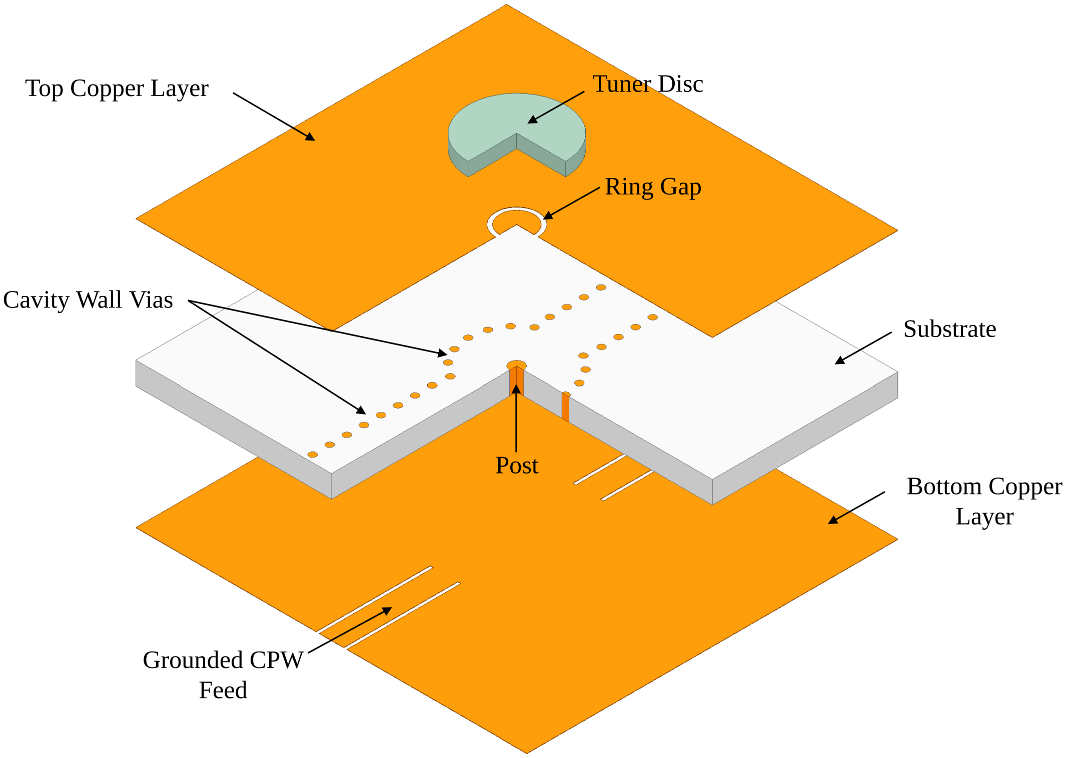

Figure 3.6: SIW implementation of the contactless-tuned evanescent-mode cavity resonator. The exploded view of resonator layers is labeled in the figure.

quality factor. For starting the cavity design process, the largest possible values for the cavity radius and cavity height are chosen, while the values of the ring radius and ring width w_r are minimized as per manufacturing constraints. The post radius a and minimum gap size g_0 is tuned to satisfy the TR and quality factor specifications. This procedure was used to realize octave-tunable resonators for S-band and X-band applications, as detailed in the sections below.

3.3.1 S-Band Tunable Resonator

Based on the trade-offs between tunability and quality factor, a contactless-tuned cavity resonator is designed for S-Band applications. The design dimensions of the designed

EVA-mode contactless-tuned resonator are shown in Fig. 3.7. The resonator is implemented on Rogers TMM3 (ϵ_r = 3.27, tan δ = 0.002), with a substrate thickness of 125 mils and copper cladding of 17.5 μm. The cavity radius is 14 mm (b), while the post-patch radius (r) is 1.5 mm. As per fabrication feasibility, the ring width was minimized to a value of 250 μm. The center post is formed using four smaller vias with a diameter of 0.4 mm. Using multiple vias to form the post is essential to reduce the fringing electric fields associated with C_{ring} that pass through the substrate. Based on the design guidelines for SIW structures in [61], the diameter of the cavity via is 0.8 mm, and the spacing between vias is 1.57 mm.

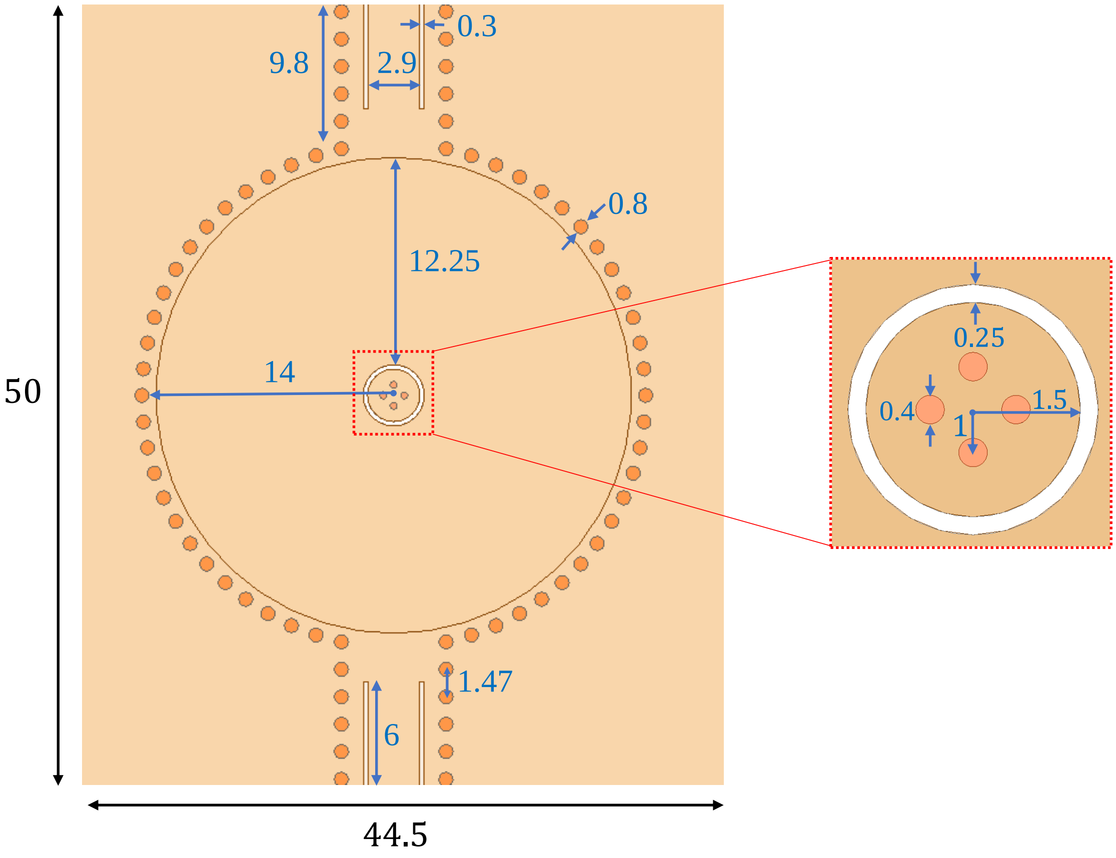

Figure 3.7: Design dimensions of the contactless-tuned resonator (in mm)

The full cavity is designed and simulated using ANSYS High-Frequency Structure Simulator (HFSS) in a Modal Solution set-up. The cavity and post vias are assigned as

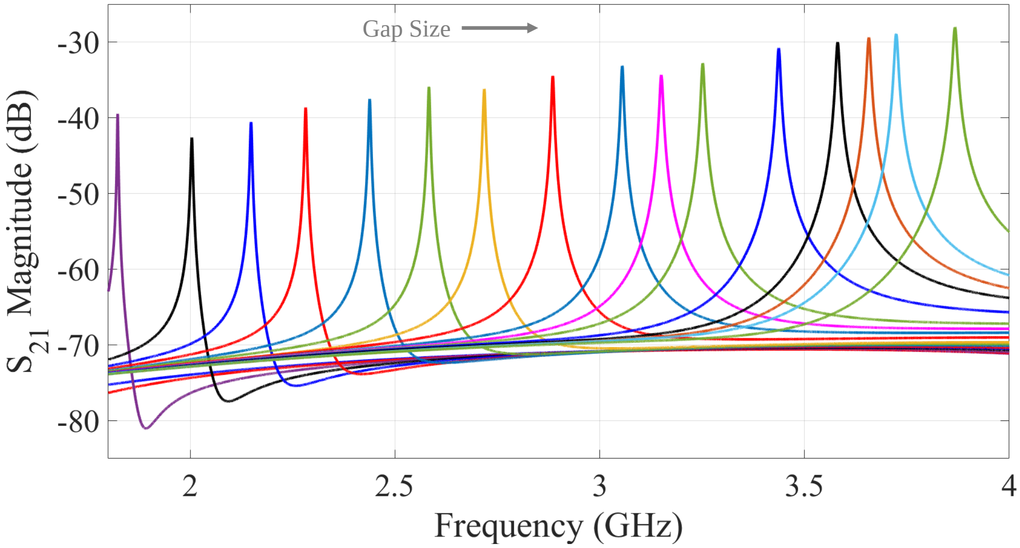

Figure 3.8: Simulated transmission response, S_{21} of the contactless-tuned resonator exhibiting continuous tuning from 1.75 GHz to 3.9 GHz.

finite conductivity boundaries, with an assigned conductivity of copper (5.8×10^8 S/m). Due to the sensitivity of the gap size above the post, additional mesh operations should be added to the post-top to ensure the accuracy of the simulated design. The ring gap and the gap g_0 above the post are assigned the material properties of air. The boundary on the ring circumference is assigned as the Perfect magnetic conductor (Perfect-H) boundary to emulate the radiation fields on the open aperture. Simulation results of the resonator's S_{21} transmission response are shown in Fig. 3.8. As the gap size varies from 18 μm to 900 μm, the resonator shows continuous tuning from 1.75 GHz to 3.9 GHz.

A prototype of the designed resonator was fabricated, as seen in Fig. 3.9. The surface ring and the GCPW feed were patterned using the LPKF Proto-Laser U4 machine. The floating tuner disc shown in Fig. 3.6 is realized by routing a circular plate from a 60-mil-thick Rogers 4350B substrate. Linear actuators provided by M3-L technologies were used for vertically displacing the tuner [62]. The M3-L module is packaged in a compact module with an integrated driver and close-loop control system to direct motion commands from a standard serial interface. These actuators provide a total travel range of 6 mm, with a step

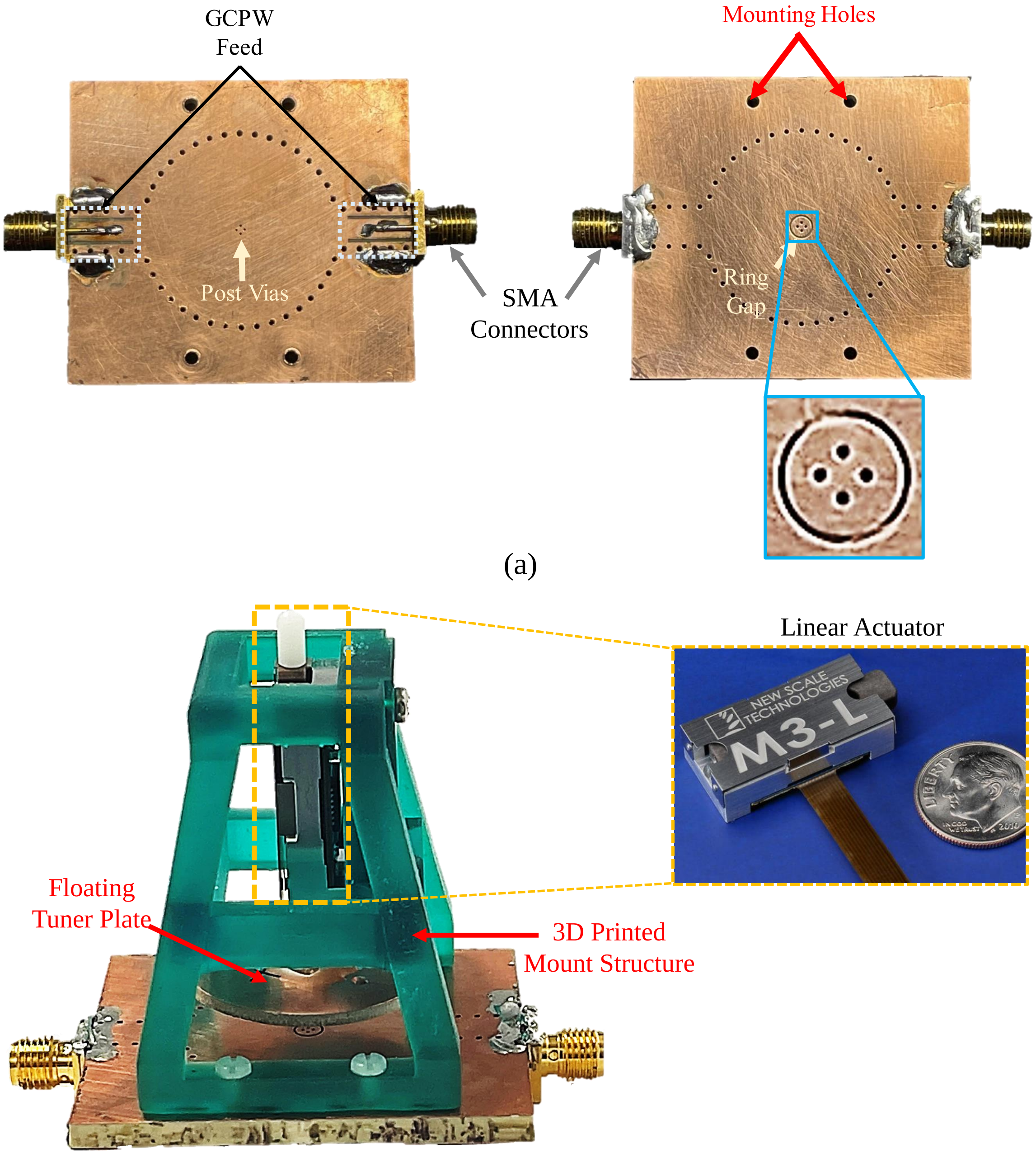

(a)

(b)

Figure 3.9: Fabricated Prototype for contactless-tuned resonator (a) Top-View and Bottom-view (b) Full assembly with long-range M3-L Linear actuators.

size of 0.5 μm. The provided actuation range is enough for the resonator to tune across the simulated frequency range from 1.75 GHz to 3.9 GHz. A 3D-printed mounting structure was constructed to hold the linear actuator. The mount is assembled on top of the substrate

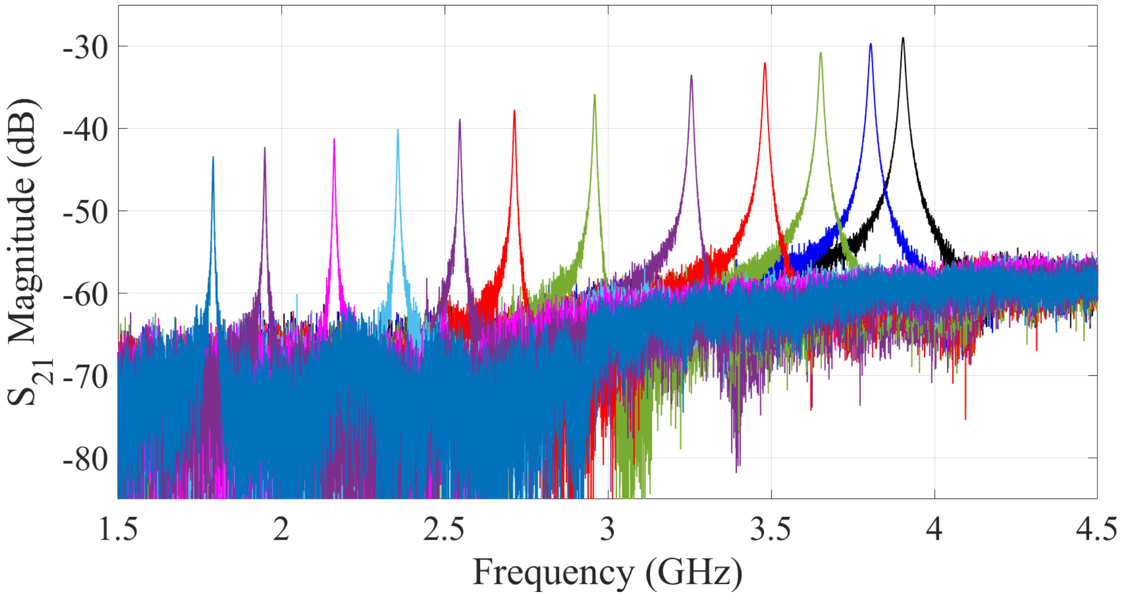

Figure 3.10: Measured transmission response of the contactless-tuned resonator, exhibiting tuning from 1.79 GHz to 3.9 GHz. The initial gap is about 20 μm, and the total actuation range is 550 μm, as extracted from measurements.

using nylon screws. The circular PCB plate is attached to one end of the actuator using quick-setting epoxy. A picture of the complete assembly with the mounting structure is shown in Fig. 3.9(c).

The measured transmission response of the fabricated resonator, as seen in Fig. 3.10, shows continuous frequency tuning from 1.79 GHz to 3.9 GHz, with 74% tuning. The required actuation range is approximately 980 μm. The simulated and measured unloaded resonator quality factor, Q_u, is plotted in Fig. 3.11. A best-fit polynomial curve is applied to characterize the variation of Q_u across the tuning range. As the gap size is decreased, the simulated Q_u increases from 382 to 578. The measured quality factor ranges from 311 to 571 when the resonator is tuned from 3.9 GHz to 1.8 GHz.

The primary loss mechanism for smaller values of g_0 is due to conduction losses. For the curve corresponding to simulated Q_u, it is observed that the quality factor shows a slight improvement and reaches a peak value with increasing frequency. This is mainly due to the dominance of Q_{cond}, which increases with frequency, as noted in Section 3.2.2. After a

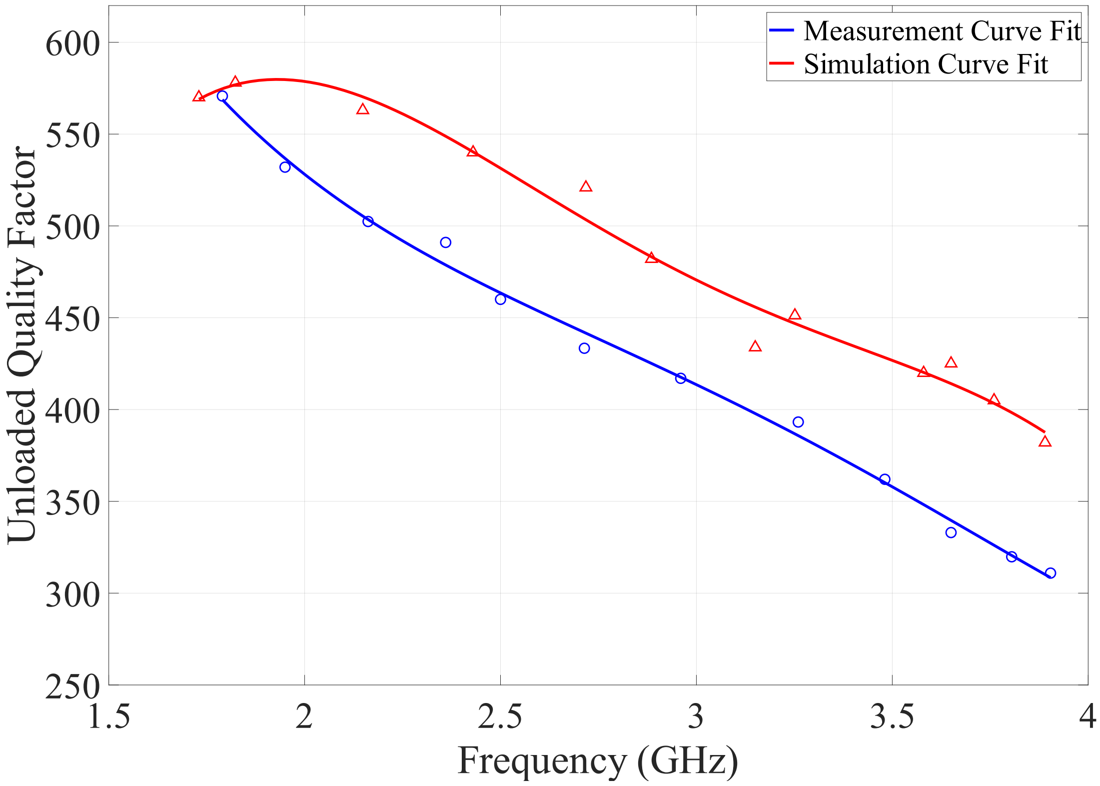

Figure 3.11: Comparison of the unloaded quality factor for the simulated and measured S-Band contactless-tuned resonator

resonant frequency of about 2 GHz, there is a downward trend of Q_u due to the dominance of Q_{die} and Q_{rad}, which decrease with increasing frequency. The Q_{die} reduction is primarily due to the C_{sub} effect that forces some fringing electric fields to pass through the cavity substrate.

The degradation of measured and simulated Q_u at the higher end of the frequency tuning range is also due to the radiation leakage from the ring-gap circumference, which reduced Q_{rad}. The ring is electrically larger at higher frequencies, so the radiation leakage increases with the ring's circumference. However, the measured quality factor is still higher than 300 across the whole tuning range from 1.79 GHz to 3.9 GHz. The overall deviations in measured and simulated resonator quality factors across the tuning range can be attributed to fabrication tolerances. Specifically, the resonator is simulated with an ideal copper

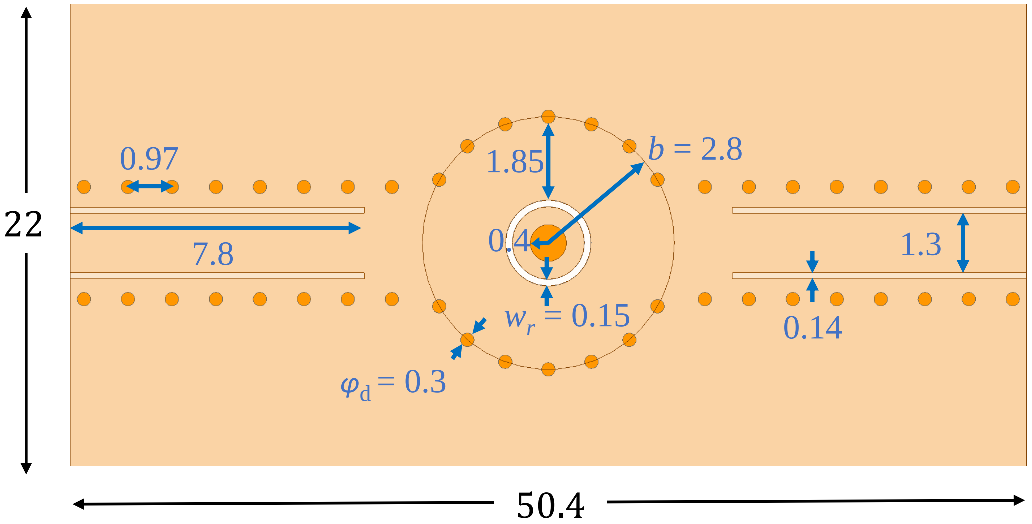

Figure 3.12: Design Dimensions of the X-Band EVA-mode resonator implemented with contactless tuning scheme

conductivity of 5.8 $\times 10^7$ S/m. In practical implementation, attaining the ideal copper conductivity through in-house electroplating processes is challenging. The imperfect copper deposition may result in non-zero surface roughness in the plated via holes of the cavity and post. Therefore, some deviations in the measured quality factor are expected for the in-house fabricated resonators. Despite this, the overall quality factor of the octave-tunable resonator remains greater than 300 across the entire tuning range.

3.3.2 X-Band Tunable Resonator

To demonstrate the frequency scalability of the contactless tuning scheme, the design of an X-band tunable EVA-mode cavity resonator is presented in this section. The same procedure outlined in Section 3.3.1 is followed to achieve a tuning range of at least 8-12 GHz.

The final design dimensions of the simulated X-band resonator are shown in Fig. 3.12. The resonator is implemented on a 60 mil thick Rogers 3003 substrate with a dielectric constant of $\epsilon_r = 3$. As seen from the simulated transmission response in Fig. 3.13, the resonator demonstrates frequency tuning from 7.8 GHz to 12.1 GHz. The initial gap size

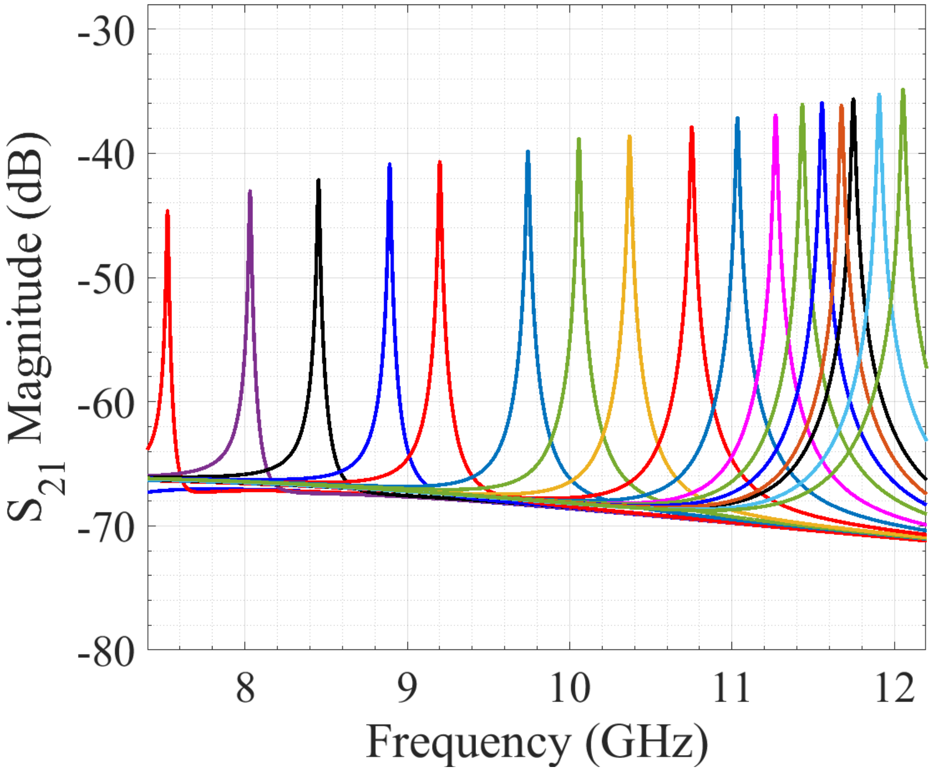

Figure 3.13: Simulated transmission response, S_{21} of the contactless-tuned resonator exhibiting continuous tuning from 7.8 to 12.1 GHz.

needed is 36 μm, and the total actuation range is approximately 648 μm.

The unloaded quality factor, Q_u of the resonator, was extracted from the transmission response, and the variation of Q_u across the tuning range is plotted in Fig. 3.14(a). At the lower resonant frequency of 7.8 GHz, the quality factor is 750. With increasing gap size, Q_u shows a slightly increasing trend until 8.5 GHz. As noted previously in Section 3.2.2, this is due to the dominant conduction loss mechanism, which improves with increasing gap size. Beyond this point, the resonator Q_u curve shows a downward decreasing slope until reaching a minimum Q_u of 458 at the highest tuning frequency of 12.1 GHz. The decrease in Q_u is again attributed to the radiation losses at higher frequencies.

Overall, the quality factor of the resonator remains greater than 450 across the entire tuning range, which is higher than the octave-tunable S-band resonator in Section 3.3.1. This is because of the inherent trade-off between the tunability and quality factor of EVA-mode resonators [57]. The X-Band resonator is designed for a tuning ratio of 1:1.55, whereas the resonator in Section 3.3.1 demonstrated a tuning ratio of 1:2.2, from 1.71 GHz to 3.9 GHz.

3.4 Conclusion

In this chapter, the realization of high-Q tunable resonators with evanescent-mode cavity technology was established. Instead of the widely used electronically controlled piezo-electric disks, a contactless-tuning scheme using external long-range linear actuators was implemented to realize high-Q octave tunable resonators with simplified manufacturing processes. To demonstrate the frequency scalability of the contactless-tuning scheme, resonators were designed at both S-band and X-band. The resonators, realized using SIW, showed a quality factor greater than 300 across the tuning range.

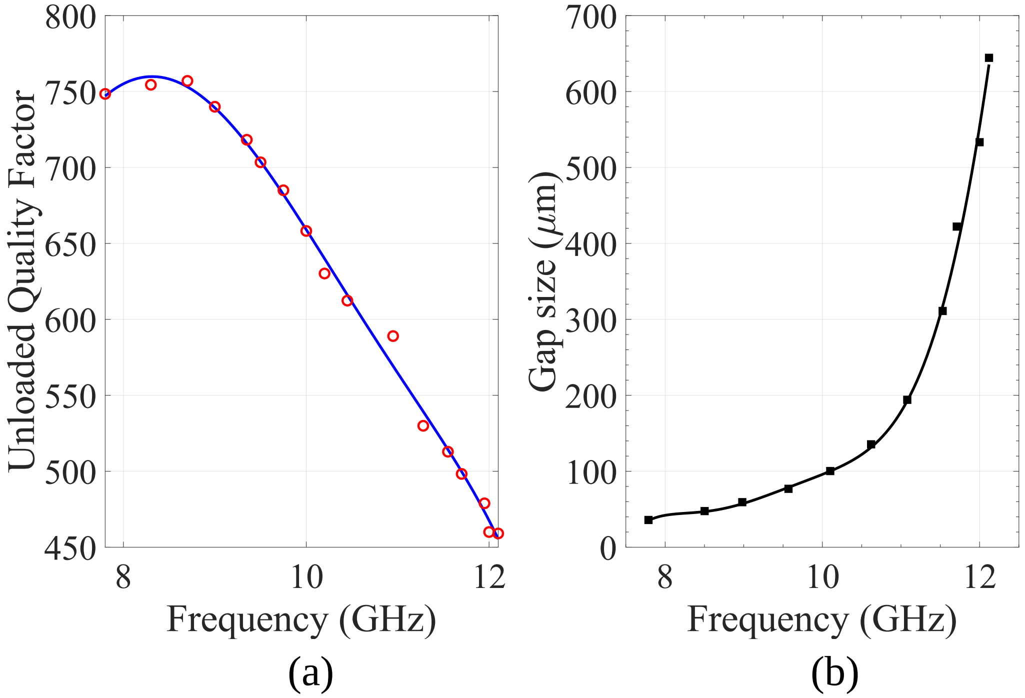

Figure 3.14: (a) Extracted Quality factor with a curve-fit for the extract Q_u data points. (b) Tuning curve for the X-band resonator - Gap size as a function of the resonant frequency.

The contactless-tuned evanescent-mode resonator technology has been used throughout this work to realize the filtenna's first building block, which is a high-performance microwave resonator. The contactless tuning scheme using external long-range linear actuators is also applied in the design and development of a tunable slot antenna and a tunable filtenna, as detailed in the next chapter, Chapter 4.

Chapter 4

Tunable Antenna and Filtenna for S-band Applications using Contactless Tuning

The tunable evanescent-mode cavity resonator technology, presented in Chapter 3, is used to design the filtenna's first building block. The second building block of the filtenna is the antenna which contributes a second pole to the filtering response while also providing radiation functionality. In this work, a slot antenna structure is chosen due to its easy integration into a planar structure. Slot antennas can also be accommodated with a cavity-backing to enable uni-directional radiation, which is beneficial for array integration.

The first section of the chapter presents the design and implementation of a tunable slot antenna integrated with an evanescent-mode cavity resonator. By leveraging the contactless capacitive tuning of the resonator, the antenna's operating frequency is made reconfigurable across a wide range. Next, the tunable cavity-backed antenna is integrated into a filtenna architecture using traditional filter synthesis techniques. The concept, design, implementation, and measurement results of both the antenna and filtenna are discussed in detail. A power-handling capability analysis is also documented to investigate the performance of the tunable devices under high-power operating conditions.

4.1 Contactless-tuned Cavity Backed Slot Antenna

4.1.1 Antenna Design and Tuning Concept

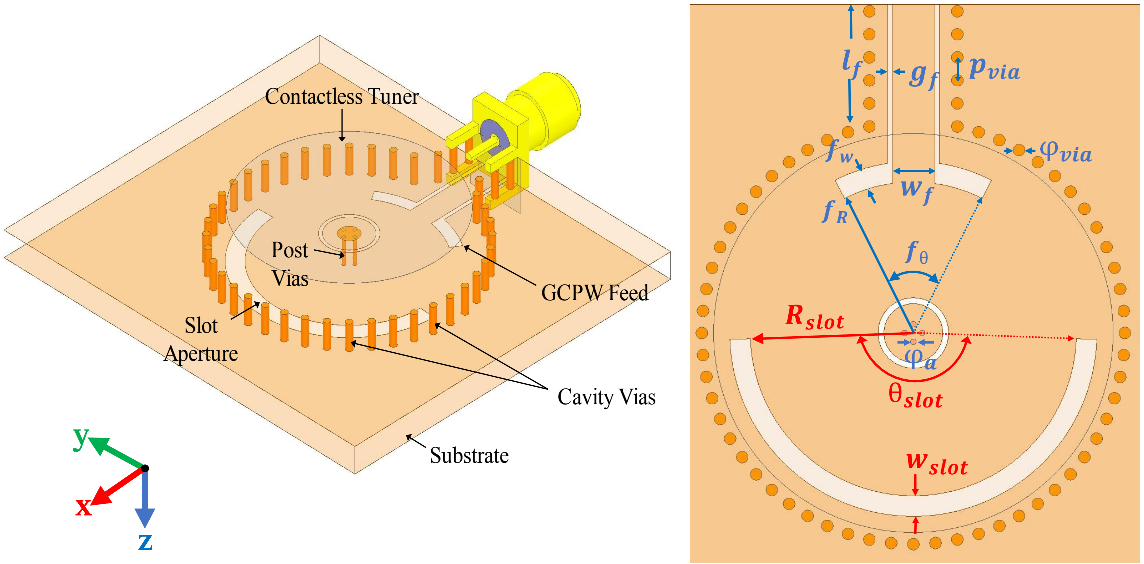

(a) (b)

Figure 4.1: 3-D view and top view of the proposed ECBSA integrated with contactless tuners. Primary design variables of the annular slot aperture and the GCPW feed structure are labeled, and the values are listed in Table 4.1.

The passive antenna structure is realized by isolating an annular slot aperture in the ground plane of a ring-gap loaded EVA-mode cavity resonator, as seen in Fig. 4.1(a). The overall design is implemented using SIW technology with metal vias that form the post and cavity walls. A flared-wing grounded co-planar waveguide (GCPW) feed is used to couple RF energy into the antenna. Primary design dimensions of the antenna and feed are labeled in Fig. 4.1(b).

To accommodate frequency reconfigurability, the contactless tuning method proposed in [57] for tuning EVA-mode cavity filters is used. The addition of the radiating slot in the cavity's ground plane significantly changes the tuning behavior of the cavity structure. The resonant frequency of the dominant mode as a function of the tuning gap g_0 for an unloaded and a slot-loaded cavity is plotted in Fig. 5.9(a). An additional loading effect of the slot aperture is observed due to the magnetic field perturbation in the cavity, which increases the current path along the slot's perimeter. As a result, the tuning curve is shifted down to lower frequencies. Furthermore, there is a decrease in the frequency tuning sensitivity as a function of g_0 due to the slot's loading effect. The antenna's tuning range can be optimized by adjusting the physical dimensions of the cavity and slot aperture.

An antenna prototype was designed based on the evaluation of the trade-offs between tuning range and radiation efficiency. The substrate used for the antenna is Rogers TMM3 ($\epsilon_r = 3.27$, tan $\delta = 0.002$), with a thickness of 125 mils. Based on the design guidelines for SIW structures in [61], the diameter of the cavity via, ϕ_{via}, and post vias, ϕ_a, is 0.8 mm and 0.4 mm respectively. The spacing between vias, p_{via}, is 1.57 mm.

Based on the iterative design procedure in [57], dimensions of the cavity radius b, post radius a, and ring radius r are optimized for a given substrate thickness h to ensure a wide tuning range of the unloaded cavity. The cavity's ring-gap width, w_r, is minimized for low radiation leakage through the ring aperture. All the design dimensions of the ECBSA prototype are listed in Table 4.1.

A parametric study was completed to investigate the effect of the slot's physical dimensions on the resonant frequency f_0 and the frequency tuning range. The cavity dimensions were held constant while varying the physical dimensions of the slot. First, the radial distance between the slot edge and post center, R_{slot}, is varied to determine the location of the radiating aperture in the cavity. As seen in Fig. 5.9(b), maximum tunability and largest aperture are achieved when the slot is located towards the edge of the cavity. The slot angle θ_{slot} has the most significant impact on the tuning range of the antenna, Fig. 5.9(c). Increasing θ_{slot} results in a larger slot length, which is imperative for high radiation efficiency. However, the tuning sensitivity of the slot-loaded cavity also decreases with a larger θ_{slot}. Therefore, there is an inherent trade-off between the tunability and radiation performance

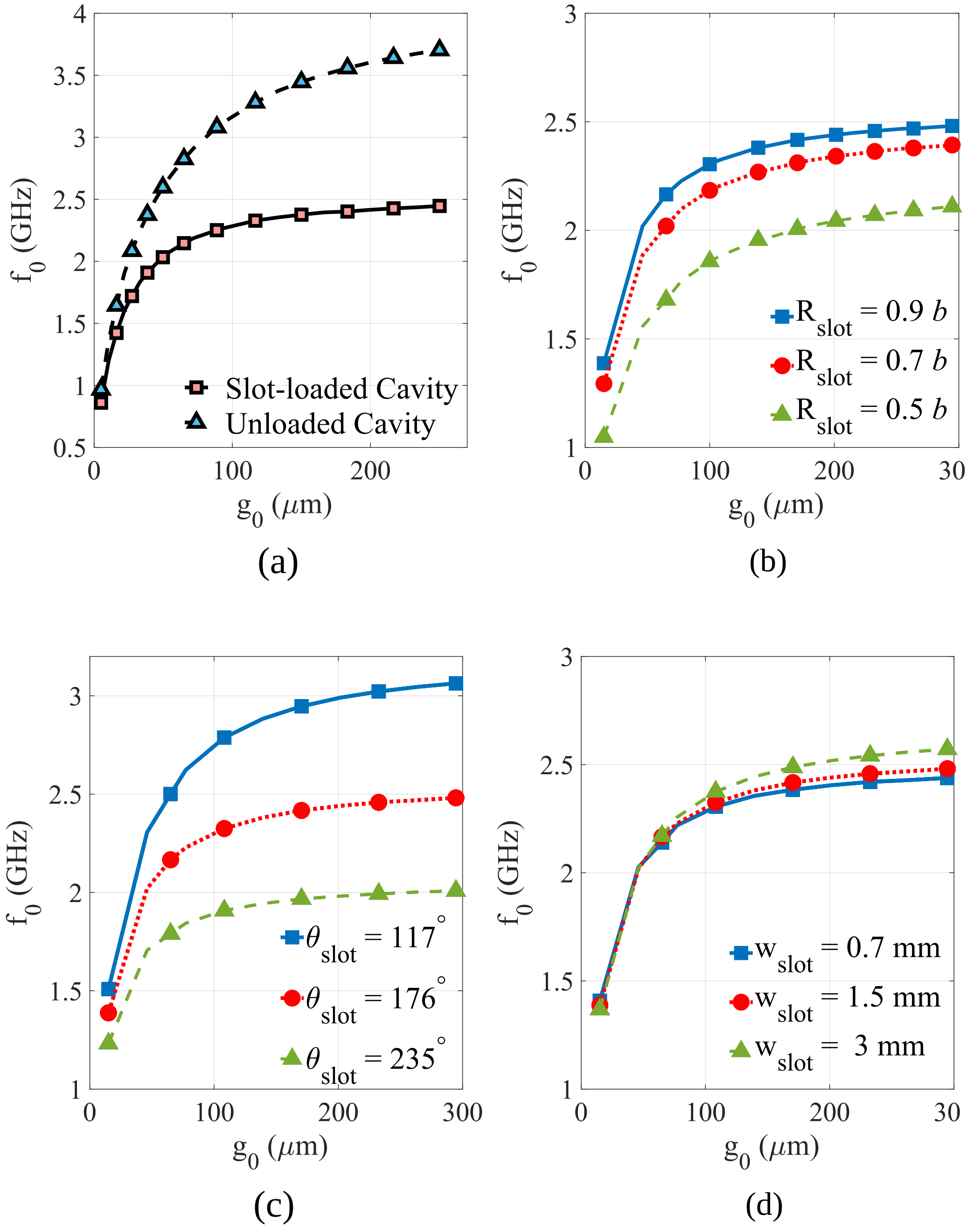

(a) (b)

(c) (d)

Figure 4.2: Parametric analysis of resonant frequency tuning behavior of ECBSA as a function of gap size g_0. Default values for the variables are listed in 4.1 (a) Comparison with an unloaded cavity (b) Effect of the slot radius - R_{slot} (c) slot angle - θ_0, and (d) slot width - w_{slot}.

Table 4.1: Dimensions of the ECBSA using contactless tuning scheme

Slot width	w_{slot}	3.6 mm
Slot radius	R_{slot}	12.5 mm
Slot angle	θ_{slot}	176°
Cavity radius	b	14 mm
Post radius	a	1 mm
Cavity height	h	3.175 mm
Ring width	w_r	250 μm
Ring radius	r	1.5 mm
Feed radius	f_r	11 mm
Feed Angle	f_θ	54.1°
GCPW length	l_f	9.4 mm
GCPW gap	g_f	0.3 mm
GCPW width	w_f	3 mm

in this class of slot-loaded EVA-mode cavities. The width of the slot does not significantly affect the resonant frequency nor the tuning sensitivity of the antenna, Fig. 5.9(d). Therefore, in the proposed ECBSA structure, the slot angle and radius are the two major parameters that can be used to optimize the tuning range.

The magnitude of field distributions in the slot-loaded cavity, operating in its fundamental TM_{010} mode, is shown in Fig. 4.3. The strongest regions of the electric (E) field are concentrated around the surface ring gap and above the post (Fig. 4.3(a)), where the capacitive loading is maximum to accommodate tunability. The E-field is transversal across the slot width, with its maximum around the center of the slot's arc length. Correspondingly, the magnetic (H) field, as seen in Fig. 4.3(b), is maximum at the terminated ends of the slot aperture and minimum at the center. Note that there is a significant H-field presence around

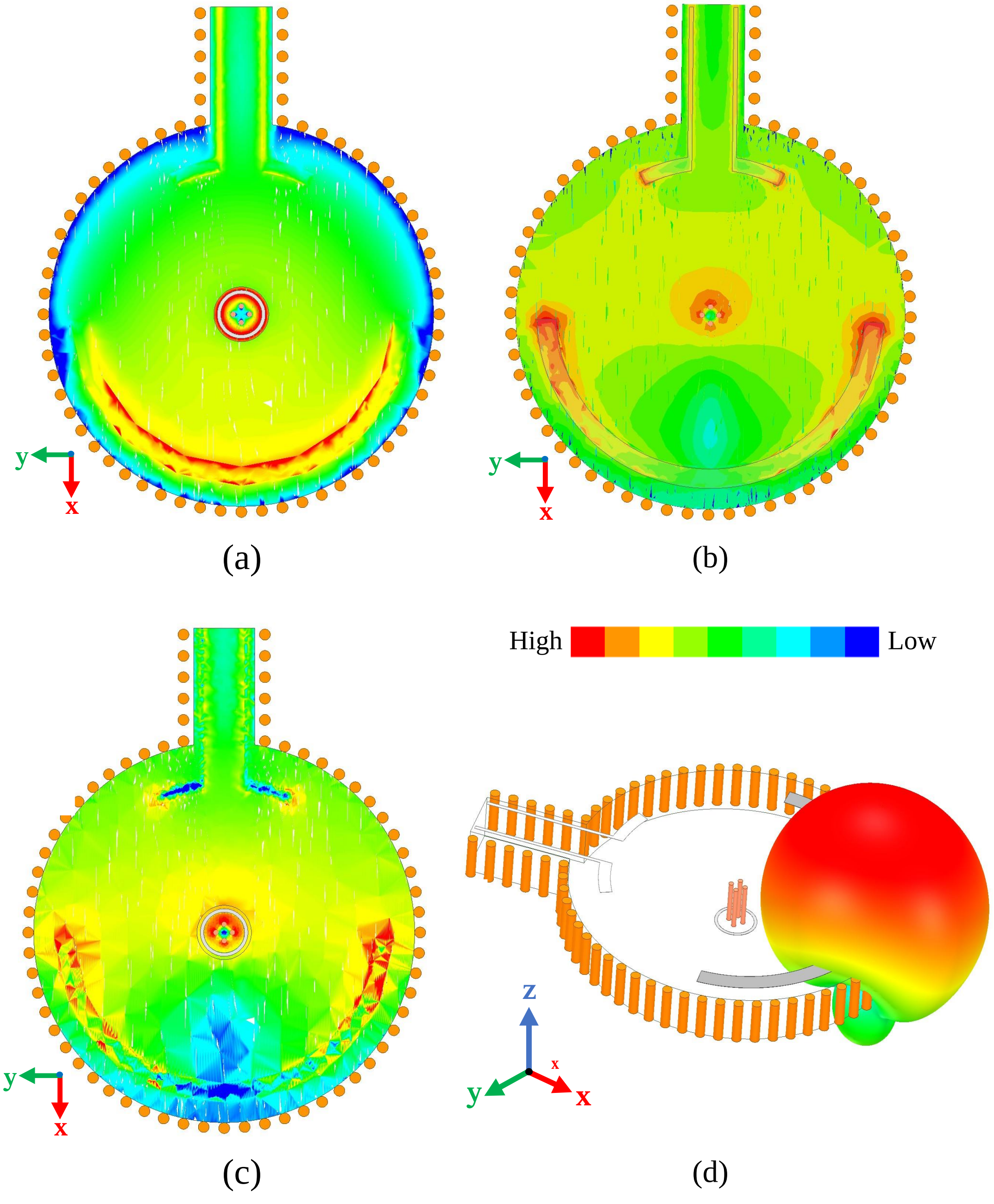

Figure 4.3: Magnitude (in dB) of (a) Electric-field (b) Magnetic-field and (c) Surface current distributions on the slot-loaded EVA-mode cavity operating in its first mode. The 3-D radiation pattern of the linearly-polarized ECBSA is shown (d).

the ends of the GCPW feed due to the strong input coupling into the cavity. As seen in Fig. 4.3(c), the magnitude of surface current decreases from the slot edge to the center. The field distributions resemble a half-wavelength slot resonating in its first resonant mode. The 3-D radiation pattern of the ECBSA in Fig. 4.3(d) shows that the maximum gain is directed perpendicular to the slot aperture due to the presence of the cavity-backing.

4.1.2 Simulated Antenna Design

Simulation results of the antenna's S_{11} magnitude response are shown in Fig. 4.4(a). The antenna can be tuned from 1.6 GHz to 2.6 GHz, with an initial gap of 20 μm and a total actuation range, Δg, of 430 μm. A return loss of greater than 10 dB is maintained across the tuning range.

As seen in Fig. 4.4(b), the peak realized gain ranges from 1.75 dB at 1.7 GHz to 5.6 dB at 2.6 GHz. The total antenna efficiency varies from 30% to 80% from 1.7 to 2.6 GHz. Reduction in radiation efficiency at the lower end of frequency is mainly due to the reduced electrical length of the slot aperture at 1.71 GHz, which is $0.31\lambda_g$ as compared to $0.49\lambda_g$ at 2.6 GHz, where λ_g is the guided wavelength which is determined using

$$\lambda_g = \frac{\lambda_0}{\sqrt{0.5\,(\epsilon_r + 1)}}, \tag{4.1}$$

where λ_0 is the free-space wavelength, and ϵ_r is the relative permittivity of the cavity substrate. The relation in (4.1) is given as a first-order approximation for the effective dielectric constant inside the cavity.

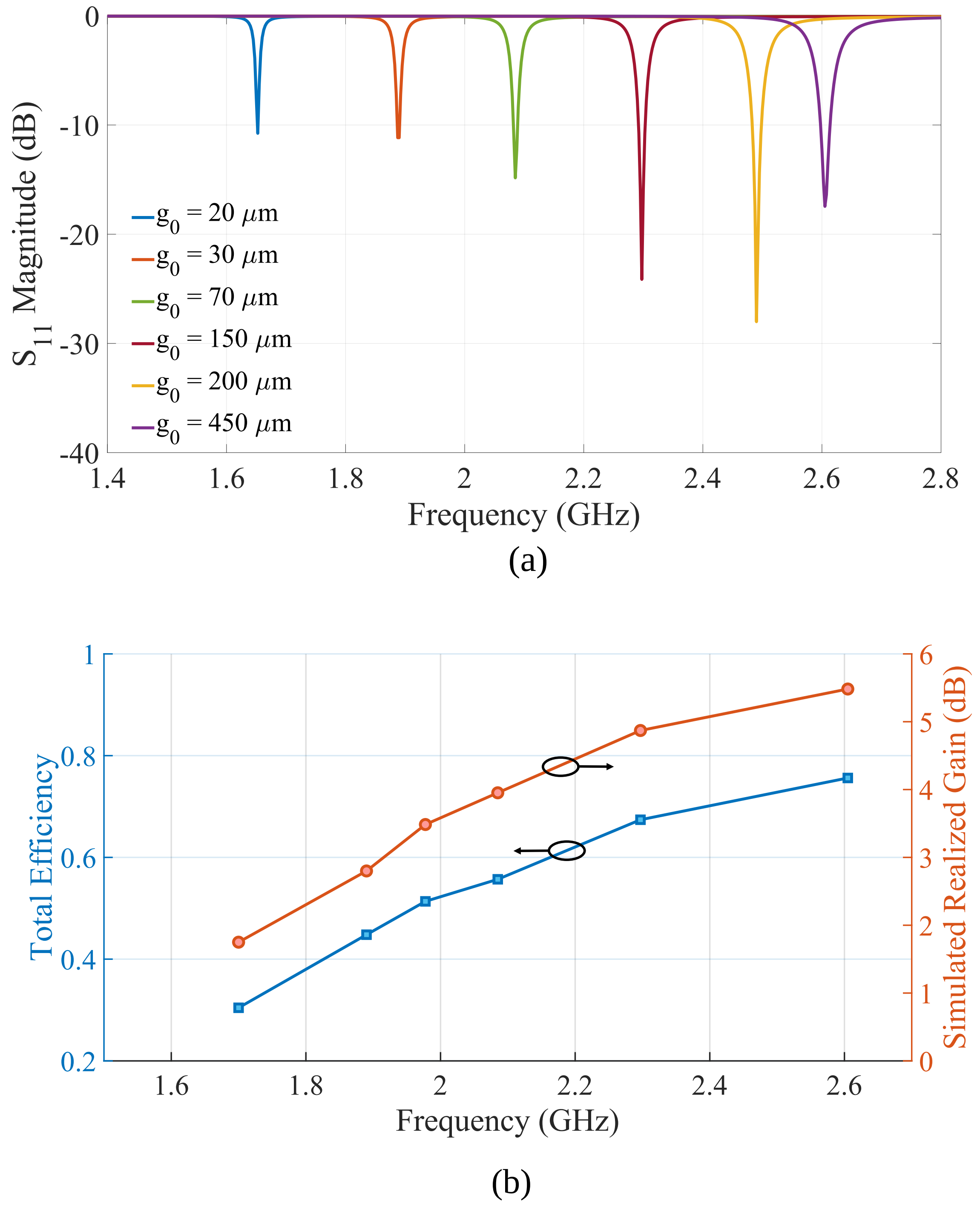

Figure 4.4: (a) Simulated Response of the S_{11} frequency tuning with a gap size variation of 20μm-450μm. (b)Simulated Peak Realized Gain and Antenna Efficiency across the antenna tuning range from 2 GHz to 2.6 GHz.

4.1.3 Fabrication and Measurement

A prototype of the simulated antenna design was manufactured to validate the concept. The floating tuner disc shown in Fig. 3.4 is realized by routing a circular plate from a 60-mil-thick Rogers 4350B substrate. Linear actuators provided by M3-L technologies were used for vertically displacing the tuner. The M3-L module consists of an integrated driver and close-loop control system which directs motion commands from a standard serial interface. These actuators provide a total travel range of 6 mm, with a step-size of 0.5 μm [62].

A 3D-printed mounting structure was constructed to hold the linear actuator. The mount is assembled on top of the substrate using nylon screws. The circular PCB plate was attached to one end of the actuator using quick-setting epoxy. The surface ring, GCPW feed, and slot aperture were patterned using the LPKF Proto-Laser U4 machine. Images of the manufactured antenna and the complete assembly with tuner mount structure are shown in Fig. 4.5.

The manufactured antenna was measured with Agilent Technologies N5225A PNA Network Analyzer. Measurement results of the S_{11} magnitude response in Fig. 4.6 show that the antenna can be tuned from 1.71 GHz to 2.58 GHz while maintaining a return loss of greater than 10 dB. The approximate actuation range Δg is 508 μm for the fabricated prototype, which is an approximately 18$\%$ increase from the simulated design. This slight deviation is caused due to fabrication and mount assembly errors. A direct comparison of the simulated and measured S_{11} curves is shown in Fig. 4.7. Across the tuning range of the fabricated ECBSA, from 1.71 GHz to 2.58 GHz, the shape of the measured S_{11} curve closely follows that of the simulated response.

In Fig. 4.7, g_0 for the measured response is estimated as the effective gap size between the capacitive tuning disk and the post-top. In practicality, the actual gap size cannot be

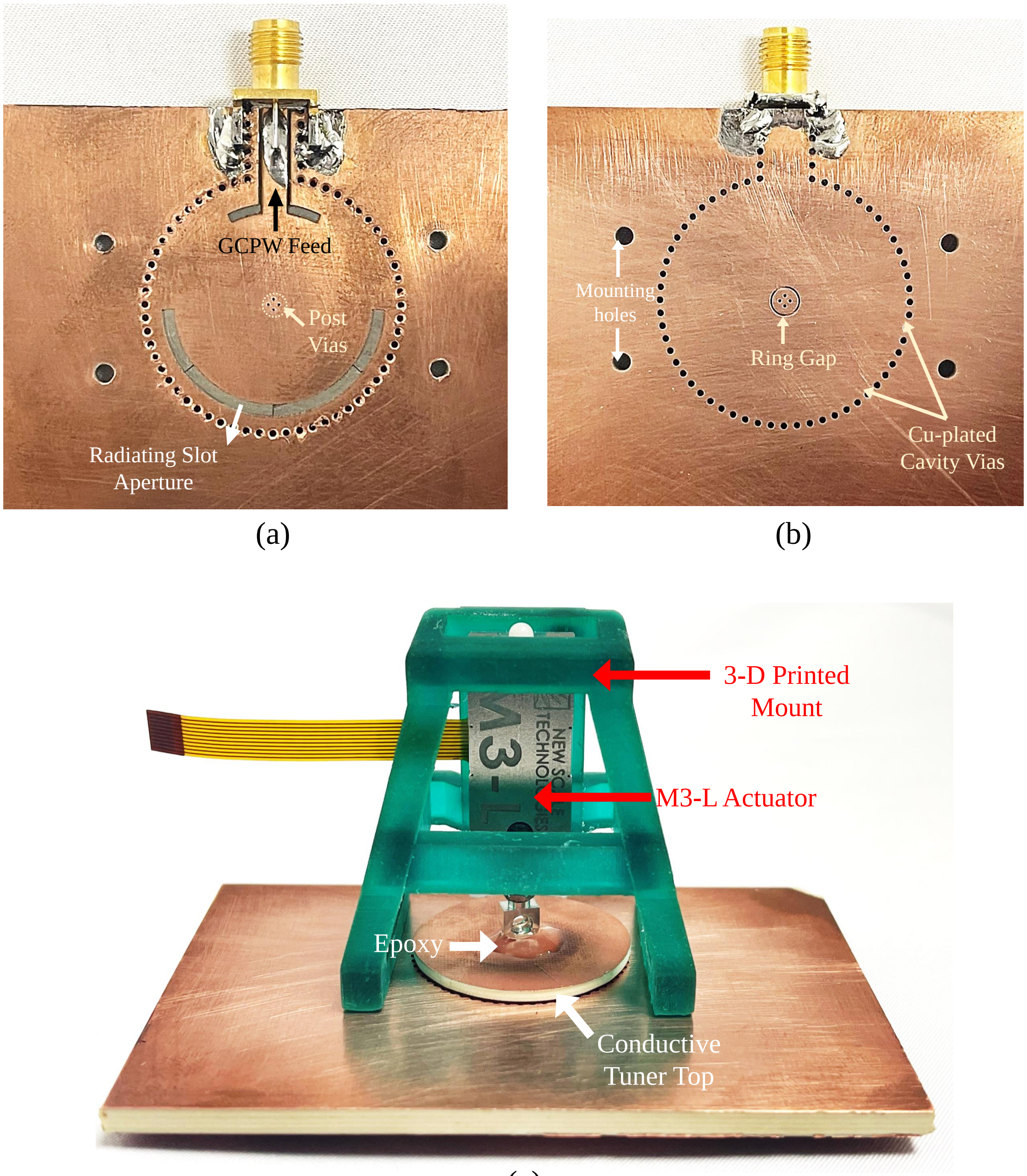

(a)

(b)

(c)

Figure 4.5: Fabricated Prototype (a) Bottom-view with the feed and radiating slot aperture (b) Top-View (c) Full assembly with the M3-L linear actuator and the 3-D printed mount. Dimensions of the ground plane are 90 mm x 60 mm.

determined to a micrometer precision due to several non-idealities, including the uneven surface and deburring effects along the edges of the post top and tuning disk. Additionally,

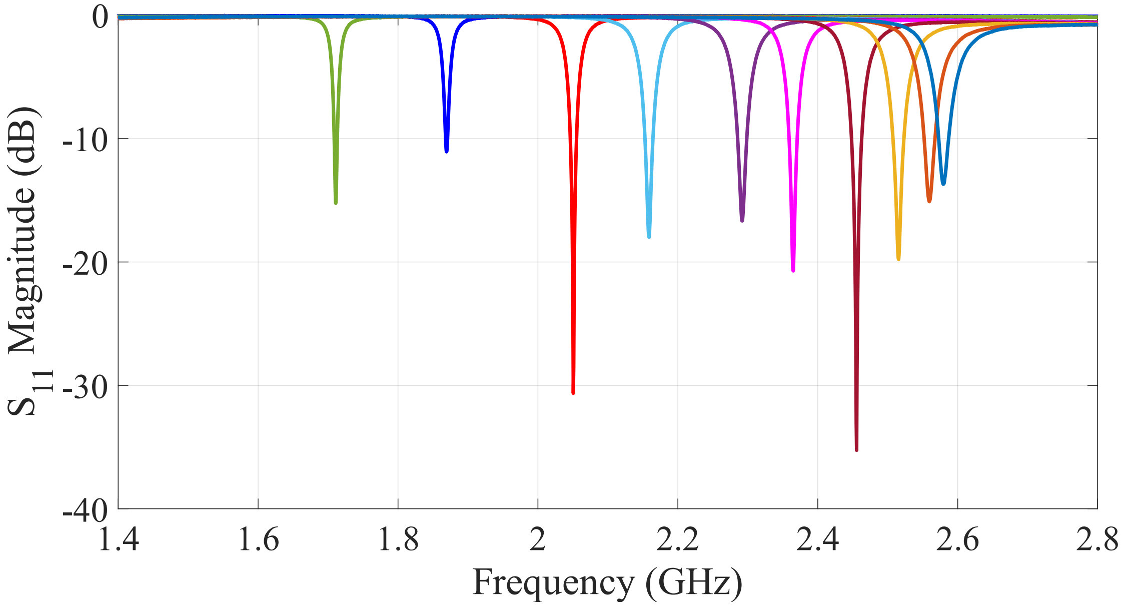

Figure 4.6: Measured S_{11} magnitude response across frequency. The manufactured antenna shows 40% continuous tuning from 1.71 GHz to 2.58 GHz within an actuation range of approximately 508 μm.

the epoxy attachment of the disk to the end of the actuator can cause uneven contraction of the tuning disk in the drying process. The major effect of these non-idealities is an imprecise parallel-plate alignment of the capacitive disk as the linear actuator vertically displaces it. The slightest misalignment of the tuner disc can alter the antenna's tuning sensitivity. Therefore, the effective gap size is an approximation to characterize the antenna's tuning behavior when subject to practical limitations.

The set-up for the radiation pattern measurements of the contactless-tuned ECBSA is shown in Fig. 4.8. An additional support structure was constructed to hold the antenna when measuring the radiation patterns across different cut planes. Measured radiation patterns of the ECBSA are shown in Fig. 4.9. The antenna's peak realized gain varies from 1.45 dB to 5.48 dB as the operating frequency is tuned from 1.71 GHz to 2.58 GHz. At the operating frequency of 2.3 GHz, the measured gain is 4.85 dB. The degradation of realized gain at the lowest frequency of 1.71 GHz is due to a smaller electrical length of

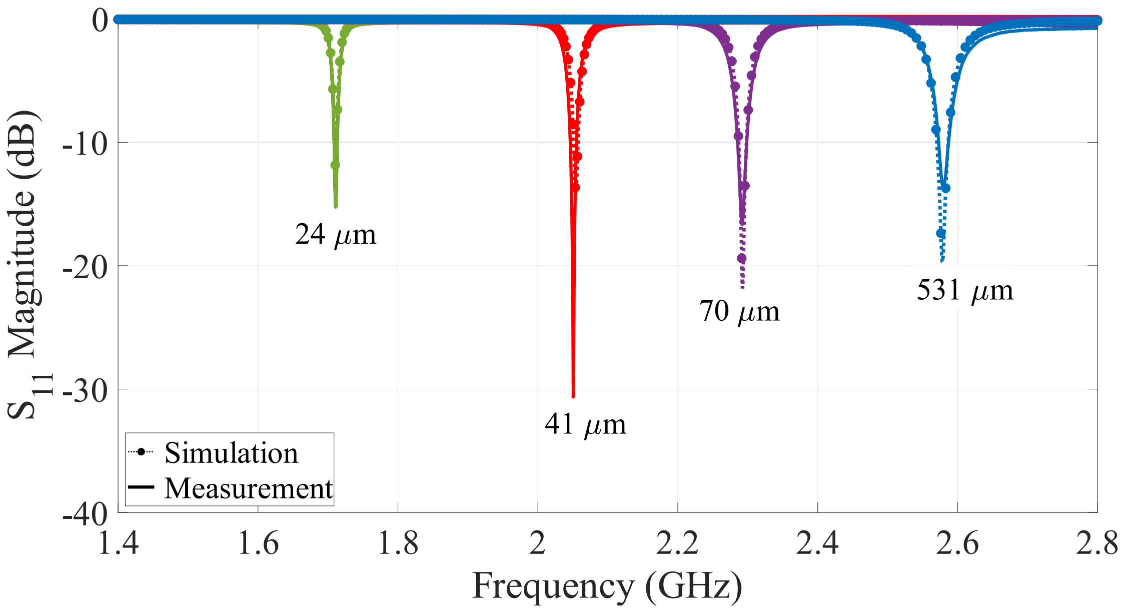

Figure 4.7: Comparison of simulated (dotted line) and measured (solid line) S_{11} magnitude response for the contactless-tuned ECBSA across the measured tuning range from 1.71 GHz to 2.58 GHz. The effective gap sizes are labeled below the corresponding operating frequencies.

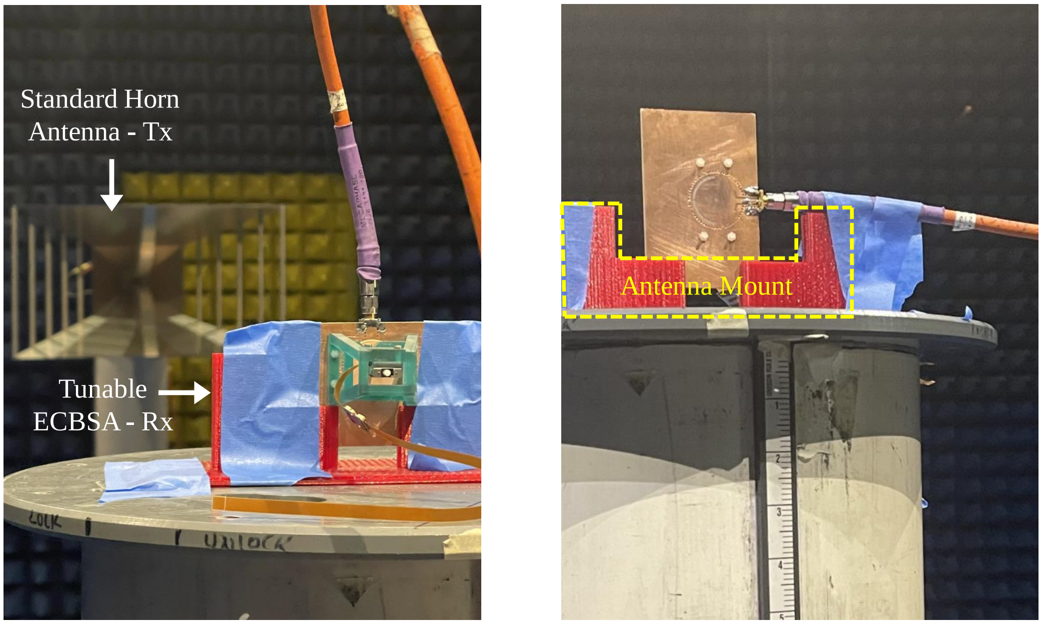

(a) (b)

Figure 4.8: Measurement set-up in the anechoic chamber (a) Vertically-polarized (horizontal orientation) (b) Horizontally-polarized (vertically oriented)

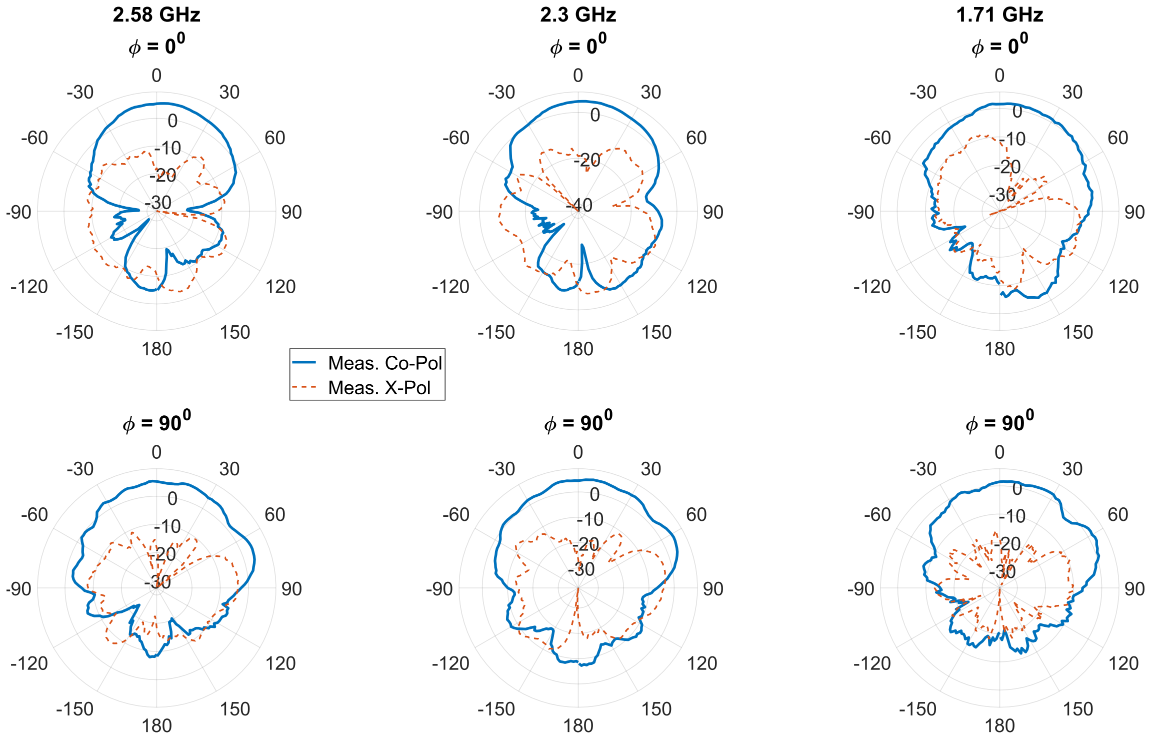

Figure 4.9: Measured radiation patterns across the tuning range of ECBSA at 2.58 GHz, 2.3 GHz, and 1.71 GHz. Both co-polarization and cross-polarization patterns are shown in two cut planes - $\phi = 0°$ and $\phi = 90°$, as per the coordinate system defined in Fig. 4.3.

the slot at maximum loading. Additionally, a small gap size is required to tune the antenna at 1.71 GHz. Due to the complications of accommodating the closed-loop control system during chamber measurements, the gap size cannot be constantly monitored during radiation pattern scanning. Therefore, even a small gap variation during measurements can shift down the operating frequency of the antenna. Due to the narrow-band nature of the antenna, the shift may correspond to a lower measured gain. In a practical application, the close loop monitoring system will constantly be active during the antenna's operation, and therefore fluctuations in gap size can be accounted for by the actuator control system. Furthermore, the above-mentioned non-ideal effects of the imprecise parallel plate alignment and gap size sensitivities may cause detrimental effects only for very small gap sizes and is not an issue for gap sizes larger than 30 μm.

Note that the 3D mount structure assembly is on the opposite side of the main lobe and does not significantly impact the co-polarized radiation pattern. However, the mount does contribute to cross-polarization pollution. Other factors affecting the higher cross-polarization level are feeding coaxial cables and the metal encasing of the linear actuator.

4.1.4 Power Handling Tests

For the proposed contactless-tuned ECBSA, the dominant power breakdown mechanism is the ionization breakdown of the air dielectric in the capacitive gap between the post-patch and the tuner. For critical gap-sizes of more than $10\ \mu$m, microwave discharge in gases is found to be the major limiting factor for PHC in EVA-mode resonators and filters [51]-[50]. The majority of the electric field is concentrated in the sensitive capacitive region between the post-patch and tuner plate. With increasing input power, the electric-field strength within the capacitive gap rapidly increases until the microwave gas breakdown mechanism takes place, as detailed in [51], [50], and [52].

To predict the peak PHC of EVA-mode-based resonators and filters, a method is presented in [52] using full-wave electromagnetic (EM) solvers to extract the electric field in the sensitive capacitive region of EVA-mode cavities. A simplified version of the procedure in [52] is applied to predict the peak PHC, P_{max}, of the ECBSA from ANSYS HFSS Modal simulation,

$$P_{max} = \left(\frac{E_{breakdown}}{E_{max-sim}}\right)^2 \times P_{sim} \tag{4.2}$$

where $E_{breakdown}$ is the air breakdown electric field 7.9 V/μm as reported in [50], $E_{max-sim}$ is the normalized maximum electric field extracted from the capacitive-gap between post-patch and the tuner, and P_{sim} is the input power of the modal simulation set-up which is set at 1 Watt. As seen in Fig. 4.10, the fields are heavily concentrated in the critical capacitive gap, so they can be directly extracted from the post-patch.

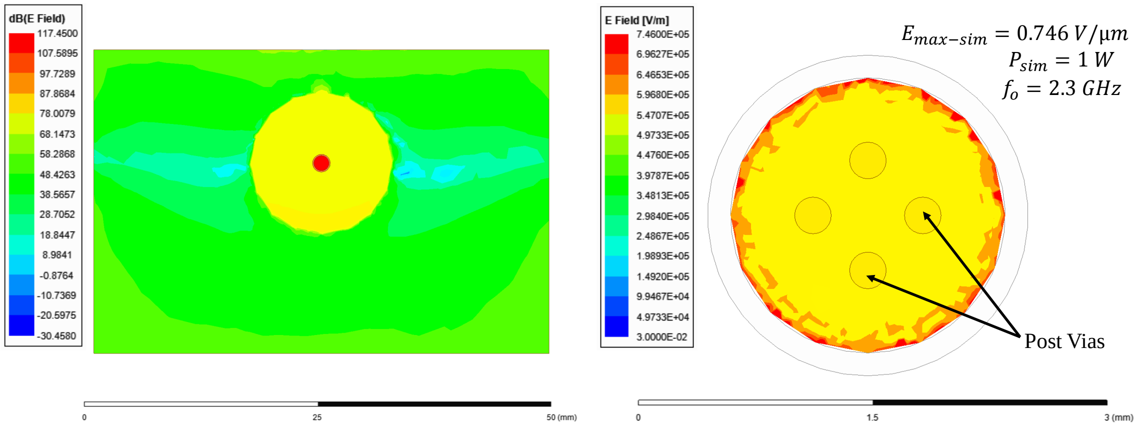

(a) (b)

Figure 4.10: Electric field distributions in the ECBSA when tuned to 2.3 GHz (a) Log magnitude of E-field distribution throughout the structure, showing maximum E-field in the post-patch (b) Peak electric field extracted from the capacitive gap.

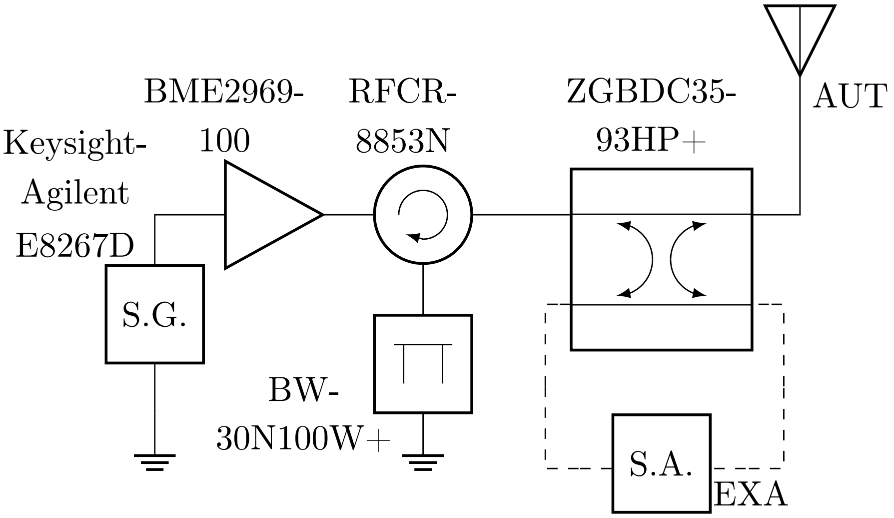

Figure 4.11: Block diagram of the high-power measurement set-up to test ECBSA's power handling capability.

To experimentally evaluate the power-handling capability of the proposed antenna, a high-power measurement set-up, capable of providing up to 100 W of power, was assembled, as illustrated in Fig. 4.11. The front end consists of a circulator, bi-directional coupler, and pi-network attenuator to protect the power amplifier and signal analyzer (SA). The bi-directional coupler's coupled lines were used in conjunction with a spectrum analyzer and SCPI scripts to record the magnitude of the incoming and reflected waves. The reflection coefficient was calculated by taking the ratio of the incoming and reflected waves.

Results of the high-power tests for the proposed ECBSA are shown in Fig. 4.10. To evaluate the power breakdown mechanism, the S_{11} response of the antenna is tracked across the tuning range for different input powers. Based on the operational frequency range of the components in the measurement set-up, power-handling tests were carried out with the antenna tuned to operating frequencies of 2.3 GHz, 2.4 GHz, and 2.6 GHz. The input power was swept gradually up to a maximum of 100 W. At the operating frequencies of 2.58 GHz and 2.4 GHz, the ECBSA can handle more than +50 dBm, or 100 W, of input power. The effective gap size corresponding to the operating frequency of 2.58 GHz and 2.4 GHz is 500 μm and 95 μm, respectively. Due to the deployed contactless tuning scheme, the available range of gap sizes is much higher than the typically used piezoelectric discs. As a result, the maximum power handling capability is much higher for the contactless-tuned ECBSA at larger gap sizes.

When the antenna is tuned to a frequency of about 2.3 GHz, the antenna's S_{11} response shows performance degradation at 100 W. With a finer sweep of input powers, it was found that the breakdown effects started to occur at about +49.4 dBm, or about 87 W. The slight discrepancy between the simulated and measured breakdown power is attributed to non-uniformity in the air gap and sharp edges formed on the post-patch during the fabrication and assembly process [52]. The relatively lower PHC at the lower frequency is expected due to the smaller gap size. The PHC of the proposed ECBSA design can be further increased by redesigning the antenna to have a smaller tuning range and larger gap sizes across the entire tuning range.

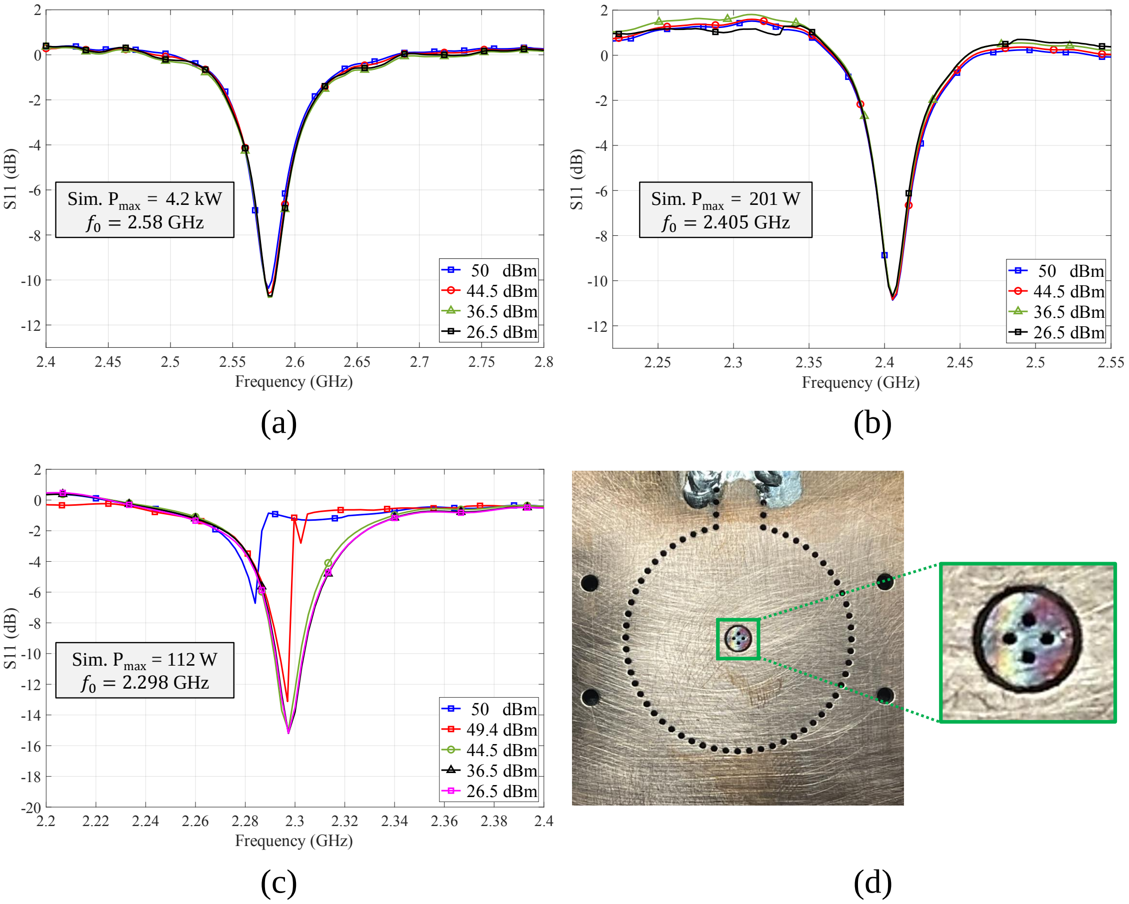

Figure 4.10: Measured S_{11} magnitude Response is tracked for different input powers and antenna operating frequencies at (a) 2.58 GHz (b) 2.405 GHz (c) 2.3 GHz. The proposed ECBSA can withstand over 100 W of input power at 2.58 GHz and 2.4 GHz. At 2.3 GHz, corresponding to a gap size of 70 μm, the antenna exhibited breakdown at about 87 W (+49.4 dBm). A visual imprint of the air-dielectric breakdown due to the concentration of E-field above the post is seen in (d).

4.1.5 Performance Evaluation

Table 4.2 provides a performance comparison of the proposed ECBSA with other state-of-the-art tunable cavity-backed slot antennas. The tuning range, TR, is calculated based on the maximum frequency (f_H) and minimum frequency (f_L) of the tuning range, given as

$$TR = \frac{(f_H - f_L)}{(f_H + f_L)/2} \times 100\%. \tag{4.3}$$

As seen in Table 4.2, the antennas tuned with semiconductor devices in [63] and [64] exhibit a large tuning range with a small footprint. However, they have low power-handling capacity, lower radiation efficiencies, and degraded linearity performance. The contactless-tuned ECBSA presented in this work exhibits the largest tuning among the high-power mechanically tunable antennas while also maintaining high linearity, good tuning reliability (in terms of long-term operation), and a low profile.

Table 4.2: Comparison with state-of-the-art frequency reconfigurable cavity-backed slot antennas

Ref.	**Structure**	**Tuning mechanism**	**Tuning Range (TR)**	**Speed**	**PHC**	**Reliability**	**Electrical footprint (in λ_g*)**
[63]	SIW	4 PIN diodes	67%	Very fast	Low	Low	0.6 × 0.4× 0.02 †
[64]	Metal	1 Varactor	62%	Very fast	Low	Low	0.4× 0.4× 0.02 †
[65]	SIW	48 PIN diodes	LP: 3.8% CP: 1.7%	Very fast	Low	Low	0.7× 0.6× 0.01
[66]	Metal	2 Tuning screws	Single band - 13.6% Wide band - 5.6% Dual band - 11.5% / 18.3%	Slow	High	High	0.7×0.7× 0.5 0.9× 0.7× 0.6
[67]	Metal	1 Piezoelectric disk	25%	Fast	High	Low	0.4× 0.4 × 0.08
This work	SIW	1 Linear Actuator	40%	Fast	High ‖	High	0.6× 0.6× 0.03

PHC: Power Handling Capacity, LP: Linear Polarization, CP: Circular Polarization.

* Guide wavelength, λ_g, is approximately calculated at the center operating frequency f_c of the tuning range.

† λ_g is calculated with respect to the dielectric inside the cavity for the two-dielectric layer structures.

‖ Power handling evaluation based on experimental results presented in this work.

4.2 Contactless-Tuned Filtenna

4.2.1 Filtenna Design and Concept

The fundamental building block of the filtenna structure is an EVA-mode cavity resonator. The central metal post of the resonator is short-circuited to the top conductive layer, and an annular ring-gap aperture is isolated. The ring-loaded EVA-mode resonator forms the first resonator of the second-order filtenna topology seen in Fig. 4.11. The second resonator of the filtenna is an evanescent-mode cavity-backed slot antenna (ECBSA), which is realized by patterning a radiating slot aperture in the cavity's ground plane. The filtenna is implemented with SIW technology in a single PCB substrate. Metal vias form the cavity walls and central posts of the two resonators.

A conceptual depiction of the frequency tuning mechanism for the filtenna is illustrated in Fig. 4.13 (a). By placing two contactless conductive plates above the ring-loaded EVA-mode cavities, the structure can be capacitively loaded. The floating conductive plate introduces

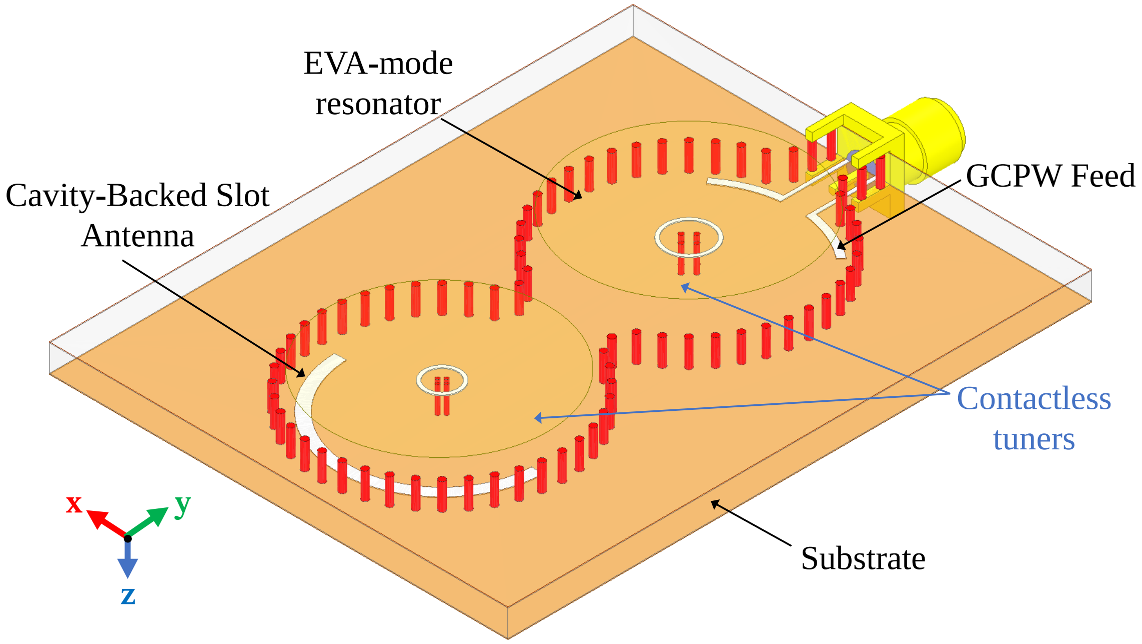

Figure 4.11: 3D view of the S-Band Filtenna

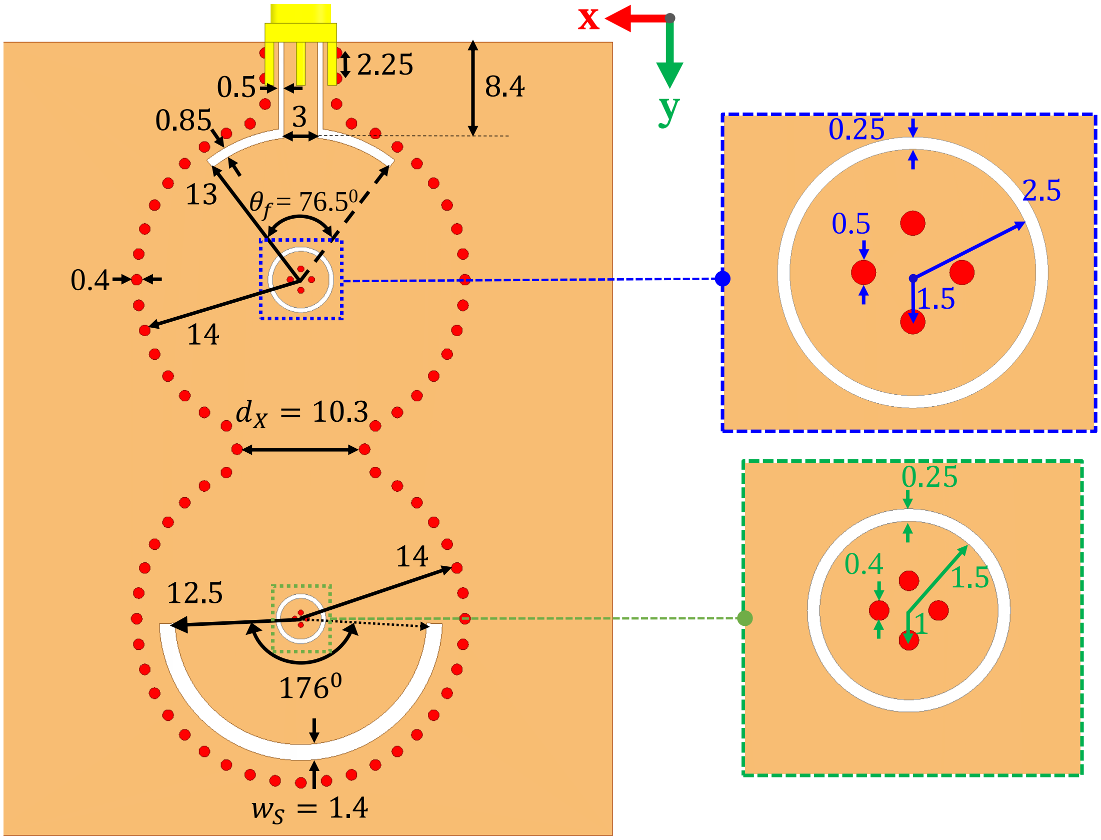

Figure 4.12: Final dimensions of the designed filtenna: feed angle $\theta_f = 76.5°$, iris width $d_X = 10.3$ mm, slot width $w_S = 1.4$ mm. The ground-plane size is 70 mm×75 mm.

additional series capacitance above the ring gap, labeled as C_{t1} for the EVA-mode cavity and C_{t2} for the ECBSA in Fig. 4.13 (a). By changing the vertical gap size g_1 and g_2 of the cavity and ECBSA, respectively, the loading capacitances C_{t1} and C_{t2} can be varied, and the center-frequency of both resonators can be tuned.

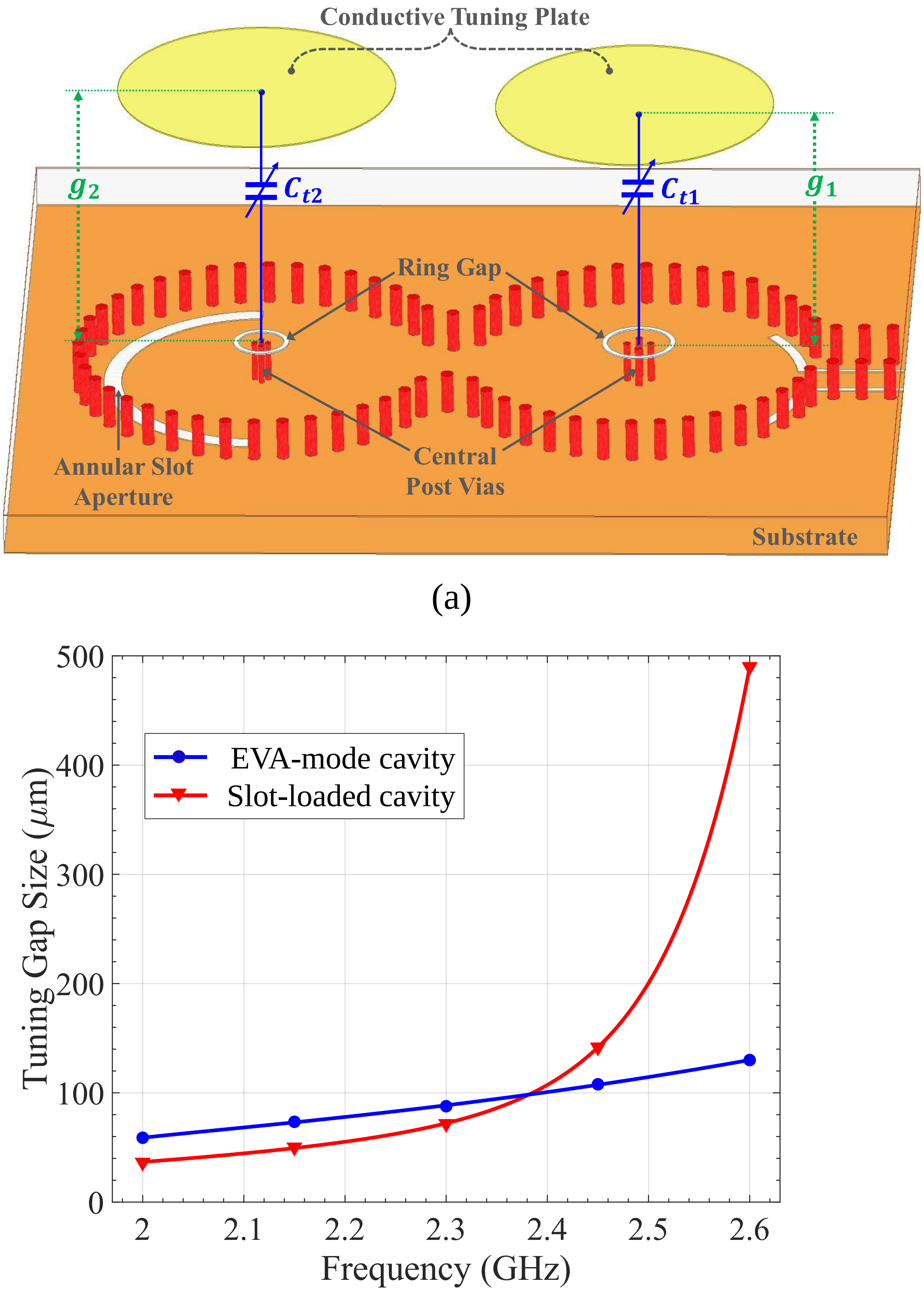

(a)

(b)

Figure 4.13: (a) Contactless tuning scheme applied in the design of a filtenna (b) Comparison of the tuning sensitivity for the individually tuned EVA-mode cavity and slot-loaded cavity, or ECBSA. Default dimensions are shown in Fig. 4.12.

As noted in Section 4.1, the frequency tuning behavior as a function of gap size is different for the slot-loaded EVA-mode cavity as compared to the unloaded cavity. Considering the cavity's dominant TM_{010} mode, the addition of a radiating slot aperture perturbs the toroidal magnetic field distribution in the cavity and increases the current path along the slot's perimeter. As a result of the field perturbation due to the slot structure, the tuning sensitivity of the cavity's resonant frequency as a function of the gap size reduces. A comparison of the tuning curves for a slot-loaded and unloaded EVA-mode cavity, seen in Fig. 4.13 (b), depicts the de-sensitization of the electric field in the capacitive-gap for the ECBSA structure. As a result, the required vertical displacement to tune the antenna increases by almost six times, as compared to the unloaded EVA-mode resonator.

4.2.2 Filtenna Synthesis Procedure

The individual building blocks of the filtenna and the contactless tuning scheme used for frequency reconfiguration were detailed in Section 4.2.1. The next step is to integrate the EVA-mode resonator and cavity-backed slot antenna into a second-order filtenna unit by applying traditional bandpass filter synthesis techniques. The EVA-mode based filtenna is implemented in a 125 mil thick Rogers TMM3 substrate ($\epsilon_r = 3.27$, tan $\delta = 0.002$). The filtenna's coupling routing diagram and the equivalent circuit model are illustrated in Fig. 4.14. In order to synthesize a specific filtering response, the filtenna's physical dimensions must be designed to match the inter-resonator coupling coefficient k_{12}, and the external quality factors at the input, Q_{ext1}, and the output port, Q_{ext1}. For proof-of-concept, a second-order Butterworth filtering response with 1.5% fractional bandwidth is synthesized at a center frequency of 2.3 GHz. The required values of k_{12}, Q_{ext1}, and Q_{ext2} can be calculated using Eq. (2.2) as,

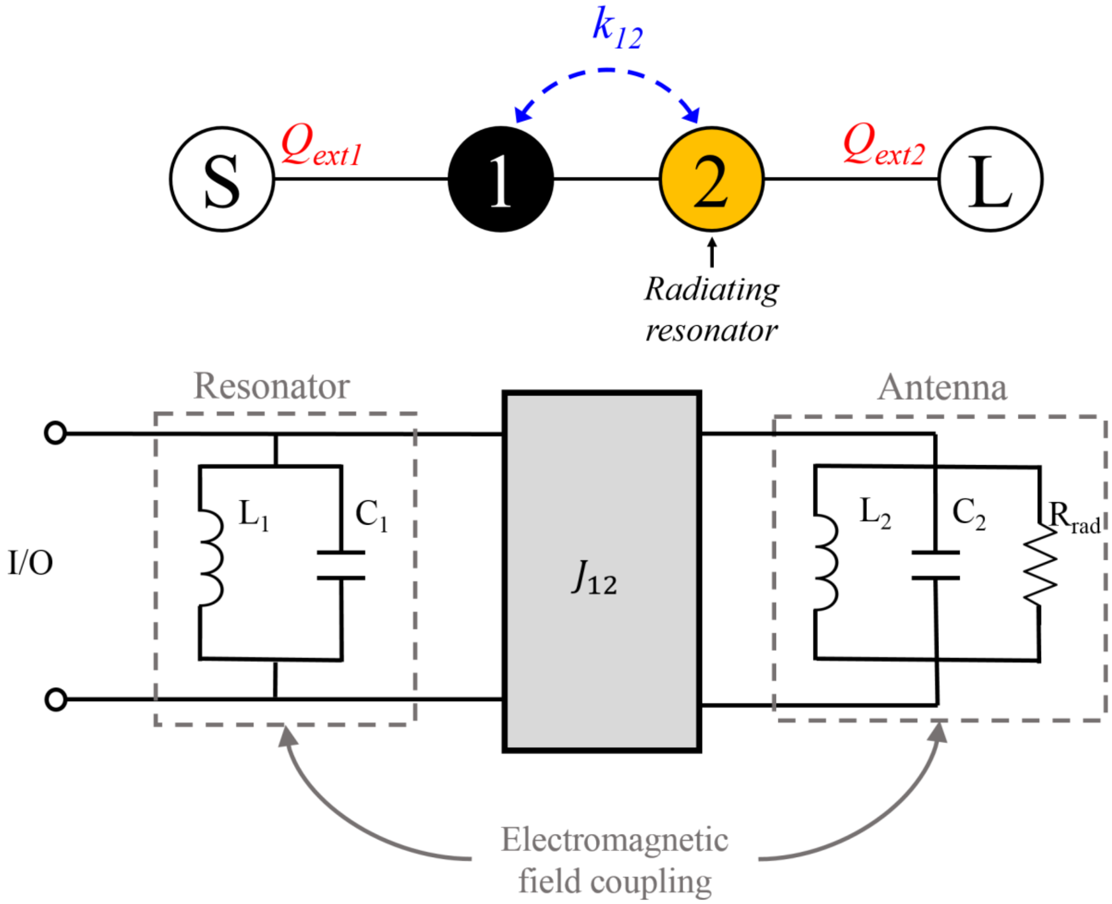

Figure 4.14: Concept of second-order filtenna realization depicted through coupling routing diagram and the equivalent circuit representation. The radiating resonator, which is represented by an LC circuit along with a radiation loss resistance, contributes an additional pole to the filtering response.

$$Q_{ext1} = Q_{ext2} = 94.28 \quad \text{and} \quad k_{12} = 0.0106 \tag{4.4}$$

The external input coupling into the resonator, Q_{ext1}, is realized using a Grounded Co-planar Waveguide (GCPW) feed. Additional semi-circular slots, forming a flared-wing structure, are added to the end of the GCPW feed to increase the magnetic field coupling between the feed and the cavity. The GCPW feed's sector angle, θ_f, is primarily used for adjusting Q_{ext1}, as seen in Fig. 4.15. Increasing the feed angle increases the coupling at

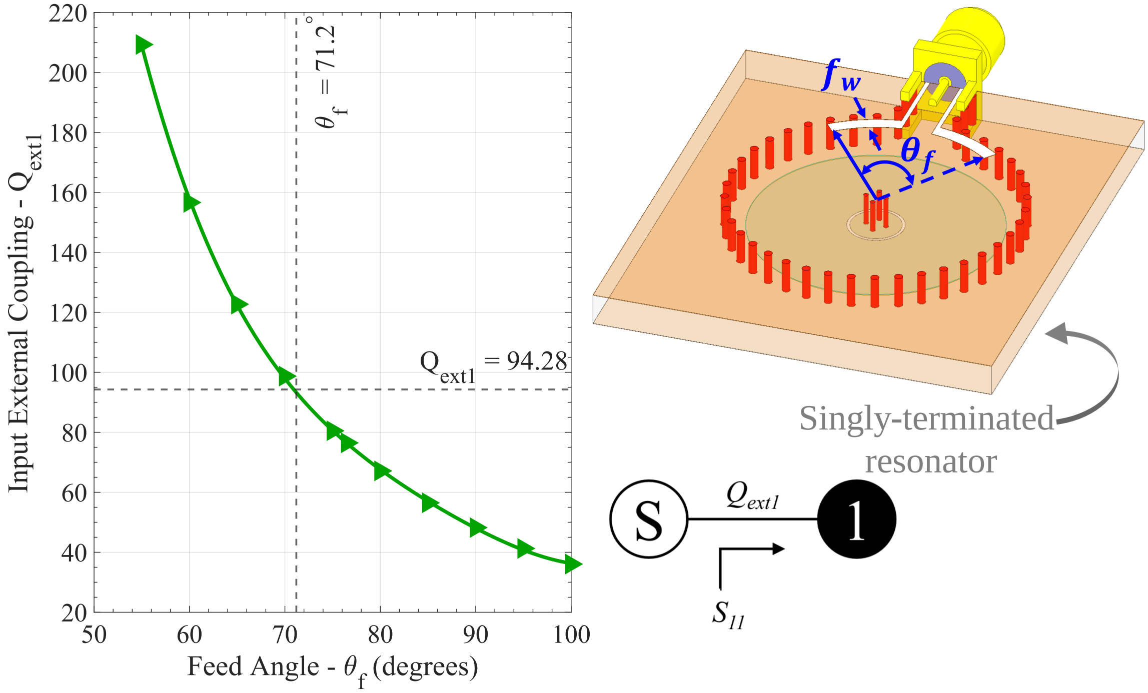

Figure 4.15: Q_{ext1} as a function of GCPW Feed Angle with singly-terminated resonator

the input port. A stronger input coupling reduces the quality factor Q_{ext1}. The feed width, f_w, does not significantly impact Q_{ext1}, but it can be used for fine-tuning. It should be noted that increasing the feed angle leads to additional loading of the structure due to an increase in the total current path across the perimeter of the short-circuited GCPW wings. To accurately extract Q_{ext1}, the cavity's center frequency needs to be re-tuned by increasing the cavity's critical gap size. As described in Section 2.1.1, the simulation of a single-terminated EVA-mode cavity resonator enabled the extraction of the design curve corresponding to Q_{ext1} as a function of the feed's sector angle.

Next, the inter-resonator coupling between the EVA-mode cavity resonator and the cavity-backed slot antenna is realized through an iris opening to facilitate an overlap of the magnetic fields in the two cavities. The value of the inter-resonator coupling coefficient, k_{12}, is extracted as a function of the iris-width d_x, as seen in Fig. 4.16. The method proposed in [43] for extracting a filtenna's coupling coefficient from the transmission response can be

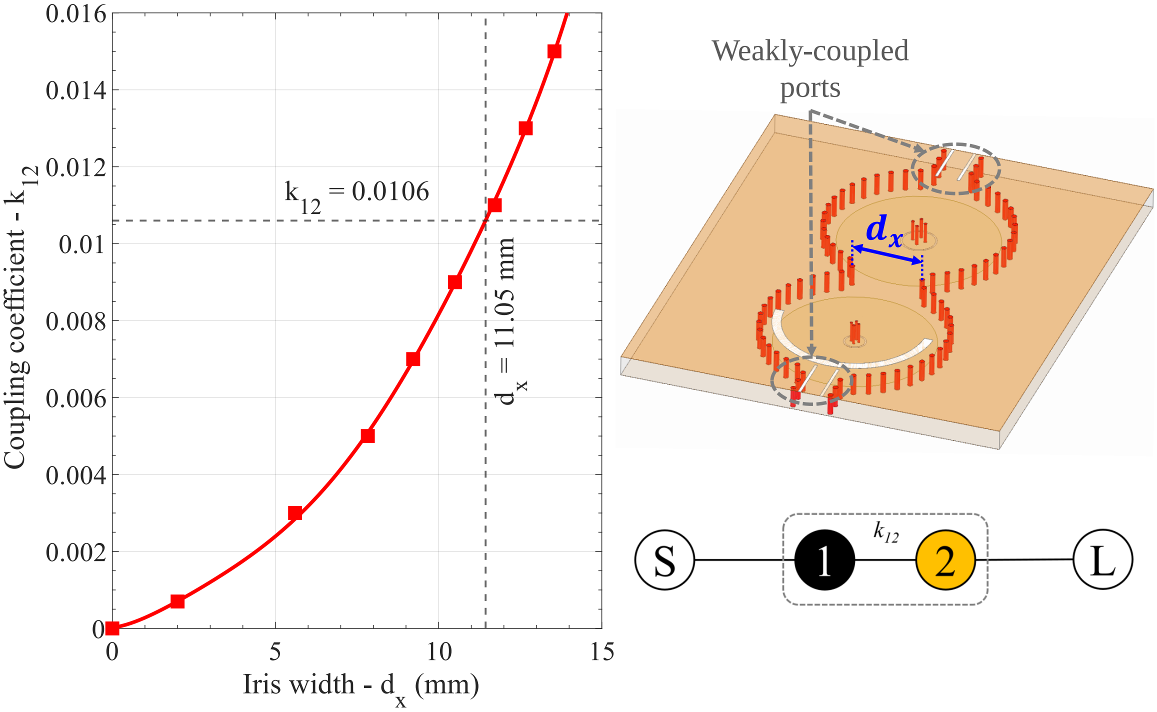

Figure 4.16: Extracted k_{12} function of the iris width using the split-pole technique.

used to extract the design curve corresponding to k_{12}.

The external coupling between the radiating slot-loaded resonator and the free space is adjusted to accurately match the value of Q_{ext2}. The free-space coupling mechanism takes place through the radiating slot aperture. By matching the lossless radiation quality factor of the antenna, Q_{rad}, to the required value of Q_{ext2}, the specified filter response can be generated. For the ECBSA, the Q_{rad} value was primarily adjusted using the slot aperture width, w_s, since it has minimal impact on the antenna's resonant frequency. The design curve corresponding to Q_{ext2} as a function of the slot width is plotted in Fig. 4.17.

The coarse tuning method using the coupled-resonator synthesis technique is an initial step for designing the filtenna. Then, the time-domain tuning technique, described in Section 2.2, is applied to fine-tune the filtering response. As seen in Fig. 4.18, the time-domain response of the coarse-tuned filtenna mainly indicated a mistuned resonance of the

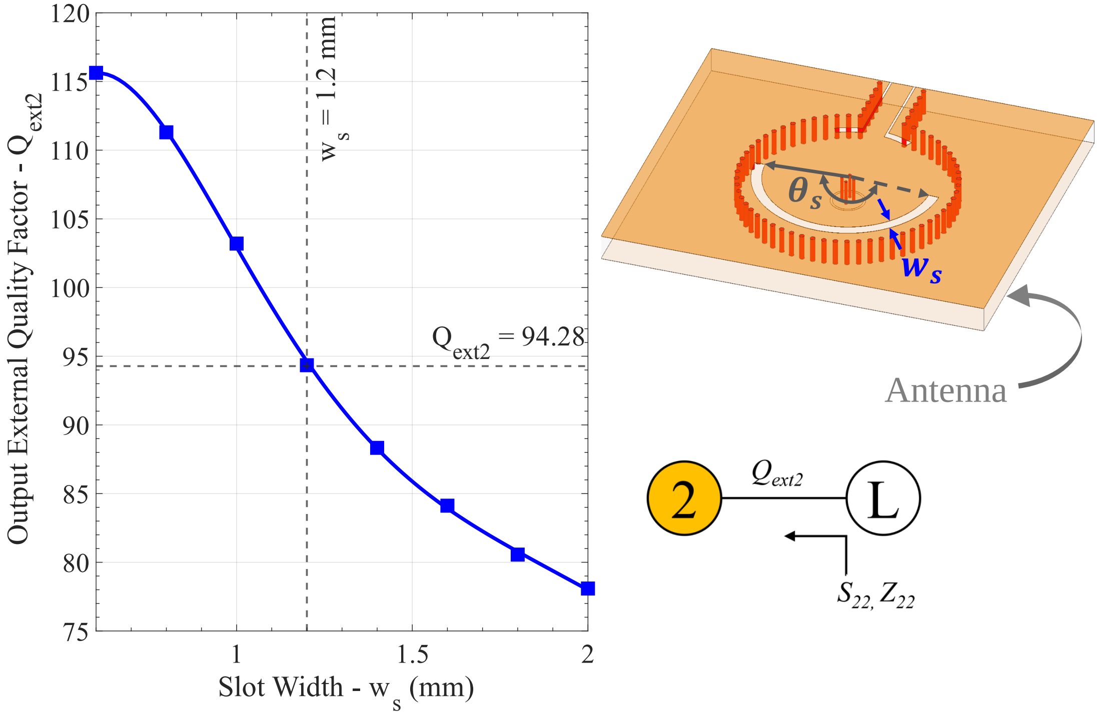

Figure 4.17: Output External Coupling of the filtenna, Q_{ext2} as a function of the ECBSA slot-width. The design curve is extracted by analyzing the antenna's impedance response.

antenna and a low external coupling at the input and output. After adjusting the respective couplings, the final fine-tuned response closely matches the ideal time-domain response based on the filter specifications.

The simulated frequency-domain response of the synthesized filtenna at a center frequency of 2.3 GHz is shown in Fig. 4.19. The simulated filtenna displays a peak realized gain of 4.7 dB at 2.3 GHz. By changing the critical gap sizes g_1 and g_2 of the resonator and slot-loaded antenna, the designed filtenna is tuned across a frequency range of 2 GHz to 2.6 GHz. The simulated peak realized gain is 3.2 dB at 2 GHz, increasing to 5.4 dB at 2.6 GHz. The fractional bandwidth of the filtenna varies from approximately 1.32% to 1.6 from 2 GHz to 2.6 GHz, respectively. The variation in fractional bandwidth across the tuning range is expected due to the different electrical lengths of the iris, which changes the value of k_{12}. At 2 GHz, the iris is electrically smaller, leading to an under-coupled response.

At 2.6 GHz, the iris is electrically larger, which leads to an over-coupled response and a wider bandwidth. Also, note that the S_{11} match is different across the tuning range from 2 GHz to 2.6 GHz due to varying electrical lengths of the input GCPW feed and the slot length and aperture of the antenna at the output.

The maximum operating frequency of the filtenna is mainly limited by the maximum operating frequency of the contactless-tuned ECBSA. As noted in Section 4.1, loading the evanescent-mode cavity with an annular slot in the ground results in a perturbation in the cavity's magnetic field. As a result, the tuning sensitivity of the slot-loaded cavity is reduced compared to that of an unloaded cavity. Therefore, the filtenna's maximum operating frequency corresponds to the maximum operating frequency of the contactless-tuned ECBSA, which is 2.6 GHz.

Compared to a single antenna, the gain response of the filtenna shows a much higher out-

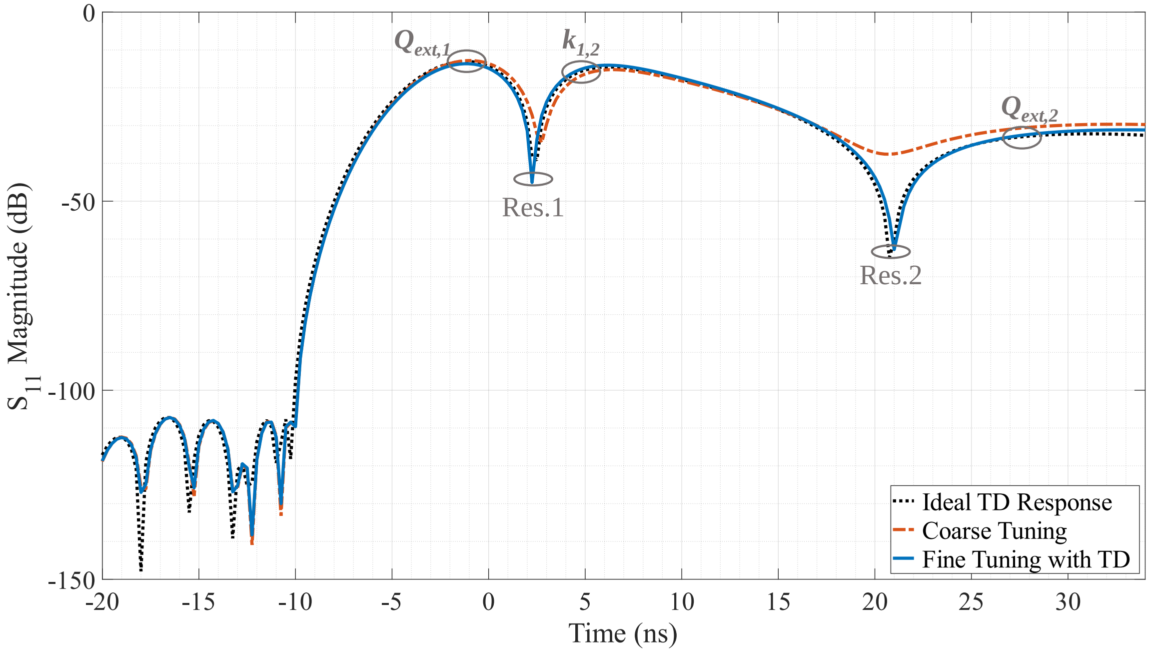

Figure 4.18: Time-domain magnitude response of S_{11} for the synthesized filtenna at a center frequency of 2.3 GHz.

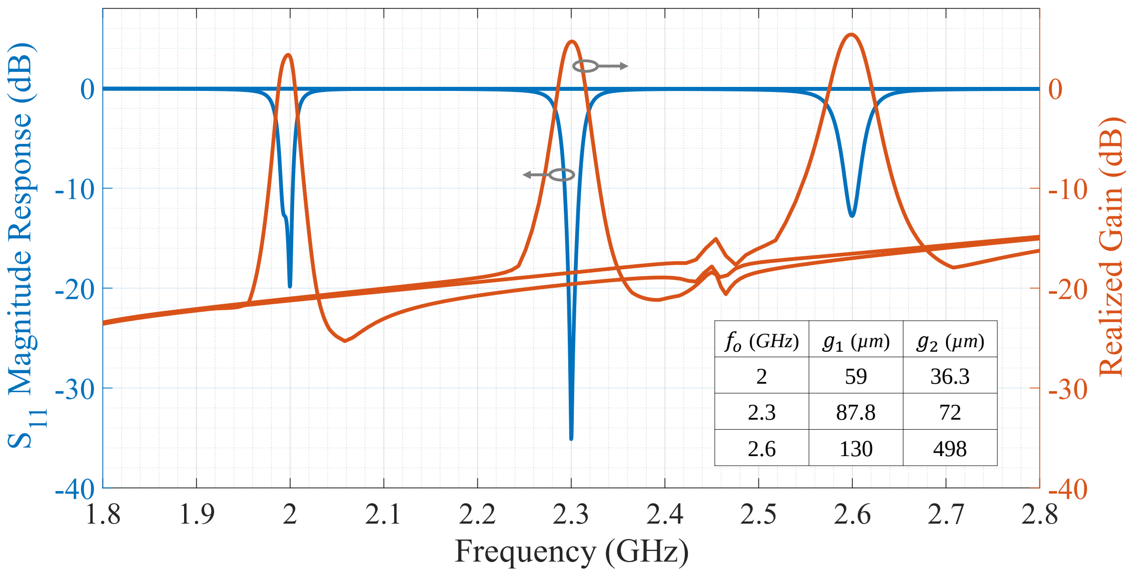

f_o (GHz)	g_1 (μm)	g_2 (μm)
2	59	36.3
2.3	87.8	72
2.6	130	498

Figure 4.19: Simulated S_{11} magnitude response and realized gain of the synthesized filtenna across the frequency tuning range from 2 GHz to 2.6 GHz. The corresponding tuning gap sizes for the cavity (g_1) and the antenna (g_2) are listed in the inset table.

of-band radiation suppression across frequency, as seen in Fig. 4.20. This enhanced radiation filtering characteristic can limit cross-coupling between closely spaced components, for instance, in an array configuration.

The final dimensions of the filtenna are labeled in Fig. 4.12. Note that the ring radius r and the post radius a of the EVA-mode resonator, labeled in Fig. 3.4, are designed to be larger than those of the slot-loaded EVA-mode resonator. A larger ring radius increases the minimum gap needed to tune the EVA-mode resonator at the filtenna's lower operating frequency of 2 GHz. The first advantage of increasing the cavity's minimum gap size is an increase in the power-handling capability of the filtenna. Additionally, to achieve very small gap sizes, the fabrication and assembly of the tuning structure need to be extremely precise. The second advantage of having a larger tuning gap size is that the filtenna is more resilient toward manufacturing and assembly tolerances. Due to the possible difficulties of tuning the small gap sizes due to manufacturing constraints, the minimum gap size to tune the filtenna

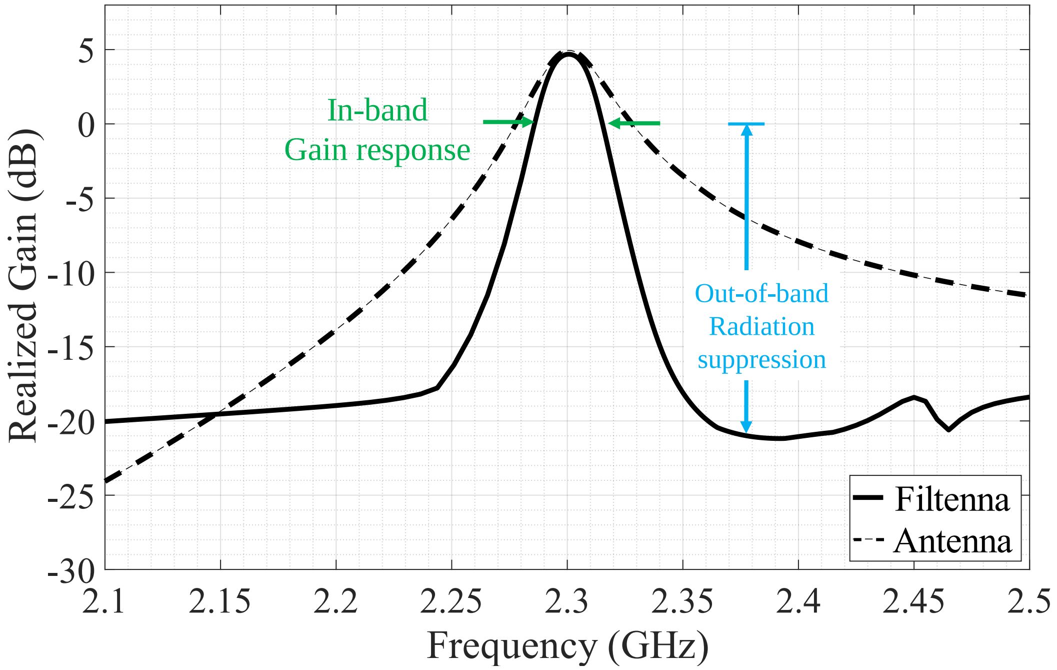

Figure 4.20: Comparison of a single antenna and filtenna gain response across frequency. The ECBSA and EVA-mode filtenna were tuned to a center frequency of 2.3 GHz for comparison.

is increased by slightly reducing the tuning sensitivity of the resonator.

Given that external linear actuators are used to tune the filtenna, a mounting structure for holding the actuators is also required. To analyze the effect of the added mount, the filtenna structure and the entire mount assembly, including the actuator metal box and mounting screws, were added to the simulated model seen in Fig. 4.22. The actuator box is made of aluminum, whereas the screws have a material assignment of PVC plastic with a dielectric constant of 2.7. The mount body is constructed through stereo-lithography (SLA) 3D printing. The specific material used for the mount is Grey Pro Resin from Formlabs. The material's dielectric constant is not published due to the resin mixture being a proprietary technology of Formlabs. However, based on the reported characterization of additive manufacturing materials, the Grey resin's dielectric constant is approximately 2.8 for operation at S-Band [37][68]. The simulated radiation patterns, seen in Fig. 4.23, show

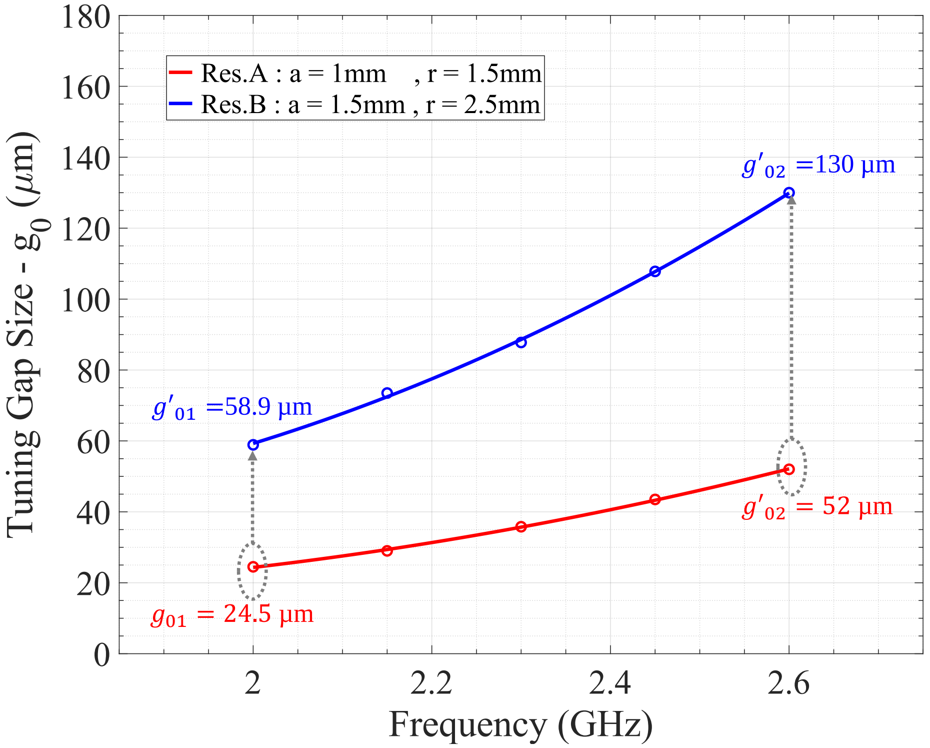

Figure 4.21: Effect of the resonator post and ring radius on the tuning sensitivity as a function of the frequency tuning sensitivity. The variable a is for the post radius, and r is for the ring radius, as labeled in Fig. 3.4.

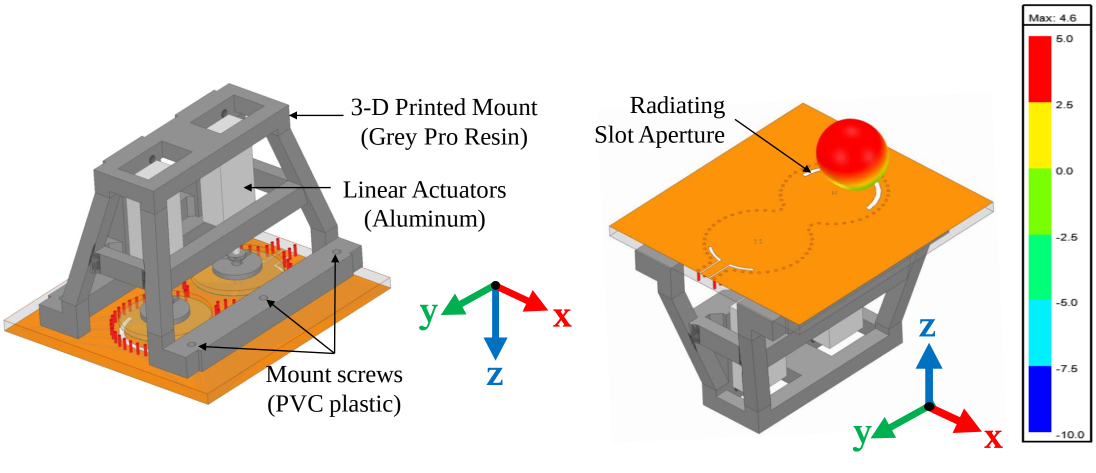

Figure 4.22: Simulated filtenna model with complete mount assembly structure. The material assignment for each assembly component is labeled in the figure. The added amount has no significant impact on the radiation of the filtenna. As seen in the 3D radiation plot of the filtenna tuned to 2.3 GHz, the main beam is directed away from the cavity backing.

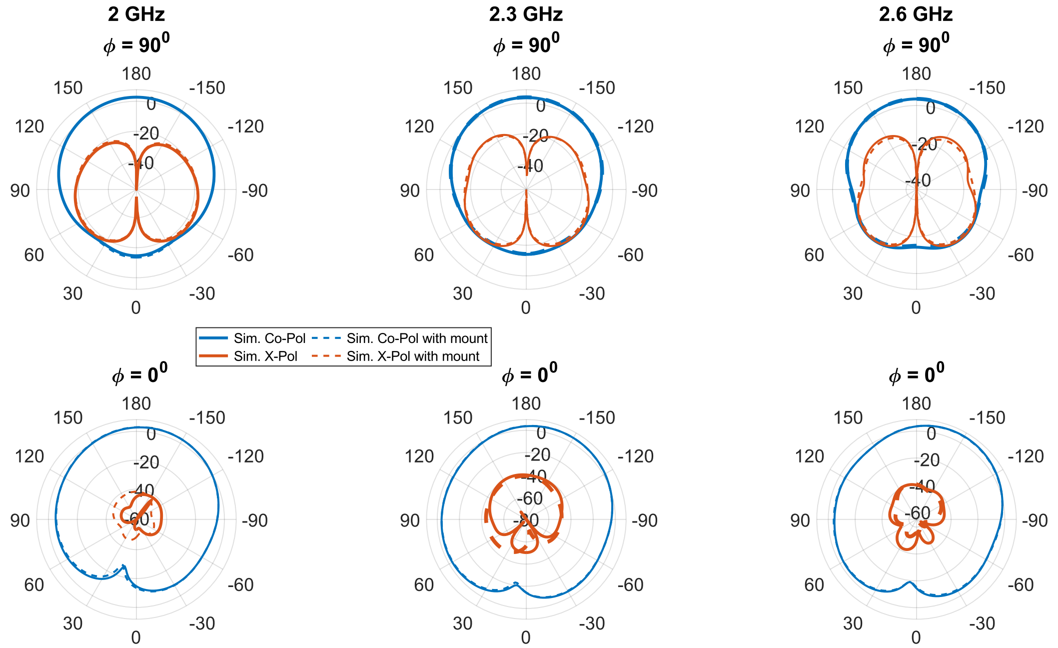

Figure 4.23: Simulated Radiation patterns of the filtenna with and without actuator mount structure at different operating frequencies - 2 GHz, 2.3 GHz and 2.6 GHz.

that the tuning assembly has no significant impact on the co-polarized or cross-polarized radiation patterns.

4.2.3 Experimental Results

A prototype of the contactless-tuned evanescent-mode filtenna was manufactured to validate the design concept. The final fabricated filtenna with the entire tuner assembly is shown in Fig. 4.24. The two circular tuner plates are routed out of Rogers 4350B copper-clad substrate and attached to the actuator push-tip's end using a flat-head screw. Extreme care must be taken to minimize the deburring effects and surface roughness on the PCB plates. The top copper should be polished as much as possible, especially above the post-patch and ring gaps, forming the sensitive capacitive tuning gap. A quick-setting epoxy adhesive was used to bond the circular plates onto the end of the actuator. The surface ring, GCPW feed lines, and the annular slot aperture were patterned using the LPKF Proto-Laser U4 machine.

The fabricated filtenna was measured with an Agilent Technologies N5225A PNA Network Analyzer. The two linear actuator motors were controlled using the New Scale Pathway software, allowing for step size and speed control. In addition, the closed-loop monitoring was deployed throughout the measurement duration to ensure minimum errors in the tuning gap sizes. The measurement setup to the filtenna's S_{11} response is shown in Fig. 4.25.

Filtenna Tuning Range

The measured S_{11} response shows continuous frequency tuning from 2 GHz to 2.6 GHz, as seen in Fig. 4.26. A comparison of the simulated and measured S_{11} curves of the contactless-tuned filtenna are plotted in Fig. 4.27. The S_{11} curve of the manufactured filtenna prototype shows a very close agreement with the simulated S_{11} across the entire tuning range.

The measured tuning gap sizes for the resonator, g_1, and the antenna, g_2, to tune the filtenna from 2 GHz to 2.6 GHz are plotted in Fig. 4.28. The actuator motor displacement determines the vertical distance between the post-patch and tuner top, as displayed on the New Scale Pathway software interface. The starting gap size is measured by completely shorting the tuner plates to the post-top and using that as a reference level for the gap size measurements. The data is extracted from the New Scale Pathway software with the closed-loop monitoring mechanism actively deployed to ensure minimal displacement errors of the actuator in the duration of measurements.

The initial gap size for tuning the resonator to 2 GHz is 53.5 μm, with the total actuation range, Δg_1, is 70.5 μm. The antenna's initial tuning gap is 33.5 μm, and the minimum total actuation range, Δg_2, is 483.5 μm. It should be noted that the resonator can be tuned to a higher frequency than 2.6 GHz. However, the antenna's maximum operating frequency saturates at 2.6 GHz.

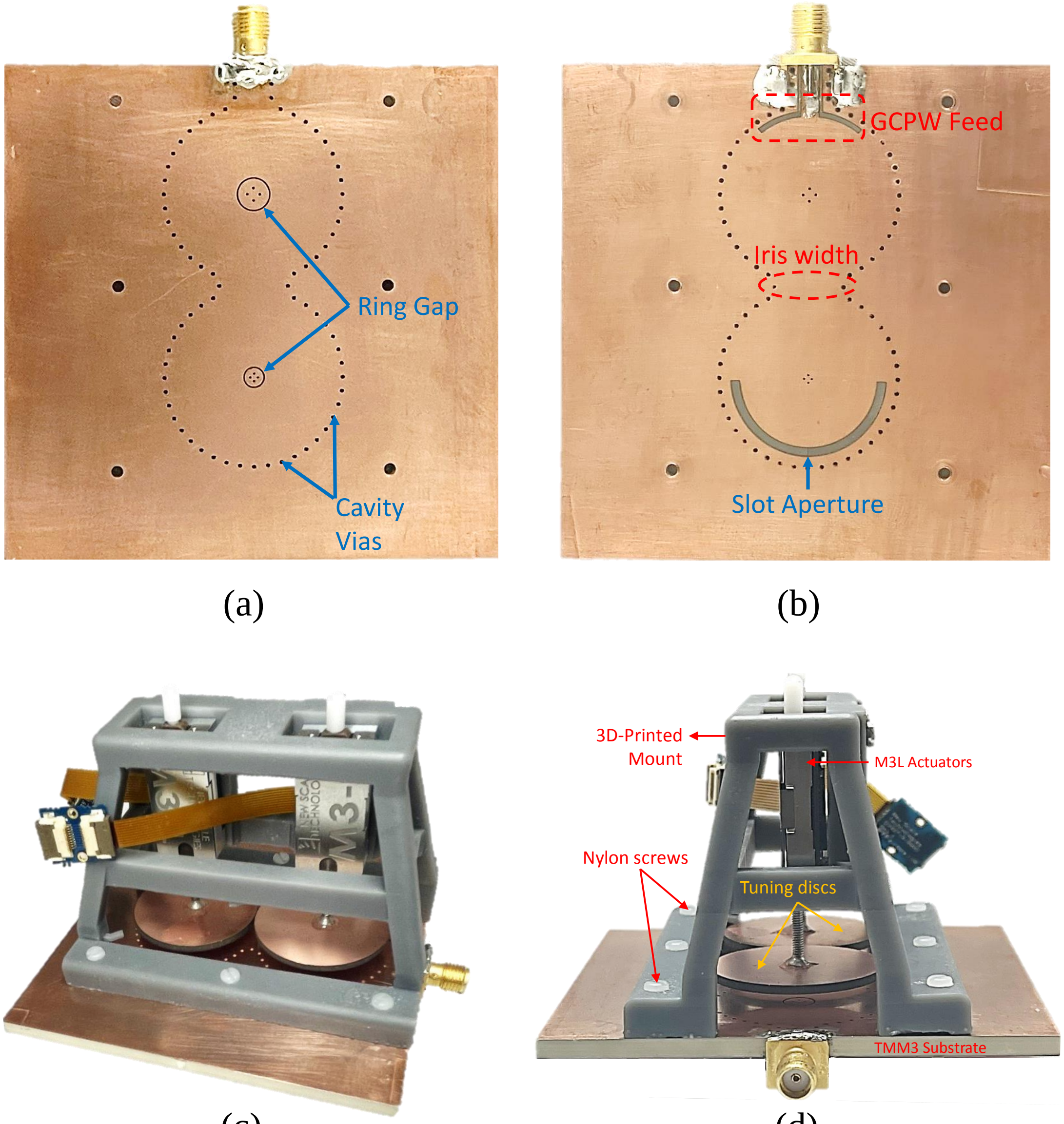

(a) (b)

(c) (d)

Figure 4.24: Manufactured Prototype of the contactless-tuned filtenna (a) Bottom View (b) Top View (c) Full Assembly with linear actuators (d) Side-view

Radiation Pattern and Gain Measurements

The radiation pattern and gain measurements of the manufactured filtenna were conducted in the anechoic chamber. The measurement set-up is shown in Fig. 4.29. The simulated and measured peak realized gain across frequency are compared in Fig. 4.30. The measured

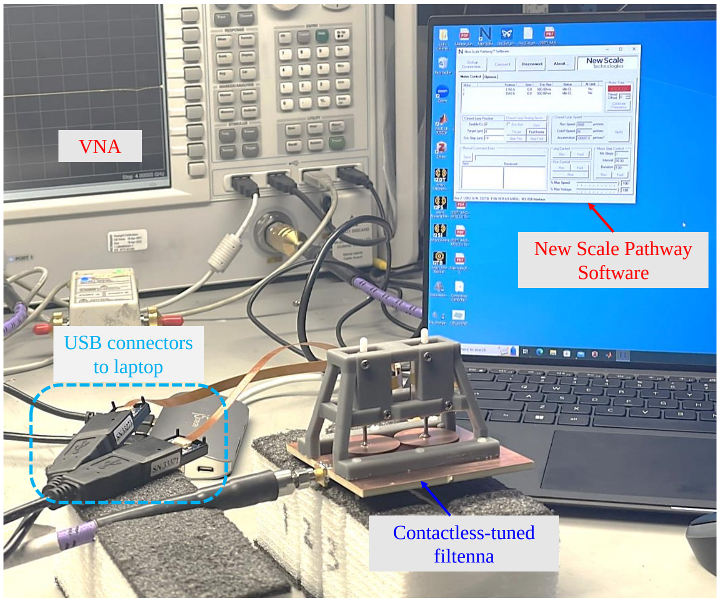

Figure 4.25: Measurement setup for the contactless-tuned filtenna's S_{11} response using a Vector Network Analyzer and a laptop to control the M3-L linear actuators.

broadside realized gain of the antenna is 4.2 dB at the center frequency of 2.3 GHz. Across the tuning range from 2 GHz to 2.6 GHz, the filtenna's maximum realized gain increases from 2.7 dB to 5.173 dB, respectively. The scattered peaks in the out-of-band gain response are primarily due to the non-idealities of chamber measurements, including multi-path fading effects and chamber noise. Overall, there is a close agreement in the measured and simulated peak realized gain curves seen in Fig. 4.30. Note that the filtenna shows high out-of-band rejection due to the integrated filtering functionality.

The radiation pattern measurements of the filtenna at 2 GHz, 2.3 GHz, and 2.6 GHz are plotted in Fig. 4.31, Fig. 4.32, and Fig. 4.33, respectively. The patterns show a maximum gain in the broadside direction due to the evanescent-mode cavity-backing of the antenna. The higher levels of cross-polarization are due to the non-idealities of the chamber measurement set-up, which include feeding coaxial cables connected to the antenna. It should be noted that the closed-loop monitoring system for the actuators was deployed throughout the gain measurements and radiation scanning process. The active monitoring mechanism minimizes the risk of de-tuning the filtenna due to any gap size discrepancies. Long USB cables connected the actuators inside the chamber to a laptop with the New scale Pathway software outside the chamber. Therefore, any deviations in the gap size measurements could be monitored and corrected in real time.

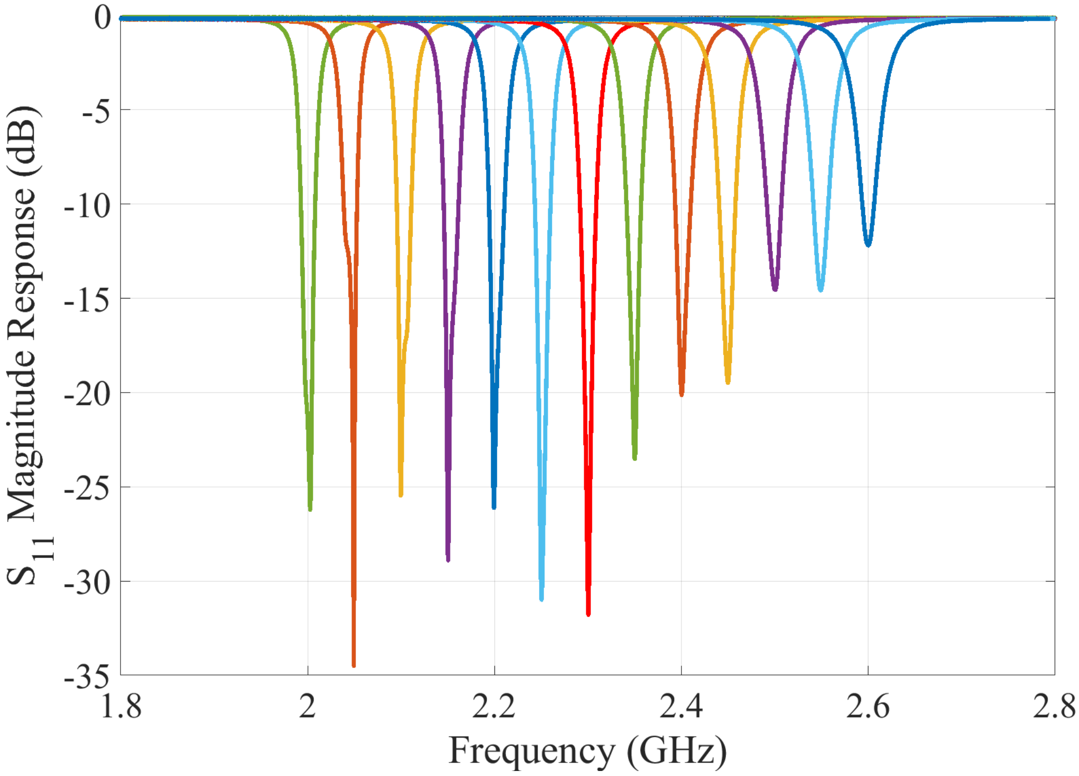

Figure 4.26: Measured $|S_{11}|$ of the manufactured filtenna with continuous frequency tuning from 2 GHz to 2.6 GHz

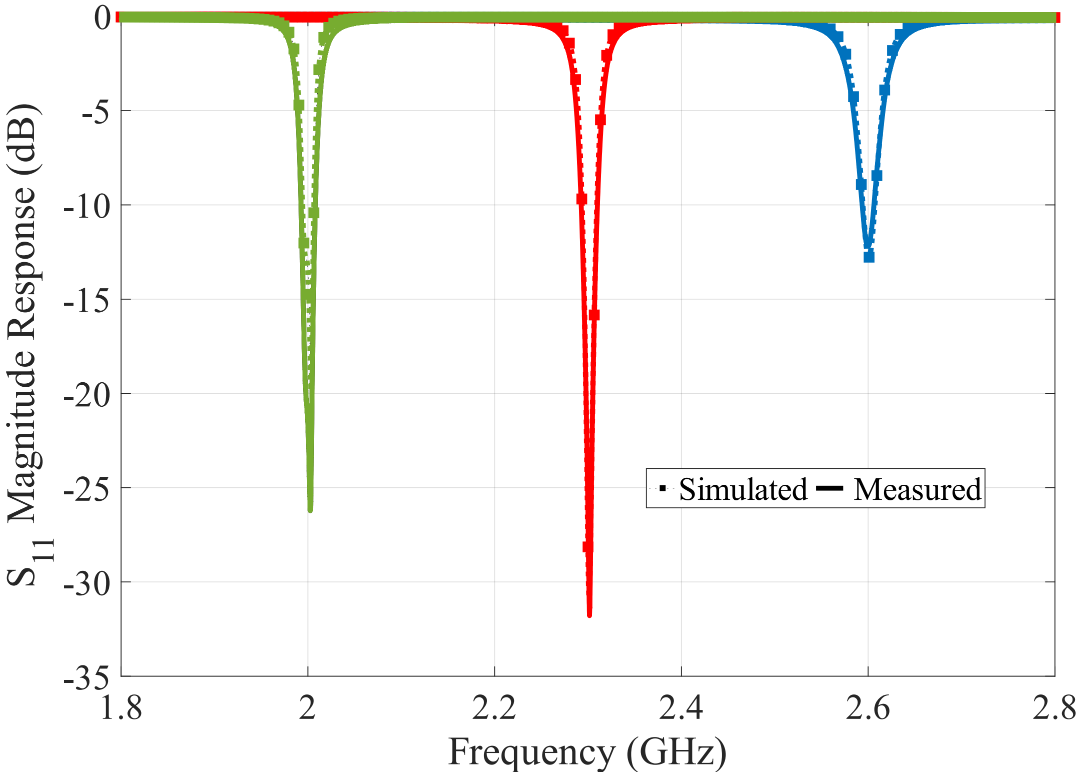

Figure 4.27: Comparison of the simulated and measured S_{11} response at minimum (2 GHz), maximum (2.6 GHz), and the center frequency (2.3 GHz).

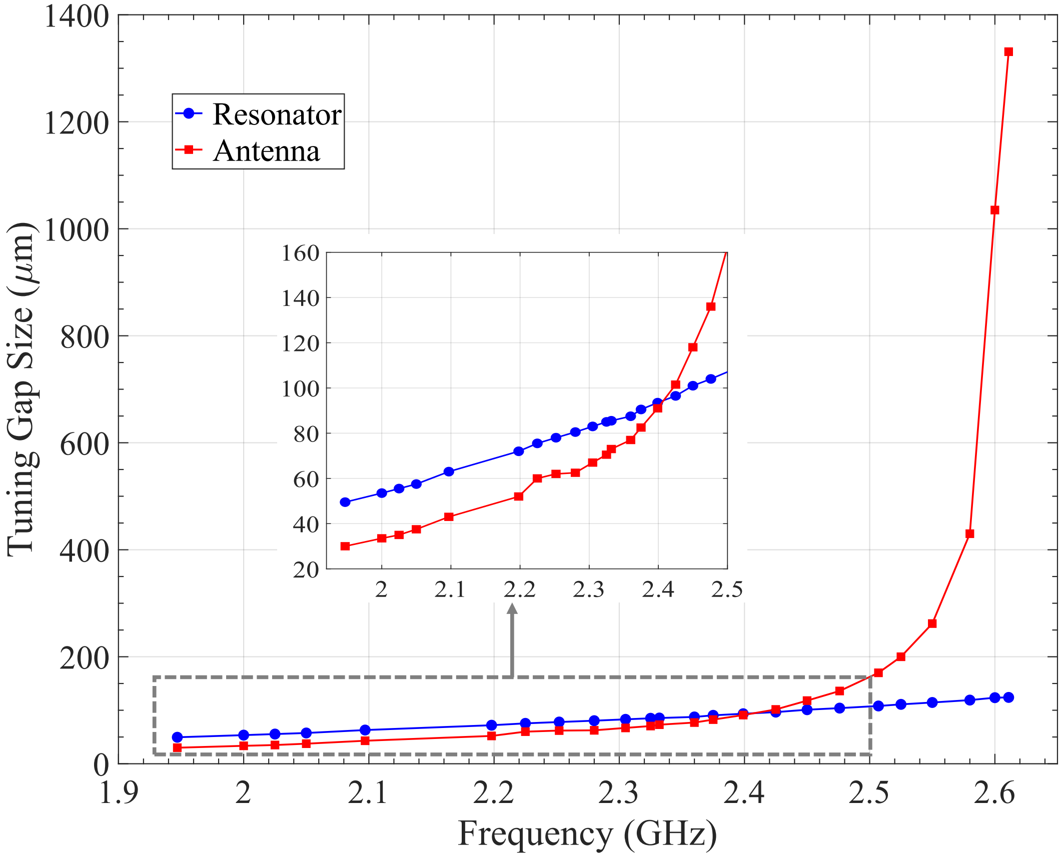

Figure 4.28: Measured tuning gap sizes for the resonator and antenna across the filtenna's tuning range from 2 GHz to 2.6 GHz. The extracted gap sizes have a mean error of ±0.5 μm, as reported by the M3-L Linear actuator data sheet [62].

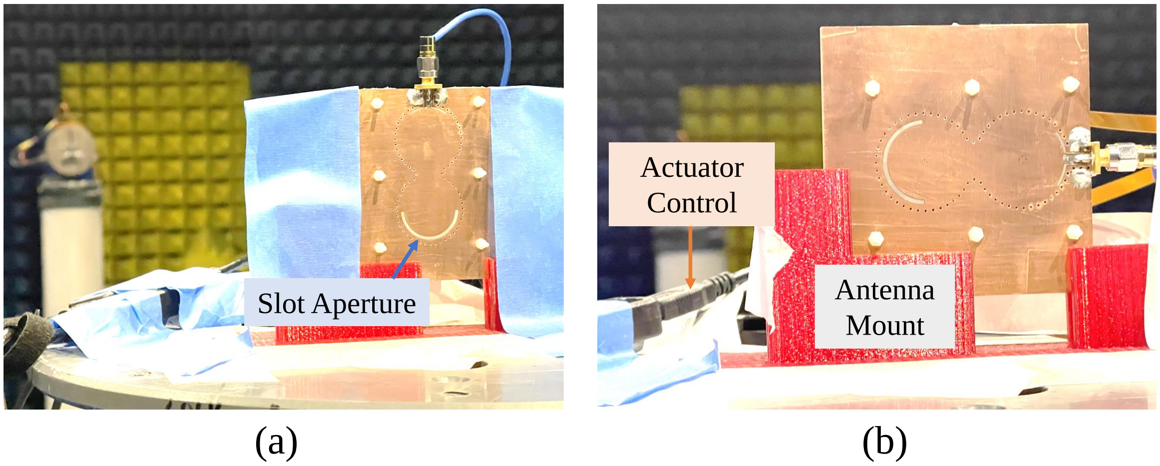

(a) (b)

Figure 4.29: Anechoic Chamber Measurement Set-up for the S-band filtenna (a) Horizontally polarized (b) Vertically Polarized configuration.

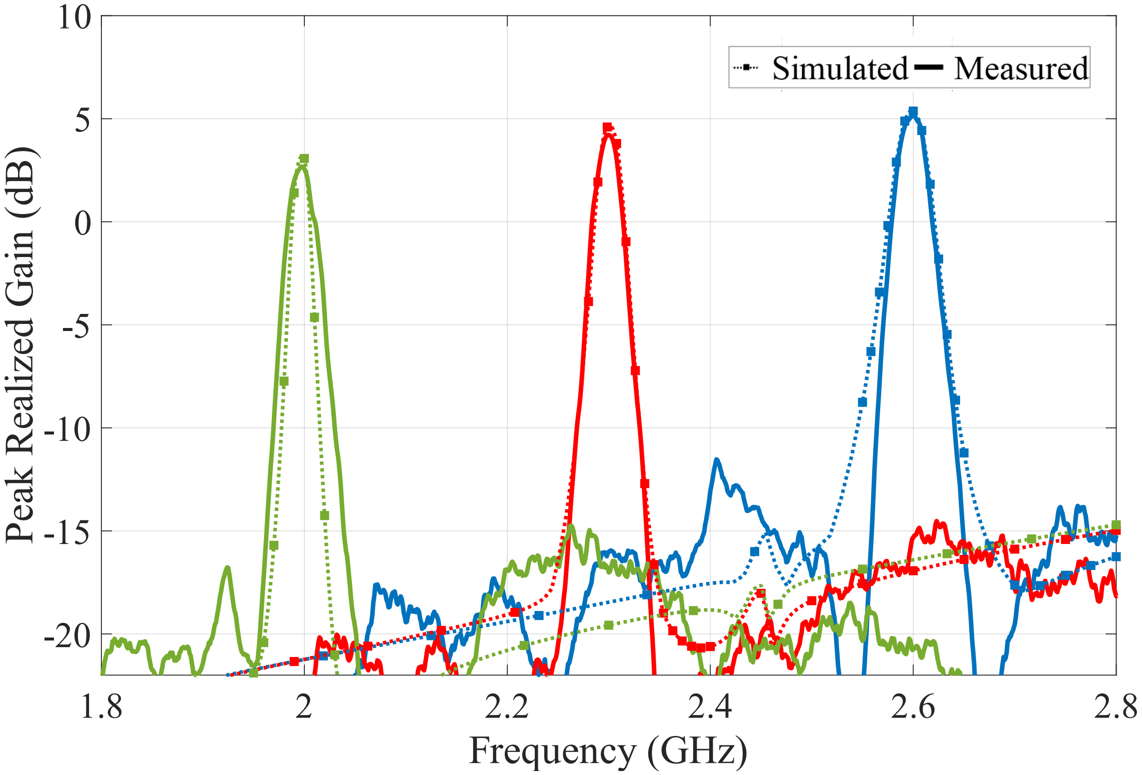

Figure 4.30: Comparison of the simulated and measured peak realized gain across frequency, at broadside. The filtenna is tuned to 2 GHz, 2.3 GHz, and 2.6 GHz, and the measured gain ranges from 2.7 dB to 5.173 dB. The in-band gain response and out-of-band radiation suppression of the manufacture filtenna follow the simulated curve closely.

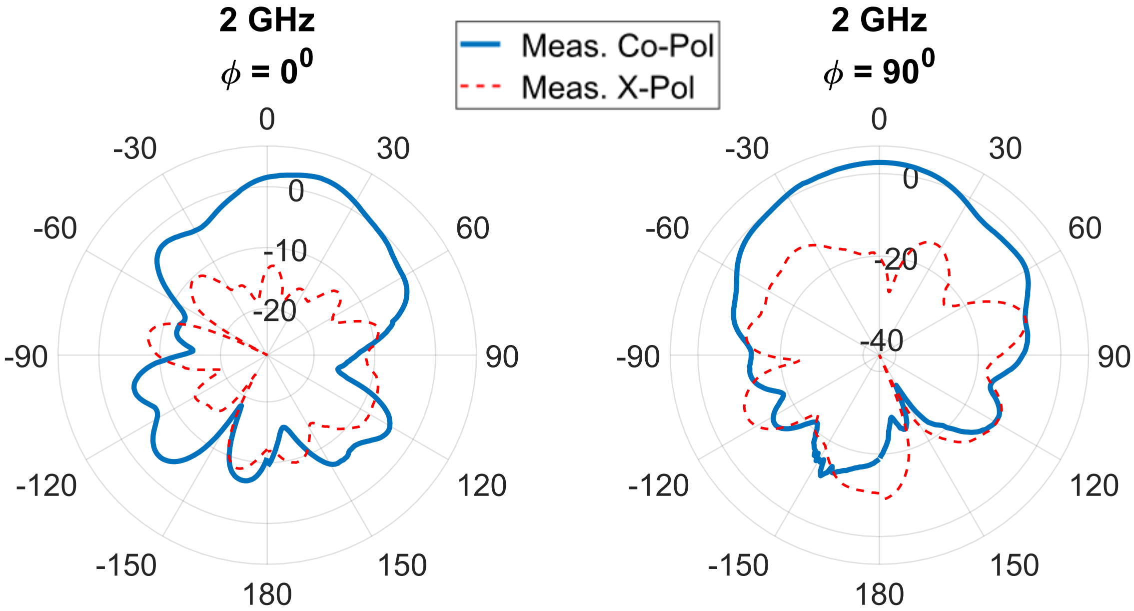

Figure 4.31: Measured filtenna radiation pattern at the lowest operating frequency of 2 GHz.

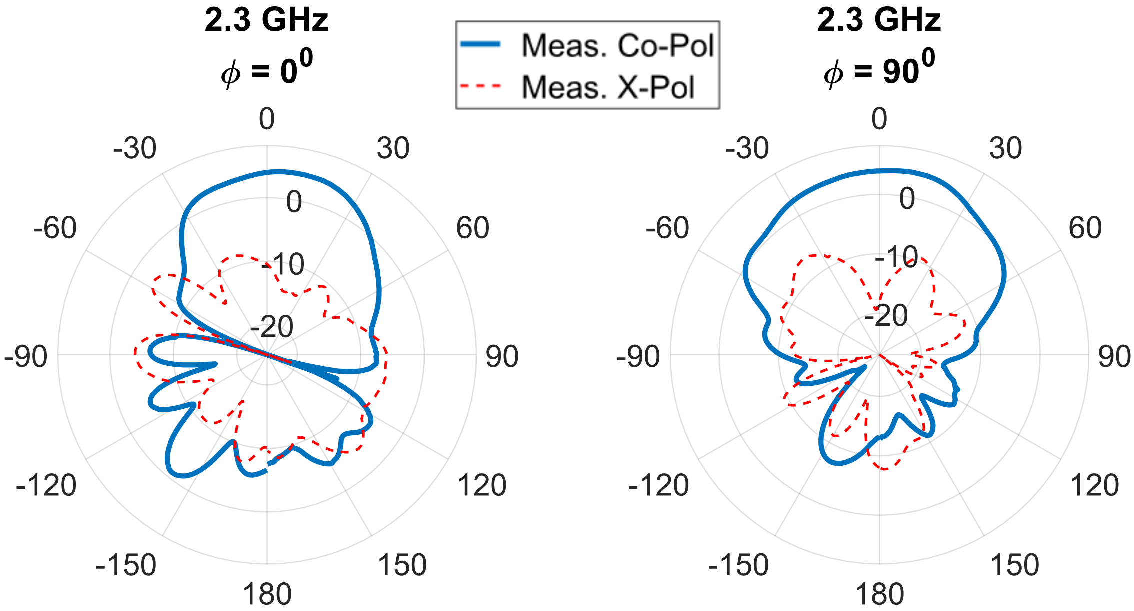

Figure 4.32: Measured filtenna radiation pattern at the center operating frequency of 2.3 GHz.

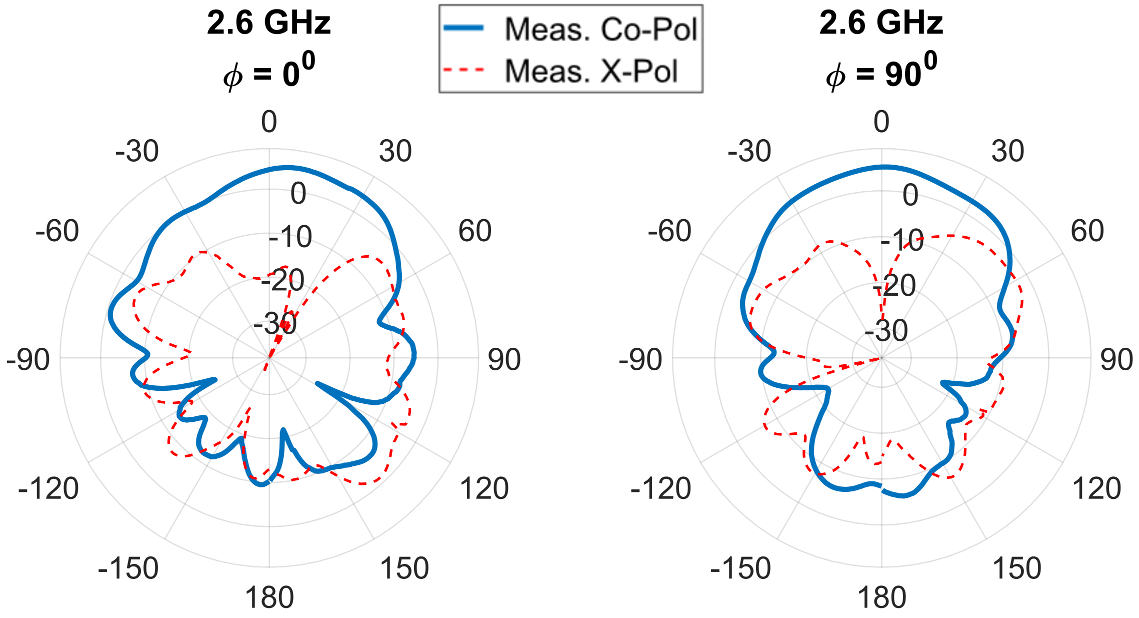

Figure 4.33: Measured filtenna radiation pattern at the highest operating frequency of 2.6 GHz.

4.2.4 Power Handling Prediction

The filtenna's power handling capability is predicted from simulations by extracting the electric fields above the post-patch of the resonator and ECBSA, as seen in Fig. 4.34. The method explained in Section 4.1.4 is applied to scale the electric field to break down and extract the peak PHC. The breakdown power of the filtenna is predicted to range from 13 W at 2 GHz, 32 W AT 2.3 GHz, and 58 W at 2.6 GHz. The EVA-mode cavity resonator mainly limits the overall power handling due to the smaller range of gap sizes needed for tuning compared to the antenna. The electric field is desensitized in the antenna's capacitive tuning gap due to the cavity field perturbation and additional loading from the radiating slot aperture. In the case of the unloaded EVA-mode resonator, the field strength is more heavily concentrated in the post-patch. Due to the existence of higher field strength in a smaller capacitive gap, the resonator has a lower power-handling capacity. The filtenna's PHC can be improved by redesigning the resonator and the cavity-backed antenna to exhibit a much smaller tuning range but a higher power-handling capacity.

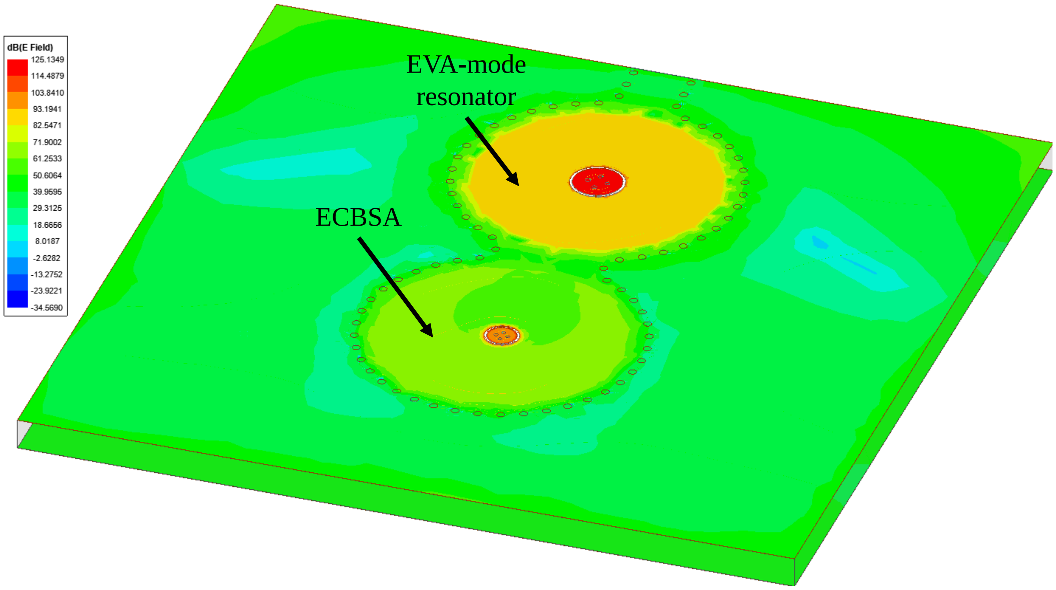

Figure 4.34: E-field distribution in the filtenna structure shows a higher concentration above the EVA-mode resonator's post-patch, as compared to that of the ECBSA.

4.2.5 Performance Evaluation

Most frequency-tunable filtennas in the existing literature are based on microstrip-based topologies. Semiconductor switches like PIN diodes and varactor diodes are the commonly used tuning elements for the microstrip-based filtenna implementations [18]-[29]. The main limitation of microstrip-based resonant structures is their low unloaded quality factors, which directly impact the insertion loss of the filter response. In a filtenna topology, the insertion loss in the filtering section is absorbed into the antenna's radiation efficiency. As a result, the low-quality factor of microstrip-based resonators lowers the filtenna's radiation efficiency and realized gain. Furthermore, incorporating low-Q semiconductor tuning elements into the passive filtenna structure introduces resistive losses that harm the filtenna's radiation performance.

Metallic waveguide and cavity-based filtenna structures exhibit significantly lower losses than microstrip implementations due to the higher unloaded-Q of the constituent resonant structures [35],[36],[69]-[71]. However, metal-based structures are inevitably bulky, expensive, complex to manufacture, and occupy a large volume. Alternatively, cavity-based filtennas implemented using SIW technology offer a relatively high-Q performance compared to microstrip filtering elements, exhibit easier integration, and can be manufactured using simple PCB manufacturing techniques. Owing to these benefits, several non-tunable SIW cavity filtennas have been presented in the literature [72]-[74]. However, the research on tunable SIW-based cavity filtennas is limited. In [75], varactor diodes were integrated into SIW-based cavity filtennas to reconfigure the center frequency of the filtenna structure. Due to the losses of the varactor, the filtenna exhibited lower gain and efficiency across its tuning range. The design concept is presented in detail but not experimentally validated. In [37] and [44], an evanescent-mode cavity filtenna is presented using SIW technology. Experimental results for the S_{11} response are included in [44]; however, the gain and radiation pattern measurements have not been presented due to the instability of the piezo-disk tuning element. Integrating a slot antenna within evanescent-mode cavities was also explored in [76] using a metal-based implementation, with tuning screws as the reconfiguration technique. However, experimental results were not presented.

To the best of the author's knowledge, the contactless-tuned filtenna presented in Section 4.2 is the only SIW-integrated tunable filtenna with complete experimental validation of the tuning and radiation performance. The tunable filtenna presented in this work is compared with other state-of-the-art tunable cavity-based filtennas in Table 4.3. Although the metal filtennas exhibit higher gains across the tuning range, they occupy a very large volume. On the other hand, it is evident that the SIW implementation and evanescent-mode cavity integration of the proposed filtenna significantly reduce the electrical footprint of the structure. Furthermore, the contactless-tuning scheme using long-range linear actuators enables a moderately high-frequency tuning range while improving the tuning speed compared to the metal-based filtennas tuned with metal screws.

Table 4.3: Comparison with State-of-the-art Tunable Cavity-based 3D Filtennas

Ref.	**Structure**	**Tuning Element**	f_c **(GHz)**	**TR**	**Speed**	**Gain (dB)**	**Size (in** λ_g***)**
[35]	Metal	Tuning screws	3.03	31%	slow	8-10	$1.3\times1\times2.1$
[36]	Metal	Tuning screws	10	15%	slow	≥ 6.5	$1.3\times0.7\times1$
This Work	SIW	Linear actuators	2.3	26%	fast	2.7-5.2	$0.5\times0.6\times0.4$ †

TR: Tuning Range f_c : center-frequency of TR * Guide wavelength, λ_g ,is calculated at f_c

† Calculated electrical size also includes the height of the mount-structure used for the linear actuators.

4.3 Conclusion

The concept of contactless capacitive tuning is applied in the design of cavity-backed slot antennas for the first time in this work. A novel tunable SIW-based Evanescent-mode Cavity-Backed Slot Antenna (ECBSA) was designed and experimentally tested. The antenna demonstrates the largest tuning range among the existing EVA-mode cavity-based reconfigurable antennas while also providing high power-handling capability and better tuning reliability than conventionally used piezoelectric disk actuators. Furthermore, changing the critical gap between the post and tuner allows the antenna's operating frequency to be tuned from 1.71 GHz to 2.58 GHz (40%).

The contactless-tuned ECBSA was combined with a tunable EVA-mode cavity resonator into a filtenna topology. The contactless-tuned filtenna demonstrated tuning from 2 GHz to 2.6 GHz while maintaining a measured realized gain greater than 2.7 dB across the tuning range. Due to the integrated filtering functionality, the filtenna unit demonstrates superior out-of-band radiation suppression compared to the conventional antenna. The reconfigurable antenna and filtenna demonstrate state-of-the-art performance and can be used in the next-generation multi-functional RF Front-ends.

The tunable antenna and filtenna proposed in this chapter were designed for S-band applications in the range of 2-4 GHz. In the next chapter, Chapter 5, the frequency scalability of the filtenna is thoroughly investigated for X-band applications (8-12 GHz). It will be shown that simply scaling the electrical size of the device for high-frequency applications does not work. A novel tuning scheme and passive structure of the antenna are proposed. The antenna is next integrated into a tunable filtenna topology for X-band applications.

Chapter 5

Varactor-tuned Antenna and Filtenna for X-band Applications

In this chapter, the frequency scalability of a frequency-agile filtenna element for X-band applications is investigated. The design of the filtenna's first resonator was demonstrated in Chapter 3, where an evanescent-mode cavity with a contactless tuning scheme was scaled for implementation at the X-band frequency range. The primary focus of this chapter is the design and implementation of the filtenna's second resonator, which is the antenna element, and the final implementation of a tunable X-band filtenna.

5.1 Frequency Scalability of Contactless-tuned Slot Antenna

In Chapter 3, the contactless-tuning scheme was successfully applied to design an X-band tunable EVA-mode cavity resonator. The same tuning scheme using external linear actuators is re-evaluated here to realize an X-band frequency-agile antenna using the contactless capacitive tuning scheme. Consider the contactless-tuned EVA-mode Cavity-backed Slot Antenna (ECBSA) presented in Chapter 4 for S-band operation. Scaling the S-Band ECBSA for X-band applications presents several issues, particularly due to the deployed tuning method consisting of external linear actuators. The dimensions of the actuator metal box are labeled in Fig. 5.1, in terms of its electrical length at 10 GHz, which is at the center of the X-band frequency operation range. The first issue to be noted is that the longest dimension of

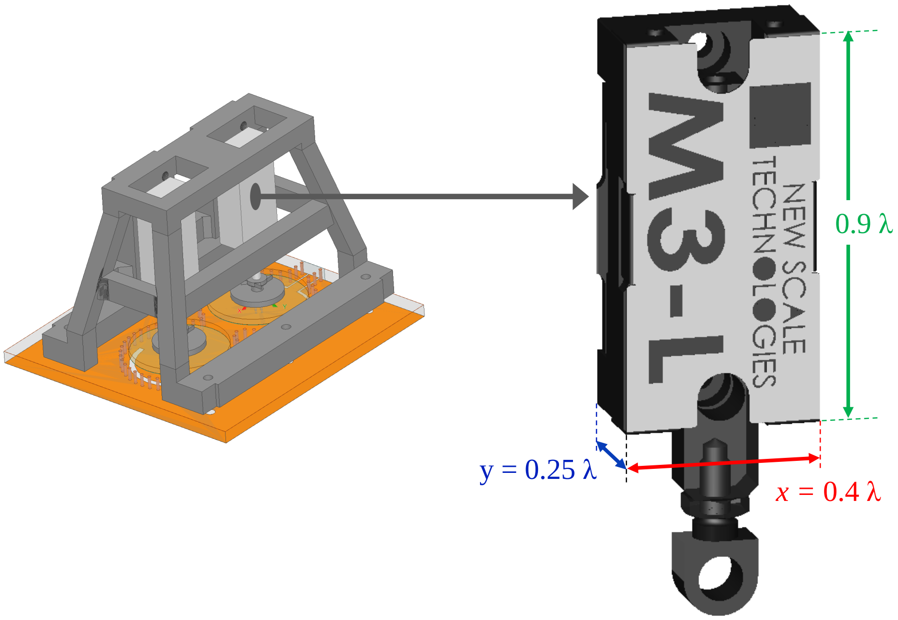

Figure 5.1: Dimensions of the M3-L Linear Actuator from New Scale Technologies [62]. The encasing of the actuator is made of aluminum metal. At a center frequency of 10 GHz, the electrical length of the housing is $0.9\lambda \times 0.4\lambda \times 0.25\lambda$.

the actuator is about a wavelength long, which may interfere with the radiation performance of the antenna at the X-band frequency range. Furthermore, the box's width and length are almost a quarter and half-wavelength, respectively, and accommodating two or more of these in a filtenna configuration is not practically feasible. At present, the M3-L linear actuators are the most miniaturized high-resolution positioning system available commercially. Due to the limitations in the available state-of-art linear actuators, the contactless-tuning method cannot be directly scaled for applications at X-band frequencies.

An alternate method for tuning the slot-loaded EVA-mode cavity is by accommodating surface-mount varactors on top of the ring-loaded cavity, as illustrated in Fig. 5.2. The variable junction capacitor of a varactor diode can be used to vary the ring-gap capacitance, C_{ring}. This concept of tuning has been applied before to tune post-loaded resonators and octave-tunable filters [60]. However, due to the low tuning sensitivity in the ring gap, several varactors have to be placed along the ring circumference to achieve high tunability.

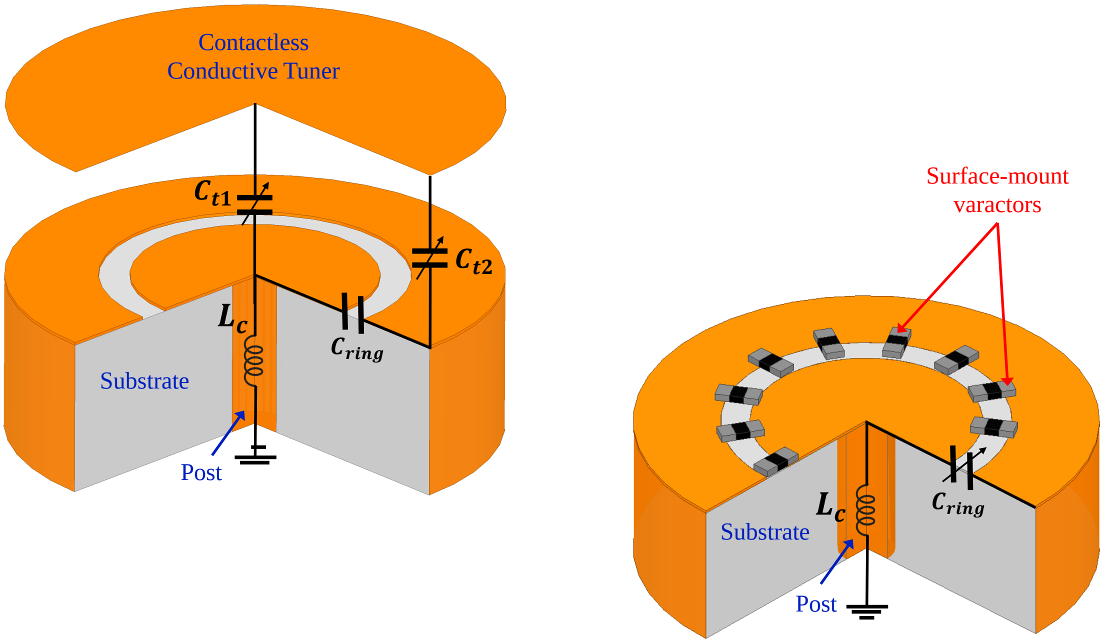

Figure 5.2: Tuning configuration for coaxial cavity resonators using surface mount varactor diodes, as proposed in [60] to tune bandpass filters. The surface-mount components can be easily integrated into the structure. However, the losses can degrade the overall performance.

This may lead to unwanted interference with the radiating structure. Additionally, varactor diodes typically have low-quality factors and can lead to a degradation in the antenna's radiation performance, as will be discussed in Chapter 6. Due to the tuning limitations of the EVA-mode-based antenna structure, a new concept of the cavity-backed slot antenna and a new tuning scheme had to be investigated.

5.2 Half-Mode SIW-based Tunable Slot Antenna

A method was presented in [37], where the open aperture of a bisected EVA-mode cavity was integrated with a slot antenna. The cavity operates as a Half-Mode Substrate-Integrated Waveguide (HMSIW). The TM_{110} field pattern is mostly undisturbed by removing half of the conventional SIW cavity through its symmetrical plane, as seen in Fig. 5.3. Many resonant antenna structures have been realized by utilizing the open aperture of HMSIW, as

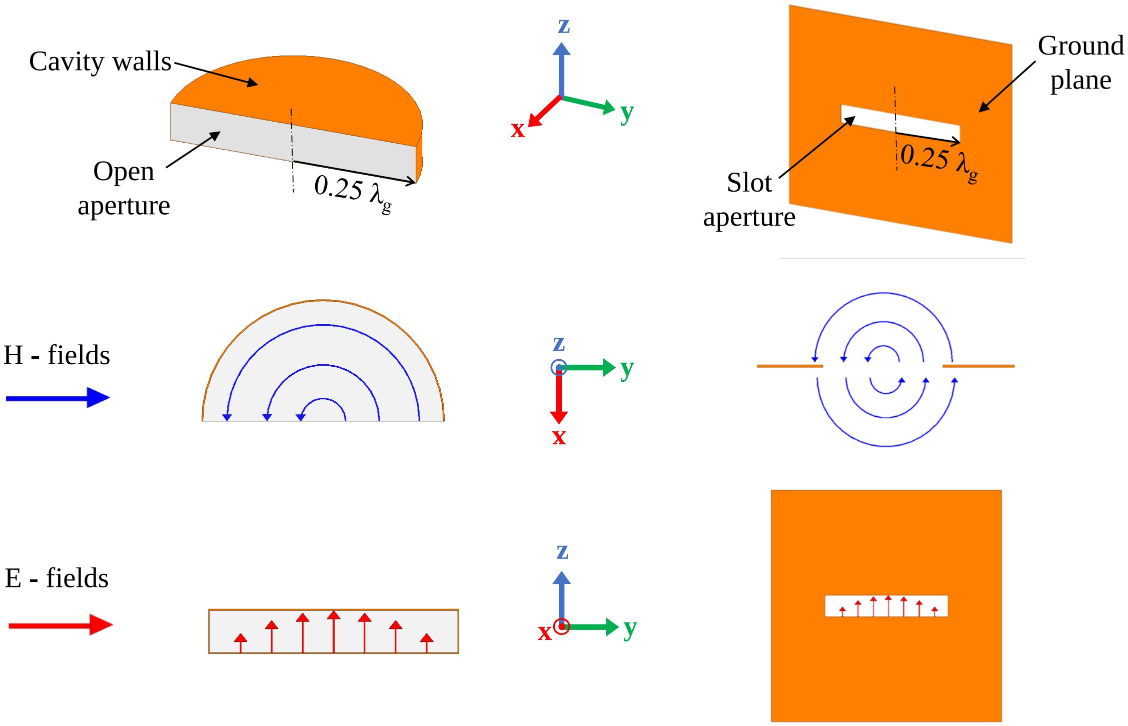

Figure 5.3: Field distributions between a half-mode SIW and a slot antenna, operating in their respective fundamental modes. Note the resemblance between sinusoidal distribution across the slot aperture and HMSIW open aperture.

summarized in [77].

If we look at the electric and magnetic field distributions of a bisected circular cavity and a slot aperture on a ground plane, it is observed that the field distributions show a close resemblance (Fig. 5.3). In order to operate in the fundamental mode, the cavity diameter and slot length need to be $\lambda_g/2$ long, where λ_g is the guided wavelength. Therefore, the HMSIW can function as a cavity-backing for the slot aperture on a finite ground plane.

Based on the HMSIW concept, a bisected evanescent-mode cavity-backing was integrated with the slot antenna in [37] and [44], and the operating frequency was tuned using a movable metal post at the cavity's center. The antenna demonstrated octave tunability across the entire S-band. However, such a mechanical actuation method cannot be directly applied to X-band. There are several complications of placing a moving metal post in

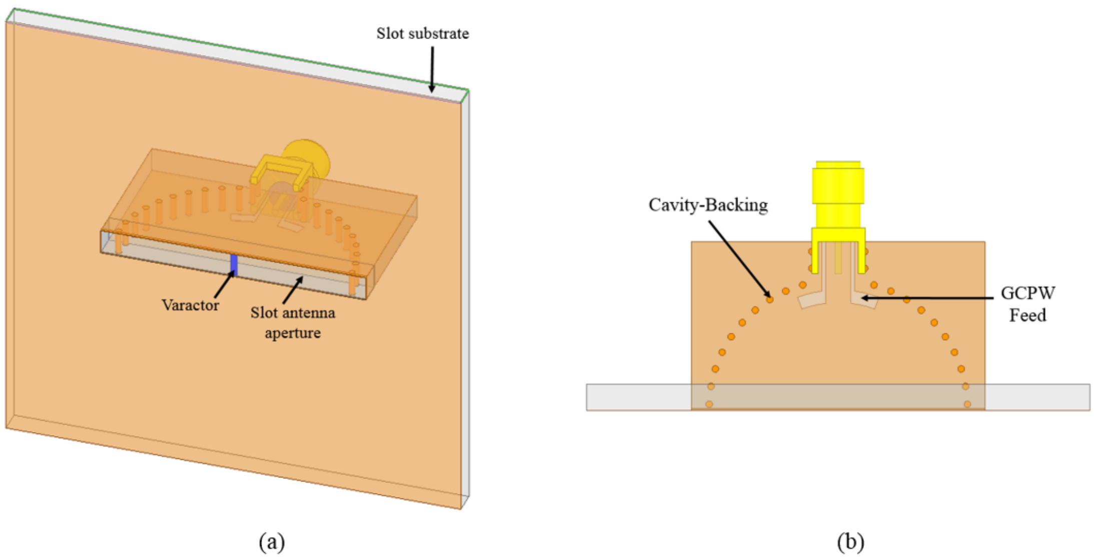

Figure 5.4: (a) 3-D view of the initial design for a varactor-loaded cavity-backed slot antenna (b) Top-view showing the cavity-backing insert implemented using SIW technology.

a module with a smaller form factor. In addition, limitations on the tuning speed, precision, and reliability of the mechanical actuation method make the design impractical for higher-frequency applications. Therefore, electronic reconfiguration using varactors was chosen in this work for accommodating tunability into the antenna structure. Varactors are semiconductor PN-junction devices that function as voltage-controlled variable capacitors. Varactor diodes can be easily integrated into miniaturized modules due to their compact size. Their tuning speed and precision are significantly better than other actuation methods, as analyzed in Table 1.2.

A design concept of the varactor-loaded Cavity-Backed Slot Antenna (CBSA) for X-band is presented in Fig. 5.4. The HMSIW cavity is realized through metal vias using SIW technology, and a GCPW feed is used to couple energy into the antenna structure. The substrate used for the slot substrate and the cavity-backing insert is Rogers 3003 (ϵ_r = 3, $tan\,\delta$ = 0.001), with a thickness of 60 mils. For the first mode, it is observed that the electric field is highest at the center of the aperture, Fig. 5.3. The varactor was mounted at the center

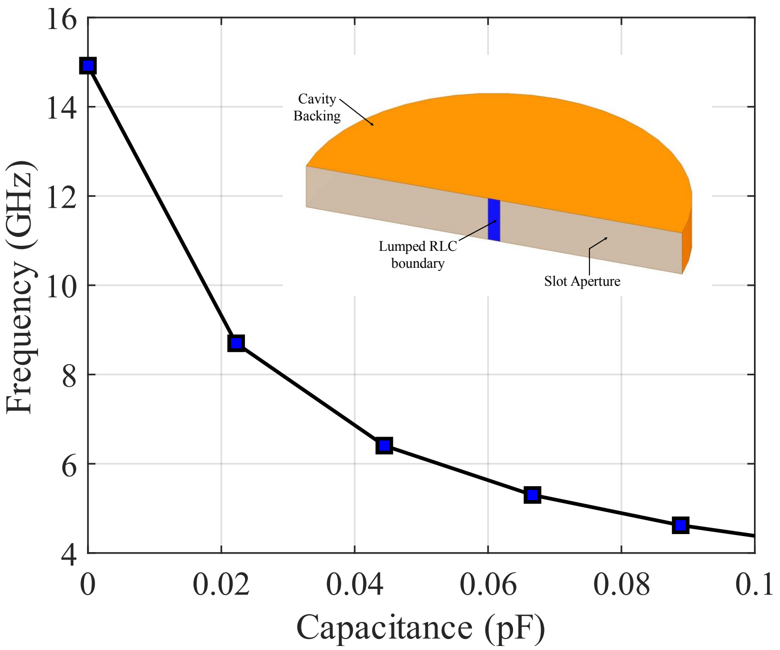

Figure 5.5: Initial Tuning Curve for the varactor-tuned HMSIW-based slot antenna. The inset shows the simplified Eigenmode model for investigating tuning.

to achieve a high capacitive tuning sensitivity, which ensures wider tunability of the antenna across frequencies.

A simplified Eigenmode model was set up to investigate the required capacitance range to tune across the X-band, as seen in the inset of Fig. 5.5. It is observed that the magnetic field in the cavity is nearly perpendicular to the aperture plane, and therefore the slot aperture can be approximated as a perfect magnetic conductor (PMC). To emulate the slot fields in an eigenmode simulation, the slot aperture is assigned a perfect-H boundary condition. The varactor is modeled by a lumped RLC boundary. For initial investigations, only the capacitive loading of the varactor is considered.

Results from eigenmode simulations indicated a capacitance range of 0.01-0.03 pF to tune across the entirety of the X-band. However, no commercially available varactors can provide such small values of capacitance. Typically, 0.15-0.28 pF of minimum capacitive loading is provided by most manufacturers. In order to make the antenna practically

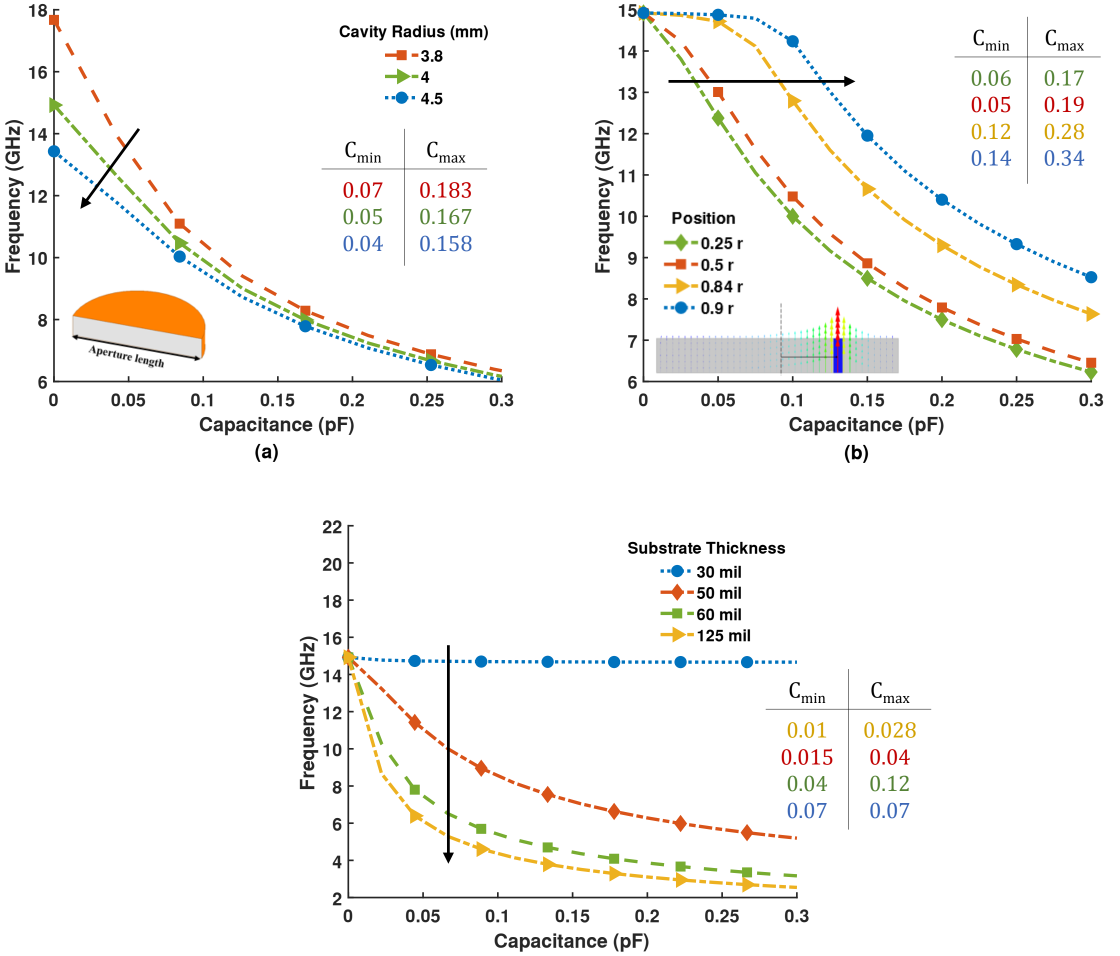

Figure 5.6: Eigenmode parametric analysis of the varactor-loaded slot (a) variation of cavity radius (b) Effect of varactor position (along the slot length) on capacitance tuning range vs frequency. (c) Substrate thickness variation. C_{min} and C_{max} refer to the capacitances required to tune the antenna at the highest (12 GHz) and lowest (8 GHz) operating frequencies, respectively.

realizable, the minimum value of capacitance for tuning at 12 GHz had to be increased.

Several methods were tried to shift the minimum load capacitance value to higher values, as provided by commercially available varactors. Firstly, a highly loaded slot antenna was designed by decreasing the slot length. The reduced electrical size at the operating frequency increases the capacitive loading required to tune the antenna to 12 GHz. As seen in Fig. 5.6(a), after shifting the unloaded operating frequency of the first mode up to as high as 17.8 GHz, the minimum capacitance required to tune at 12 GHz is 0.07 pF, which is still not practically feasible. The substrate thickness was also parameterized, with the tuning sensitivity decreasing with decreasing thickness. However, the minimum tuning capacitance was less than 0.07 pF in all cases.

Another solution was investigated to reduce the minimum load capacitance. At the slot aperture's mid-point, where the varactor is placed, the electric field strength is highest (Fig. 5.3), which causes that region to be sensitive to small capacitance changes. By positioning the varactor away from the center, the E-field strength is reduced, which desensitizes the capacitive tuning. As a result, the minimum capacitance for operating the antenna at 12 GHz can be increased, as seen in Fig. 5.6(b). When the varactor is moved from the center towards the slot edge, the minimum capacitance increases at the cost of tuning sensitivity. However, the resulting shift in the minimum capacitive loading is still below the practical bounds of 0.15-0.3 pF.

A direct and simple solution to the issue of small tuning capacitance is to place multiple varactors in series. However, a series varactor configuration will cause a degradation of the antenna's radiation performance due to the added losses introduced by multiple varactors. The equivalent circuit of a packaged varactor die is the series combination of a resistor, variable tuning capacitance provided by the PN junction, and additional parasitic reactance due to the packaging effects. When multiple varactors are placed in series, the resistances will add, therefore leading to more losses and reduced radiation efficiency of the antenna. These effects are due op the practical limitations of tuning varactors, which will be further explained in Chapter 6. Therefore, a method of realizing this series capacitance without adding significant losses and maintaining the tuning performance needed to be investigated.

5.3 Superstrate-loaded Tunable Cavity-backed Slot Antenna

The physical realization of equivalent series capacitances with the varactor was implemented by loading the cavity-backed slot antenna with a superstrate, as shown in Fig. 5.7. The superstrate is placed above the ground plane of the slot's ground plane. Copper mounting pads are placed above the superstrate, which forms additional series capacitances, C_{ss}, with the varactor's tuning capacitance, C_{tune}, as seen in Fig. 5.8. The additional capacitance introduced by the superstrate layer is a function of the area of copper pads, A, superstrate's thickness t_1, and dielectric constant, ϵ_{r1}. An adhesive bonding film of dielectric constant ϵ_{r2} and thickness t_2 is used to bond the superstrate with the copper cladding of the slot substrate.

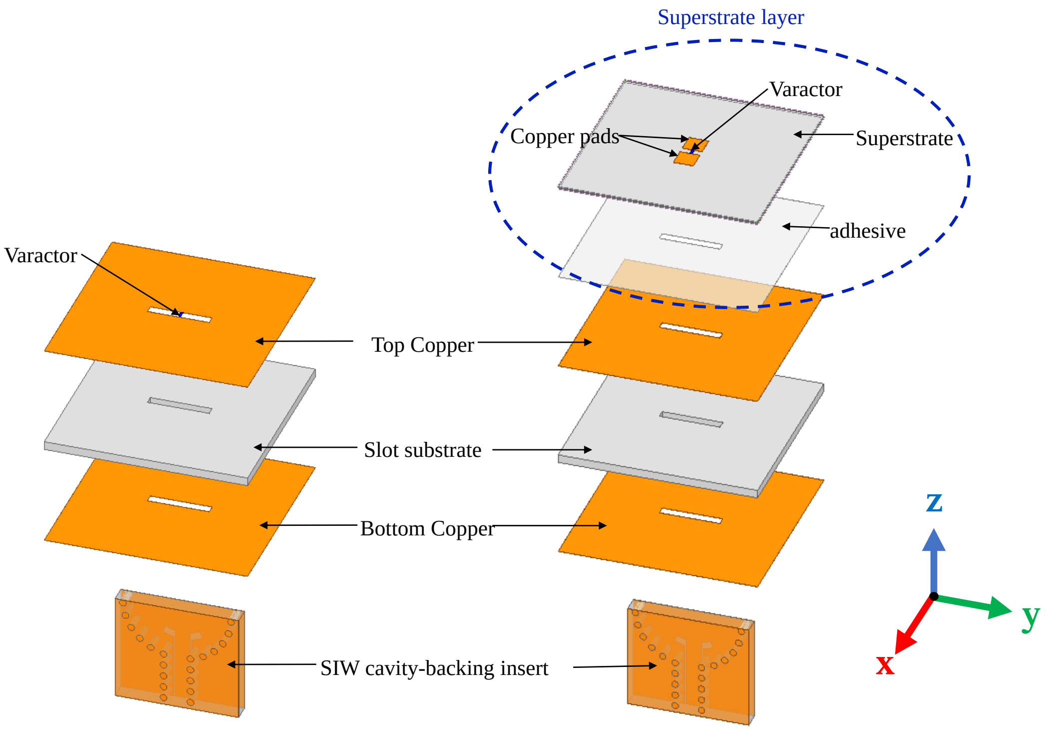

Figure 5.7: Exploded view of the superstrate-loaded antenna structure, as developed from the initial varactor-tuned slot antenna.

As a result, the total capacitance contributed by the superstrate layer, C_{ss}, is

$$C_{ss} = \frac{A\epsilon_0\epsilon_{r1}}{t_1} + \frac{A\epsilon_0\epsilon_{r2}}{t_2} \tag{5.1}$$

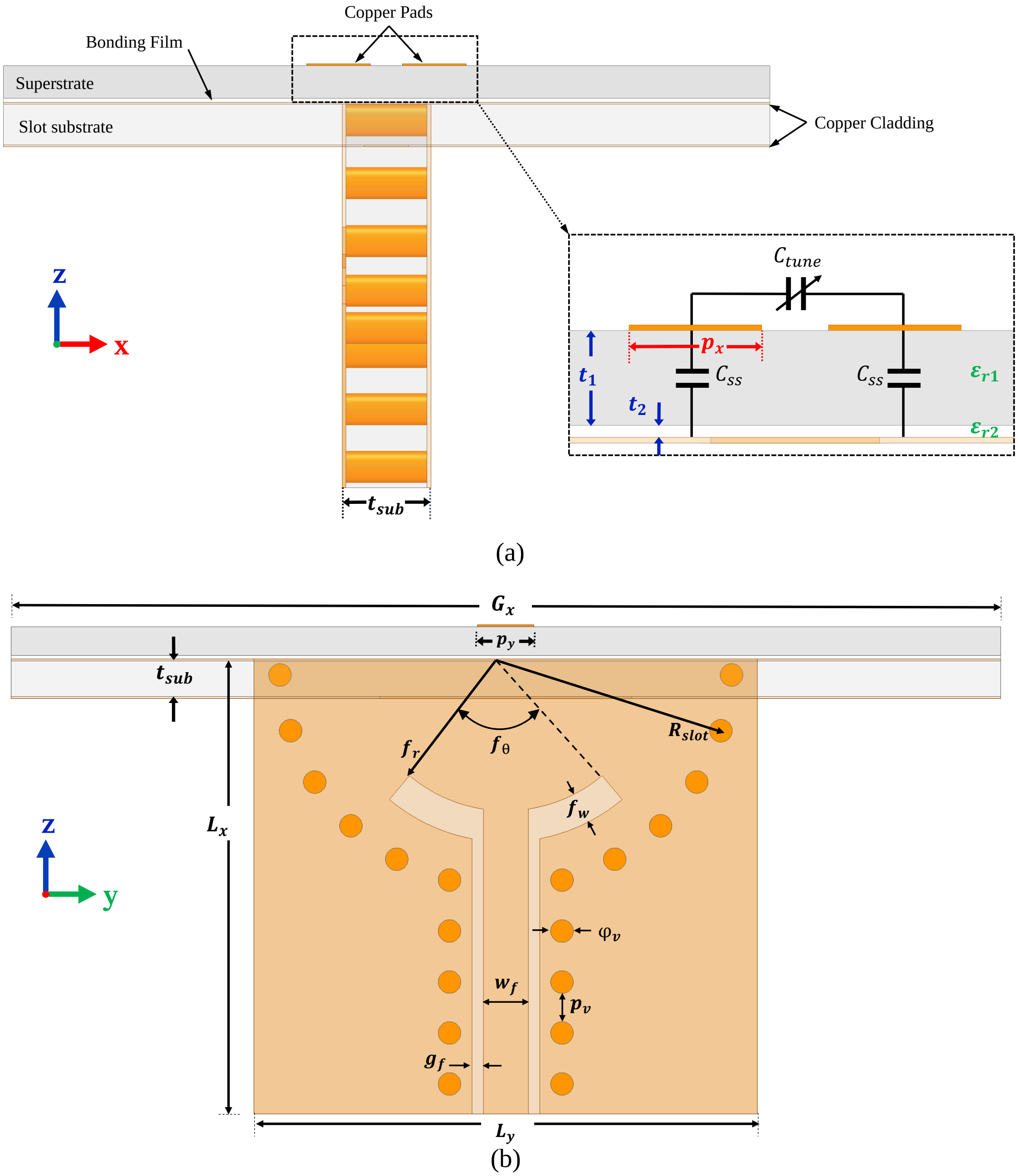

(a)

(b)

Figure 5.8: (a) Superstrate loading concept and the series capacitance network formed in the structure (b) Primary design Variables for the antenna cavity-backing insert.

The total series capacitance realized above the slot, C_{total} is given as,

$$C_{total} = \left(\frac{2}{C_{ss}} + \frac{1}{C_{tune}}\right)^{-1} \tag{5.2}$$

With the added superstrate layer, the strict requirement on the varactor's minimum tuning capacitance is alleviated. By adjusting the superstrate material properties and area of the copper mounting pads, the same C_{total} can be realized with a larger value of C_{tune}.

5.3.1 Parametric Analysis of Superstrate Layer

Parametric studies were carried out to evaluate the effect of the superstrate layer on the antenna's frequency tuning. The main parameters evaluated were the superstrate thickness, t_1, dielectric constant ϵ_{r1}, and the length of the square copper pads, p_x, patterned on the superstrate. The cavity radius, R_{slot}, was left unchanged to maintain the same unloaded frequency of about 14 GHz without the superstrate layer. The slot was allowed to resonate above the highest frequency of 12 GHz because further loading from the superstrate and varactor will only decrease the resonant frequency.

Simulation results of the frequency tuning curves as a function of varactor's loading capacitance and superstrate parameters, t_1, ϵ_r, and p_x, are plotted in Fig. 5.9. The default values of the parameters are listed in Table 5.4. The trends observed are summarized as follows:

1. As the superstrate's thickness is increased from 5 mils to 30 mils, the slope of the tuning curve decreases substantially. Furthermore, there is a shift in the unloaded frequency from 13.6 GHz to 12.6 GHz when increasing the value of t_1. As shown by Eq. (5.1), the superstrate's capacitance C_{SS} is inversely proportional to the layer's thickness t_1. Consequently. the overall capacitive loading is reduced for a thicker superstrate, which in turn decreases the antenna's tuning sensitivity.

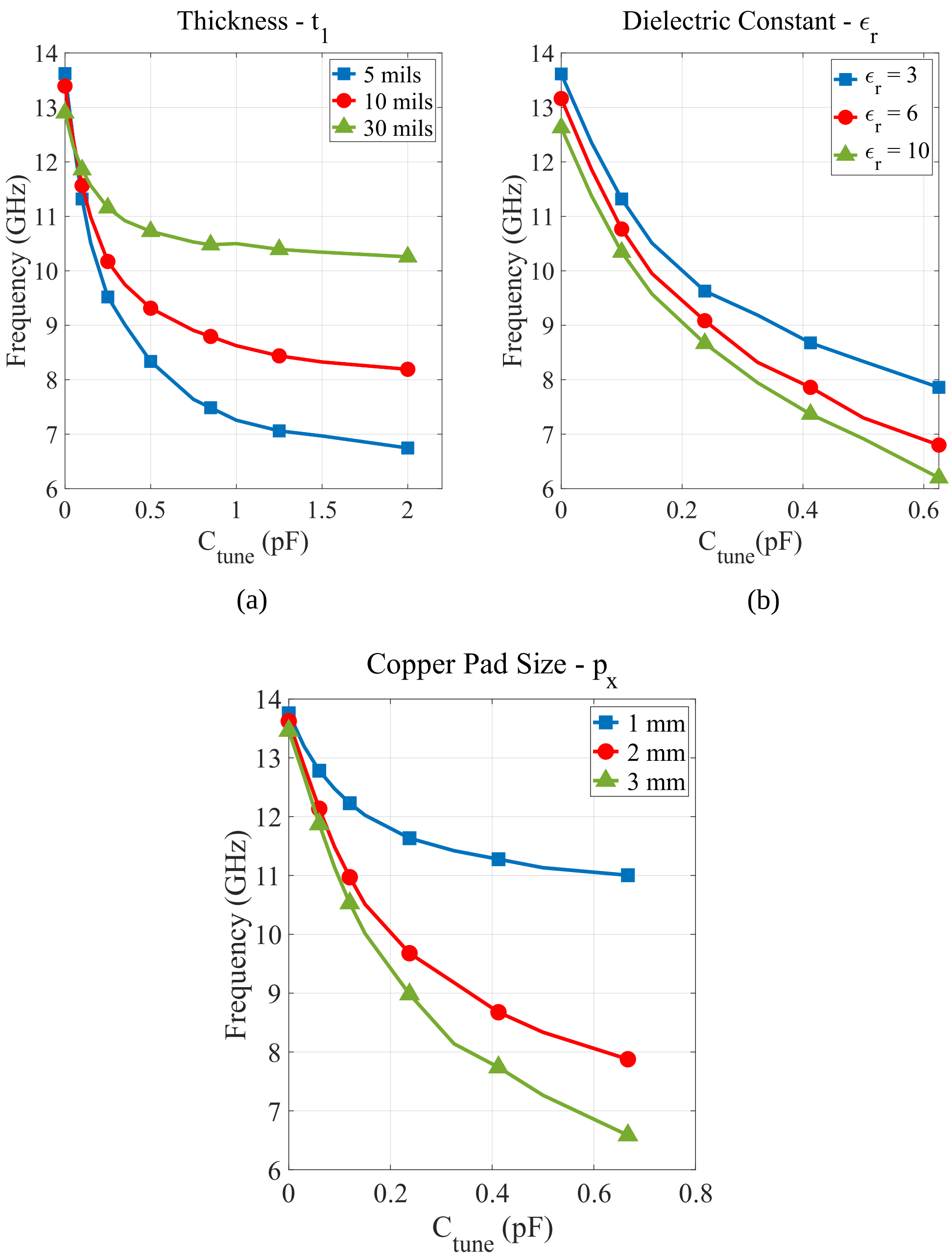

(a) (b)

(c)

Figure 5.9: Parametric analysis of the superstrate layer parameters and its effect on the varactor-tuned CBSA's frequency tuning behavior. (a) Thickness, (b) the dielectric constant of the superstrate, and (c) the effect of the square copper pad size. Default values for the other dimensions of the antenna are listed in Table 5.4.

2. The main impact of superstrate's dielectric constant, ϵ_{r1}, is on the unloaded frequency of the structure. Parametric analysis was conducted with values ϵ_{r1} of 3, 6, and 10 based on the range of material availability. As ϵ_{r1} is increased from 3 to 10, the loading capacitance increases, thereby resulting in a decrease of the unloaded frequency from 13.6-12.6 GHz. A smaller value of ϵ_{r1} reduces the capacitive loading on the structure and increases the unloaded frequency. Due to higher loading, the antenna's tuning sensitivity increases. As a result, the tuning ratio for a given change of load capacitance is maximum for superstrate materials with a lower dielectric constant.

3. The length of the copper pads patterned on top of the superstrate also has an impact on the tuning sensitivity of the structure. To simplify the investigation, a square pad with an edge length p_x was chosen. As observed in Fig. 5.9, for a given capacitance ratio, the frequency tuning ratio is maximized for a larger pad length due to the increase of surface area A. As dictated by Eq. (5.1). a larger area increases the capacitive loading, therefore increasing the tuning sensitivity of the antenna. Note that the unloaded frequency remains comparatively constant as the pad length is varied.

Based on the parametric studies, it is evident that the material properties and physical design of the superstrate layer can be selected and fine-tuned to attain a given frequency tuning ratio based on the varactor's capacitance. Ideally, a very thin superstrate material with a low dielectric constant ranging from 2 to 4 will ensure higher frequency tunability. The patterned copper pad area can be adjusted to fine-tune the antenna's frequency over a range of available varactor capacitances.

5.4 Antenna Implementation and Trade-off Analysis

With the knowledge of the tuning concept of the varactor-tuned superstrate-loaded CBSA, the design parameters can be optimized to realize a specific frequency change ratio for a given range of varactor capacitances. The main limitation of designing the antenna for a wide tuning range is a reduction in the antenna's efficiency and realized gain. In this section, this trade-off between tuning and radiation performance is demonstrated with the design of two antenna prototypes. Note that for the purposes of this discussion, the term radiation performance only encompasses the realized gain and efficiency parameters. Prototype-1 is designed to demonstrate a larger frequency tuning ratio, covering the entire X-band range. On the other hand, Prototype-2 is designed to maintain a higher radiation efficiency and gain across a smaller frequency tuning range within the X-band.

5.4.1 Prototype-1

The design parameters of Prototype-1 were optimized to demonstrate tuning across the entirety of the X-band from 8 to 12 GHz. A capacitance tuning range of 0.15-2 pF was to be accommodated, which is provided by a commercially available varactor (MACOM

Table 5.1: Design dimensions of superstrate-loaded Antenna (all dimensions are in mm)

Dimension	Prot. 1	Prot. 2	Dimension	Prot. 1&2
t_1	0.0508	0.127	f_w	0.55
ϵ_{r1}	3.25	3	g_f	0.13
p_x	1.2	1.15	p_v	0.5
f_θ	56°	52°	ϕ_v	0.4
f_r	3.2	4	w_f	1.11
R_{slot}	4	5	ϵ_{r2}	2.8
L_x	8	9	t_2	0.0127
L_y	9	11	G_x	25
p_y	1.2	1.15	t_{sub}	1.524

46580-1209 [78]). As inferred from the parametric studies of the antenna, a superstrate material with very low thickness and dielectric constant would yield a maximum frequency tuning range.

A 2-mil thick Liquid Crystalline Polymer (LCP) circuit material was used for the superstrate in the Prototype=1 design, which has a dielectric constant of 3.05. The DuPont Pyralux LF1500 adhesive, with a dielectric constant of 2.8 and thickness of 12.7 μm (0.5 mils), is used to bond the superstrate onto the top copper cladding of the slot substrate. It is important to note that there are several complications with conductor effects on the apparent dielectric constant of thinner substrates, as detailed in [79]. With a rougher copper foil on thin materials, a higher value of the dielectric constant is measured. On an experimental basis, the loss tangent associated with this material was reported to be 0.002. To account for these anomalies associated with thinner substrates, the LCP material is modeled with a dielectric constant of 3.25 at 10 GHz. This estimate is based on the curve-fit data presented in [79].

The S_{11} response of the antenna prototype-1 with a 2 mil thick superstrate is plotted

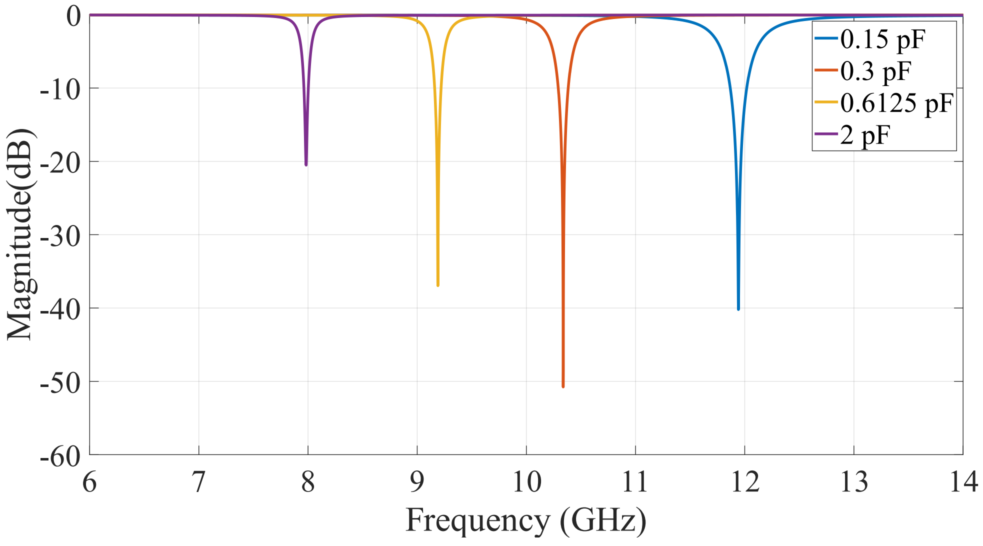

Figure 5.10: Prototype-1 $|S_{11}|$ Response of the superstrate-loaded varactor-tuned CBSA. The fractional bandwidth varies from 0.5% to 1.26% across the tuning range.

in Fig. 5.10. Within the available range of varactor capacitances, the antenna can be tuned across most of the X-band. At a minimum loading of 0.15 pF, the antenna operates at 11.94 GHz. With a maximum load capacitance of 2 pF, the antenna operates at 7.98 GHz, as seen in Fig. 5.10. A return loss of greater than 10 dB is maintained across the X-band tuning range.

Radiation patterns at the highest and lowest capacitive loading are shown in Fig. 5.11. The peak realized gain ranges from 2.14-6.36 dB, while the radiation efficiency varies from 37.6% to 88.7% when tuning from 7.98 GHz to 11.94 GHz. The degradation of radiation performance is due to the higher loading of the slot antenna structure. At a load capacitance of 2 pF, the frequency shift is almost half of the unloaded frequency of the first resonant mode, which is at 16.1 GHz. The smaller electrical size of the antenna enables greater tunability due to the higher capacitive loading of the superstrate structure. However, it comes at the cost of radiation performance with a smaller realized gain and antenna efficiency.

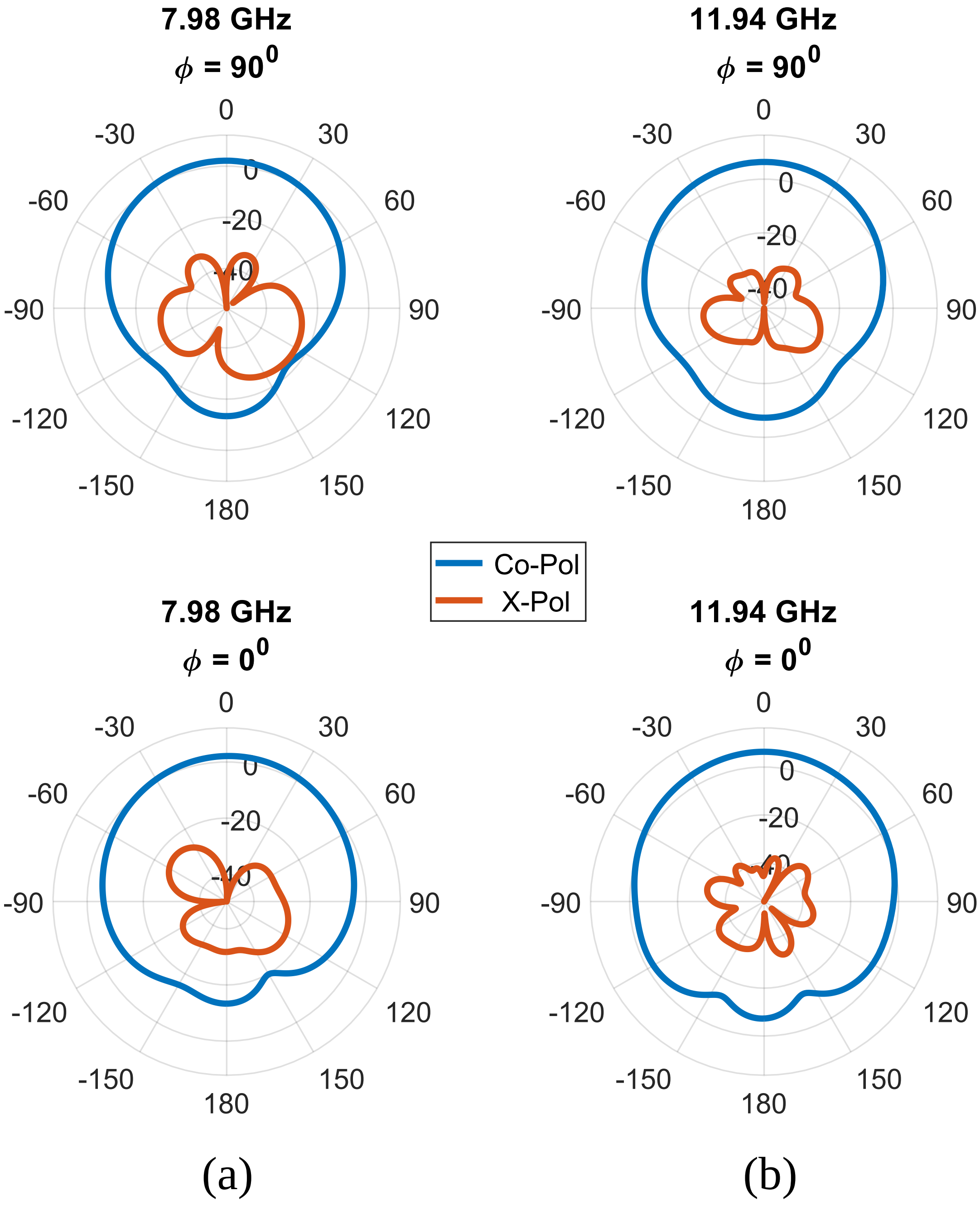

Figure 5.11: Radiation Patterns of Prototype-1 at (a) 7.98 GHz and (b) 11.94 GHz. The blue line is the co-polarization component, and the red line represents the cross-polarization (X-Pol). The X-Pol is below -24 dBi in all cut planes. The cut-planes are defined as per the coordinate system in Fig. 5.7.

5.4.2 Prototype-2

In order to demonstrate the trade-offs between the antenna's tuning range and radiation efficiency, a second prototype was designed with a smaller tuning range but higher radiation efficiency and realized gain across frequency. The design of the antenna was changed to decrease the overall loading of the passive structure, specifically by lower the superstrate layer's additional capacitance. Dimensions of the second prototype are listed in Table 5.4.

As dictated by Eq. (5.1), a thicker superstrate with a lower dielectric constant will reduce the total load capacitance at the slot aperture. Therefore, the thickness of the superstrate was increased from 2 mils to 5 mils. Based on the substrate material availability for 5 mil thicknesses, Rogers 3003 material was selected for the superstrate. Furthermore, the cavity radius was increased from 4 mm to 5 mm to increase the slot aperture's electrical size. and ensure a higher gain of the antenna. With these design changes, the unloaded frequency of the antenna was decreased from 16.1 GHz to 12.8 GHz, as compared to the antenna

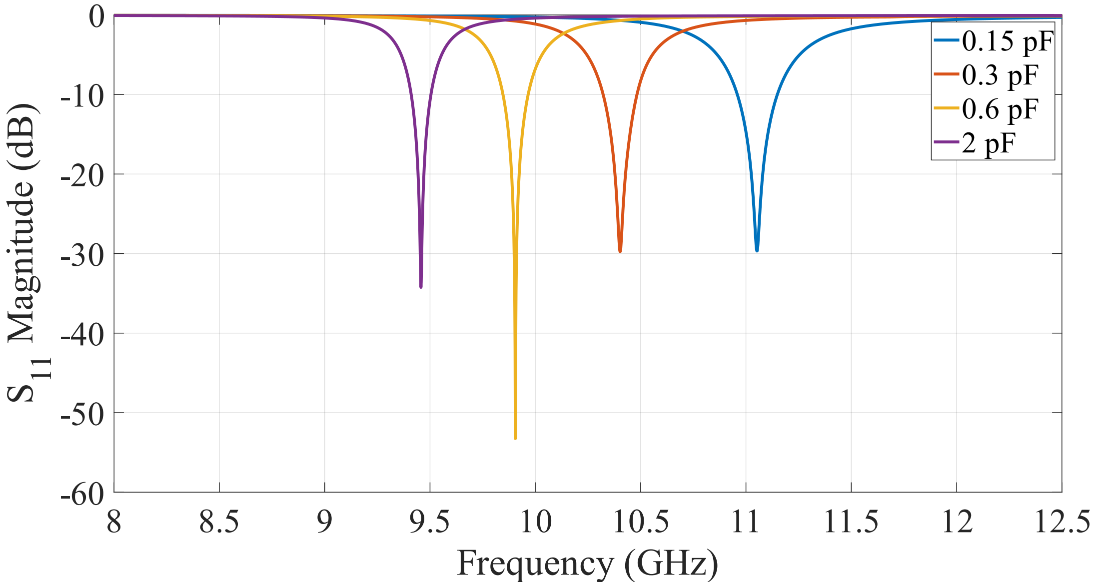

Figure 5.12: Prototype 2 - S_{11} Magnitude response of the SS-Loaded antenna across frequency. The exhibited tuning range is approximately between 9.5 GHz to 11 GHz.

prototype-1 design.

As seen in Fig. 5.12, the antenna demonstrates 15% tunability, from 9.48 GHz to 11.05 GHz as the varactor's capacitance is decreased from 2 pF to 0.15 pF. Simulated realized gain of prototype-2 is 5 dB at 9.48 GHz, and 8 dB at 11.05 GHz, with a greater than 77 % efficiency across the tuning range (Fig. 5.14). As compared to prototype-1, the tunability of the second design is much smaller (64 % reduction) due to decreased loading of the antenna structure. However, as seen in Fig. 5.14, the second prototype's radiation performance is significantly improved across the tuning range, especially at the lower range of frequency where the antenna is maximally loaded and is electrically smaller.

The tuning and radiation performance of the antenna prototype-1 and prototype-2 are compared and evaluated in Fig. 5.13 and Fig. 5.14, respectively. The trade-off between the tunability and antenna efficiency is clearly observed in the plots. Note that without the superstrate structure, the minimum loading capacitance required to tune to 12 GHz is 0.08 pF for prototype-1 and 0.05 pF for prototype-2. Commercially available varactors cannot provide such small capacitance values. With the addition of the superstrate structure, the minimum loading capacitance is increased, thereby making the antenna physically realizable. However, the tuning sensitivity of the antenna is reduced due to the added loading of the superstrate, as seen in Fig. 5.13. This is expected since the superstrate is directly placed above the radiating slot aperture. However, by accurately designing the superstrate layer, a very wide frequency tuning range can still be achieved.

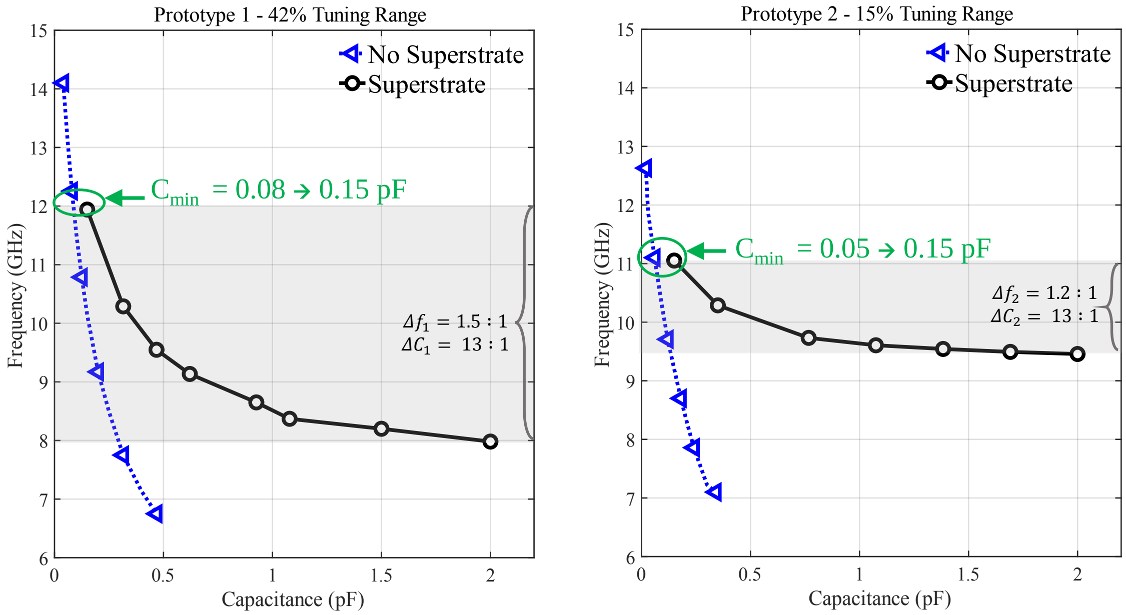

(a) (b)

Figure 5.13: Loading effect of the superstrate on the varactor-tuned antenna. The capacitance tuning and frequency tuning ratios are represented as Δf and ΔC, respectively. The added substrate shifts the minimum capacitance required to tune at 12 GHz from 0.08 pF to 0.15 pF.

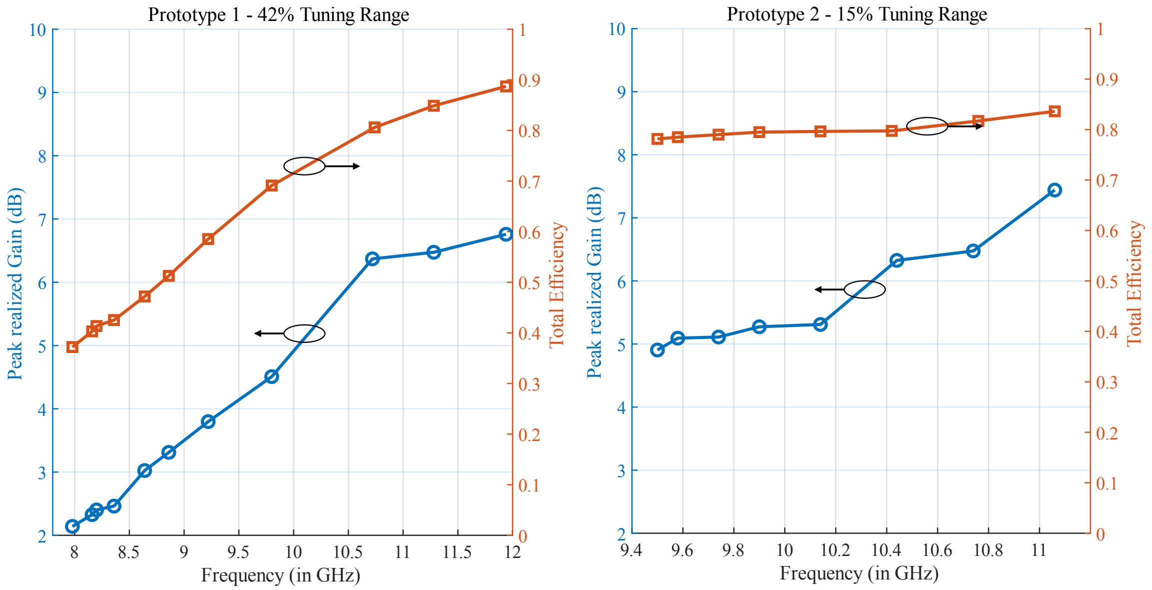

(a) (b)

Figure 5.14: Comparison of radiation efficiency and peak realized gain across frequency for Prototype-1 and Prototype-2.

5.5 Varactor Diode Biasing Network

Varactors require an external DC bias voltage to provide the variable junction capacitance required to tune the superstrate-loaded antenna. When active devices like varactors are integrated into the RF circuitry, it is crucial to ensure proper isolation between the RF currents and DC bias circuitry. Since the reverse-bias current through the varactor diode is comparatively small, a DC blocking capacitor is not generally required to prevent the DC current from reaching the RF port. However, an RF choke network is necessary to minimize RF coupling with the DC bias circuit. In this chapter, several approaches are investigated for the superstrate-loaded antenna's bias circuitry. The efficacy of the designed bias network is determined by evaluating the antenna's operating frequency, and radiation quantities, including realized gain and efficiency, as well as the radiation patterns.

5.5.1 DC Bias Lines

For the design of the X-band tunable slot antenna, the varactor is mounted directly on the superstrate, which is stacked on the radiating aperture itself (Fig. 5.7. The applied voltage should therefore be across the patterned copper pads across which the varactor is terminated. To provide a bias voltage across the varactor's terminals, two narrow high-impedance DC bias lines were extended from the ends of the copper pads, which are on top of the superstrate. The width of the DC bias line must be as small as possible to ensure that it presents a high-impedance path for the RF currents. Based on fabrication feasibility, the DC line width was set to 100 μm. The lines were extended towards the extreme ends of the superstrate to ensure minimal interference in the slot aperture and superstrate loading region. Additional DC connection pads were added at the end of the bias line to facilitate soldering to DC wires.

First, the lines were placed transverse to the slot aperture, as seen in the inset of Fig. 5.15.

In Fig. 5.15, the simulated S_{11} response of the antenna structure with and without the DC Bias lines is compared. The responses are compared at the lowest and highest varactor load capacitance values, at 0.15 pF and 2 pF, respectively. As observed by the detuning of S_{11} response, the DC bias lines were severely coupling with the antenna structure across the entire tuning range. Increased capacitive loading of the DC lines with the slot ground plane resulted in the downward shift of the antenna's operating frequency.

Next, the DC lines were placed parallel to the slot aperture's length, as seen in Fig. 5.16. However, the S_{11} response showed similar de-tuning effects as that of the transverse bias lines. Higher-order line resonances were observed in both configurations at minimum and maximum varactor load capacitance. As seen in Fig. 5.15(b), the additional resonances were formed along the length of the DC bias lines at 12.8 GHz and 13.2 GHz for the maximum and minimum varactor loading, respectively. To eliminate the high-order resonances, the DC lines were shortened. However, this caused a worse loading effect due to the placement

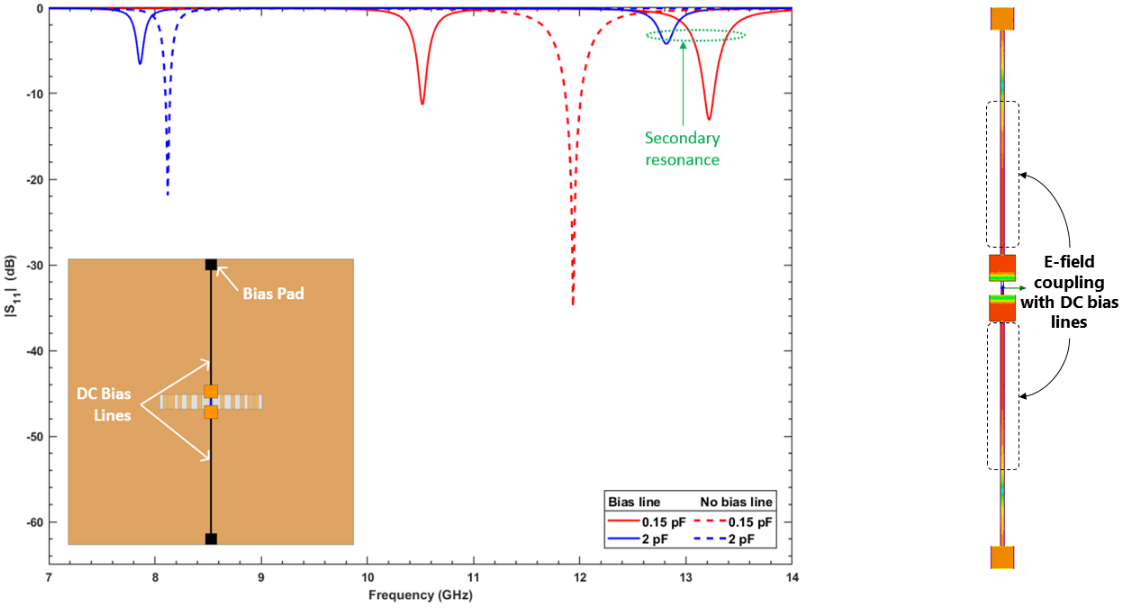

(a)

(b)

Figure 5.15: Effect of transverse high-impedance DC Bias lines on the S_{11} response at minimum (0.15 pF) and maximum (2 pF) capacitive loading

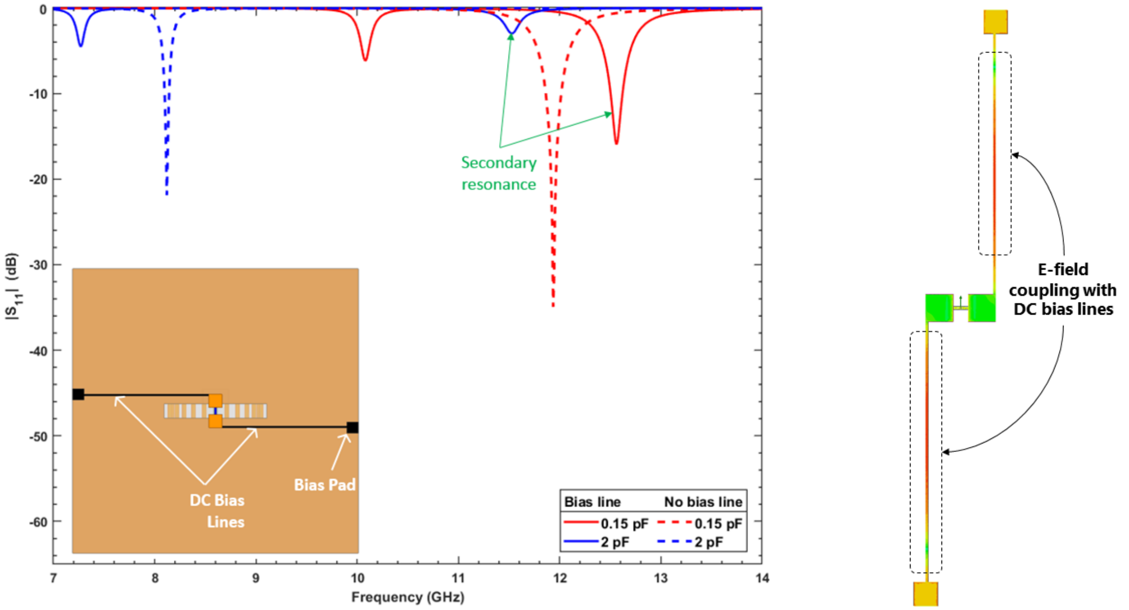

(a) (b)

Figure 5.16: Effect of longitudinal high-impedance DC Bias lines on the S_{11} response at minimum and maximum capacitive loading

of DC bias pads placed close to the slot aperture. The superstrate thickness is very small, about 2 mil thick, which required an even thinner bias line for achieving a high enough impedance to choke the RF currents. However, further reduction in the line width was not feasible due to fabrication constraints. Therefore, other means of stopping the RF currents along the DC bias path had to be investigated.

5.5.2 Lumped Element Bias Circuit

There were several difficulties in suppressing RF coupling along the DC bias lines across the entire tuning range of 8-12 GHz for prototype 1 of the superstrate-loaded slot antenna. Therefore, to simplify the design process for the biasing structure, further designing of the bias network was conducted on the second prototype, which exhibited a smaller tuning range from 9.5 GHz to 11 GHz.

As an initial investigation, 100 kΩ resistors were connected to the biasing lines to

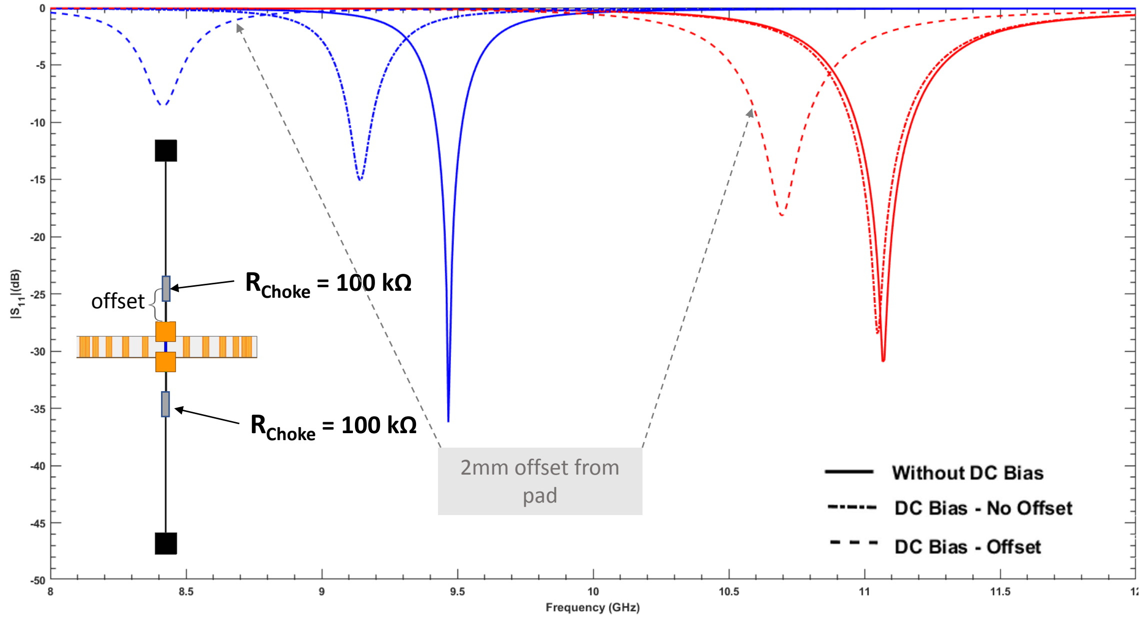

Figure 5.17: Comparison of the S_{11} response with and without the DC bias network with additional 100-kΩ resistors. As the resistor is placed slightly away from copper pads, the S_{11} response of the antenna with the bias network is severely de-tuned.

function as RF Chokes to minimize RF currents that might couple into the bias wires and leak into the antenna. The simulated S_{11} response with and without the resistor bias network is shown in Fig. 5.17. The results indicate that the RF and DC path isolation is very closely maintained at the lowest capacitance loading of 0.15 pF at 12 GHz. However, the response de-tunes at the lower end of the tuning range, at 9.5 GHz, for a bias capacitance of 2 pF. In addition, the slightest offset of the resistor from the end of the copper pad results in severe interference between the RF and DC path, as seen in Fig. 5.17.

Bias lines constructed using lumped elements like series inductors and bypass capacitors are some other common methods of providing isolation between the DC and RF paths [80]. The purpose of a bypass capacitor is to provide a lower impedance path for the RF to prevent it from entering the DC bias circuitry. The bypass capacitor can therefore provide an efficient path to ground the RF energy and suppress any RF ”noise” along the DC bias

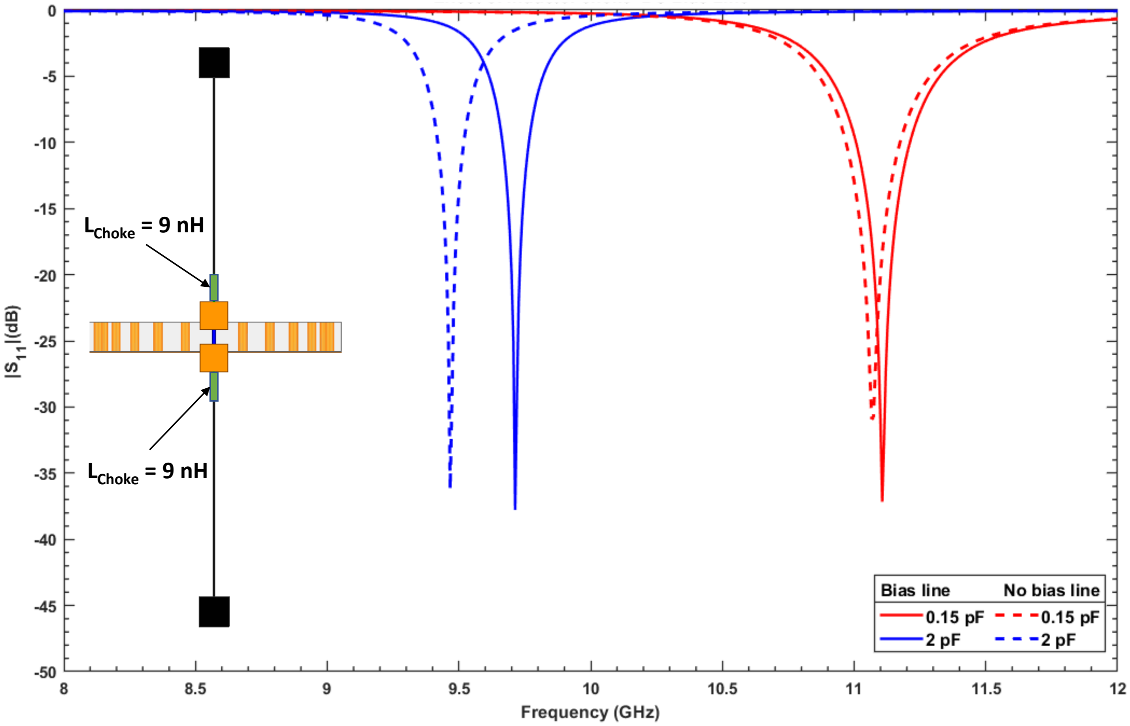

Figure 5.18: Effect of loading the DC bias with 9 nH inductors to choke the RF coupling from the DC-bias lines

lines. However, with the design structure of the superstrate, the bias voltage is referenced between the copper pads, and there is no direct path to ground the RF energy. To implement the bypass capacitor in the bias network, the DC lines would have to be moved to the bottom of the slot ground plane through a via. However, a via through the superstrate layer would interfere with the superstrate's capacitive network with the slot ground plane and affect the antenna's radiation properties. Therefore, a bypass capacitor was not a viable biasing technique for the bias circuit of this antenna structure.

Another common method of achieving RF-DC isolation is to place RF chokes, or series inductors, on the DC supply line. An ideal RF Choke is essentially an inductor that only passes DC while rejecting all the other frequencies. The choke inductance must be selected to provide a high enough impedance to suppress the RF currents across the frequency tuning range. For initial investigations, 9 nH inductor chokes were placed on either end of the DC bias lines. A large inductance value was chosen to ensure higher RF-DC isolation. Based on the simulation results of the resistor bias circuit (Fig. 5.17), the inductors were placed close to the bias pads to enable higher suppression of RF signal on the DC path. The simulated S_{11} response in Fig. 5.18 shows that the RF-choke provides a high enough impedance at 11 GHz. However, at the lower operating frequency, the impedance provided by the inductor is not large enough to suppress the RF currents along the DC line. As a result, the antenna de-tunes and shifts from 9.5 GHz to 9.7 GHz for a varactor load capacitance of 2 pF.

A higher value of choke inductance could potentially isolate RF currents from the DC path across the entire tuning range. However, practical surface-mount inductors are not ideal, and they generally have a self-resonant frequency (SRF) due to the presence of parasitic capacitance in the packaging. Above the SRF, the inductive behavior changes to that of a capacitive, failing the RF choking mechanism. Increasing the inductance to provide better RF suppression would simultaneously decrease the SRF. Based on commercially available data for RF choke inductors, any inductance greater than 5 nH had an SRF at and below the X-band frequency range. The choke network was required to work in the X-band tuning range with minimal effects on the DC bias network. Due to these constraints, a lumped inductor choke was not considered for the varactor bias network of the antenna.

5.5.3 Radial-Stub Bias Network

Another way of mitigating RF interference on the DC bias path is to accommodate lowpass filters, resonators with stopband characteristics, or band-stop filters to suppress RF coupling in the desired frequency range. These filtering structures should function efficiently in a bias network to choke off RF transmission over its stopband while passing direct current to the active element. Based on the model and requirements of the superstrate-loaded tunable antenna, a varactor bias network with a band-stop response in the X-band was deemed appropriate.

Defected ground structures (DGS) have been used to design band-stop filters, wherein intentional defects are employed on the ground plane, providing band rejection property due to their resonance characteristics [81]. The main advantage of DGS topology, when used for biasing, is to move the DC circuitry away from the radiating structure. However, these ground-plane defects may cause unwanted back-radiation for the superstrate-loaded cavity-backed slot antenna.

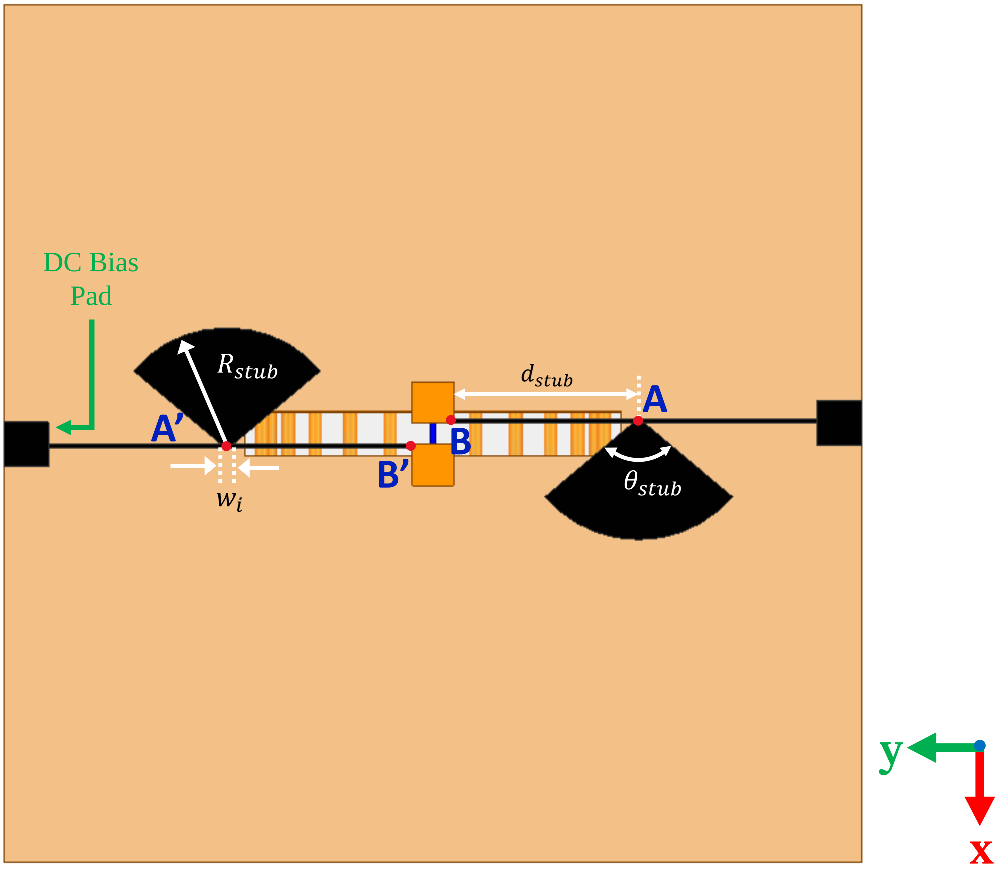

Figure 5.19: Superstrate-loaded Slot Antenna with added radial stub bias network. Design dimensions of stub bias for prototype-2: d_{stub} = 5.45 mm, w_i = 0.338 mm, θ_{stub} = 100°, R_{stub} = 3 mm. The DC bias pad dimensions are 1.3 mm × 1.3 mm.

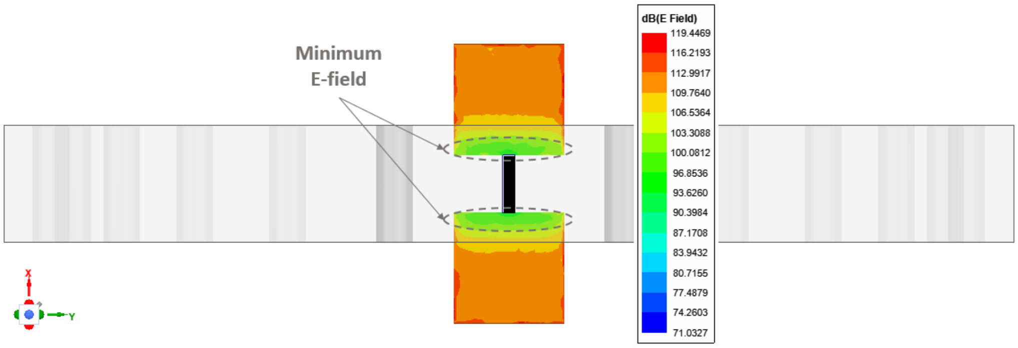

Figure 5.20: Electric field distribution across the bias pads without the bias network. The highlighted region corresponds to the E-field minima.

A more straightforward method is to place quarter-wavelength open-circuited transmission line stubs along the bias line to achieve a stopband response at a specified frequency. However, this would result in a narrow-band solution. To increase the bandwidth of the stopband, the conventional quarter-wavelength rectangular stubs can be replaced with radial stubs for having low impedance levels in a wide frequency band. Several RF applications utilize radial stubs as a part of their bias-circuitry [82]-[84].

For the superstrate-loaded slot antenna, the radial stubs are placed on top of the superstrate along the length of the DC bias lines. To implement the biasing network with minimum RF energy loss in the bias line and dc source, the input impedance of the bias line should be an RF open-circuit or an RF short-circuit. As seen in Fig. 5.19, the stub is positioned at point A, which is at a distance d_{stub} = $\lambda/4$ from the end of the copper pad (point B), where λ is the guided wavelength at the center frequency. Therefore, the broadband RF short-circuit at point A can be transformed into an RF open-circuit at point B. Geometric parameters of the radial element can be tuned to shape the stopband response - the stub radius (R_{stub}) will determine the center frequency of the stopband. In contrast, the vertex angle(θ_{stub}) can be used to control the bandwidth of the stopband. The termination width of the stub at the bias line, w_i, is kept as small as possible to ensure a well-defined RF short-circuit at point A.

Detailed theoretical and mathematical analysis of the stub parameters and their effects can be found in [83].

Note that the DC lines are placed parallel to the slot length and elongated through the terminal points of the varactor at point B (Fig. 5.19). The electric-field distribution on the pads without the bias network (Fig. 5.20) indicates a point of the minimum electric field at point B. Since the same mode is being tuned, the point of the minimum E-field does not shift across the tuning range. Therefore, running DC lines from point B minimizes the capacitive loading of the bias line on the superstrate layer across the X-band.

5.5.4 Antenna performance with bias network

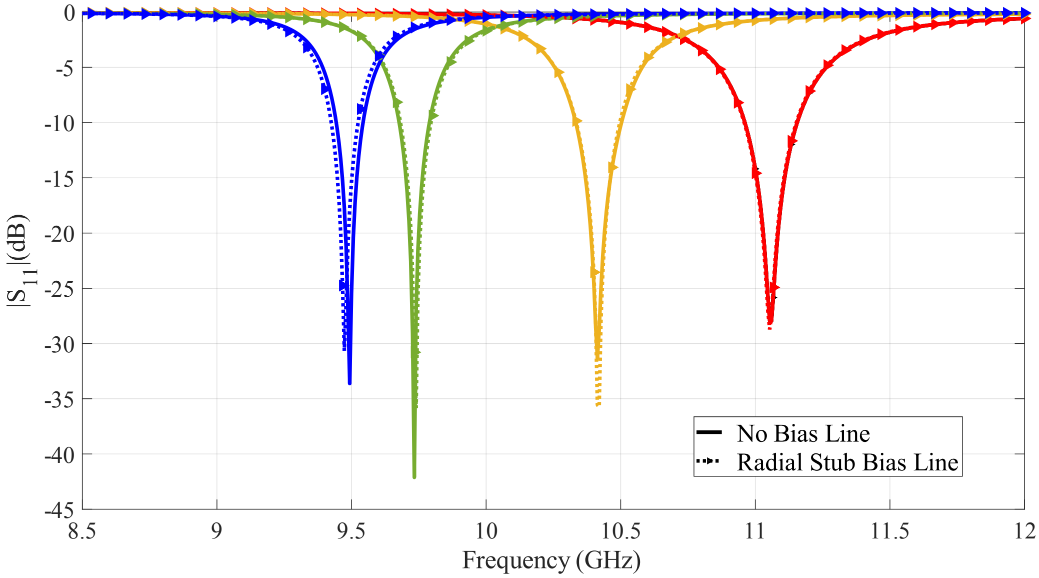

Figure 5.21: S_{11} response of the superstrate-loaded antenna with and without the radial stub bias network. The simulated results indicate no significant RF-DC coupling across the tuning range.

The design dimensions of the radial-stub bias circuit for the superstrate-loaded antenna are listed under Fig. 5.19. To ensure the accuracy of simulation results, it is recommended to add finer mesh on the entire bias network, including the copper pads patterned on the

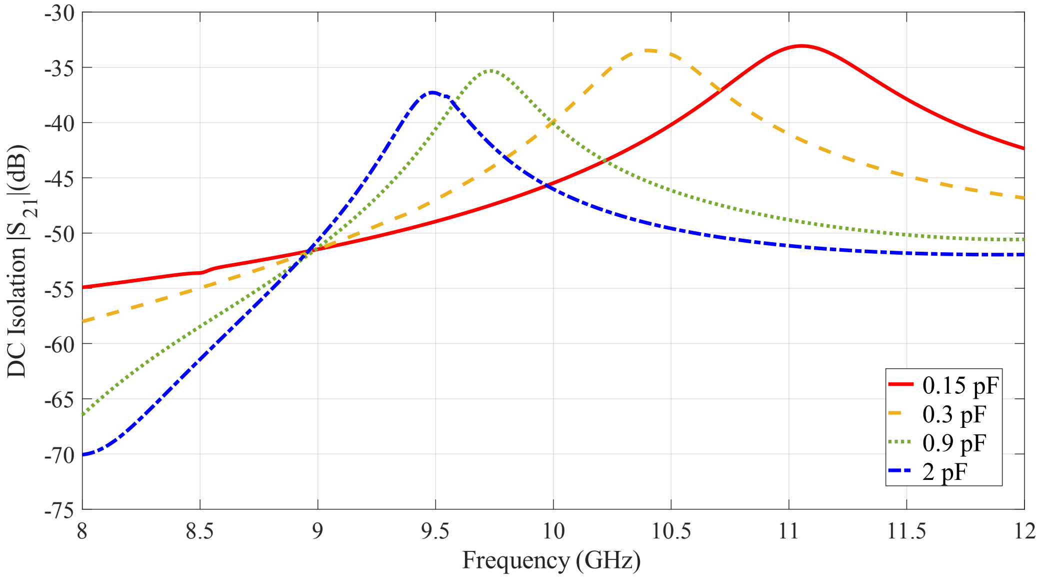

Figure 5.22: Isolation between DC and RF ports S_{21} across frequency tuning range

superstrate. The S_{11} response with and without the radial stub DC-bias is shown in Fig. 5.21. Simulation results indicate that adding a bias network to the antenna does not affect the antenna's operating frequency. At a maximum load capacitance of 2 pF, there is a minor deviation of the operating frequency at minimum S_{11}, from 9.49 GHz to 9.47 GHz.The frequency shift can be attributed to the lower attenuation level of the radial stub at lower loading. There is a good agreement between the S_{11} curves with and without the added radial-stub bias network.

An additional wave port was placed at the DC connect pads to show the isolation between the RF (port 1) and the DC port (port 2). As seen by the S_{21} curves in Fig. 5.22, the isolation is better than 33 dB across the tuning range. Electric field distributions across the copper pad and the DC bias network are plotted at the superstrate-loaded slot antenna structure's minimum and maximum load capacitance, Fig. 5.20. The minimum E-field is concentrated through the bias network across the radial stubs and the DC bias lines.

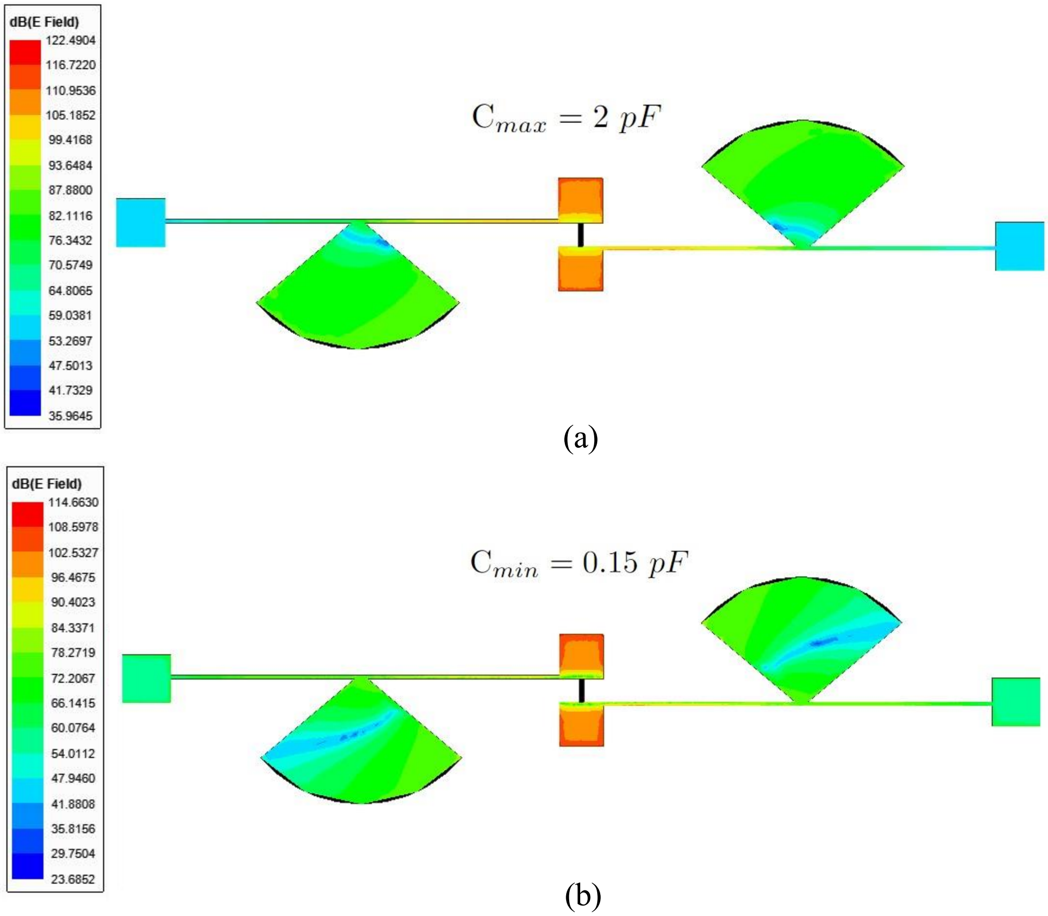

(a)

(b)

Figure 5.23: Electric-field distributions across the DC bias network (a) at minimum (0.15 pF) and (b) maximum (2 pF) varactor capacitive loading. Note that the maximum E-field region is concentrated at the copper pads.

Since the bias network is placed directly on top of the radiating structure, it is important to ensure that the antenna's radiation patterns are not significantly affected by the added bias network. Any radiation from the radial stubs would cause unwanted interference in the radiation patterns, especially in the direction of the main beam. Polar plots of the realized gain patterns in the azimuth plane with and without the bias network are shown in Fig. 5.24. The co-polarized radiation is unaffected with and without the bias network, which again proves that an excellent is maintained between the RF energy from the antenna and the DC Bias circuit. However, the level of cross-polarization pollution is increased due to the addition of the radial stub DC bias. This interference is mainly due to the electrical lengths of the radial stubs, which are about a quarter wavelength long at the center frequency of the tuning range.

Table 5.2: Peak Realized Gain of the varactor-tuned superstrate-loaded antenna (prototype-2)

Frequency	Without Bias				With Bias			
	$\phi = 90°$		$\phi = 0°$		$\phi = 90°$		$\phi = 0°$	
	Co-Pol	X-Pol	Co-Pol	X-Pol	Co-Pol	X-Pol	Co-Pol	X-Pol
9.5 GHz	5.15 dB	-23 dB	6.15 dB	-32.4 dB	5.54 dB	-17.1 dB	6.9 dB	-30.3 dB
11.1 GHz	6.9 dB	-28.5 dB	6.9 dB	-30.3 dB	6.9 dB	-20.5 dB	6.9 dB	-21.3 dB

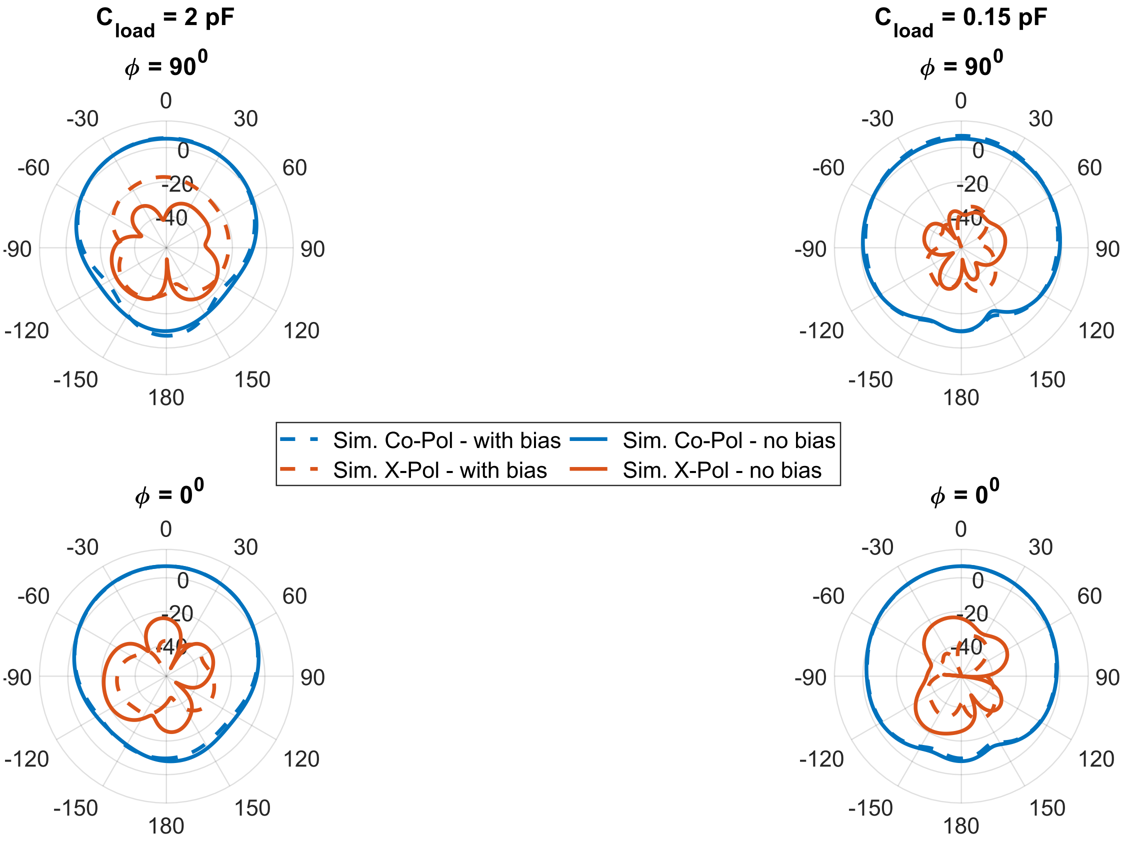

Figure 5.24: Radiation patterns with and without the bias network. Patterns are shown in different cut planes at maximum (2 pF) and minimum capacitive loading (0.15 pF) (a) $\phi = 0\,\text{deg}$ and (b) $\phi = 90\,\text{deg}$. The reference coordinate system is labeled in Fig. 5.19.

5.6 Varactor-tuned Filtenna Design

The procedure of bandpass filter design using coupled resonators is applied to synthesize the X-band tunable filtenna. For proof-of-concept, a second-order filtenna is designed in this work, but the design can be easily scaled to synthesize higher-order filtenna. The building blocks consist of the contactless-tuned evanescent-mode cavity (Section 3.3.2) and superstrate-loaded CBSA (Section 5.3) as the first and second resonators of the filtenna, respectively. For the first external coupling at the input port, a short-circuited flared wing GCPW feed is used. The inter-resonator coupling is realized through an iris opening between the cavity resonator and cavity-backing of the CBSA, as seen in Fig. 5.25. The second

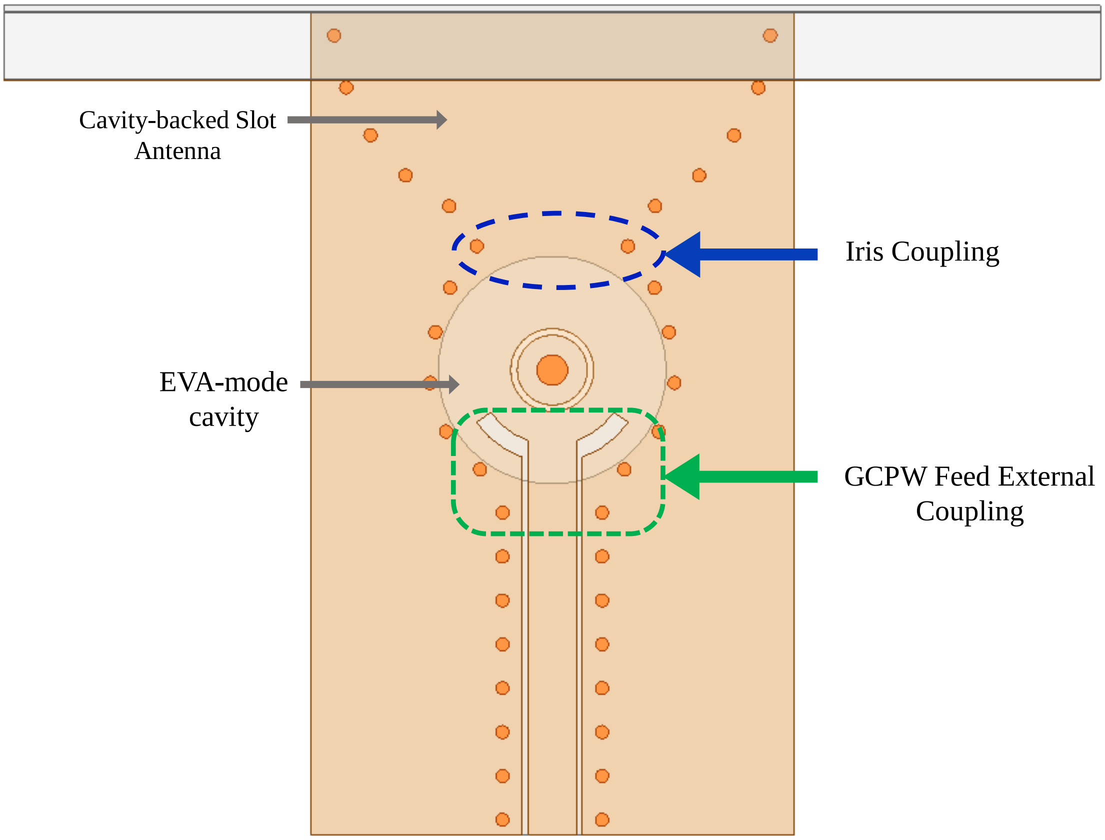

Figure 5.25: Filtenna implementation with the external input coupling provided by a flared-wing GCPW feed and the inter-resonator coupling realized through a magnetic iris opening between the EVA-mode cavity and the cavity-backing of the slot antenna.

external coupling occurs through the antenna's radiating aperture with the free space.

The filtenna's tunability is constrained by the tuning range of the superstrate-loaded varactor-tuned antenna since the cavity resonator can be tuned all across X-band as demonstrated in Section 3.3.2. Based on the trade-off analysis between tuning and radiation performance, the antenna prototype-2, with a tuning range from 9.5 GHz to 11 GHz, is used as the filtenna's second resonator. A second-order filtenna is synthesized at the center point of the tuning range, at 10.25 GHz, to generate a Butterworth filter response with 3% fractional bandwidth. The values of Q_{ext1}, Q_{ext2} and k_{12} is calculated using Eq. (2.2) as,

$$Q_{ext1} = 47.17 = Q_{ext2} \;\; , \;\; k_{12} = 0.021 \tag{5.3}$$

To meet the filter specifications, the external and inter-resonator couplings need to be adjusted so as to match the values of Q_{ext1}, Q_{ext2}, and k_{12} with the calculated values in Eq. (5.3). Following the same procedure used in Section 4.2, a systematic process is adopted to design the X-band filtenna. The parameter extraction method, as explained in Chapter 2, is used as a preliminary step to initiate the filtenna synthesis process. Next, the filtenna is coarse-tuned in the time domain to match the ideal time-domain reflection response. In the last step, the filtenna is fine-tuned with the added varactor bias network.

5.6.1 Parameter Extraction

The addition of semi-circular slots, or wings, to the end of the GCPW lines ensured stronger external coupling at the feed. This is due to the magnetic field coupling between the short-circuited ends of the slots and the magnetic field in the cavity resonator. The physical dimensions of the GCPW feed are labeled in Fig. 5.26(b), which consists of the feed radius R_f, sector angle between the short-circuited slot edges θ_f, and the width of the slot w_f.

The effect of each parameter on Q_{ext1} was investigated through a parametric study.

A singly-terminated evanescent-mode cavity with the GCPW feed was set up in HFSS Modal Network simulation, as seen in Fig. 5.26(a). The reflection delay response technique described in Section 2.1.1 is used to extract Q_{ext1} values as a function of the feed dimensions. The S-parameters were de-embedded to the point of feed termination inside the cavity for a precise value of Q_{ext1}.

As seen in Fig. 5.27, variation of the feed sector angle θ_f has the largest effect on the external coupling. The width w_f also has a significant effect on the external coupling. The effect of feed radius on Q_{ext1} is negligible for a fixed value of θ_f and w_f. Therefore, the feed angle θ_f was primarily used to tune Q_{ext1}, and the feed width was used for fine-tuning. Based on the simulation results in Fig. 5.27(c), the required value of $Q_{ext1} = 47.17$ is achieved with $\theta_f = 110°$, $w_f = 0.4$ mm and $R_f = 2.1$ mm.

In order to determine the appropriate iris width, d_x, to match the coupling coefficient k_{12}, the split-pole technique for filtenna synthesis, as described in Section 2.1.2 and in

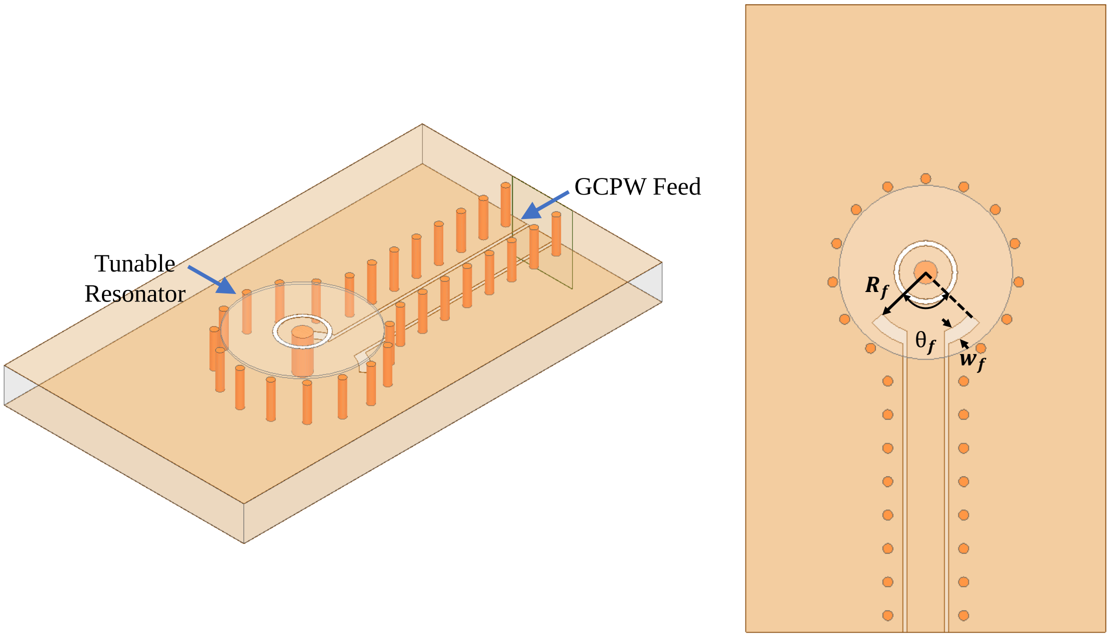

(a) (b)

Figure 5.26: Extraction of input coupling Q_{ext1} with the singly-terminated EVA-mode resonator, as shown in (a). Primary GCPW feed dimensions for controlling Q_{ext1} are labelled in (b).

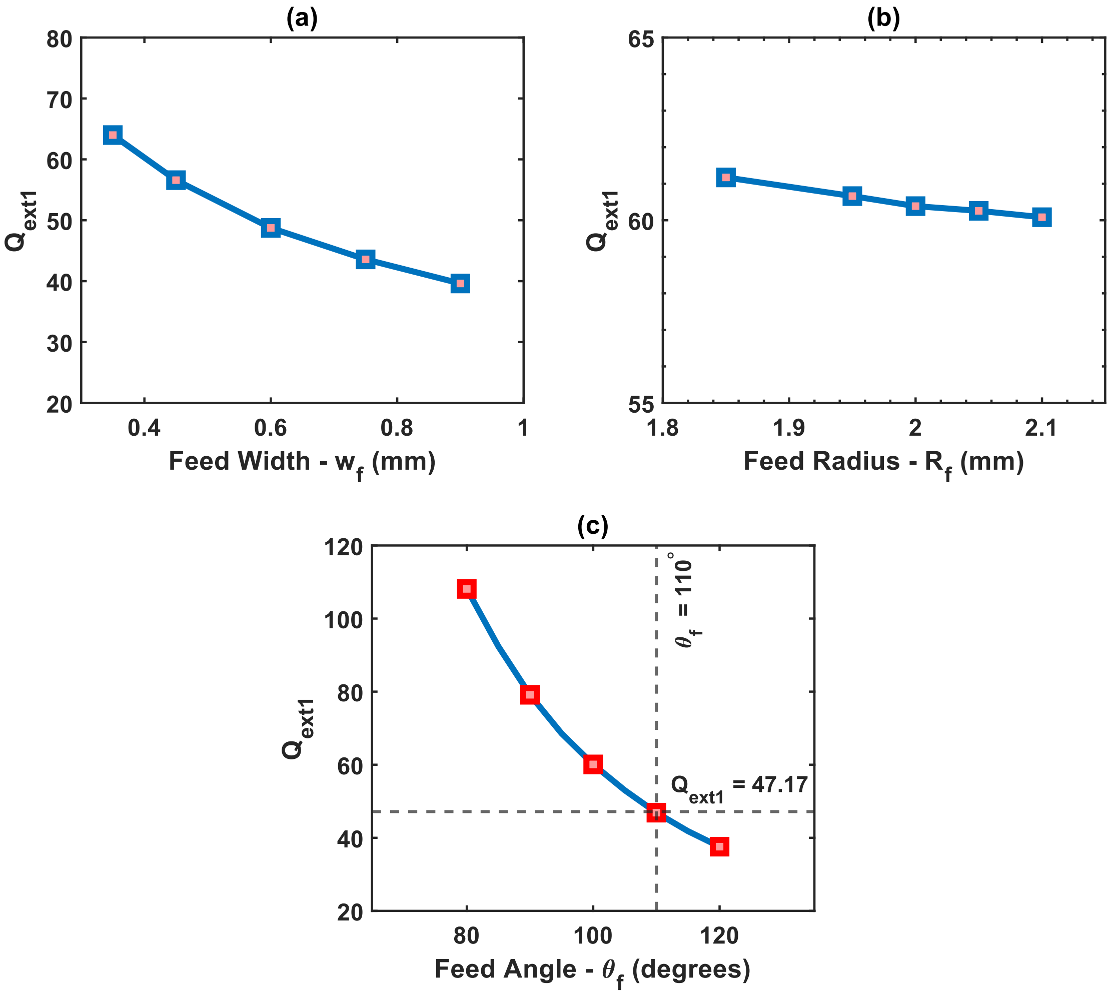

Figure 5.27: External Coupling parametric analysis of GCPW feed (a) Feed width (b) Feed radius, and (c) feed angle.

reference [43], can be applied. One limitation of the method in [43] is its requirement of weak-external coupling structures at both the input and output ports, which may not be compatible with all filtenna geometries. Consider the superstrate-loaded filtenna structure design. Weak coupling at the input can be controlled by reducing coupling from the GCPW feed. However, there is no way to control the external coupling of RF energy at the output port of the radiating slot aperture. Due to these complications, the method proposed in [43] cannot be applied to the current X-band filtenna design.

Instead, HFSS Eigenmode simulations can be used to observe the splitting of poles with

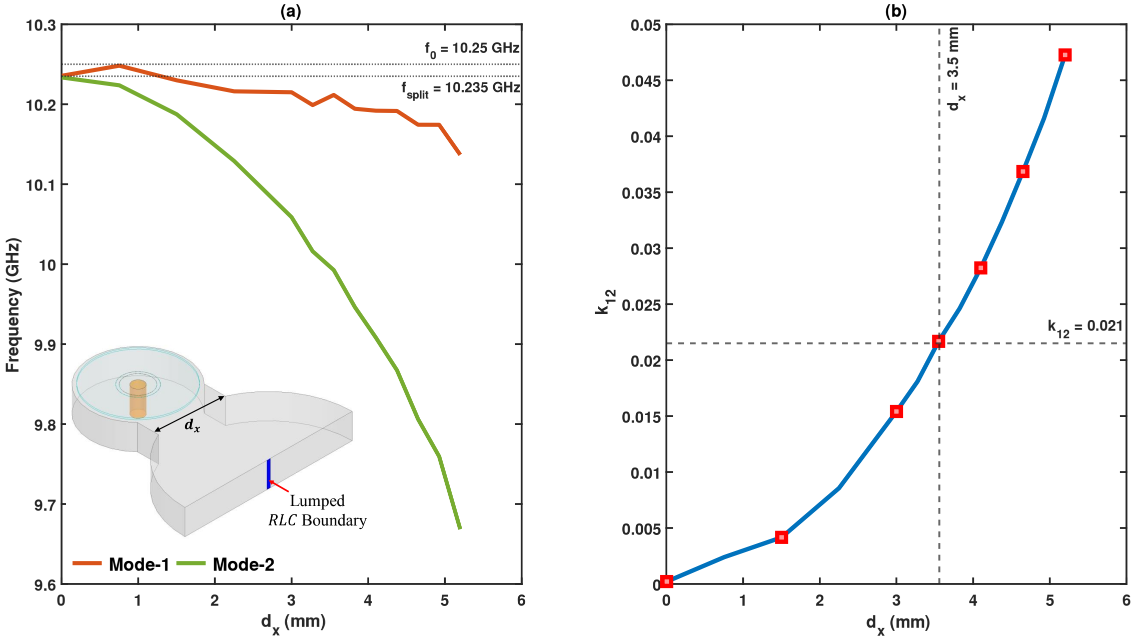

Figure 5.28: Extraction of the coupling coefficient k_{12} as a function of the iris width d_x. An eigenmode simulation was used to observe the splitting of poles between the first and second modes.

no requirement of an input and output feed geometry. The eigenmode solver calculates all the natural resonances in the structure based on the physical dimensions, materials, and assigned boundary conditions. Another benefit of using eigenmode simulation is that the radiation losses from the antenna are not considered. The slot aperture is assigned as a Perfect-H boundary, which forces the field distribution on the aperture to resemble the fields on a slot antenna. However, the antenna does not function as a lossy radiator, and the low unloaded quality factor of the antenna due to radiation losses is not accounted for by the Eigenmode solver. Therefore, the splitting of poles with an increasing inter-resonator coupling can be observed clearly.

With these advantages of using an eigenmode solver, a simplified structure of the iris-coupled resonator and antenna is created, as seen in the inset of Fig. 5.28(a). Note that using the superstrate dielectric in eigenmode simulations can render inaccurate results due to the superstrate being considered a dielectric resonator by the Eigenmode solver. Since the superstrate layer was designed as an additional series capacitive loading structure for the antenna, an equivalent lumped capacitor is used to represent the superstrate's loading effect. A separate eigenmode simulation of the single antenna structure with a lumped capacitor boundary showed that a capacitance value of 0.06 pF was equivalent to the total capacitance seen at the slot aperture with the superstrate layer.

The eigenmode simulation results for extracting the coupling coefficient are plotted in Fig. 5.28(a). Observe that as the iris width is increased, the two resonant modes degenerate, and the frequencies split. The splitting occurs in the same direction due to the iris-coupling mechanism between the two cavities being almost purely magnetic. Note that there is an overall decrease in the resonant frequency of the system from 10.25 GHz to 10.235 GHz, due to the slight volume enlargement of the resonators as the iris width is increased. This effect can be compensated by re-tuning the resonators back to 10.25 GHz, by varying the gap size of the EVA-mode resonator and the varactor load capacitance at the slot aperture. The coupling coefficient k_{12}, as calculated from Eq. (2.6), is plotted as a function of the iris width in Fig. 5.28. The required value of $k_{12} = 0.0212$ corresponds to an equivalent iris-width d_x of 3.5 mm.

5.6.2 Filtenna Time-domain Tuning

Coarse tuning with the parameter extraction method serves as an initial step for the filtenna synthesis. Fine-tuning of different couplings in the structure is accomplished by using the time-domain tuning method discussed in Section 2.2. With the extracted values of the GCPW feed dimensions and iris width, the filtenna model was set up within HFSS modal network. The corresponding time-domain reflection response of the coarse-tuned filtenna is shown in Fig. 5.29. Note that the ideal time-domain response is synthesized from the coupling matrix specified by the given filter specifications. Due to over-coupling from the

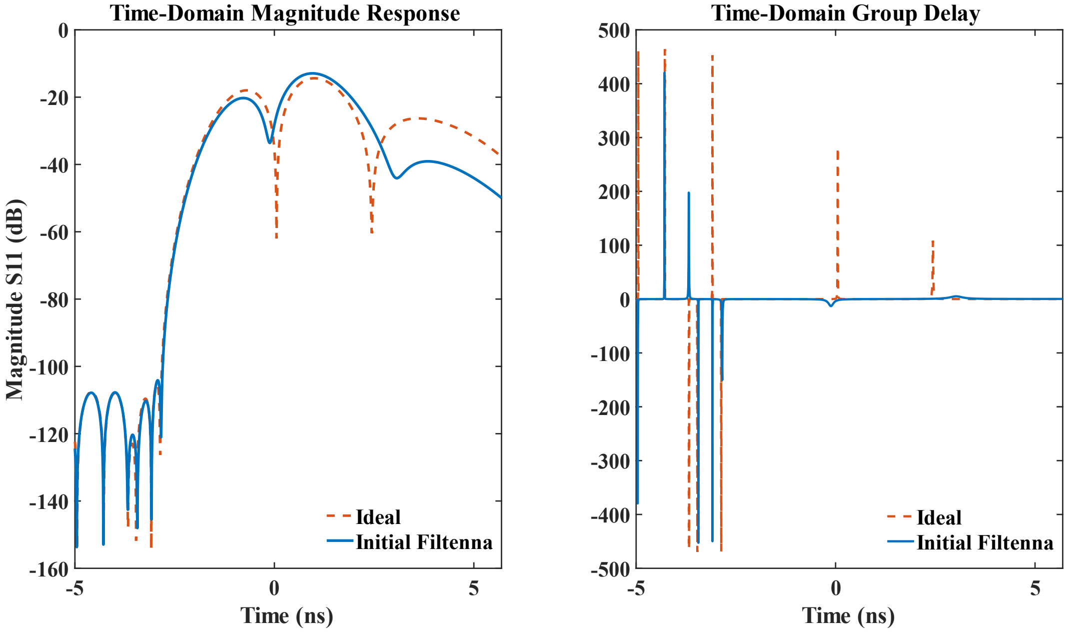

Figure 5.29: Initial Time-Domain Response at 10.25 GHz using parameter extraction method and no time-domain tuning.

external GCPW feed, the first peak is shifted lower in time than the ideal. The opposite effect is observed for the inter-resonator coupling, which is under-coupled and spaced further in time. Also, note that both the resonator and antenna are not tuned accurately to the center frequency of 10.25 GHz. The antenna is tuned to a higher frequency, whereas the resonator is tuned to a lower frequency, as observed from the group delay TD response in Fig. 5.29.

The fine-tuning process using the time-domain method is first started by maximizing the depth of each null by accurately tuning the resonator and antenna to a center frequency of 10.25 GHz. The gap size for the contactless-tuned resonator was increased from 90 μm to 103.5 μm to decrease the capacitive loading and shift the resonant frequency to a higher value. The varactor capacitance was decreased from 0.36 pF to 0.34 pF to tune the antenna at 10.25 GHz. Next, the filtenna's Q_{ext1} value was adjusted by reducing the feed angle from 110° to 97.4° to lower the GCPW feed coupling at the input port. The inter-resonator coupling was matched by increasing the iris width from 3.5 mm to 4.1 mm. The final

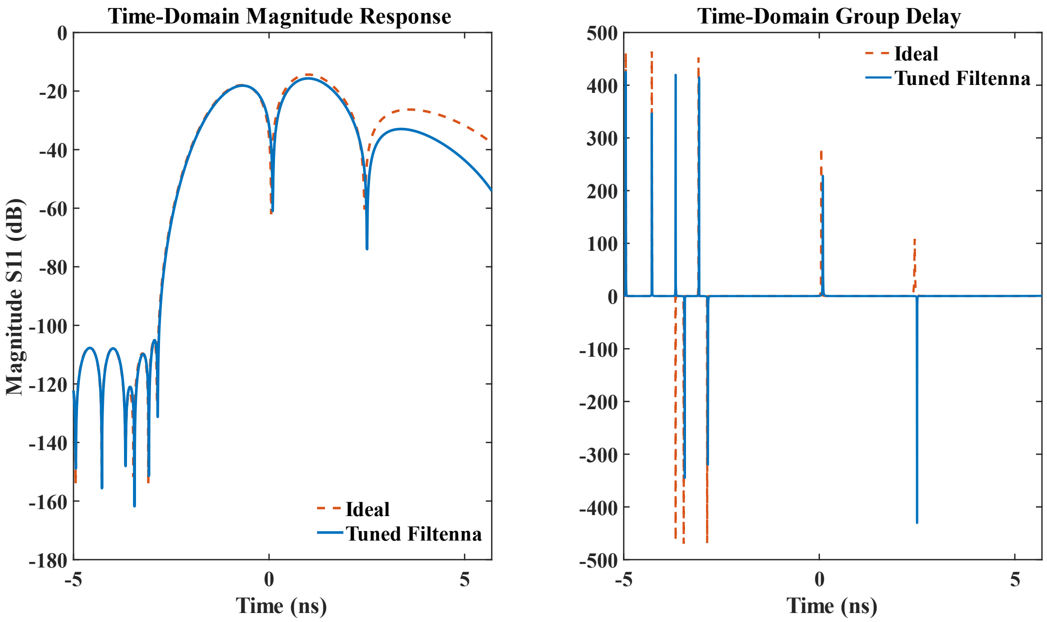

Figure 5.30: Final Time-Domain response at 10.25 GHz after fine-tuning with the TD tuning method

time-domain reflection magnitude response and group delay plots are shown in Fig. 5.30. There is a very good agreement between the ideal and simulated filtenna response in the time domain.

5.6.3 Filtenna Simulation Results

The corresponding S_{11} magnitude response in frequency-domain is plotted in Fig. 5.31. The return loss is about -26 dB at the center frequency of 10.25 GHz. The peak realized gain across frequency shows good in-band radiation performance with a maximum gain of 2.3 dB at 10.25 GHz. The out-of-band rejection of the filtenna is also high due to the integrated filtering functionality.

The main limitation on filtenna's tuning range is imposed by the varactor's available range of capacitances, which ranges from 0.15 pF to 2 pF. The EVA-mode contactless tuned resonator can be tuned across the entire X-band due to the large actuation range of the tuner. The filtenna's tuning range is investigated by varying the load capacitances of the varactor to maximum and minimum values. First, the filtenna was tuned at the minimum varactor capacitance of 0.15 pF, where it operated at a maximum frequency of 10.9 GHz, as seen in Fig. 5.32. When the varactor load capacitance is maximized to 2 pF, the filtenna operates at 9.5 GHz, shown in Fig. 5.33.

Note that both the time-domain responses at maximum and minimum frequency show deviations from the ideal response and do not precisely satisfy the filter specifications. As explained in Section 4.2.3, this is due to the non-tunability of the external input and inter-resonator coupling across frequency. As a result, the bandwidth and return loss vary over the tuning range. At 10.9 GHz, the iris width is electrically longer than the center frequency of 10.25 GHz. Therefore, the resonators demonstrate over-coupling, as seen in the time-domain response of Fig. 5.32. The opposite effect is observed at 9.5 GHz, where

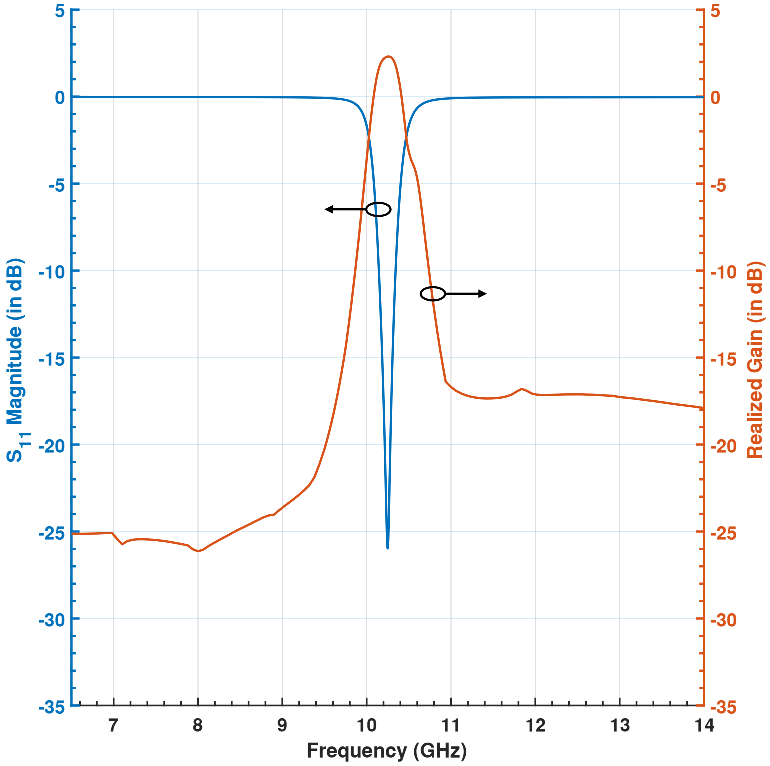

Figure 5.31: $|S_{11}|$ Magnitude response and Realized Gain (dB) for synthesized filtenna at 10.25 GHz. The peak realized gain is 2.34 dB at 10.25 GHz.

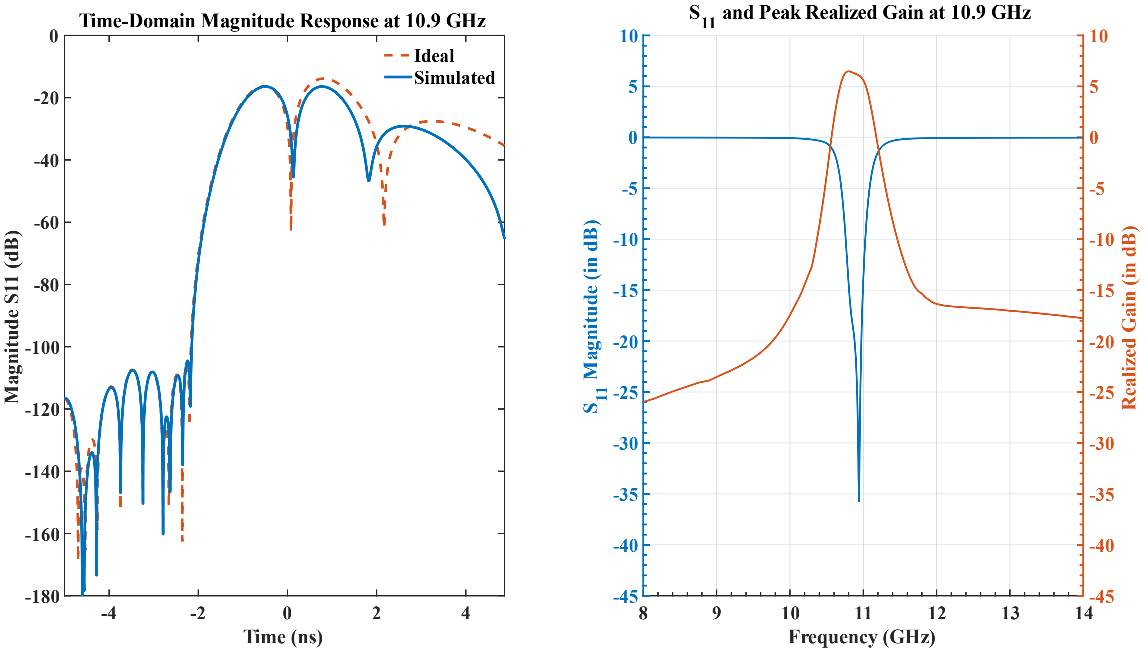

Figure 5.32: Filtenna response at the Forward Tuning Limit - 9.5 GHz. The bandwidth of the filtenna is lower than that of the center frequency of 10.25 GHz due to under-coupling.

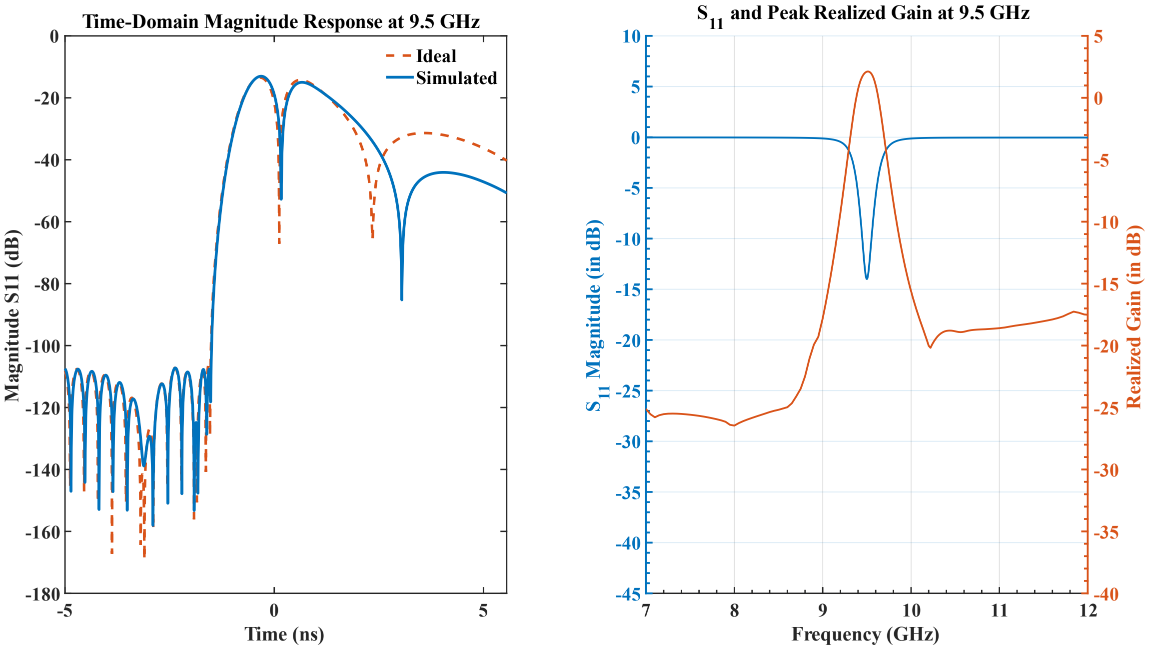

Figure 5.33: Filtenna response at the Reverse Tuning Limit - 10.9 GHz. Filtenna bandwidth is larger than it is at a center frequency of 10.25 GHz due to over-coupling.

the inter-resonator coupling is under-coupled due to the smaller electrical length of the iris.

The realized gain ranges from 2 dB at 9.5 GHz to 5.2 dB at 10.9 GHz. The total efficiency varies from 38% to 75% at maximum and minimum loading, respectively. As will be discussed in Chapter 6, the main cause for the drop in peak realized gain and radiation efficiency is due to the varactor series resistance. Additionally, the antenna is maximally loaded at 9.5 GHz and is electrically much smaller, which results in a smaller realized gain.

Filtenna with Varactor Bias Network

After the synthesis process, the varactor bias network needed for tuning the antenna was added to the tunable filtenna structure. The goal was to investigate the effect of the bias network on the filtenna's RF performance and ensure good isolation between the RF circuitry and DC bias lines. The radial stub bias network, designed in Section 5.5.3, was added to the superstrate layer. The bias network parameters, consisting of the stub sector angle and stub radius, were fine-tuned to ensure minimal disturbance to the RF performance of the filtenna. Simulation results of the S_{11} magnitude response and peak realized gain across frequency with the added bias are plotted in Fig. 5.37 and Fig. 5.38, respectively. The RF Choke network effectively blocks any RF coupling between the filtenna and bias lines across the entire operating range. As seen in Fig. 5.39, the isolation between RF and DC is better than 34 dB across the filtenna tuning range from 9.5 GHz to 10.9 GHz.

The simulated radiation patterns of the varactor-tuned filtenna with the added bias network are plotted in Fig. 5.40. The added bias network does lead to an increased cross-polarization pollution, mainly due to the presence of the radial stubs. However, the filtenna's co-polarized radiation is resilient to any interference from the bias network.

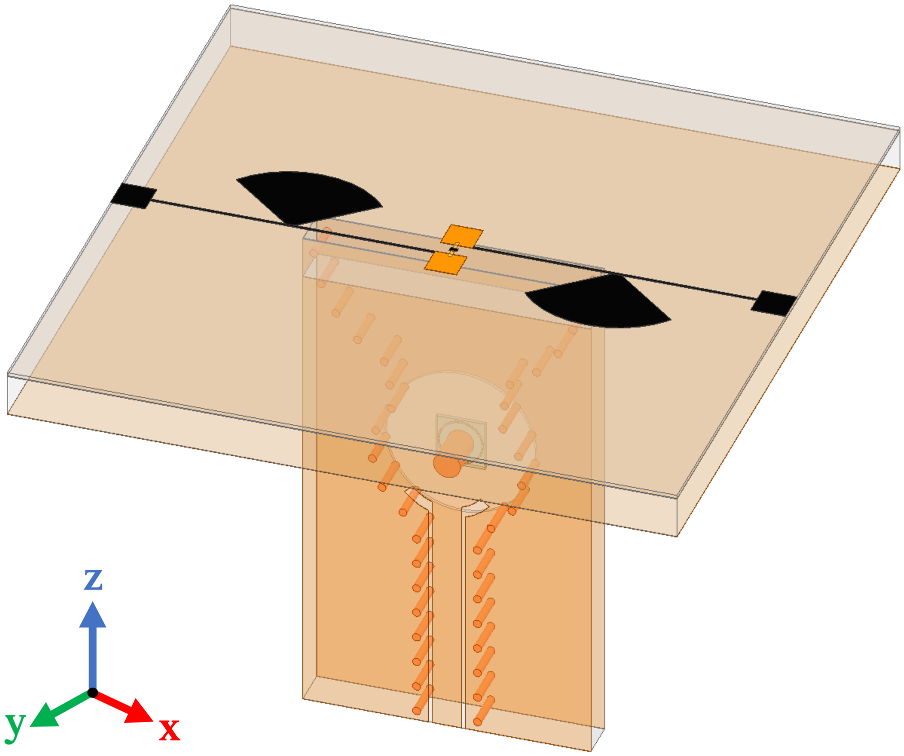

Figure 5.34: 3-D model of the varactor-tuned X-Band filtenna with added radial stub DC-bias network

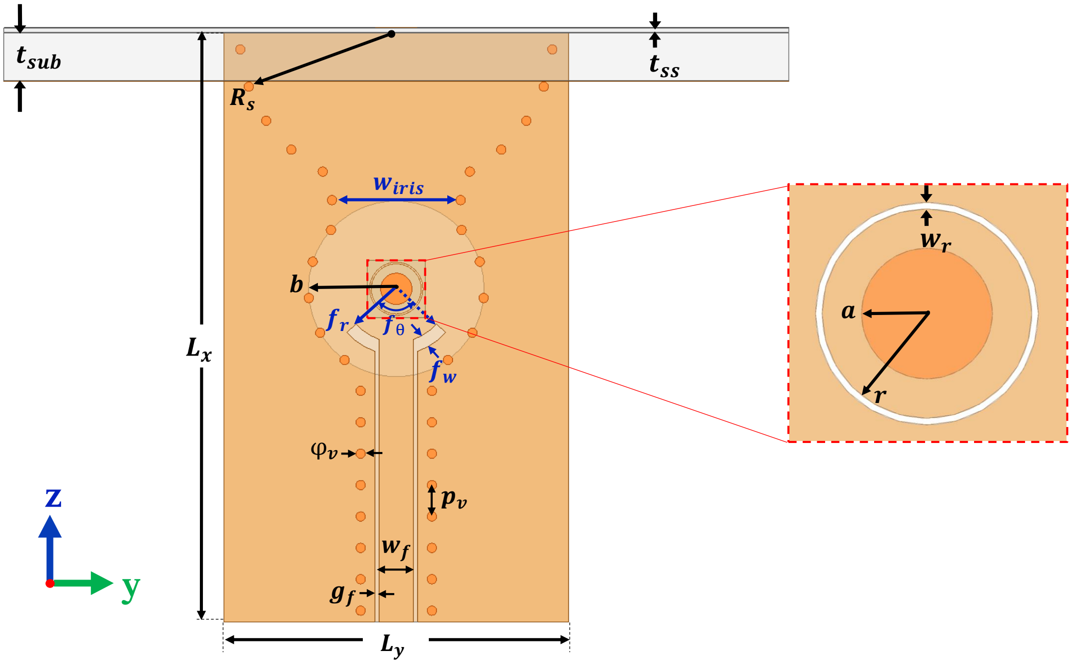

Figure 5.35: Primary design variables of the X-band synthesized filtenna are labeled. The values are listed in Table 5.3

Table 5.3: Design dimensions of superstrate-loaded varactor-tuned filtenna (all dimensions are in mm)

Dimension	Value	Dimension	Value
t_{ss}	0.127	f_w	0.4
s	0.36	g_f	0.13
p_x	1.3	p_v	1
f_θ	97.4°	ϕ_v	0.3
f_r	2.1	w_f	1.11
R_{slot}	5	ϵ_{r2}	2.8
L_x	18.75	t_2	0.0127
L_y	11	G_x	25
t_{sub}	1.534	r	0.8
w_r	0.05	a	0.5

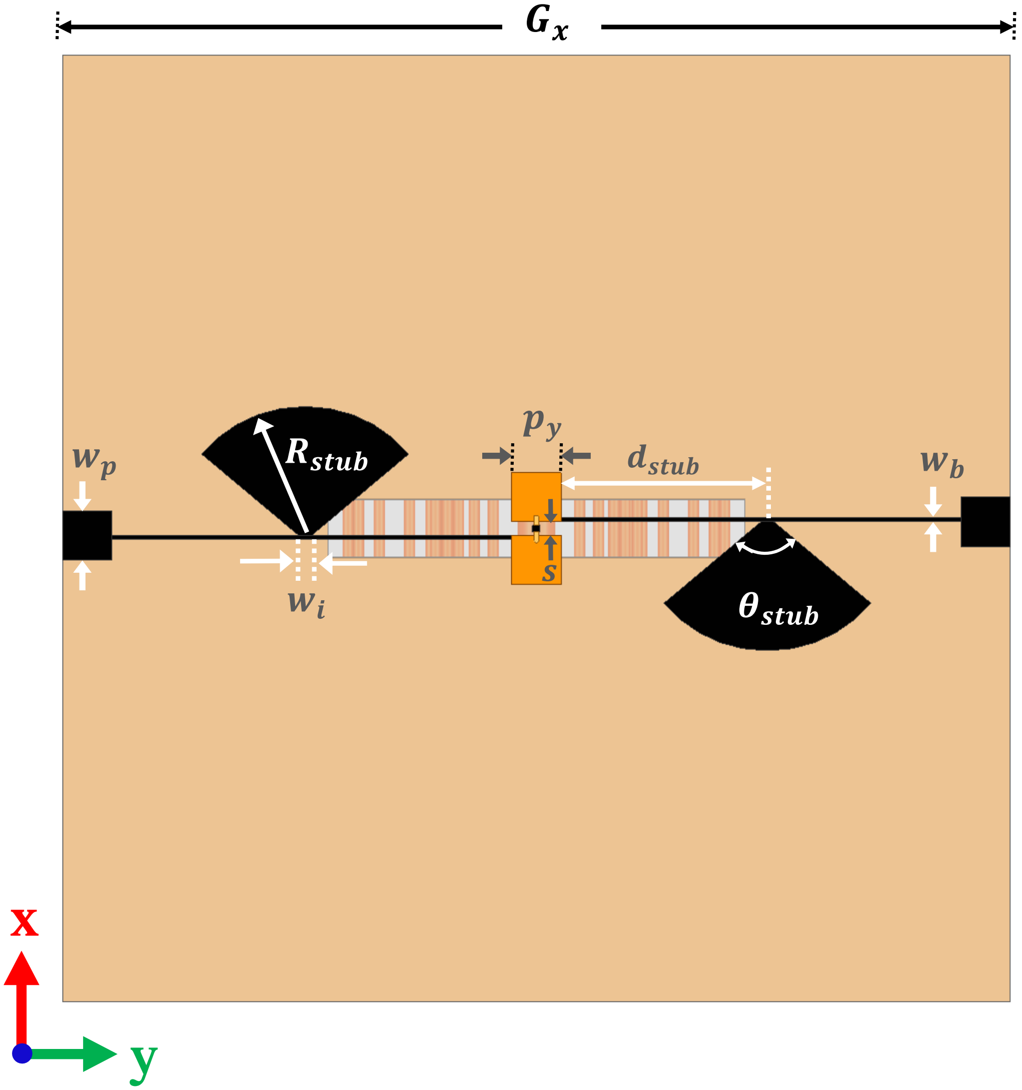

Figure 5.36: Primary dimensions of the radial-stub bias network for the filtenna: $w_p = 1\ mm$, w_b = 100 μm, R_{stub} = 3 mm, $\theta_{stub} = 100°$, d_{stub} = 5.45 mm, w_i = 0.335.

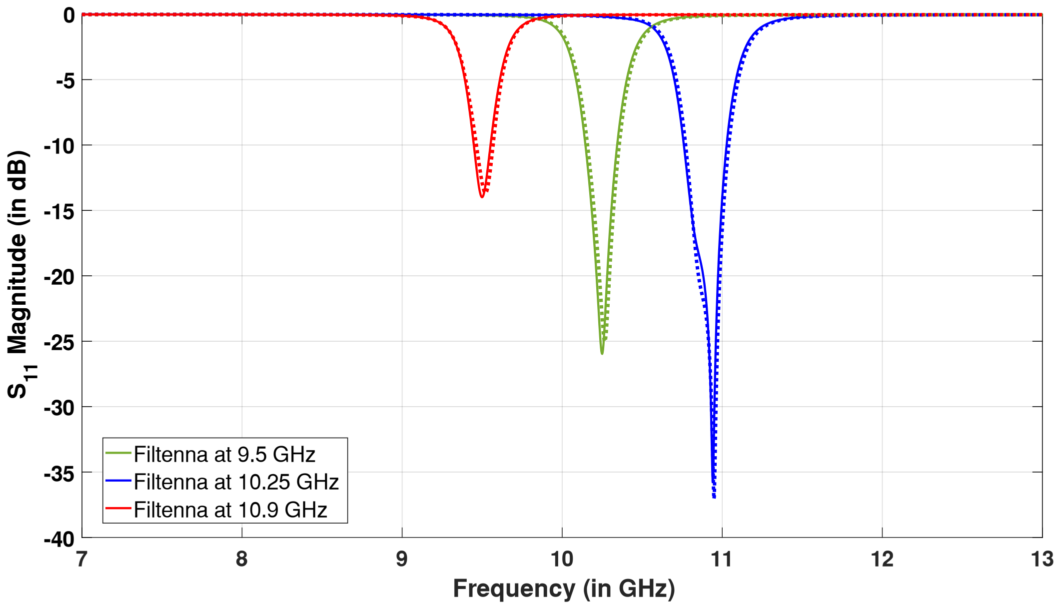

Figure 5.37: Effect of Radial-Stub Network on the S_{11} response across the filtenna tuning range from 9.5 GHz to 10.25 GHz. The solid line corresponds to the filtenna response without bias, and the dotted line is with bias.

Table 5.4: Peak Realized Gain of the varactor-tuned filtenna across tuning range with and without the bias network

Frequency	Without Bias				With Bias			
	$\phi = 90°$		$\phi = 0°$		$\phi = 90°$		$\phi = 0°$	
	Co-Pol	X-Pol	Co-Pol	X-Pol	Co-Pol	X-Pol	Co-Pol	X-Pol
9.5 GHz	1.71 dB	-28.7 dB	1.71 dB	-43 dB	1.7 dB	-21.8 dB	2.1 dB	-23 dB
10.25 GHz	1.96 dB	-24.2 dB	2.3 dB	-40.4 dB	1.86 dB	-24.1 dB	2.25 dB	-34.6 dB
10.9 GHz	6.21 dB	-21 dB	6.21 dB	-24 dB	6.27 dB	-20 dB	6.27 dB	-34 dB

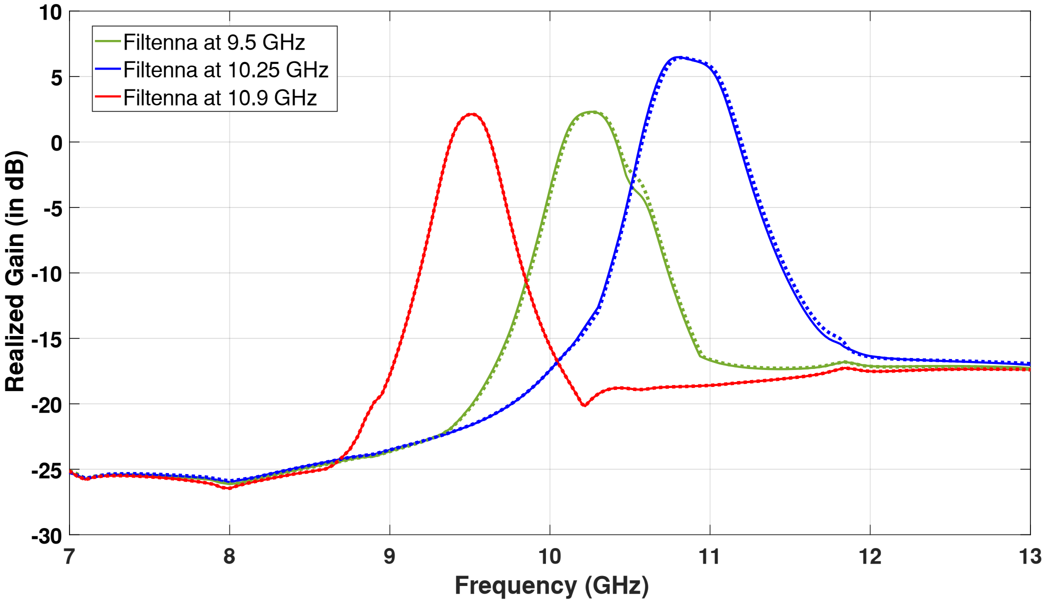

Figure 5.38: Effect of Radial-Stub Network on the realized gain (dB) response across the filtenna tuning range. The solid line corresponds to the filtenna response without bias, and the dotted line is with bias.

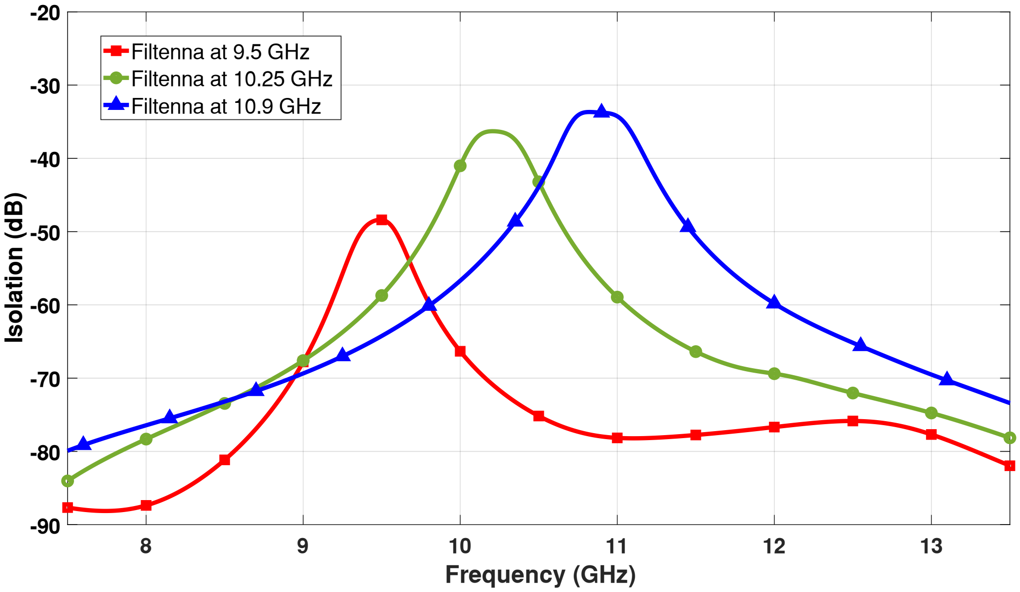

Figure 5.39: RF and DC port isolation of the antenna for the varactor-tuned filtenna. Better than 34 dB of isolation is maintained across the tuning range.

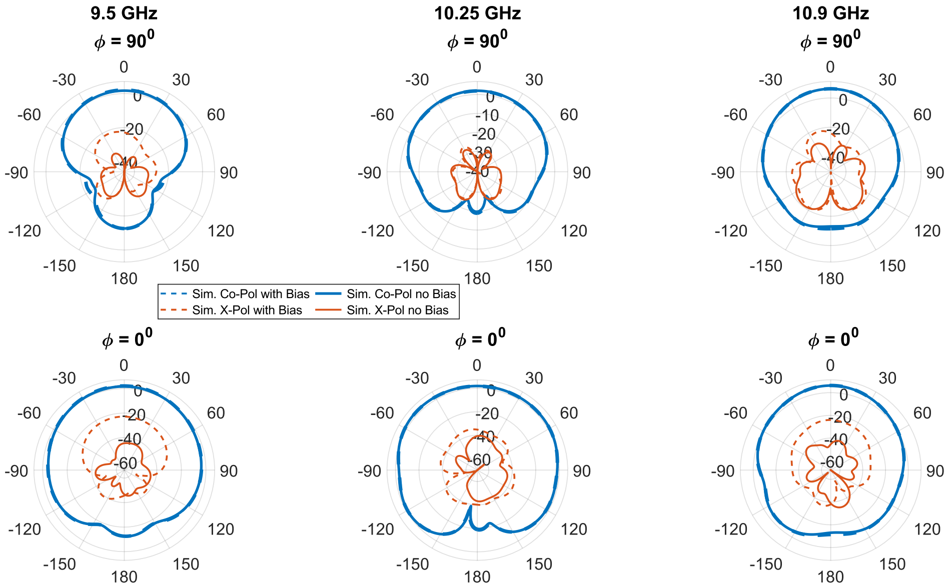

Figure 5.40: Effect of Radial-Stub Network on the radiation patterns across the tuning range. The antenna planes are defined by the coordinate system labeled in Fig. 5.35 and Fig. 5.36. An increased cross-polarization level is observed in the presence of the radial stubs. However, the co-polarized radiation pattern remains undisturbed.

5.7 Conclusion

The theory, concept, and synthesis of a novel frequency-agile filtenna element for X-band applications were presented in this chapter. Based on the performance trade-offs between high-frequency state-of-art tuning technologies, electronic reconfiguration using varactor diodes was used to accommodate frequency reconfiguration in the antenna and filtenna element.

The concept of a SIW-based superstrate-loaded cavity-backed slot antenna was detailed. Two antenna prototypes were designed to demonstrate the trade-off between tuning range and antenna efficiency. The first prototype was designed to cover the whole X-band frequency range, from 8 GHz to 12 GHz, while the second prototype was designed to tune from 9.5 GHz to 11 GHz. A radial-stub bias network was incorporated on the superstrate layer to provide the external bias voltage for the semiconductor varactor diodes. The bias network was carefully designed to ensure good isolation between the antenna's RF energy and the varactor's DC bias lines. Finally, a frequency-agile filtenna was designed using coupled-resonator filter theory. The building blocks comprised the contactless-tuned resonator and the superstrate-loaded varactor-tuned slot antenna. By varying the resonator's capacitive gap and the antenna's varactor capacitance, the filtenna demonstrated frequency tuning from 9.5 GHz to 10.9 GHz.

In the next chapter, Chapter 6, a loss analysis of the filtenna is completed by analyzing the effects of the series resistance introduced by the semiconductor varactor diode. Furthermore, a new varactor loss characterization method is presented for applications at microwave frequencies.

Chapter 6

Practical Limitations of Tuning Varactors

Ideally, a tuning varactor diode is a two-terminal PN junction semiconductor device that functions as a voltage-controlled variable capacitor. However, in practical applications, several non-idealities associated with the diode may reduce the available capacitance tuning ratio and add to the overall losses in the structure. Furthermore, the effect of the varactor's non-idealities is more detrimental when operating at microwave frequencies. This work incorporates a varactor tuning element into an antenna and filtenna for X-band applications, presented in Chapter 5. Varactor diodes are integrated into many reconfigurable designs, including voltage-controlled oscillators, tunable filters, tunable antennas, tunable filtennas, and beam-scanning phased array systems. Given the wide range of applications that use varactors, it is vital to evaluate the effects of varactor's non-idealities to ensure optimal system performance at microwave frequencies.

The goal of this chapter is to summarize, characterize and analyze the practical limitations of tuning varactor when used at higher microwave frequencies. The first section discusses the fundamentals of the semiconductor PN junction operation of the varactor diode. The next section outlines the modeling of varactors at microwave frequencies using a lumped element equivalent circuit. Several non-idealities, including parasitic reactance and loss resistances, are accounted for in the equivalent circuit model. In the last section, a method is presented to estimate the quality factor of a tuning varactor at microwave frequencies.

6.1 Semiconductor PN junction operation

The structural overview of a semiconductor varactor diode is shown in Fig. 6.1. The die consists of a heavily-doped P-type material, a lightly-doped N-type material, and a heavily-doped N+ layer at the bottom. The P-layer consists of acceptor atoms (electron holes), resulting in a net negative charge, whereas the N-type material provides donor atoms with a net positive charge. The additional N+ layer functions as a mechanically robust platform onto which the other layers are deposited. In the adjoining region separating the N and P layers, excess electrons recombine with the holes in the P-layer, forming a volume devoid of free carriers. This region is known as the ”depletion region,” forming at the PN junction. The portion of P and N layers separated from the depletion region can be considered conductors, while the depletion region forms a nearly perfect dielectric.

Therefore the PN junction meets the definition of a capacitor, with the capacitance of

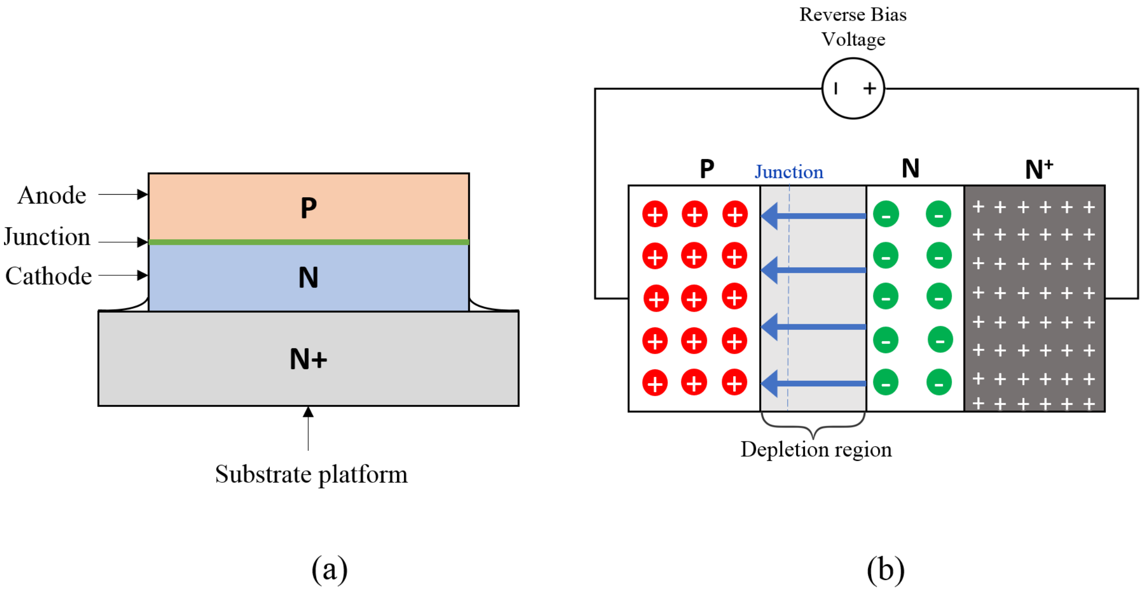

Figure 6.1: (a) Semiconductor layers of a varactor diode (b) Junction capacitance and depletion region development in the presence of an external-reverse bias voltage.

the diode, C_V, expressed as:

$$C_V = \frac{\epsilon A}{d} \tag{6.1}$$

where A is the area of the cross-section area of the semiconductor contacts, ϵ is the permittivity of the semiconductor material, and d is the width of the depletion region. The diode's physical design and material type sets the area A and permittivity ϵ. Thus, tunability of the junction capacitance is achieved by varying the width of the depletion region. This is accomplished by applying an external reverse bias voltage (negative terminal of source connected to P layer) across the diode terminals. The width of the depletion layer is directly proportional to the magnitude of applied reverse-bias voltage. The varactor junction capacitance, $C_j(V_R)$,as a function of the applied reverse-bias voltage magnitude, V_R, can be well-described by the following equation [85],

$$C_j(V_R) = \frac{C_j(V_R = 0)}{(1 - \frac{V_j}{\psi_0})} \tag{6.2}$$

where ψ_0 is the built-in voltage of the semiconductor at no bias, $C_j(V_R = 0)$, is the junction capacitance at 0 V bias, and m is the slope exponent whose value is determined by the specific doping profile of the varactor.

The doping structure introduced within the semiconductor can be controlled to provide a specific range of capacitance values and capacitance-tuning ratio. Based on the doping profile, varactors can be categorized as linear, abrupt, and hyper-abrupt. Linear (m = 1/3) and abrupt (m = 0.5) doping profiles are formed when the doping concentration of the cathode N-layer remains nominally constant with respect to the PN junction depth. As a result, the achievable capacitance-change ratio is limited. For hyper-abrupt varactors (m $\geq$ 0.5), the carrier concentration in the N-layer rapidly reduces with increasing distance from the junction, allowing the edge of the depletion layer to sweep through its thickness much more rapidly [86]. Therefore, a hyper-abrupt varactor can achieve a significantly

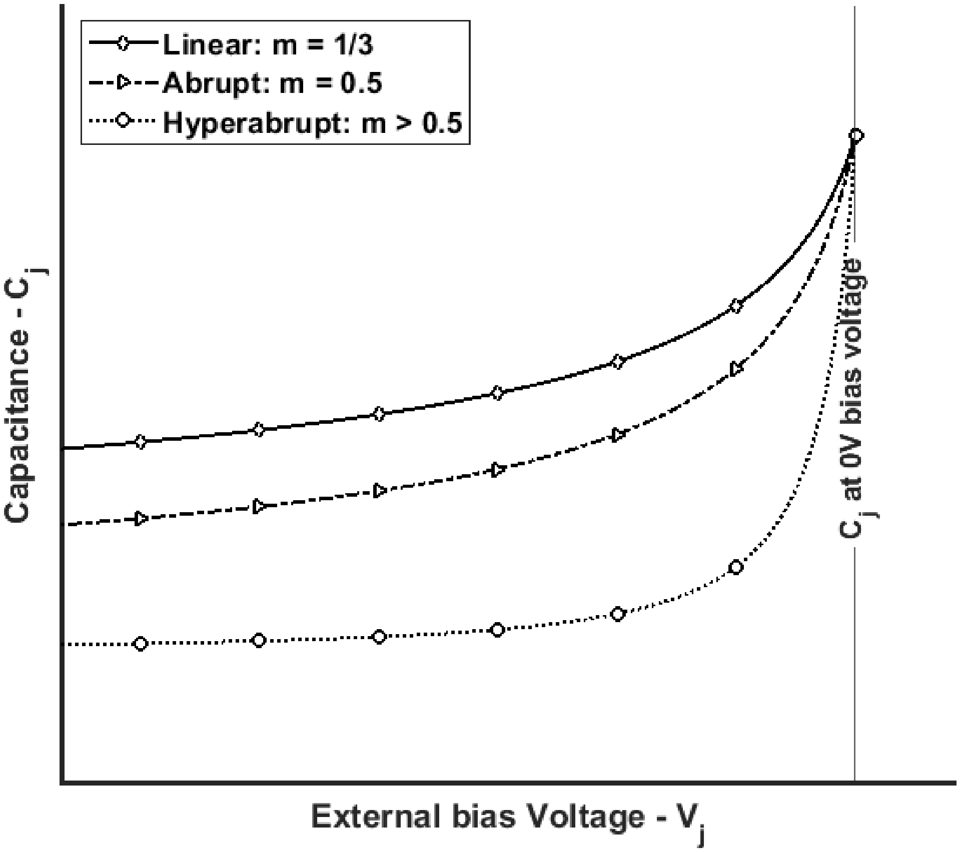

Figure 6.2: Effect of doping profile on a varactor's capacitance tuning sensitivity. A hyper-abrupt doping profile yields the maximum capacitive tuning ratio and much smaller values of capacitances.

larger capacitance change ratio as compared to abrupt varactor diodes. The plot in Fig. 6.2 illustrates the effect of different doping profiles on the capacitance-voltage curve. In addition to a larger capacitance ratio, a hyper-abrupt profile can also provide much smaller capacitance values than abrupt varactors.

6.2 Lumped Element Model of a Varactor Diode

6.2.1 Series Equivalent Resistance

A varactor diode's ideal lumped element model representation is just that of a variable capacitor. However, the die itself has loss resistances associated with the concentration of charge carriers in the constituent semiconductor layers, as seen in Fig. 6.1. The combined junction resistance, R_j, is the sum of resistances R_N, R_P and R_{N+} layer corresponding to the N, P, and N+ layers of the semiconductor die [86].

It is important to note that the value of R_j varies as a function of applied reverse-bias voltage. Due to the heavy-doping of P and N+ regions, R_P and R_N+ remain virtually constant with applied voltage. However, the resistance of the N-layer is inversely proportional to the magnitude of reverse-bias voltage [86]. The depletion layer is thinnest at a very low reverse bias, resulting in increased conductive path length around the junction. Therefore, at the lowest bias voltage and correspondingly maximum junction capacitance, the value of

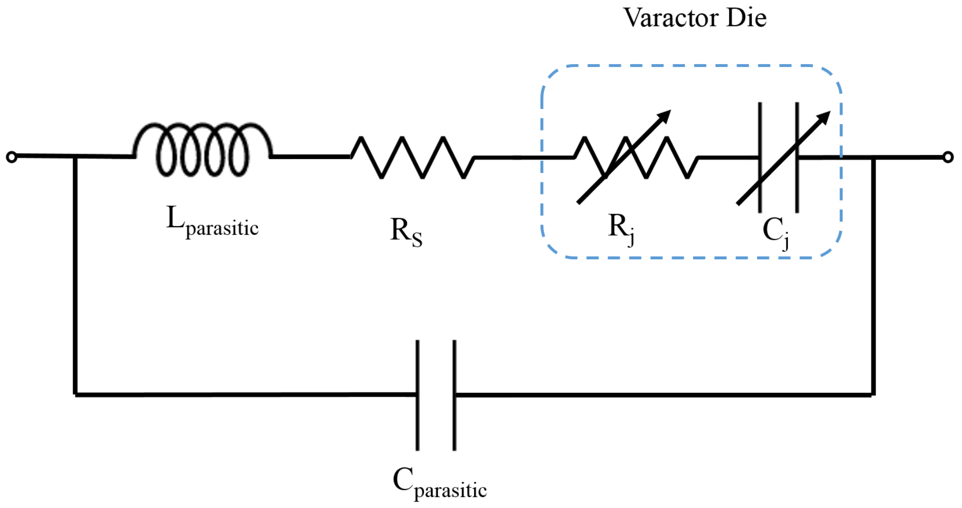

Figure 6.3: Lumped element equivalent model of a varactor diode, when modeled at microwave frequencies. Additional series resistance and parasitic reactances exist with the varactor's intrinsic junction capacitance.

R_N is the highest.

The losses explained above were associated only with the naked die. When the varactor die is attached to the rest of the RF circuitry, additional contact resistances, R_S, exist in series with the intrinsic semiconductor resistances. Therefore, the total impedance of the varactor, Z_T is given as [86],

$$Z_T(V_R) = (R_{N+} + R_P + R_N(V_R)) + R_S - \frac{j}{2\pi f C_j(V_R)} = R_T(V_R) - jX_{Cj}(V_R) \quad (6.3)$$

In Eq.(6.3), R_T is the total voltage-dependent series resistance, and f is the frequency of operation. X_{Cj} is the capacitive reactance of the depletion region.

6.2.2 Parasitic Reactance

Commercially available varactor diodes usually contain packaging to protect the bare die from physical damage and facilitate an easier connection with the rest of the circuit. The packaging results in unwanted parasitic reactance that can be detrimental to the performance

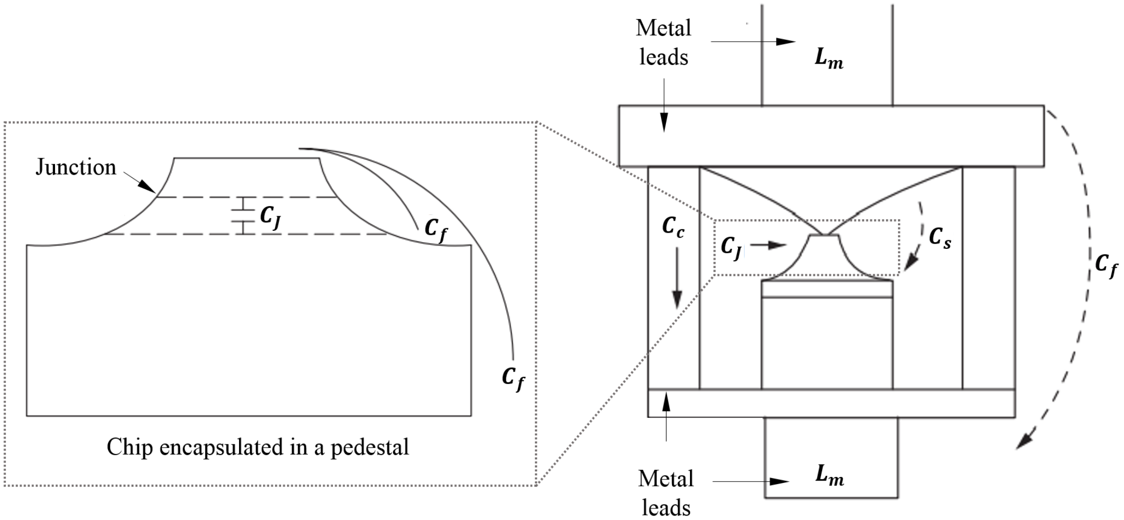

Figure 6.4: Parasitic reactances due to the packaging effects of a varactor diode. An equivalent parallel capacitance and series inductance exists with the varactor's intrinsic junction capacitance.

of the varactor, specifically on the capacitance tuning ratio. Consider the model of a varactor chip mounted in a typical metal-ceramic package, as seen in Fig. 6.4. The chip rests on a metal pedestal, with bonding straps connecting to the top of the chip. The die is encapsulated in a ceramic envelope, with metal pieces attached to seal the package and also to provide mounting prongs to attach to the rest of the circuitry. The resulting parasitic impedances and their effect on the varactor's electrical performance are summarized as follows:

1. Parasitic Capacitance - $C_{parasitic}$

   As seen in Fig. 6.4, there are several stray capacitances associated with packaged die. A capacitance C_s is formed between the top straps and the base, whereas C_c represents the capacitance within the ceramic envelope. Additionally, there are more fringing capacitances C_f from the top of the package to the bottom and the surrounding region. These capacitances can be together lumped into a single parasitic capacitance value, $C_{parasitic}$, which is in parallel with the varactor's junction capacitance, given as [86],

   $$C_j(V_R) = \frac{C_j(V_R = 0)}{(1 - \frac{V_j}{\psi_0})} + C_{parasitic} \tag{6.4}$$

   The main effect of $C_{parasitic}$ is the reduction of the overall capacitance ratio available from the diode compared to that of the bare varactor die. It should also be noted that the reduction of the available capacitance ratio is more severe for very small values of junction capacitance and is negligible for larger values of capacitance.

2. Parasitic Inductance - $L_{parasitic}$

   Metal leads are required to provide mounting prongs for the die to be attached to the rest of the circuit. These result in a parasitic inductance, $L_{parasitic}$, which exists in series with the varactor's junction capacitance. As a result, the self-resonant frequency f_{sf} of the varactor is lowered due to the formation of series and parallel resonances, given as

$$f_{sf} = \frac{1}{2\pi\sqrt{C_{j(max)}\, L_{parasitic}}} \tag{6.5}$$

where $C_{j(max)}$ is the maximum junction capacitance. The parasitic inductance value places an upper limit on the diode's operational frequency. Based on the range of the varactor's capacitance values and packaging inductance, a circuit designer must ensure that the self-resonant frequency is above the diode's intended frequency range of operation.

6.3 Varactor Quality Factor

The quality factor, Q, is often used as a figure of merit to express the ideality of a reactive component. For a varactor, the quality factor is defined as the ratio of energy stored in the junction's capacitive reactance to that dissipated in the loss resistance. Based on the lumped element model in Fig. 6.3, the varactor quality factor can be expressed as [86],

$$Q = \frac{\Im m\left(Z_T(V_R)\right)}{\Re e\left(Z_T(V_R)\right)} = \frac{1}{(2\pi f)\, C_j(V_R)\, R_T(V_R)} \tag{6.6}$$

where $R_T = R_S + R_j$ is the total voltage-dependent series resistance. It is important to note that the varactor Q is also a function of the operating frequency. Most manufacturers specify the Q at one frequency, typically 50 MHz. To determine the Q at another frequency, Eq. (6.12) can be used to get [86],

$$Q(f) = \frac{(Q_{specified})\,(f_{specified})}{f} \tag{6.7}$$

The varactor Q calculated Eq.(6.7) should be considered the maximum attainable Q. In practice, the actual quality factor is generally lower than predicted by the above equation.

6.4 Effect of varactor non-idealities on Antenna Performance

The superstrate-loaded cavity-backed slot antenna, introduced in Chapter 5, uses a varactor as the tuning element to change the overall capacitive loading at the slot aperture. Based on the non-idealities of tuning varactors discussed in the above sections, it is evident that the varactor diode's practical limitations may significantly affect the antenna's performance, specifically in terms of the achievable tuning range and radiation performance. Additionally, the antenna operates at a relatively higher frequency in the X-band, resulting in a more detrimental effect that needs to be accurately investigated and accounted for. Several design decisions were taken to mitigate these issues, which are summarized in the following sections.

6.4.1 Antenna Tuning Range

The main limitation of the antenna's achievable tuning range is the presence of package parasitics. For the antenna to tune across X-band, the required junction capacitance range is from 0.15 pF to 2 pF. To ensure that the self-resonant frequency of the varactor is above the X-band frequency range, the maximum allowable parasitic inductance is calculated to be 0.08 nH using Eq. (6.5), with $C_{j(max)}$ = 2 pF. In the most widely used commercially available packages like SOT-23, SC-79, SOD-882, etc., the minimum series inductance is at least 0.4 nH. Furthermore, the lowest parasitic capacitances of these packages are more than 0.1 pF, which is almost comparable to the minimum junction capacitance (0.15 pF) required by the superstrate-loaded antenna to tune at 12 GHz. Therefore, a varactor with minimal package parasitics is required to ensure proper operation of the antenna in the X band frequency range.

Beam-lead diodes are particularly suited for applications where low parasitic reactance and small size are prime requirements. This is the case for many varactor-tuned applications

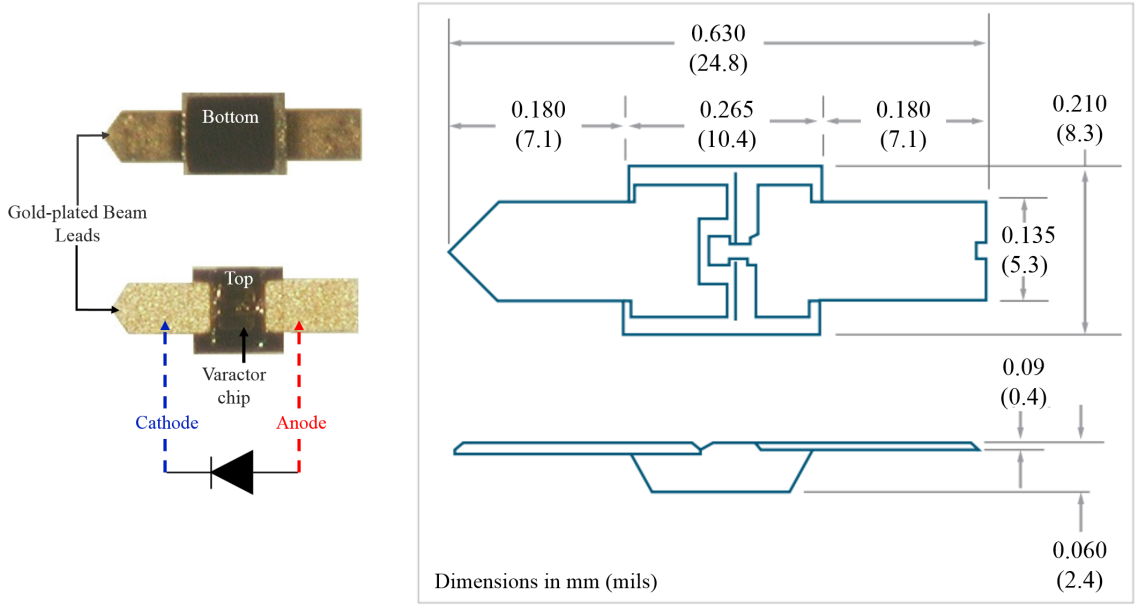

Figure 6.5: Beam lead varactor diode layout with the typical dimensions of commercially available chips. The beam-lead topology is well-suited for varactor applications with minimal parasitic reactances.

at higher microwave frequencies. Depending on the exact case style, lower than 0.05 nH of parasitic inductance and less than 0.07 pF of a parallel parasitic capacitance can be achieved. The layout of a typical beam lead-diode is shown in Fig. 6.5. It consists of the main chip (silicon or Gallium Arsenide), with co-planar gold-plated tabs or ”beams” protruding 6 to 9 mils beyond the edge of the chip. Beam lead diodes are generally the smallest chips available in the diode family, facilitating easier integration in high-frequency applications where space is a limiting factor. Based on the required range of tuning capacitance, beam-lead Gallium Arsenide varactor from MACOM technology MA46580 (0.15 - 2 pF) was selected for the superstrate-loaded antenna and filtenna in this work. A large capacitance ratio is achieved due to the diode’s hyper-abrupt doping profile, which enables the antenna to tune across a wide tuning range.

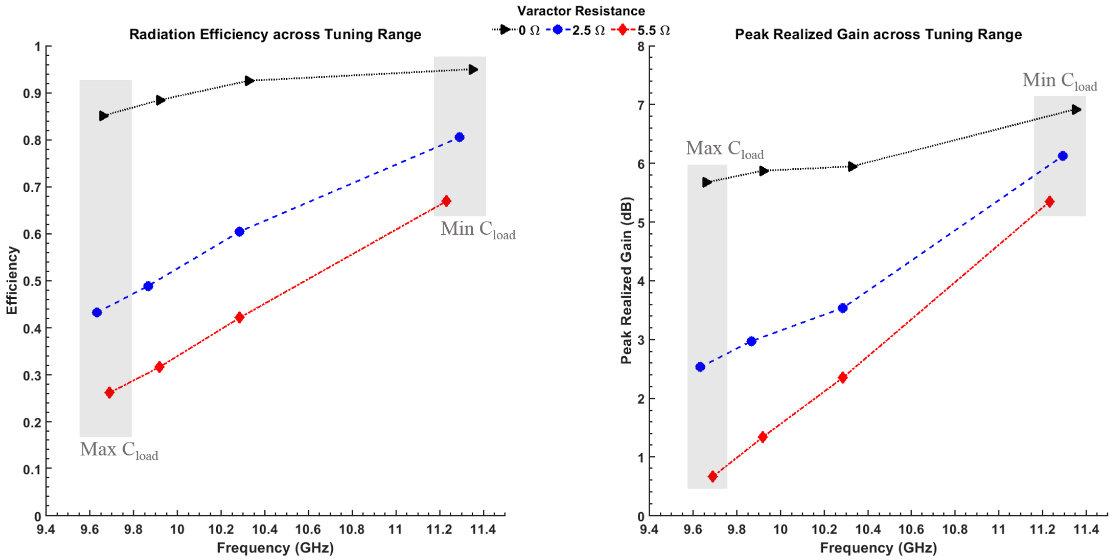

Figure 6.6: Effect of varactor's equivalent series resistance on radiation efficiency and realized gain of the superstrate-loaded antenna design (Prototype-2)

6.4.2 Radiation Performance

The effect of series resistance in the varactor lumped element model of Fig. 6.3 is to have additional losses and consequently lower the varactor's quality factor. In terms of an antenna's performance, the efficiency and realized gain show significant degradation with increasing R_T. This is evident in the simulated efficiency and peak realized gain plots of the superstrate-loaded antenna across its tuning range, as seen in Fig. 6.6. As the value of R_T increases from 0 Ω to 5.5 Ω, the maximum radiation efficiency degrades from 95 % to 67 % at the minimum load capacitance. Also note that the degradation of the antenna's efficiency and realized gain is more severe at maximum loading capacitance, where the antenna operates at the lower end of the frequency tuning range. At the highest loading, the antenna's electrical size is much smaller, and the combined effects of miniaturization and varactor losses cause a dramatic decrease in the antenna's radiation performance.

Determining the exact behavior of loss resistance value or varactor Q across a given range of frequencies and capacitance values is very challenging. Manufacturers usually specify the varactor's Q at a much lower frequency of 50 MHz and at an arbitrary reverse-bias voltage (typically 4V). As noted earlier, the series resistance is a function of the applied reverse bias voltage. However, most data sheets do not contain the range of resistance values as a function of junction capacitance. An underlying assumption made in Eq.(6.7) to determine the varactor Q is that the only frequency-dependent quantity is the junction's capacitive reactance. This is a faulty assumption because, at microwave frequencies, additional losses (due to skin effect, etc.) significantly lower the varactor's quality factor. The resulting inaccuracies in estimating varactor quality factors can cause overly optimistic design and misleading results in practice. To guarantee an acceptable RF performance of the manufactured design, the losses contributed by the varactor must be accurately characterized.

6.5 Estimation of Varactor Q at Microwave Frequencies

Some methods to extract a varactor's quality factor have been investigated in the existing literature. In earlier research works for diode characterization, for instance, in [87] and [88], varactors are characterized using resonant structures in a reduced-height waveguide and coaxial line measurement systems. However, these setups are space-consuming, complex, and incompatible with the present-day chip varactor topologies. Furthermore, the measurement setup is significantly different from the actual mount environment of the varactor in a practical tuning application.

As noted in [89], a straight-forward method of extracting a varactor's quality factor is to mount it at the end of a 50 Ω transmission line, measure S-parameters using a network analyzer and extract the impedance of the diode. However, this method requires precise calibration at the reference plane where the diode is mounted. This method can also lead to significant errors in the value of the varactor's resistance since the S_{11} curve is very close to the edge of the Smith Chart.

Alternate methods are described in [89], [90], and [91], where electromagnetic simulation software with a built-in optimizer is used to minimize the errors between the varactor's SPICE model and measured data. These procedures depend on standard calibration techniques to negate the effect of test fixtures. A disadvantage of these optimization-based methods is that they do not capture the varactor's intrinsic bias-dependent junction resistance. In addition, the process is time-consuming as several iterations of optimization are needed to match the simulated model with measured data. Furthermore, the data's accuracy also depends on the calibration precision at the reference plane where the diode is mounted.

As an alternative, a simplified method to estimate the varactor's Q without any calibration, de-embedding, or complex setup is presented in this paper. A varactor is integrated into a tunable microstrip combline resonator, with weak external coupling at the input and output ports to allow for the resonator's unloaded Q extraction. The varactor's Q is determined by replacing the varactor with an equivalent high-Q capacitor. As a proof-of-concept, the theoretical method is validated through simulations, with varactor capacitances ranging from 1.4-2.4 pF over a frequency range of 8.2 GHz to 8.5 GHz. The proposed method can be applied for different values of varactor capacitances and at higher microwave frequencies.

6.5.1 Proposed Method for Varactor-Q Extraction

The proposed technique is based on extracting a microwave resonator's unloaded quality factor, Q_u, using two-port S-Parameter measurements. The total loaded quality factor of the measured system Q_L, is related to the unloaded Q, Q_u, and the external quality factor, Q_e, as [92],

$$\frac{1}{Q_L} = \frac{1}{Q_e} + \frac{1}{Q_u} \tag{6.8}$$

Lowering the external coupling increases the value of Q_e, and the measured Q_L approaches the value of Q_u. The loaded quality factor is determined from the 3 dB bandwidth of the transmission response,

$$Q_L = \frac{f_0}{\Delta f_{3dB}} \tag{6.9}$$

where f_0 is the resonant frequency and Δf_{3dB} is the half-power bandwidth of the resonator (where the transmission response is 3 dB lower than at resonance)[92]. An accurate extraction of Q_u can be made from the peak value of the transmission response magnitude, $|S_{21}|$, at resonance, through the relation

$$Q_u = \frac{Q_L}{1 - |S_{21}|}. \tag{6.10}$$

The total Q_u of the varactor-tuned resonator consists of the resonator's quality factor Q_{res} and the varactor's quality factor Q_{var}. The value of Q_{res} represents the conduction, dielectric, and radiation losses. The resonator's losses can be isolated from the varactor loss by replacing the varactor with a high-Q capacitor. With the extracted values of Q_u and Q_{res}, the varactor Q can be determined using,

$$\frac{1}{Q_{var}} = \frac{1}{Q_u} - \frac{1}{Q_{res}} \tag{6.11}$$

The equivalent series resistance value R_T can be determined from Q_{var} using [86],

$$R_T(V_R) = \frac{1}{(2\pi f_0)\, C_j(V_R)\, Q_{var}(V_R)} \tag{6.12}$$

where V_R is the reverse-bias voltage needed to realize a junction capacitance C_j.

6.5.2 Resonator Design

A varactor-tuned microstrip combline resonator was chosen to validate the proposed technique due to its compatibility with a capacitive tuning element. As seen in Fig. 6.7(b), the varactor is loaded at the one end of the stub resonator, with the anode terminated to the ground through a via hole. For the varactor-tuned resonator, a quarter wavelength line is added instead of the typically short-circuited cathode end of the varactor. The quarter wavelength transforms the open-circuit end to a short-circuit at the stub resonator's end. The resonator's characteristic impedance Z_R, electrical length θ_0, and the load capacitance C_L determine the resonant frequency. Input and output couplings are realized using 50 Ω microstrip lines, short-circuited at one end.

The combline topology was chosen for its feasibility of replacing the capacitor with a tuning varactor diode. The resonator is implemented on a 30 mil thick Rogers 3003 substrate ($\epsilon_r = 3$) substrate. All the primary design variables and dimensions are shown in Fig. 6.7. The varactor is loaded at the one end of the stub resonator, with the anode terminated to the ground through a via hole. The DC biasing is implemented using a radial-stub RF choke. Based on the manufacturing feasibility, the bias line width is designed to be 100 μm. Weak external coupling to the input and output ports is achieved by increasing the feed-gap distance x_0.

6.5.3 Simulation Validation

The simulated transmission (S_{21}) magnitude response of the designed resonator is shown in Fig. 6.8. The resonator can be tuned from 8.2 GHz to 8.5 GHz for a capacitance junction variation of 2.4 pF to 1.4 pF, respectively. A junction resistance of 1 Ω and 2 Ω was added to the ideal varactor capacitance in simulation. By comparison with a high-Q capacitor ($R_T \approx 0$ Ω), the varactor Q was extracted for different values of junction capacitance using the proposed technique.

As seen in Fig. 6.9, the extracted Q_{var} closely follows the theoretical values, which are calculated using Eq. 6.12 across the tuning range. Therefore, the presented method can be used to experimentally estimate the Q-factor of practical tuning varactors for reconfigurable antenna applications at microwave frequencies.

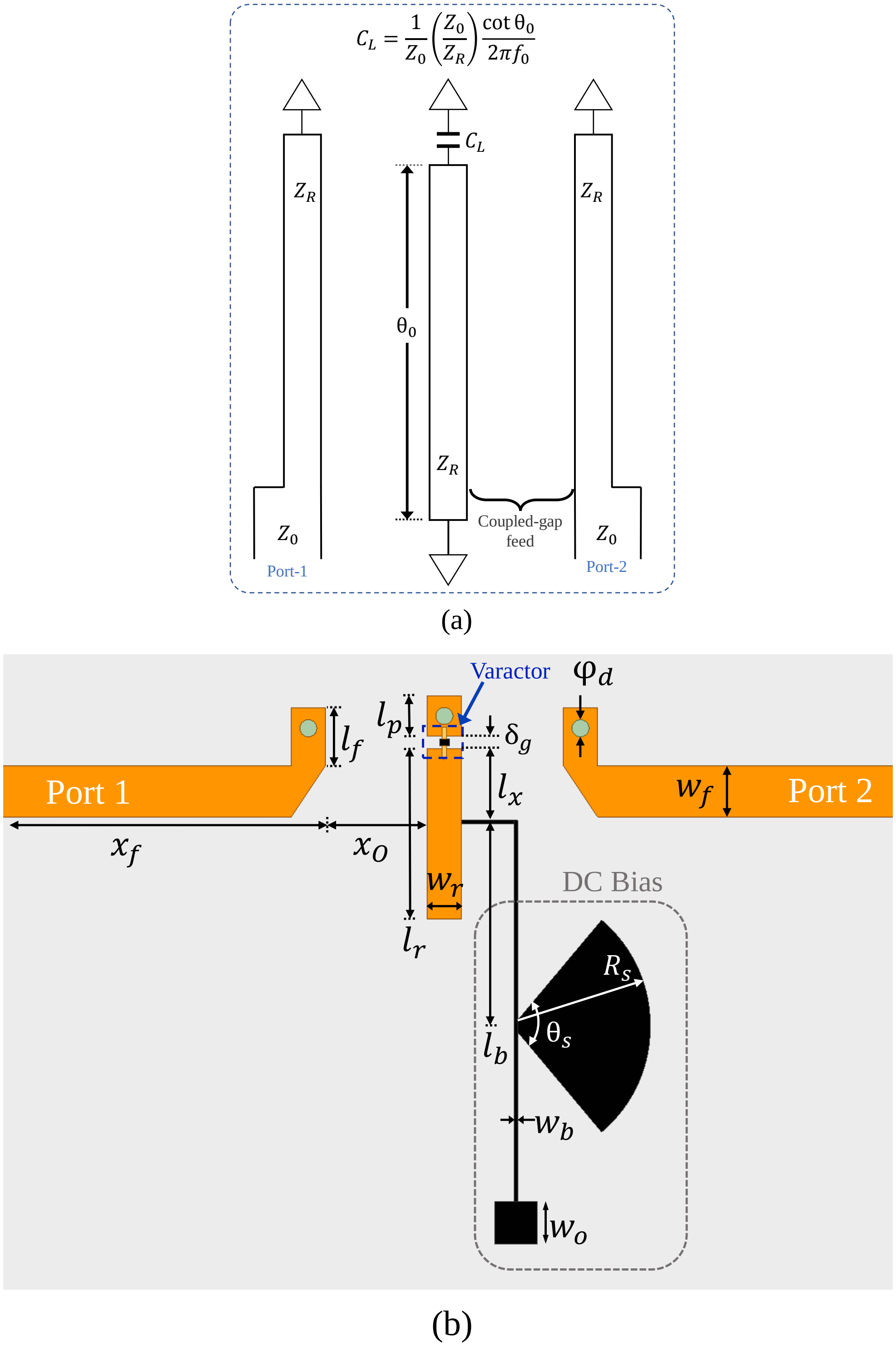

Figure 6.7: (a) Combline Resonator Topology (b) Implementation for varactor Q extraction: $x_f = 12$, $x_0 = 2.4$, $\delta_g = 0.36$, $l_f = 1.7$, $l_x = 2.1$, $l_r = 5$, $l_p = 1.2$, $l_b = 6$, $w_r = 1$, $w_f = 1.5$, $w_b = 0.1$, $w_0 = 1$, $\phi_d = 0.3$, $R_s = 4$ (all dimensions are in mm), and $\theta_s = 100°$. Overall top dimensions of the substrate is 25 mm × 30 mm.

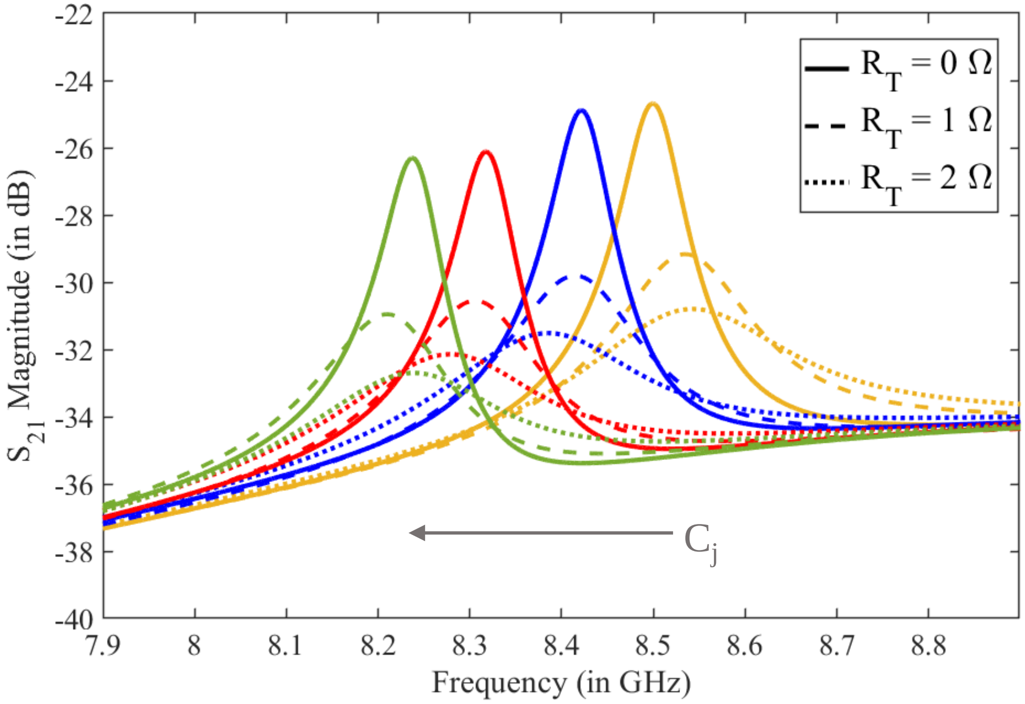

Figure 6.8: Transmission response for the tunable combline resonator at different varactor capacitance C_j. The zero resistance value (R_t = 0 Ω) represents the high-Q capacitor loaded resonator. Note that the S_{21} peaks are below 20 dB to accurately extract Q_u.

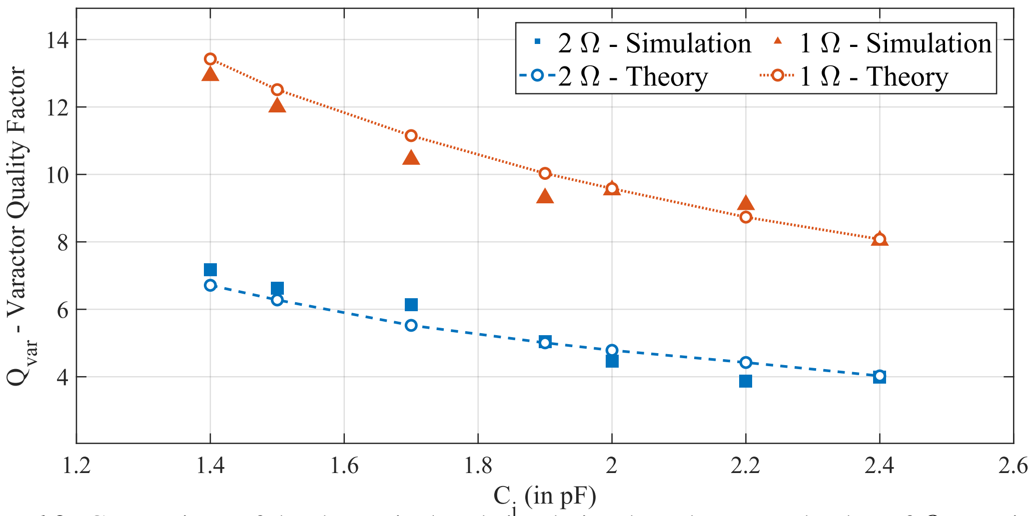

Figure 6.9: Comparison of the theoretical and simulation-based extracted value of Q_{var} using the proposed technique for a junction resistance $R_T = 1\ \Omega$ and $R_T = 2\ \Omega$.

6.5.4 Practical Considerations

In order to experimentally extract a varactor's quality factor, certain practical aspects of the method proposed in Section 6.5.1 need to be addressed. Firstly, the capacitor-loaded and varactor-loaded resonator designs should be manufactured using a single PCB board with the same copper electroplating processing cycle. This is important to ensure that the consequent reduction in the resonator Q_u due to conduction losses of imperfect electroplating is accurately captured in both the capacitor-loaded and varactor-loaded resonators. Doing so would ensure that the losses due to the varactor can be isolated with minimal errors.

The second consideration is regarding the finite quality factors of the lumped capacitors. In the simulation, the quality factor of the ideal lumped capacitor is infinite. This is obviously not true in practice, as the capacitors have a high Q corresponding to a low value of loss resistance. For instance, a prototype was manufactured for the test fixture presented in Section 6.5.1, with a 2 pF lumped capacitor from KYOCERA AVX (04022J0R3ZBTTR),

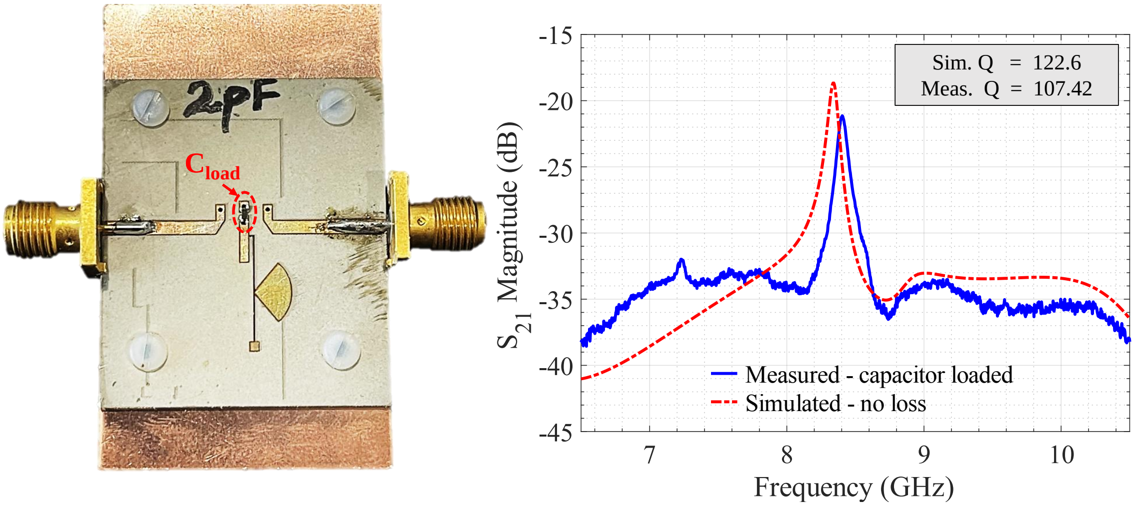

(a) (b)

Figure 6.10: Measured transmission response of a 2 pF capacitor-loaded combline resonator. (a) Fabricated Resonator prototype with a 2 pF capacitor soldered at one end of the stub. (b) Measured Vs. Simulated Transmission Response

as seen in Fig. 6.10 (a). The measured transmission response and the simulated response, assuming zero loss resistance and infinite Q are plotted in Fig. 6.10. The measured total Q shows a 14% reduction from simulation due to slightly higher conduction losses with in-house fabrication, as well as the finite losses of the capacitor itself. Therefore, to experimentally extract a varactor diode's Q accurately, the comparison should be done with a similar prototype of a capacitor-loaded resonator.

6.6 Conclusion

This chapter summarized and analyzed the practical non-idealities of tuning varactors when used at higher microwave frequencies. Specifically, the series junction resistance which exists with the varactor's junction capacitance can add high losses and degrade an antenna's radiation efficiency. The loss resistance value, R_T, is extracted from the varactor's quality factor, generally specified in data sheets at an arbitrary reverse-bias voltage and a lower frequency of 50 MHz. However, additional losses at microwave frequencies can further lower the varactor's Q, which can be challenging to predict.

To guarantee an acceptable RF performance of the manufactured design, the losses contributed by the varactor must be accurately characterized. In this chapter, a theoretical method to characterize the quality factor (Q) of varactor diodes for tunable antenna applications at microwave frequencies was presented. The proposed technique is based on extracting the unloaded quality factor of a tunable microwave resonator. The method's efficacy is validated through simulation results to extract the quality factor as a function of applied bias voltage and operating frequency. The proposed technique is not subject to calibration and de-embedding errors due to the weak coupling of the resonator at the input and output ports.

The varactor's Q-factor analysis is extremely relevant to characterize the varactor-tuned superstrate-loaded filtenna presented in Chapter 6. Furthermore, the characterization can be used to estimate the bias and frequency-dependent varactor quality factor for any reconfigurable RF and microwave device that incorporates varactor diodes for tunability. The future implications and improvements that can be performed on the characterization method are summarized in the conclusions section of the last chapter, Chapter 7.

Chapter 7

Conclusions and Future Work

7.1 Summary of Work

The goal of this thesis was to develop frequency-agile filtennas to improve the multi-functionality of next-generation RF Front-ends while also satisfying a system's size, weight, and power requirements. Traditional bandpass filter synthesis using coupled-resonator theory was applied in the design and implementation of reconfigurable filtennas. In the BPF-based filtenna synthesis method, the antenna is used as the last resonator of a bandpass filter and contributes a pole to the filtering response. As a result, a higher-order filtering response is derived using lesser resonators. Due to the integrated filtering and radiating characteristics, a filtenna can prove to be an excellent candidate for next-generation RF Front-ends.

A tunable microwave resonator forms the first building block of a filtenna unit, and an evanescent-mode (EVA-mode) cavity topology is used in the resonator implementation throughout this work. Several widely tunable, high-performance, and miniaturized bandpass filters have been implemented using the evanescent-mode technology, but they have not been broadly explored in the design of tunable filtennas and antennas.

First, a frequency-agile antenna was realized by integrating the EVA-mode resonator as a cavity-backing for an annular radiating slot aperture. A contactless tuning scheme was incorporated to tune the antenna across a frequency range of 1.7 GHz to 2.6 GHz using external long-range linear actuators. The antenna was experimentally tested to demonstrate high power handling capacity and was realized using simple manufacturing processes. The contactless-tuned EVA-mode antenna was then integrated into a filtenna topology. The filtenna demonstrated frequency agility from 2 GHz to 2.6 GHz using electronically controlled linear actuators.

Following the demonstration of tunable filtenna for S-Band applications, a new concept was conceived to scale the design for X-band (8-12 GHz) applications. The design process started by building the structure for a varactor-tuned cavity-backed slot antenna. To improve the compatibility with state-of-the-art tuning varactors, the antenna was loaded with a superstrate layer on the slot aperture. Finally, the superstrate-loaded varactor-tuned antenna was integrated into a frequency-agile filtenna for operation at the X-band frequency range.

In the last section of the thesis, the practical limitations of a varactor diode for high-frequency applications were studied and analyzed. The lower quality factors of varactor didoes can have a detrimental impact on the performance of the passive structure. In an antenna or a filtenna, these losses can lead to a reduction in radiation efficiency. From a system point of view, these losses can degrade the overall Signal-to-Noise ratio. However, there is a lack of characterization and extraction methods in the existing literature to accurately quantify the varactor's quality factor, especially at higher frequencies. Therefore, a new method to estimate the quality factor of a varactor diode was presented. With a relatively simple test procedure using no calibration or de-embedding techniques, the varactor's bias and frequency-dependent quality factor can be experimentally extracted. The proposed technique was validated through simulation results, and a framework for experimental tests was outlined.

7.2 Contributions

The work presented in this thesis has contributed to the field of frequency reconfigurable filtennas and antennas in several ways, which are summarized as follows,

- Theory, design, and fabrication of a high-power and widely tunable SIW-based evanescent-mode cavity-backed slot antenna using long-range external linear actuators [93].
- Design concept and fabrication of a SIW-integrated contactless-tuned filtenna based on evanescent-mode cavity resonators.
- Conceptual design and implementation of X-band tunable superstrate-loaded cavity-backed slot antenna with state-of-the-art varactor diodes.
- Design demonstration of a superstrate-loaded varactor-tuned filtenna for X-band applications.
- Proposal of a new method to accurately characterize the quality factor of varactor diodes for operation at microwave frequencies.

7.3 Future Work

Fabrication and Experimental validation of the X-Band filtenna

The next step for the presented work is to complete the fabrication and experimental validation of the varactor-tuned superstrate-loaded antenna and filtenna. Before the manufacturing process, it would be worthwhile to first experimentally extract the quality factor of the deployed beam-lead varactor didoes at the X-band frequency range, using the technique proposed in Section 6.5.1. This will enable a more accurate prediction of the antenna's and filtenna's radiation efficiency by taking into account the actual losses due to the varactor diode. Additionally, it will be interesting to quantify the deviation of the experimentally extracted varactor's quality factor from that predicted inaccurately by the generally used frequency scaling equation in Eq. (6.7).

Improvements in varactor-Q extraction method

In this thesis, the practical limitations due to a tuning varactor diode were studied in view of its effect on the tuning range and radiation performance of a filtenna. However, varactors also display unwanted non-linear effects due to inter-modulation distortion and are known to have very low power handling. The quality-factor extraction technique proposed in this work does not account for the non-linearity of the varactor diode. Therefore, further work can be done to improve the method by investigating and incorporating the effect of diode non-linearity and power handling capacity. Some foundational work on non-linear varactor diode characterization, presented in [94], can be used to extend the proposed Q extraction method for better diode characterization. To account for these practical limitations in the simulation and design process of varactor-tuned networks, co-simulation methods can be deployed to combine full-wave EM solvers with other user-defined nonlinear circuit element models in softwares like Advanced Design System (ADS). Such a combined simulation and design method can be used to precisely capture the impact of a varactor's non-idealities on the RF performance.

Performance enhancement of the varactor-tuned filtenna

The multi-functionality of the filtenna structures proposed in this work can be further improved by incorporating bandwidth control of the filtering response. This can be implemented by incorporating a tuning element to control the inter-resonator coupling between the resonators and radiating element. Furthermore, a tuning mechanism can also be incorporated at the input and output ports to control the group delay or out-of-band attenuation level. These developments would enhance the filtering response of the filtenna at the lower and higher end of the frequency range while also allowing a method to correct post-fabrication errors.

To improve the non-linearity issues exhibited by the varactor diode, an anti-series configuration can be used for the tuning varactor in the superstrate-loaded antenna structure presented in Chapter 5. The anti-series varactor configuration, seen in Fig. 7.1, has been shown to improve the linearity performance by enforcing a distortion cancellation mechanism [95]-[98]. An improvement in the power-handling capability of a varactor can also be made by implementing a multiple stack-up of the anti-series varactor units [98]. This configuration, shown in Fig. 7.2, results in a distribution of the RF voltage between an increased number of varactors, thereby increasing the device's power handling capacity.

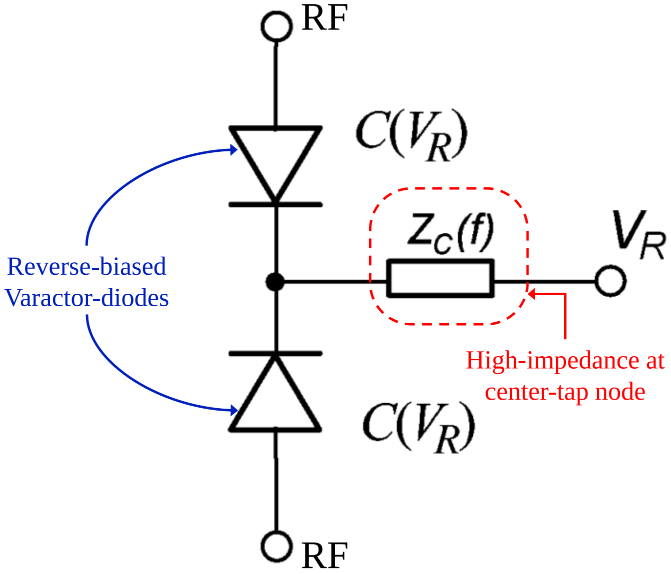

Figure 7.1: Anti-series varactor diode configuration for improved linearity performance [96]. Theoretically, if the center-tap impedance Z_C is infinitely high, the diode will not exhibit any intermodulation distortion under two-tone excitation [96].

In order to improve the varactor Q and drastically improve the power handling, the

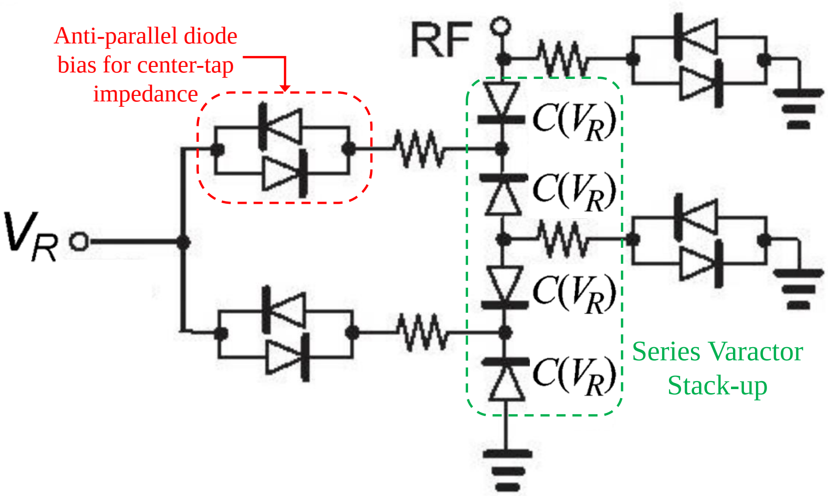

Figure 7.2: Multiple varactor stack-up topologies to improve varactor diode power handling, as detailed in [98].

intrinsic properties of the varactor's semiconductor material need to be altered. This work uses Gallium Arsenide (GaAs) varactor diodes which exhibit better quality factors than silicon-based diodes, but they still exhibit losses at higher frequencies and have low power handling capability. Therefore, alternate semiconductor varactor materials can be investigated to improve the filtenna performance. For instance, there is a rapid advancement in wide band-gap semiconductor materials like Gallium Nitride (GaN) and Silicon Carbide (SiC), which exhibit higher breakdown field strengths [97]-[102]. The maximum electric field strength is established by the maximum voltage that the semiconductor can withstand, after which avalanche breakdown occurs [100].

As seen in Table 7.1, the breakdown field strength of GaN and SiC are nearly ten times higher than that of silicon, making them capable of handling high-power conditions. Therefore, there is a potential for improving the performance of tunable microwave devices by developing GaN or SiC-based varactor diodes.

Table 7.1: Comparison of different semiconductor materials used in varactor diodes

Semiconductor Type	**Band-Gap (eV)**	**Breakdown E-Field (MV/cm)**
Si	1.1	0.3
GaAs	1.43	0.4
GaN	3.4	3.5†
SiC	3.3	3†

† Values differ based on the semiconductor base doping [99]; range is from 2.5 - 5 MV/cm.

References

[1] A. M. Wyglinski, R. Getz, T. Collins, and D. Pu, *Software-defined radio for engineers*. Artech House, 2018.

[2] H. Chan, "Advanced microwave technologies for smart flexible satellite," in *2011 IEEE MTT-S International Microwave Symposium*. IEEE, 2011, pp. 1–4.

[3] R. R. Mansour, F. Huang, S. Fouladi, W. D. Yan, and M. Nasr, "High-Q tunable filters: Challenges and potential," *IEEE Microwave Magazine*, vol. 15, no. 5, pp. 70–82, 2014.

[4] K. Entesari, A. P. Saghati, V. Sekar, and M. Armendariz, "Tunable SIW structures: antennas, VCOs, and filters," *IEEE Microwave Magazine*, vol. 16, no. 5, pp. 34–54, 2015.

[5] J. Uher and W. Hoefer, "Tunable microwave and millimeter-wave band-pass filters," *IEEE Transactions on Microwave Theory and Techniques*, vol. 39, no. 4, pp. 643–653, 1991.

[6] R. L. Haupt and M. Lanagan, "Reconfigurable antennas," *IEEE Antennas and Propagation Magazine*, vol. 55, no. 1, pp. 49–61, 2013.

[7] J. Aberle, S.-H. Oh, D. Auckland, and S. Rogers, "Reconfigurable antennas for wireless devices," *IEEE Antennas and Propagation Magazine*, vol. 45, no. 6, pp. 148–154, 2003.

[8] A. Petosa, "An overview of tuning techniques for frequency-agile antennas," *IEEE Antennas and Propagation Magazine*, vol. 54, no. 5, pp. 271–296, 2012.

[9] H. Friis, "Noise figures of radio receivers," *Proceedings of the IRE*, vol. 32, no. 7, pp. 419–422, 1944.

[10] C. X. Mao, Y. Zhang, X. Y. Zhang, P. Xiao, Y. Wang, and S. Gao, “Filtering antennas: Design methods and recent developments,” *IEEE Microwave Magazine*, vol. 22, no. 11, pp. 52–63, 2021.

[11] C.-X. Mao, S. Gao, Y. Wang, Q. Luo, and Q.-X. Chu, “A shared-aperture dual-band dual-polarized filtering-antenna-array with improved frequency response,” *IEEE Transactions on Antennas and Propagation*, vol. 65, no. 4, pp. 1836–1844, 2017.

[12] M. Troubat, S. Bila, M. Thevenot, D. Baillargeat, T. Monediere, S. Verdeyme, and B. Jecko, “Mutual synthesis of combined microwave circuits applied to the design of a filter-antenna subsystem,” *IEEE Transactions on Microwave Theory and Techniques*, vol. 55, no. 6, pp. 1182–1189, 2007.

[13] C.-H. Wu, C.-H. Wang, S.-Y. Chen, and C. H. Chen, “Balanced-to-unbalanced bandpass filters and the antenna application,” *IEEE Transactions on Microwave Theory and Techniques*, vol. 56, no. 11, pp. 2474–2482, 2008.

[14] J. Deng, S. Hou, L. Zhao, and L. Guo, “Wideband-to-narrowband tunable monopole antenna with integrated bandpass filters for uwb/wlan applications,” *IEEE Antennas and Wireless Propagation Letters*, vol. 16, pp. 2734–2737, 2017.

[15] Y. Chen and Y. Zhou, “Design of a filter-antenna subsystem for UWB communications,” in *2009 3rd IEEE International Symposium on Microwave, Antenna, Propagation and EMC Technologies for Wireless Communications*, 2009, pp. 593–595.

[16] M. A. Abdelghany, W. A. Ali, H. A. Mohamed, and A. A. Ibrahim, “Filtenna with frequency reconfigurable operation for cognitive radio and wireless applications,” *Micromachines*, vol. 14, no. 1, p. 160, 2023.

[17] K. R. Mahmoud and A. M. Montaser, “Design of compact mm-wave tunable filtenna using capacitor loaded trapezoid slots in ground plane for 5G router applications,” *IEEE Access*, vol. 8, pp. 27 715–27 723, 2020.

[18] Y. Tawk, J. Costantine, and C. G. Christodoulou, “A varactor-based reconfigurable filtenna,” *IEEE Antennas and Wireless Propagation Letters*, vol. 11, pp. 716–719, 2012.

[19] A. H. Ramadan, K. Y. Kabalan, J. Costantine, Y. Tawk, and C. G. Christodoulou, "A tunable filtenna for cognitive radio applications," in *2015 9th European Conference on Antennas and Propagation (EuCAP)*, 2015, pp. 1–2.

[20] R. E. Lovato, T. Li, and X. Gong, "Tunable filter/antenna integration with bandwidth control," *IEEE Transactions on Microwave Theory and Techniques*, vol. 67, no. 10, pp. 4196–4205, 2019.

[21] P. F. Hu, Y. M. Pan, X. Y. Zhang, and B.-J. Hu, "A filtering patch antenna with reconfigurable frequency and bandwidth using F-shaped probe," *IEEE Transactions on Antennas and Propagation*, vol. 67, no. 1, pp. 121–130, 2018.

[22] H. A. Atallah, A. B. Abdel-Rahman, K. Yoshitomi, and R. K. Pokharel, "Compact frequency reconfigurable filtennas using varactor loaded T-shaped and H-shaped resonators for cognitive radio applications," *IET Microwaves, Antennas & Propagation*, vol. 10, no. 9, pp. 991–1001, 2016.

[23] L. Cifola, G. Gerini, and A. Morini, "Design of a low profile phased array filtenna with frequency agility and wide spurious rejection band," in *2013 7th European Conference on Antennas and Propagation (EuCAP)*, 2013, pp. 1196–1200.

[24] H. Nachouane, A. Najid, F. Riouch, and A. Tribak, "Electronically reconfigurable filtenna for cognitive radios," *Microwave and Optical Technology Letters*, vol. 59, no. 2, pp. 399–404, 2017.

[25] A. K. Gangwar and M. S. Alam, "Frequency reconfigurable dual-band filtenna," *AEU-International Journal of Electronics and Communications*, vol. 124, p. 153239, 2020.

[26] M. Patriotis, F. N. Ayoub, Y. Tawk, J. Costantine, and C. G. Christodoulou, "A compact active Ka-band filtenna for CubeSats," *IEEE Antennas and Wireless Propagation Letters*, vol. 20, no. 11, pp. 2095–2099, 2021.

[27] Y. Tawk, J. Costantine, and C. G. Christodoulou, "Reconfigurable filtennas and MIMO in cognitive radio applications," *IEEE Transactions on Antennas and Propagation*, vol. 62, no. 3, pp. 1074–1083, 2014.

[28] L. Rodrigues, T. Varum, and J. N. Matos, "The application of reconfigurable filtennas in mobile satellite terminals," *IEEE Access*, vol. 8, pp. 77 179–77 187, 2020.

[29] M. M. Fakharian, P. Rezaei, A. A. Orouji, and M. Soltanpur, “A wideband and reconfigurable filtering slot antenna,” *IEEE Antennas and Wireless Propagation Letters*, vol. 15, pp. 1610–1613, 2016.

[30] H. A. Atallah, A. B. Abdel-Rahman, K. Yoshitomi, and R. K. Pokharel, “Compact frequency tunable filtenna with wide continuous tuning range using capacitively loaded folded arms open loop resonator for interweave cognitive radio applications,” in *2016 33rd National Radio Science Conference (NRSC)*, 2016, pp. 87–93.

[31] L. Dussopt and G. M. Rebeiz, “Intermodulation distortion and power handling in RF MEMS switches, varactors, and tunable filters,” *IEEE Transactions on Microwave Theory and Techniques*, vol. 51, no. 4, pp. 1247–1256, 2003.

[32] P. Kannam, S. Ponczak, and J. Olmstead, “Design considerations of hyperabrupt varactor diodes,” *IEEE Transactions on Electron Devices*, vol. 18, no. 2, pp. 109–115, 1971.

[33] C. Huang, K. Buisman, L. K. Nanver, P. J. Zampardi, L. E. Larson, and L. C. N. de Vreede, “Design concepts for semiconductor based ultra-linear varactor circuits (invited),” in *2010 IEEE Bipolar/BiCMOS Circuits and Technology Meeting (BCTM)*, 2010, pp. 204–211.

[34] L. Silva, A. Alves, and A. Cerqueira Sodré, “Optically controlled reconfigurable filtenna,” *International Journal of Antennas and propagation*, vol. 2016, 2016.

[35] A. A. Alves, L. G. da Silva, E. C. Vilas Boas, D. H. Spadoti, and S. Arismar Cerqueira, “Continuously frequency-tunable horn filtennas based on dual-post resonators,” *International Journal of Antennas and Propagation*, vol. 2019, pp. 1–12, 2019.

[36] K.-R. Xiang, F.-C. Chen, and Q.-X. Chu, “A tunable filtering antenna based on coaxial cavity resonators,” *IEEE Transactions on Antennas and Propagation*, vol. 70, no. 5, pp. 3259–3268, 2021.

[37] M. Thibodeau, “Theory, design and fabrication of frequency agile filtenna,” Master’s thesis, University of Oklahoma, 2020.

[38] G. Matthaei, L. Young, and E. Jones, *Microwave Filters, Impedance-matching Networks, and Coupling Structures*, ser. Artech House microwave library. Artech House, 1980. [Online]. Available: https://books.google.com/books?id=cRMoAQAAMAAJ

[39] S. Saeedi, “Frequency-agile microwave filters for radars with simultaneous transmission and reception,” PhD dissertation, University of Oklahoma, 2015.

[40] R. J. Cameron, C. M. Kudsia, and R. R. Mansour, *Microwave filters for communication systems: fundamentals, design, and applications*. John Wiley & Sons, 2018.

[41] M. Dishal, “Alignment and adjustment of synchronously tuned multiple-resonant-circuit filters,” *Proceedings of the IRE*, vol. 39, no. 11, pp. 1448–1455, 1951.

[42] J. Hong, “Microstrip filters for RF/microwave applications,” 2001.

[43] Q.-S. Wu, X. Zhang, and L. Zhu, “An improved method for accurate extraction of coupling coefficient between a lossy radiator and a lossless resonator in filtering antennas,” *IEEE Access*, vol. 6, pp. 39 927–39 935, 2018.

[44] A. Bauer, “External quality factor of antennas and their use in filtenna design,” Master’s thesis, University of Oklahoma, 2022.

[45] J. P. Dunsmore, “The time-domain response of coupled-resonator filters with applications to tuning,” PhD dissertation, University of Leeds, 2004.

[46] D. Peroulis, E. Naglich, M. Sinani, and M. Hickle, “Tuned to resonance: Transfer-function-adaptive filters in evanescent-mode cavity-resonator technology,” *IEEE Microwave magazine*, vol. 15, no. 5, pp. 55–69, 2014.

[47] H. Joshi, H. H. Sigmarsson, D. Peroulis, and W. J. Chappell, “Highly loaded evanescent cavities for widely tunable high-Q filters,” in *2007 IEEE/MTT-S International Microwave Symposium*, 2007, pp. 2133–2136.

[48] S. Moon, H. H. Sigmarsson, H. Joshi, and W. J. Chappell, “Substrate integrated evanescent-mode cavity filter with a 3.5 to 1 tuning ratio,” *IEEE Microwave and Wireless Components Letters*, vol. 20, no. 8, pp. 450–452, 2010.

[49] H. Joshi, H. H. Sigmarsson, S. Moon, D. Peroulis, and W. J. Chappell, “High-Q fully reconfigurable tunable bandpass filters,” *IEEE Transactions on Microwave Theory and Techniques*, vol. 57, no. 12, pp. 3525–3533, 2009.

[50] A. Semnani, K. Chen, and D. Peroulis, “Microwave gas breakdown in tunable evanescent-mode cavity resonators,” *IEEE Microwave and Wireless Components Letters*, vol. 24, no. 5, pp. 351–353, 2014.

[51] K. Chen, A. Semnani, and D. Peroulis, “High-power microwave gas discharge in high-Q evanescent-mode cavity resonators and its instantaneous/long-term effects,” in *2013 IEEE MTT-S International Microwave Symposium Digest (MTT)*, 2013, pp. 1–4.

[52] S. Saeedi, J. Lee, and H. Sigmarsson, “Prediction of power handling in tunable, high-Q, substrate-integrated, evanescent-mode cavity bandpass filters,” *Electronics Letters*, vol. 52, no. 10, pp. 846–848, 2016.

[53] M. Abu Khater and D. Peroulis, “Real-time feedback control system for tuning evanescent-mode cavity filters,” *IEEE Transactions on Microwave Theory and Techniques*, vol. 64, no. 9, pp. 2804–2813, 2016.

[54] S. Saeedi, S. Atash-Bahar, J. Lee, and H. Sigmarsson, “Control system for piezoelectric-actuator-based tunable evanescent-mode cavity microwave filters,” *IEEE Transactions on Components, Packaging and Manufacturing Technology*, vol. 8, no. 11, pp. 1979–1989, 2018.

[55] X. Liu, A. Fruehling, L. P. B. Katehi, W. J. Chappell, and D. Peroulis, “Capacitive monitoring of electrostatic mems tunable evanescent-mode cavity resonators,” in *2011 6th European Microwave Integrated Circuit Conference*, 2011, pp. 466–469.

[56] X. Liu, L. P. B. Katehi, W. J. Chappell, and D. Peroulis, “High-Q tunable microwave cavity resonators and filters using soi-based rf mems tuners,” *Journal of Microelectromechanical Systems*, vol. 19, no. 4, pp. 774–784, 2010.

[57] M. Abdelfattah and D. Peroulis, “High-Q tunable evanescent-mode cavity SIW resonators and filters with contactless tuners,” *IEEE Transactions on Microwave Theory and Techniques*, vol. 67, no. 9, pp. 3661–3672, 2019.

[58] M. Abu Khater and D. Peroulis, “Real-time feedback control system for tuning evanescent-mode cavity filters,” *IEEE Transactions on Microwave Theory and Techniques*, vol. 64, no. 9, pp. 2804–2813, 2016.

[59] A. Semnani, G. S. Shaffer, M. D. Sinanis, and D. Peroulis, "High-power impedance tuner utilising substrate-integrated evanescent-mode cavity technology and external linear actuators," *IET Microwaves, Antennas & Propagation*, vol. 13, no. 12, pp. 2067–2072, 2019.

[60] A. Anand, J. Small, D. Peroulis, and X. Liu, "Theory and design of octave tunable filters with lumped tuning elements," *IEEE Transactions on Microwave Theory and Techniques*, vol. 61, no. 12, pp. 4353–4364, 2013.

[61] D. Deslandes and K. Wu, "Accurate modeling, wave mechanisms, and design considerations of a substrate integrated waveguide," *IEEE Transactions on microwave theory and techniques*, vol. 54, no. 6, pp. 2516–2526, 2006.

[62] New Scale Technologies, "Micro linear actuator," NewScaleTech.com, https://www.newscaletech.com/micro-motion-modules/m3-l-linear-smart-actuators/ (accessed 25 Feb 2023).

[63] A. Pourghorban Saghati and K. Entesari, "A reconfigurable SIW cavity-backed slot antenna with one octave tuning range," *IEEE Transactions on Antennas and Propagation*, vol. 61, no. 8, pp. 3937–3945, 2013.

[64] C. R. White and G. M. Rebeiz, "A shallow varactor-tuned cavity-backed slot antenna with a 1.9:1 tuning range," *IEEE Transactions on Antennas and Propagation*, vol. 58, no. 3, pp. 633–639, 2010.

[65] L. Ge, Y. Li, J. Wang, and C.-Y.-D. Sim, "A low-profile reconfigurable cavity-backed slot antenna with frequency, polarization, and radiation pattern agility," *IEEE Transactions on Antennas and Propagation*, vol. 65, no. 5, pp. 2182–2189, 2017.

[66] R.-S. Chen, L. Zhu, S.-W. Wong, X.-Z. Yu, Y. Li, W. He, L. Zhang, and Y. He, "Novel reconfigurable full-metal cavity-backed slot antennas using movable metal posts," *IEEE Transactions on Antennas and Propagation*, vol. 69, no. 10, pp. 6154–6164, 2021.

[67] A. Semnani, M. D. Sinanis, and D. Peroulis, "An evanescent-mode cavity-backed high-power tunable slot antenna," *IEEE Transactions on Antennas and Propagation*, vol. 67, no. 6, pp. 3712–3719, 2019.

[68] N. Duangrit, B. Hong, A. D. Burnett, P. Akkaraekthalin, I. D. Robertson, and N. Somjit, “Terahertz dielectric property characterization of photopolymers for additive manufacturing,” *IEEE Access*, vol. 7, pp. 12 339–12 347, 2019.

[69] Y.-M. Wu, S.-W. Wong, H. Wong, and F.-C. Chen, “A design of bandwidth-enhanced cavity-backed slot filtenna using resonance windows,” *IEEE Transactions on Antennas and Propagation*, vol. 67, no. 3, pp. 1926–1930, 2019.

[70] B.-L. Zheng, S.-W. Wong, L. Zhu, and Y. He, “Broadband duplex–filtenna based on low-profile metallic cavity packaging,” *IEEE Transactions on Components, Packaging and Manufacturing Technology*, vol. 8, no. 8, pp. 1451–1457, 2018.

[71] Q. Shi-Shan, Z. Keren, and W. Wen, “Compact Ka-band conical beam filtenna,” *IET Microwaves, Antennas & Propagation*, vol. 17, no. 3, pp. 208–215, 2023.

[72] Y. Yusuf, H. Cheng, and X. Gong, “A seamless integration of 3-D vertical filters with highly efficient slot antennas,” *IEEE Transactions on Antennas and Propagation*, vol. 59, no. 11, pp. 4016–4022, 2011.

[73] H. Cheng, Y. Yusuf, and X. Gong, “Vertically integrated three-pole filter/antennas for array applications,” *IEEE Antennas and Wireless Propagation Letters*, vol. 10, pp. 278–281, 2011.

[74] Y. Yusuf and X. Gong, “Compact low-loss integration of High- Q 3-D filters with highly efficient antennas,” *IEEE Transactions on Microwave Theory and Techniques*, vol. 59, no. 4, pp. 857–865, 2011.

[75] R. Lovato and X. Gong, “A tunable SIW integrated filter/antenna,” in *2017 IEEE International Symposium on Antennas and Propagation USNC/URSI National Radio Science Meeting*, 2017, pp. 2181–2182.

[76] T. Li and X. Gong, “Integration of slot antenna with evanescent-mode filter for tunable front-end applications,” in *2013 IEEE Antennas and Propagation Society International Symposium (APSURSI)*, 2013, pp. 580–581.

[77] N. Nguyen Trong and C. Fumeaux, “Half-mode substrate-integrated waveguides and their applications for antenna technology: A review of the possibilities for antenna design,” *IEEE Antennas and Propagation Magazine*, vol. PP, pp. 1–1, 10 2018.

[78] MACOM 46580-1209, “Macom technologies , gallium arsenide hyper-abrupt varactor diodes,” NewScaleTech.com, https://www.macom.com/products/product-detail/MA46580-1209 (accessed 20 Feb 2023).

[79] A. F. Horn, J. W. Reynolds, P. A. LaFrance, and J. C. Rautio, “Effect of conductor profile on the insertion loss, phase constant, and dispersion in thin high-frequency transmission lines,” 2010.

[80] C. S. Aitchison, R. Davies, I. D. Higgins, S. R. Longley, B. H. Newton, J. F. Wells, and J. C. Williams, “Lumped-circuit elements at microwave frequencies,” *IEEE Transactions on Microwave Theory and Techniques*, vol. 19, no. 12, pp. 928–937, 1971.

[81] B. Syrett, “Novel DGS-CSRR-based microstrip low pass filter with ultra wide suppression,” *IEEE Transactions on Microwave Theory and Techniques*, vol. 28, no. 8, pp. 925–927, 1980.

[82] R. Dehbashi, H. Oskouei, and K. Forooraghi, “A new compact biasing circuit for active integrated antenna and MMIC applications,” in *2006 IEEE Antennas and Propagation Society International Symposium*, 2006, pp. 1519–1522.

[83] B. Syrett, “A broad-band element for microstrip bias or tuning circuits (short papers),” *IEEE Transactions on Microwave Theory and Techniques*, vol. 28, no. 8, pp. 925–927, 1980.

[84] N. Jana, M. K. Mandal, and R. Shaw, “An improved design of a bias tee using a modified radial stub,” in *2019 IEEE MTT-S International Microwave and RF Conference (IMARC)*, 2019, pp. 1–4.

[85] T. H. Lee, *Planar Microwave Engineering: A Practical Guide to Theory, Measurement, and Circuits*. Cambridge University Press, 2004.

[86] R. Cory and S. Solutions, “The nuts and bolts of tuning varactors,” *High Freq. Electron*, vol. 8, no. 2, pp. 42–51, 2009.

[87] B. DeLoach, “A new microwave measurement technique to characterize diodes and an 800 Gc cutoff frequency varactor at zero volts bias,” in *PTGMTT National Symposium Digest*, vol. 63, no. 1, 1963, pp. 85–92.

[88] J. Roe and F. Rosenbaum, “Characterization of packaged microwave diodes in reduced-height waveguide,” *IEEE Transactions on Microwave Theory and Techniques*, vol. 18, no. 9, pp. 638–642, 1970.

[89] G. H. Stauffer and R. Collins, “Finding the lumped element varactor diode model,” *High Frequency Electronics*, vol. 2, no. 6, pp. 22–28, 2003.

[90] D. Xu and G. Branner, “An efficient technique for varactor diode characterization,” in *Proceedings of 40th Midwest Symposium on Circuits and Systems. Dedicated to the Memory of Professor Mac Van Valkenburg*, vol. 1, 1997, pp. 591–594 vol.1.

[91] S. Guo, Y. Zhao, Z. Cao, L. Miao, S. Bie, and J. Jiang, “Device modeling of RF varactor diodes for adjustable microwave reflectivity in active frequency selective surfaces,” *Journal of Physics D: Applied Physics*, vol. 54, no. 34, p. 345001, 2021.

[92] G. Matthaei, “Microwave filters, impedance-matching networks and coupling structures,” *Artech House Book*, pp. 775–809, 1980.

[93] R. Agasti, C. G. Blosser, J. E. Ruyle, and H. H. Sigmarsson, “Tunable SIW-based evanescent-mode cavity-backed slot antenna with contactless tuning,” *IEEE Access*, pp. 1–1, 2023.

[94] C. M. Andersson, M. Thorsell, and N. Rorsman, “Nonlinear characterization of varactors for tunable networks by active source–pull and load–pull,” *IEEE transactions on microwave theory and techniques*, vol. 59, no. 7, pp. 1753–1760, 2011.

[95] D. Berthiaume, J.-J. Laurin, and N. G. Constantin, “Anti-series varactor network with improved linearity performances in the presence of inductive and capacitive parasitics,” *IEEE Access*, vol. 9, pp. 48 325–48 340, 2021.

[96] K. Buisman, C. Huang, P. J. Zampardi, and L. C. N. de Vreede, “RF power insensitive varactors,” *IEEE Microwave and Wireless Components Letters*, vol. 22, no. 8, pp. 418–420, 2012.

[97] R. Amirpour, D. Schwantuschke, P. Brueckner, R. Quay, and O. Ambacher, “High-Q anti-series AlGaN/GaN high electron-mobility varactor,” in *2019 IEEE MTT-S International Microwave Symposium (IMS)*, 2019, pp. 599–602.

[98] K. Buisman, C. Huang, A. Akhnoukh, M. Marchetti, L. de Vreede, L. Larson, and L. Nanver, "Varactor topologies for RF adaptivity with improved power handling and linearity," in *2007 IEEE/MTT-S International Microwave Symposium*, 2007, pp. 319–322.

[99] A. Konstantinov, Q. Wahab, N. Nordell, and U. Lindefelt, "Ionization rates and critical fields in 4H silicon carbide," *Applied Physics Letters*, vol. 71, no. 1, pp. 90–92, 1997.

[100] V. Dmitriev, K. Irvine, C. Carter Jr, N. Kuznetsov, and E. Kalinina, "Electric breakdown in GaN p-n junctions," *Applied physics letters*, vol. 68, no. 2, pp. 229–231, 1996.

[101] M. Roy, R. J. Ward, and J. A. Higgins, "SiC varactor based tunable filters with enhanced linearity," in *2008 IEEE Topical Meeting on Silicon Monolithic Integrated Circuits in RF Systems*, 2008, pp. 163–166.

[102] P. C. Chen, P. M. Asbeck, and S. A. Dayeh, "Freestanding high-power GaN multi-fin camel diode varactors for wideband telecom tunable filters," *IEEE Transactions on Electron Devices*, vol. 70, no. 3, pp. 963–970, 2023.